

Plasmonic Excitations and Coupling in Atomic Wires

Von der Fakultät für Mathematik und Physik
der Gottfried Wilhelm Leibniz Universität Hannover
zur Erlangung des akademischen Grades

Doktor der Naturwissenschaften

Dr. rer. nat.

genehmigte Dissertation

von

M. Sc. Zamin Mamiyev

2020

Referent: Prof. Dr. Herbert Pfnür *Gottfried Wilhelm Leibniz Universität Hannover*

Korreferent: Prof. Dr. Mario Rocca *Università degli Studi di Genova*

Korreferent: Prof. Dr. Simone Sanna *Justus-Liebig-Universität Gießen*

Tag der Promotion: 22.09.2020

Keywords: *Atomic wires, low-dimensional plasmons, electronic correlations, surface states, adsorption*

Schlagworte: *Atomare Drähte, niedrigdimensionalen Plasmonen, elektronische Korrelationen, Oberflächenzustände, Adsorption*

Dedicated to My Family

Abstract

Metal-induced atomic wires on the semiconductor surfaces are the ultimate limit of long-range ordered quasi-one-dimensional electronic systems. In this thesis, the plasmonic excitations and their coupling with the structural parameters, as well as the role of the embedding medium on the Au atomic wires, self-organized on flat and high-indexed Si surfaces were investigated.

The atomic wire systems in the focus of this thesis, Si(111)-(5×2)-Au and Si(hhk)-(1×2)-Au, were generated by adsorption of submonolayers of gold onto the reconstructed surfaces. These systems feature a broad range of characteristics that can exemplarily be classified based on the number of atomic chains per terrace, inter-wire spacing, local structure of step edges, number of metallic bands and band filling. High-resolution EELS-LEED and SPA-LEED were used as the main experimental methods to address the mentioned properties and furthers. These experimental results were compared with the atomistic DFT calculations. Moreover, for the Si(553)-Au system, IR transmittance experiments were performed to investigate the optically active standing wave formation after oxidation.

As a prominent property of conductive electrons, collective excitation is strongly coupled to the crystal lattice, electronic band structure, electronic and spatial confinement as well as properties of the surrounding physical media. This makes plasmonic excitation an adequate tool to probe a variety of interactions and coupling between those parameters associated with metallic structures. Taking this advantage, the present thesis investigates plasmonic excitations and their coupling to structural and environmental parameters. As a result of this investigation, a strong cross-coupling of the electronic and structural properties was revealed. For example, electronic doping to the Si(553)-Au system enhances order along the wires, which also results in band gap opening at the same time. Moreover, modification of individual structural motifs on the Si(557)-Au surface leads to a unique rearrangement of the band structure while preserving the metallicity. Also, combining the plasmon dispersion with calculated band structures, the kinetic sequence of the oxidation of the different atomic groups could be studied.

For most investigated systems, an almost quantitative agreement between atomistic calculations and plasmon spectroscopy results was achieved, validating the calculated band structure and model used. In particular, the unoccupied part of the band structure was investigated for atomic wire systems. As an example, for the very first time unoccupied electronic band structure of the Si(111)-(5×2)-Au surface was investigated by comparing plasmon dispersion with the available DFT calculated bands. Moreover, doping of the latter surface with surplus Au and atomic H resulted in a metal-insulator transition. However, due to their highly robust anisotropic structure and electronic properties, the doping and oxidation of Si(hhk)-Au systems underline more specific mechanisms in the fine-tuning of metallicity. Some of these particular mechanisms include switching of bands, electronic interaction of adjacent terraces, cross-talking of dimerization and band gap opening, self-healing of defects, robust metallicity due to the site-specific oxidation, and indirect charge transfer to the metallic states, etc. have been extensively studied in this thesis.

Zusammenfassung

Metallische atomare Drahnte auf Halbleiteroberflachen stellen die physikalische die Grenze fur langreichweitige geordnete quasi-eindimensionale elektronische Systeme dar. In dieser Arbeit wurden sowohl plasmonische Anregungen und deren Kopplung mit strukturellen Parametern, als auch die Rolle des Tragermaterials auf atomare Golddrahnte untersucht, die durch Selbstorganisation auf flachen und gestuften Silizium-Flachen hergestellt wurden. Schwerpunkt der vorliegenden Arbeit sind die Systeme Si(111)-(5×2)-Au und Si(hhk)-(1×2)-Au, die durch die Adsorption von Submonolagen Gold auf rekonstruierte Siliziumoberflachen hergestellt wurden. Diese Systeme zeigen eine Reihe von Charakteristika, die anhand der Anzahl an atomaren Ketten pro Terrasse, dem Abstand der Ketten, der lokalen Struktur der Stufenkanten und der Anzahl metallischer Bander klassifiziert werden konnen. Hochauflosendes EELS-LEED und SPA-LEED wurden als experimentelle Hauptmethoden zur Analyse der genannten Eigenschaften verwendet. Die experimentellen Ergebnisse wurden mit atomistischen DFT-Rechnungen verglichen und diskutiert. Weiterhin, wurden fur das Si(553)-Au-system IR-Transmissionsexperimente durchgefuhrt, um die optisch stehenden Welle nach der Oxidation zu untersuchen. Als markante Eigenschaft metallischer Ladungstrager ist deren kollektive Anregung stark verknupft mit dem Kristallgitter, der elektronischen Bandstruktur, der raumlichen Einengung sowie mit den Eigenschaften des umgebenden Materials. Dies macht plasmonische Anregung zu einem adaquaten Werkzeug um die vielen Wechselwirkungen und Kopplungen, die mit den metallischen Strukturen verbunden sind, zu untersuchen. Basierend auf diesem Ansatz, analysiert die vorliegende Arbeit die plasmonischen Anregungen und ihre Kopplung zu strukturellen und Umgebungsparametern. Als ein Ergebnis dieser Untersuchungen, konnte eine starke Kopplung zwischen den elektronischen und strukturellen Parametern aufgezeigt werden. Beispielweise verbessert elektronische Dotierung des Si(553)-Au-Systems die Ordnung in den Ketten, bei gleichzeitiger Offnung einer Bandlucke. Weitere Modifikationen von strukturellen Gegebenheiten in dem System fuhren zu einer einzigartigen Neuordnung der Bandstruktur bei Aufrechterhaltung der metallischen Eigenschaften. Des Weiteren konnte durch eine Kombination der Plasmonendispersion und der Bandstruktur die kinetischen Sequenz des Oxidationsprozesses verschiedener atomarer Gruppen untersucht werden. Fur einen Grosteil der untersuchten Systeme, konnte eine nahezu quantitative Ubereinstimmung zwischen den atomaren Berechnungen und den Ergebnissen der Plasmonenspektroskopie erzielt werden, wodurch sowohl die berechnete Bandstruktur als auch das verwendete Modell verifiziert wurden. Im Speziellen konnte erstmalig der unbesetzte Teil der Bandstruktur atomarer Kettensysteme untersucht werden, beispielweise die unbesetzte Bandstruktur von Si(111)-(5×2)-Au, die durch den Vergleich der Plasmonendispersion mit den durch DFT Rechnungen ermittelten Bandern untersucht wurde. Eine Dotierung der genannten Oberflache mit uberschussigen Gold- oder Wasserstoffatomen fuhrt zu einem Metall-Isolator-Ubergang. Durch die Robustheit der anisotropen Struktur und der elektronischen Eigenschaften, stellt die Dotierung und Oxidation von Si(hhk)-Gold Systemen spezifische Mechanismen fur die Feinabstimmung der metallischen Eigenschaften heraus. Einige dieser

Effekte, wie das Abschalten von Bändern, elektronische Wechselwirkung zwischen benachbarten Terrassen, die gegenseitige Beeinflussung von Dimerisation und der Öffnung einer Bandlücke, Selbstheilung von Defekten, robuste metallische Charakteristika durch die positionsspezifische Oxidation, der indirekte Ladungsübertrag auf die metallischen Zustände, etc. wurden in dieser Arbeit detailliert untersucht.

Contents

I	Introduction and Fundamentals	21
1.	Motivation and Introduction	23
1.1.	General Remarks on Atomic Wires	23
1.2.	Focus of This Thesis	27
2.	Theoretical Background	29
2.1.	Low-Dimensional Electron Gas: Perturbation and Response	29
2.1.1.	Electronic and Structural Correlations	31
2.2.	Theoretical Concept of Plasmons	32
2.2.1.	Plasmons in Nearly Free Electron Gas	34
2.2.2.	Plasmons in 1D Wire Arrays	41
2.2.3.	Plasmon Life-Time and Damping	42
3.	Surface Studies with Low Energy Electrons	45
3.1.	Low Energy Electron Diffraction	45
3.1.1.	Kinematic Approximation	47
3.1.2.	H(S) and G(S) Analysis	51
3.2.	Inelastic Scattering	54
3.2.1.	Dipole Scattering	54
3.2.2.	Impact Scattering	57
4.	Experimental Technicalities	59
4.1.	UHV Chamber	59
4.2.	SPA-LEED	61
4.3.	EELS-LEED	62
4.4.	Gold Evaporator	64

4.5. Hydrogen Cracker	65
4.6. Definition of Gas Exposure	66
4.7. Si Substrates and Surface Preparation	66
4.7.1. Sample Preparation	68
4.7.2. Anisotropic Atomic Wire Growth	71
II Au Decorated Silicon Surfaces	73
5. Gold Atomic Wires on Flat Si(111)	75
5.1. Surface Structure and Properties	75
5.1.1. Recalibration of Surface Coverage	77
5.2. Plasmonic Excitations in Si(111)-(5×2)-Au	81
5.2.1. Description within the NFEG: Comparison with the Theoretical Models	83
5.3. Doping-Induced Metal-Insulator Transition in Si(111)-(5×2)-Au	87
5.4. Summary and Conclusion	91
6. Gold-Induced Atomic Wires on Stepped Si(hhk) Surfaces	93
6.1. Surface Structures and Properties	93
6.1.1. Si(553)-Au: Double Atomic Chain	95
6.1.2. Si(775)-Au: Double Atomic Chain	100
6.1.3. Spot Profile Analysis of Si(775)-Au	102
6.1.4. Si(557)-Au: Single Atomic Chain	107
6.2. Quasi-1D Plasmons in Si(hhk)-Au	109
6.3. Hybridization of Au and Si States: Evidence from Plasmon Spectroscopy	112
6.3.1. Comparison of the Plasmon Dispersion and Band Structure of Si(553)-Au	112
6.4. Plasmons on the Si(775)-Au Surface	116
6.4.1. Effect of Au Coverage on Plasmonic Excitation	119
6.5. Temperature Dependence of Plasmonic Excitations	121
6.6. Summary and Conclusion	123
III Modification of Structural and Electronic Properties	125
7. Tuning Metallicity by Selective Chemisorption	127
7.1. Chemical Modification of the Si Environment	127
7.2. Robust Metallicity of Gold Atomic Wires on Si(557)	128
7.2.1. Oxygen-Induced Electronic Modifications	131
7.3. Oxidation of the Si(553)-Au Surface	135
7.3.1. Plasmon Standing Waves by Oxidation of Si(553)-Au	137

7.3.2. Comparison with the Band Structures	141
7.3.3. Loss Intensity and Width	143
7.3.4. Oxidation of the LCWs Phase	144
7.4. Extrinsic Doping of Au Atomic Wires	146
7.4.1. Structural Enhancement on Si(553)-Au by Charge Transfer	147
7.4.2. Modification of Plasmons on Si(553)-Au by Atomic Hydrogen	148
7.4.3. Hydrogen-Induced Plasmon Localization on Si(557)-Au	155
7.4.4. Comparison with the Theoretical Model	158
7.5. Modification of the Si(775)-Au Surface	163
7.5.1. Surface Structure upon Oxygen and Hydrogen Adsorption	163
7.5.2. Plasmon Localization by Adatoms	165
7.6. Summary and Conclusion	171
8. Self Doping of Atomic Au Wires	173
8.1. Electronic and Structural Cross-Coupling on Si(553)-Au	173
8.1.1. Enforced Long-Range Atomic Ordering	174
8.1.2. Electronic Modification	179
8.2. Summary and Conclusion	183
IV Summary and Conclusions	185
9. Summary and Conclusions	187
9.1. Outlook	190
Appendix	193
A. Plasmon Resonance Studies by IR	195
B. Supplementary Materials	199
Bibliography	203
Curriculum Vitae	227
List of Publications	230
Acknowledgements	231

List of Figures

1.1.	Illustration for standing and propagating plasmons on Au-decorated Si surface	26
2.1.	Lindhard function and projection of Fermi surfaces with corresponding nesting	30
2.2.	Schematic of the 1D atomic chain with Peierls distortion and corresponding dispersion	31
2.3.	Schematic view of collective electronic excitation	32
2.4.	Plasmon dispersion in different dimensions.	33
2.5.	Effect of coupling parameter r_s^* and confinement model on 1D-plasmon dispersion	39
2.6.	Numerically derived plasmon dispersion for single wire and harmonic array	40
3.1.	Inelastic mean free path (IMFP) of electrons in solid	46
3.2.	Construction of the Ewald sphere for different surface roughness	48
3.3.	Sketch for low energy electron diffraction from stepped surface	51
3.4.	Inelastic scattering mechanism and selection rules for dipoles on the surface	55
4.1.	Sketch of the UHV chamber and sample holder	60
4.2.	Schematic setup of the SPA-LEED system	61
4.3.	Schematic drawing of the EELS-LEED setup	63
4.4.	Sketch of the gold evaporator and hydrogen cracker	65
4.5.	Si crystalline with (111) plane	67
4.6.	Stick and ball model of the Si(hhk) surface orientations	68
4.7.	SPA-LEED patterns for the pristine Si(111), Si(553), Si(557) and Si(775) surfaces	70
4.8.	Sketch illustration for surface preparation	71
5.1.	EBH and KK models for the Si(111)-(5×2)-Au surface	76
5.2.	Experimental phase diagram for submonolayers of Au on Si(111)	77
5.3.	Sketch for three 5×2 domains and LEED patterns on Si(111)	78
5.4.	Experimental ARPES bands for Si(111)-(5×2)-Au	80
5.5.	EEL spectra and the evolution of metallicity on Si(111)-(5×2)-Au	81

5.6.	Plasmon dispersion for the Si(111)-(5×2)-Au surface	83
5.7.	Electronic band structures and calculated ω_+ for the EBH and KK models	84
5.8.	FWHM and intensities of the plasmon loss on Si(111)-(5×2)-Au	86
5.9.	EEL spectra for Au doped Si(111)-(5×2)-Au surface	88
5.10.	SPA-LEED patterns of the Si(111) surface obtained for different Au coverages	89
5.11.	Plasmons on the hydrogenated Si(111)-(5×2)-Au surface	90
6.1.	Experimental ARPES bands for the Si(hhk)-Au surfaces	94
6.2.	SPA-LEED pattern and structural model for the HCWs phase on Si(553)-Au	96
6.3.	SPA-LEED pattern for different Au coverages on the Si(553) surface	98
6.4.	SPA-LEED pattern and structural model for the LCWs phase on Si(553)-Au	99
6.5.	Experimental and calculated electronic bands for the LCWs surface	100
6.6.	SPA-LEED pattern and structural model for Si(775)-Au	101
6.7.	Reciprocal space map for the Si(775)-Au OCWs surface	103
6.8.	Detailed parameters of 1D diffraction profiles for Si(775)-Au OCWs	104
6.9.	SPA-LEED patterns for Si(775)-Au at different Au concentrations	105
6.10.	1D diffraction profiles for Si(775)-Au as a function of surplus Au coverage	107
6.11.	SPA-LEED pattern and structural model for the Si(557)-Au surface	108
6.12.	EEL spectra for Si(553)-Au, and exemplary fitting procedure	110
6.13.	Plasmon dispersion for the Si(553)-Au surface	111
6.14.	Comparison of experimental and calculated electronic band structures of Si(553)-Au .	113
6.15.	Electronic band structure and ω_+ for Si(553)-Au	114
6.16.	Electronic bands and DOS for Si(553)-Au projected onto different atomic groups . . .	115
6.17.	EEL spectra and plasmon dispersion for Si(775)-Au OCWs	117
6.18.	Electronic band structure and numerically derived ω_+ for Si(775)-Au	118
6.19.	Loss spectra and the plasmon dispersion for high Au coverages on Si(775)-Au	120
6.20.	EEL spectra for the clean and hydrogenated Si(557)-Au surface at low-T	121
7.1.	LEED patterns for Si(557)-Au before and after oxidation	128
7.2.	EEL spectra for clean and oxygen adsorbed Si(557)-Au	129
7.3.	Plasmon dispersion for the clean and oxidized Si(557)-Au surface	130
7.4.	Geometrical models for step by step oxidation of Si(557)-Au	132
7.5.	Modification of the electronic band structure upon oxidation of Si(557)-Au	134
7.6.	LEED patterns for the clean and oxidized HCWs phase	135
7.7.	Loss spectra for the clean and oxidized HCWs surface	136
7.8.	Relative transmittance spectra of the clean and oxidized Si(553)-Au surfaces	138
7.9.	Dispersion relation for the clean and oxidized HCWs surface	139
7.10.	Estimated plasmon propagation length for the Si(553)-Au surface	140

7.11.	DFT-PBE calculated electronic bands for the oxidized Si(553)-Au surface	142
7.12.	Intensity and FWHM of the plasmon loss on the Si(553)-Au surface	143
7.13.	LEED patterns for clean and oxidized LCWs surface	145
7.14.	Plasmon dispersion for the oxidized LCWs phase	146
7.15.	LEED patterns for the clean and hydrogenated Si(553)-Au surface	147
7.16.	Evaluation of the $\times 2$ streaks as a function of H_2 exposure	148
7.17.	Loss spectra for the clean and hydrogenated Si(553)-Au surface	149
7.18.	Hydrogen-induced modification of the plasmon loss on Si(553)-Au	150
7.19.	Dispersion relation for the clean and hydrogenated Si(553)-Au surface	151
7.20.	Potential energy surface for adsorption of atomic H on Si(553)-Au	152
7.21.	Electronic band structure of the clean and hydrogenated Si(553)-Au surface	153
7.22.	Electronic band structures of the clean and hydrogenated HCWs phase	154
7.23.	LEED patterns for Si(557)-Au before and after hydrogen adsorption	155
7.24.	EEL spectra for the clean and hydrogen adsorbed Si(557)-Au surface	156
7.25.	Plasmon dispersion for Si(557)-Au before and after adsorption of hydrogen	157
7.26.	PES for adsorption of atomic H on Si(557)-Au	158
7.27.	Electronic band structures for the (5×2) and (5×4) unit cells on Si(557)-Au	160
7.28.	Electronic band structure for H adsorption on Si(557)-Au.	161
7.29.	Squared wave functions for Si(557)-Au at the Brillouin-zone center	162
7.30.	LEED patterns for Si(775)-Au before and after adsorption of oxygen	164
7.31.	LEED patterns for Si(775)-Au before and after hydrogen adsorption	164
7.32.	Evaluation of $\times 2$ streaks on Si(775)-Au upon adsorption of H_2 and O_2	165
7.33.	EEL spectra for Si(775)-Au clean and after hydrogen adsorption	166
7.34.	Plasmon dispersion for the clean and oxygen adsorbed Si(775)-Au surface	167
7.35.	Dispersion relation for Si(775)-Au before and after hydrogen adsorption	168
7.36.	Band structures for Si(775)-Au clean and after oxygen and hydrogen adsorption . . .	169
8.1.	Dimerization versus electronic band gap on Si(553)-Au	174
8.2.	SPA-LEED patterns of the Si(553)-Au surface upon surplus Au deposition	175
8.3.	Evaluation of the $\times 2$ streaks on Si(553)-Au as a function of surplus Au	176
8.4.	1D diffraction profiles for Si(553)-Au perpendicular to the steps	177
8.5.	PES for the adsorption of an additional Au atom on Si(553)-Au	178
8.6.	Structural model for the additional Au adsorbed Si(553)-Au surface	179
8.7.	EEL spectra and plasmon dispersion for Si(553)-Au after doping with surplus Au . . .	180
8.8.	Changes of plasmonic excitation on Si(553)-Au as a function of surplus gold	181
8.9.	Electronic band structure for Si(553)-Au before and after surplus Au adsorption	182
A.1.	Fit parameters obtained from the IR-transmittance experiments	197

LIST OF FIGURES

B.1.	Diffraction patterns for excess Au coverage on the Si(hhk) surfaces	199
B.2.	Plasmonic excitations on Si(775)-Au at higher Au concentrations	200
B.3.	Loss spectra for different Au coverages on Si(775)-Au in k_{\perp} direction	200
B.4.	Dispersion relation for the different Au coverages on Si(775)-Au	201
B.5.	Sensitivity of plasmon dispersion to a local Au coverage on Si(553)	202
B.6.	Temperature-induced modification of the Si(557)-Au system	202

Abbreviations, variables, and constants

Abbreviations

1D	One-dimensional
2D	Two-dimensional
2DEG	Two-dimensional electron gas
3D	Three-dimensional
ASP	Acoustic surface plasmon
SBZ	Surface brillouin zone
ARPES	Angle-resolved photoemission spectroscopy
DC	Direct current
DFT	Density functional theory
DOS	Density of states
EELS	Electron energy loss spectroscopy
FWHM	Full width at half maximum
HCWs	High coverage wires on Si(553)-Au
HSE	Heyd-Scuseria-Ernzerhof hybrid functionals for DFT
HWHM	Half width at half maximum
IV-LEED	Intensity and Voltage dependent LEED measurements
L	Langmuir (unit) = 1.33×10^{-6} mbar s ⁻¹
LCWs	Low coverage wires on Si(553)-Au
LEED	Low energy electron diffraction
LT	Low temperature (< 100 K if not defined otherwise)
ML	monolayer
MIT	Metal insulator transition
RHEED	Reflection high-energy electron diffraction
RMS	Root mean square

PBE	Perdew-Burke-Ernzerhof approximation in DFT
RPA	Random phase approximation
FL	Fermi liquid
NFL	Non-Fermi liquid
NFEG	Nearly free electron gas
OCWs	Optimum coverage wires on Si(775)-Au
RT	Room temperature ($\approx 22^\circ\text{C}$)
SPALEED	Spot profile analysis low-energy electron diffraction
SPE	Electron-hole single-particle excitation spectrum
STLS	Mean-field approximation by Singwi, Tosi, Land, and Sjölander
STM	Scanning tunneling microscopy
STS	Scanning tunneling spectroscopy
TLL	Tomonaga-Luttinger liquid
QMS	Quadrupole mass spectrometer
UHV	Ultra-high vacuum (pressure $< 1 \times 10^{-9}$ mbar)
GMFA	Generalized mean-field approximation
PES	Potential energy surface

Used variables

a	Width of square-well potential
b	Ground state width of harmonic potential
a_0^*	Effective Bohr radius
a_0	Surface lattice constant
a_c	Low- k plasmon normalization constant
a_x, a_y	Surface lattice vectors
χ_0	Electron gas polarizability
d_z	Step height of surface
E	Energy
E_F	Fermi energy
ϵ	Relative permittivity of the surrounding medium, to be multiplied with ϵ_0
f_n	Structure factor of atom f
\vec{G}_{\parallel}	Reciprocal surface lattice vector
$G_{\text{corr}}(k)$	Local field correction factor
g_s	Spin degeneracy factor

h_n, h	Height factor (multiplies with d_z)
I	Intensity
\Im	Imaginary part
k	Wave vector
$\vec{K}, \vec{K}_{\parallel}$	Scattering vector, its part parallel to the surface
$\vec{k}_f, \vec{k}_{\parallel,f}$	Final wave vector, its part parallel to the surface
k_F	Fermi wave vector
$\vec{k}_i, \vec{k}_{\parallel,i}$	Incoming wave vector, its part parallel to the surface
λ	Wavelength
m^*	Effective mass of electrons in a Fermi-fluid given in multiples of m_e
n	Electron density (if not index)
ω	Angular frequency ($= E/\hbar$)
ω_{\pm}	Upper and lower boundary of the electron-hole pair continuum
Φ, Ψ	Electron wave functions
\vec{r}_n	Position of atom n in lattice
r_s^*	Dimensionless electron density parameter
\Re	Real part of an imaginary number
ρ	Charge density distribution
S	Scattering phase
V_c	Coulomb interaction matrix element
v_F	Fermi velocity

Constants¹

c	Speed of light	$= 299\,792\,458\text{ m s}^{-1}$
e	Elementary charge	$= 1.602\,176\,620\,8(98) \times 10^{-19}\text{ C}$
ϵ_0	Electric constant	$= 8.854\,187\,817 \times 10^{-12}\text{ F/m} = 1/(\mu_0 c^2)$
h	Planck constant	$= 6.626\,070\,040(81) \times 10^{-34}\text{ Js}$ $= 4.135\,667\,662(25) \times 10^{-15}\text{ eVs}$
\hbar	Reduced Planck constant	$= h/2\pi$
m_e	Electron mass	$= 9.109\,383\,56(11) \times 10^{-31}\text{ kg}$
u	Atomic mass constant	$= 1.660\,539\,040(20) \times 10^{-27}\text{ kg}$

¹The listed constants have been taken from the wikipedia, https://en.wikipedia.org/wiki/Physical_constant

Part I:

Introduction and Fundamentals

Chapter 1

Motivation and Introduction

Atomic wires are one of the most elegant playgrounds to address many fundamental phenomenological questions. From a fundamental viewpoint, 1D electron systems are important since they constitute one of the simplest many-body systems of interacting fermions with fundamentally different properties than their 2D and 3D counterparts. It is noteworthy that most of their unique properties are due to their reduced size and dimensionality, as well as to the concomitant high electronic correlations. [1] The latter can be rationalized at the classical level for 1D electronic systems when two electrons approach each other with opposite velocity in a one-dimensional line and can not avoid each other, contrary to higher-dimensional systems where electrons have a higher degree of freedom. The reduction of dimension in metallic systems down to quasi-one-dimensional wires reveals a strikingly rich variability of electronic behavior such as quantization of conductance, extremes of electronic correlation manifested by charge quantization [2], Wigner crystallization [3], charge and spin density waves, triplet conductivity, etc. [4–6] As proposed by R. Peierls, the enhanced electron-phonon interaction in atomic wires triggers the formation of a charge density wave (CDW) due to periodic lattice distortion (PLD), resulting in an electronic gap opening and insulating ground state at $T = 0$ K. [7] Contrary to higher dimensions, the low energy properties of strongly interacting 1D metallic systems can no longer be described by Landau’s Fermi liquid theory. [8, 9] Instead, the gapless interacting 1D systems at low energies show Tomonaga-Luttinger liquid (TLL) behavior [10], which is given within a bosonic reformulation of the single-particle spectrum. [6, 11]

1.1. General Remarks on Atomic Wires

A Zest of Atomic Wires on Si surfaces — As a bottom-up approach, one of the essential goals of fabricating nanostructures by self-assembly is the creation of new materials with tailored electronic and

structural properties. In fact, using an appropriate substrate, the metallic nanostructures and the electronic distribution can be confined to width comparable to their Fermi wavelength (λ_F), such as in the atomic wires. The 1D character is an essential ingredient in the electronic properties of such systems that have been subject to many fundamental studies. [12–15] Indeed, with their practical accessibility, investigating several peculiar fundamental properties for low-dimensional systems became feasible. [16–20] However, their detailed electronic properties are still under intense discussion. The electronic structure of one-dimensional metallic chains was predicted to have a free-electron-like character. This was also supported by parabolic band dispersion observed in photoemission spectroscopy. [12, 21] In several pioneering works, Au atoms were considered rigidly locked to the Si substrate, but electrons near the Fermi level are completely decoupled from the substrate because they lie in the bulk silicon band gap. [12, 22, 23] However, subsequent improvement in understanding atomic wire systems showed that the strong interaction between the Au chains and the embedding environment is inevitable because Au and Si atoms are strongly hybridized. [24–27] Generally, two approaches can be put forward to describe metallic wires on semiconductor surfaces: a) doping of semiconductor surface states with metal atoms, b) downscaling of the metallicity of pure metals upon embedding them into the semiconductor surface. Obviously, in both cases, the resulting metallicity is modified due to the interaction of those electronic states. This raises the question: how much of the one-dimensionality is practically preserved after such modification? The present thesis discusses this question in more detail by means of plasmon spectroscopy and atomistic DFT calculations. New insights into the topic have opened up a new field for the tunability of the wire properties over the chemical modification of the Si environment.

One of the main remaining questions in this topic is the electronic and structural correlation. This essentially comprises temperature-induced phase transition, spin-charge separation, electron-phonon interaction, single-particle and collective electronic excitation. [28–31] In addition, adsorbate-induced charge doping and localization have been shown as relevant parameters in this context. [32–36] Recently, numerous fundamental questions regarding their variety of inherent instabilities associated with the chemical interaction between these wires of ultimate smallness and the embedded environment have been addressed. [12, 14, 15] In addition to all fundamental aspects mentioned above, extensive studies showed that they have potential applications in atomic-scale devices. [25, 37, 38]

Plasmons in Atomic Wires — Plasmons are collective excitations of an electron gas in a partially filled topmost electronic band that exists in all dimensions. [39–41] Electronic excitations and in particular plasmonic excitations have been studied for about half a century, mostly as an in-plane wave on the metallic surfaces and/or interfaces. [42–47] Moreover, in the last decade, with the development of the anisotropic metallic chain growth on a semiconductor surface, a low-dimensional plasmonic excitation associated with atomic and nano-scale wires became more prominent. [23, 48–51] Especially interesting are the plasmons of ultrathin metallic sheets or wires with a few atoms in diameter, forming 2D sheet plasmons or 1D wire plasmons [48–51], which have inherent attractive properties: a flat dispersion, which starts at zero energy for large wavelengths. Thus, much shorter wavelengths ($\lambda_{pL} < 10$ nm) can

be achieved compared with the standard volume and 3D edge plasmons, called surface plasmons, allowing for better localization, as demonstrated, e.g., in graphene nanostructures. [52] Plasmonic excitation in atomic Au wires is particularly interesting due to its almost linear $E \sim k$ dispersion relation. In 1D wire plasmons with their already built-in directionality of energy transport, the dispersion, according to theory, is intrinsically quasi-linear since it starts at long wavelengths as $E \sim k_{\parallel} \ln k_{\parallel}$. [53] Moreover, an established methodology improved the usefulness of plasmon spectroscopy to probe confinement and correlation in atomic-scale objects. The latter is not limited to just collective excitation states but can easily be extended to study the electronic band structure as well as the interaction between different surface states and their cross-coupling with structural parameters. [27, 31]

Most of the time, the almost linear dispersion of atomic wire plasmons is confused with acoustic surface plasmons (ASP) despite the fundamental differences in charge distribution, confinement, and screening that need to be clarified before such comparison. Plasmonic excitation associated with 2D metallic surface states found on Au, Cu, and Be sheets has been subject to several studies revealing ASP with almost linear dispersion. [54–58]. It should be noted that the mentioned surfaces possess Shockley surface states that cross the Fermi level. Fundamentally, the formation of an ASP requires the interaction of a 1D or 2D electron gas with another metallic system so that interaction and screening lead to the linearization of the plasmon dispersion. [44, 47] However, in the case of metallic chains on a semiconductor surface, the band alignment is such that there is no overlap between the partially filled metallic surface states and the Si bulk states. In addition, no temperature dependence of plasmon dispersion of atomic wires was found. Thus, none of the preconditions for the formation of an ASP are fulfilled. Also, in the quasi-1D case, the leading term of dispersion is already linear in k (which is $\sqrt{2}$ in an isotropic 2D), starting from zero in the long wavelength limit ($k = 2\pi\lambda^{-1} \rightarrow 0$). [39] Another reason for linearization of quasi-2D plasmon dispersion at long wavelength has been discussed considering plasmon-phonon interaction. This effect originates from the Kohn anomaly [59], which underlines the $\delta\omega(k)/\delta(k)_{k=2k_F} = \infty$ phonon mode on 2D ordinary metals due to the strong electron-phonon interactions. [60] Two kinds of plasmonic excitations associated with atomic wires, standing and propagating, are schematically described in Fig. 1.1. Due to its longitudinal nature, the direct excitation of the former requires the use of charged particles such as electrons, to transfer sufficient momentum. Such plasmon excitation appears in energy loss spectra with defined energy dispersion as a function of momentum transfer. [61] The latter appears in IR-absorption spectra with wave number related to longitudinal as well as lateral charge confinement. [40] Both plasmon modes are mostly characterized by limited lifetime due to second kind scattering events in the lattice (e.g., interaction with phonons, impurities and/or local distortions).

Beside their fundamental wealth, low-D plasmons have potential applications in sensing, energy harvesting, optoelectronics etc., technology. For example, they can be used for guiding electromagnetic waves in integrated optical circuits and interfacing with electronic components. [62] Also, their constant group velocity and unchanged wave packet enable nanophotonic waveguides for simultaneously

achieving high-speed and low-loss data transmission and/or transfer. In addition, the coupling of light frequency to plasmon enables the concentration of optical fields to dimensions well below the optical wavelength. [63]

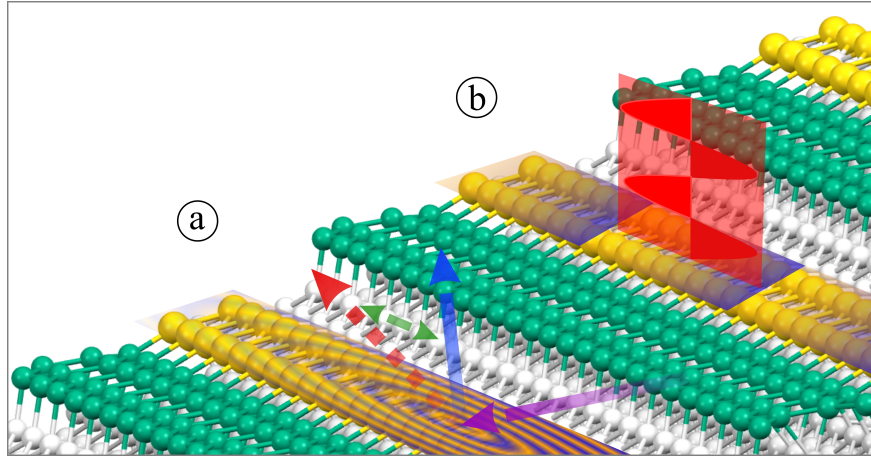


Figure 1.1: Illustration of a Au-decorated Si surface hosting two different plasmonic excitations. (a) demonstrates the momentum transfer and the resulting in-plane plasmon propagation mode. (b) illustrates plasmon standing waves excitation in a finite section of atomic chains via 's' polarized light. Green, yellow and white balls correspond to Si-HC chains, Au atoms and other Si atoms, respectively. Magenta, blue, red and green arrows stand for the incident, specular, inelastic scattering and momentum transfer parallel to Au chains, respectively.

The Concept of Tunability — As described above, the interaction between the atomic chains and the embedding environment profoundly affects the resulting surface properties. These manifold interactions allow for controlled modification of electronic and structural properties of ultimate atomic wires. In the first place, appropriate templates such as the vicinal Si surfaces serve a higher degree of freedom to tune the wire geometries and fundamental properties. [64] In this case, the number of atomic chains per terrace, local structural motifs, and interchain couplings is defined by the macroscopic relief of the template (i.e., see Table. 4.1). [65] Also, the resulting surface is often reconstructed in such a way that different atomic groups are arranged in atomically ordered superstructures to further minimize surface energy. The presence of various structural motifs, on the other hand, determines the geometry, geometry, mechanism, and nature of further bond formation on the surface and deliver more possibilities for fine-tuning. Thus, using different adsorbates, which also show site-specific adsorption, the properties of established systems can be tuned. Interestingly, such modification works almost as proximity, while the additional adsorbates mainly modify the surrounding of embedded metallic chains. Moreover, the strong interrelation of electronic and structural parameters enables tuning of one over another. Such fine-tuning of atomic chains over physical and chemical interactions is one of the main objectives of the present thesis and will be comprehensively discussed in Part II and Part III.

1.2. Focus of This Thesis

The eventual rationale of the present work is to understand the interactions between wires of ultimate smallness and the surrounding environment. In this regard, the response of atomic wires to external perturbation and intrinsic charge redistribution has been carefully studied. Primarily plasmonic excitations associated with single and double Au strands will be discussed and compared with the theoretical models that have been developed in parallel to the experiments. For a comprehensive understanding of surface structures and electronic properties, the effect of Au coverage, local surface structures, preparation conditions, etc., are systematically analyzed.

One of the central tasks of this thesis is to learn about the modification of atomic wires by selective chemisorption. Hydrogen and oxygen adsorption on Si(557)-Au, Si(553)-Au, Si(775)-Au surfaces have been extensively investigated as examples in this regard. Such selective chemisorption also shows site selectivity due to different adsorption energy at specific Si atoms (i.e., Si-adatoms, restatoms, step edges). The experimental results are comprehensively compared with atomistic DFT calculations to extend insights on atomic-level interactions between adsorbate and surface atoms.

In addition to the Au atomic chains on stepped Si surfaces, Au wires on a 1° miscut (almost flat) Si surface have also been studied. In fact, this is the first comprehensive study of plasmonic excitation on the Si(111)-(5 \times 2)-Au surface. Moreover, plasmons on this surface will be evaluated as a function of Au coverage. In this regard, single and multi-domain 5 \times 2 superstructures on flat Si(111) are compared structurally and electronically. Using the developed methodology, the electronic band structure, in particular the unoccupied part of the metallic atomic chains, was extensively investigated by plasmon spectroscopy. Moreover, for the first time, the changes in electronic states following the chemical modification of the embedding environment were studied in detail using this advanced approach. The results obtained underline the interaction of the Au-induced and Si surface states, and, therefore, modification of one-dimensional metallicity in these systems.

After substantially addressing the hybridization between the metallic and Si surface bands, one of the remaining questions is the contribution of each surface state to the overall surface conductivity. This question has carefully been addressed using the combination of plasmon spectroscopy and atomistic DFT. Although the plasmon spectroscopy can not separately map electronic states of individual structural motifs, their different interaction mechanism with oxygen and hydrogen could beneficially be used to distinguish the underlying interaction with metallic bands. Such a procedure was successfully applied for the Si(557)-Au surface. As mentioned above, the correlation of structural and electronic properties is an essential ingredient of atomic wires. Such strong cross-coupling was realized after charge doping to the Si(553)-Au system. Further studies are envisaged in order to clarify the role of the silicon substrate and its interaction with the gold chains in this system.

Chapter 2

Theoretical Background

This chapter gives a detailed overview of the theoretical concept of 1D metallic chains and their electronic characteristics. The possible reasons and implications of crossover to higher dimensions will be addressed on the basis of the theoretical models available, such as the nearly free electron gas (NFEG) model. Collective electronic excitations and their theoretical treatment will be given for low-dimensional metallic systems, particularly for quasi-1D metals. An interplay between structural and electronic parameters will be discussed at the end of this chapter. The latter will be applied to describe relevant experimental and theoretical findings in the next chapters.

2.1. Low-Dimensional Electron Gas: Perturbation and Response

One of the key aspects of the low-dimensional electron gas is its response to external perturbations. Within the framework of linear response theory, the response of an electron gas to an external time-independent potential is described via static susceptibility function or Lindhard response function as follows:

$$\chi(\vec{q}) = \frac{1}{V} \sum_k \frac{f(E_k) - f(E_{k+q})}{E_k - E_{k+q}} \quad (2.1)$$

where E_k is the energy of electronic state of momentum k , $f(E_k)$ is the Fermi-Dirac distribution function, q is the charge density wave (CDW), k and V are the state and volume of the system.

The k dependence of the Lindhard function for a 1D free electron gas together with 2D and 3D cases is illustrated in Fig. 2.1(a). In contrast to the 2D and 3D cases, the response function logarithmically diverges in 1D at the Fermi wave vector (k_F). [67] This peculiar singularity originates from the specific

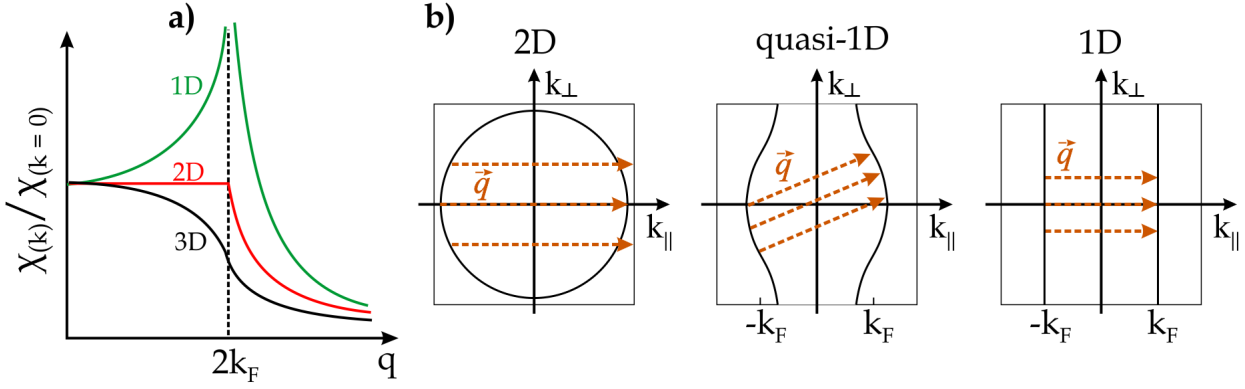


Figure 2.1: Static dielectric susceptibility or Lindhard function for different dimensions (a) and projection of the Fermi surfaces for metals in different dimensions with corresponding nesting conditions (b). isotropic-2D (or just 2D), quasi-1D, and ideal 1D metallic systems, from left to right. The square background stands for the Brillouin zone of a rectangular crystal lattice, which is overlapped with the Fermi surface only in the 1D case. In graph (b), the arrows stand for pairs of states (empty and full). Only for an ideal 1D surface, perfect nesting condition is appropriate, which means that each k_F point can be connected linearly. However, it is replaced by many nonequivalent nesting vectors in higher dimensions with a poor connection between the Fermi vectors. (Please note that the projection of isotropic 2D (cylindrical) and 3D (spherical) Fermi surfaces look the same, and also many nesting conditions can be realized in these dimensions; therefore, only the 2D case is presented here). Adapted from Ref. [66].

surface of 1D free electron gas. Following Eq. 2.1, a large $\chi(\vec{q})$ requires a large numerator and a small denominator. It worth to note that the sum in Eq. 2.1 gets a nonzero value when either $E_k > E_F > E_{k+q}$ or $E_{k+q} > E_F > E_k$ is satisfied. [68] According to Eq. 2.1, the integral divergence is due to the pairs of empty and full states, which have the same energy but differ by wave vector $q = 2k_F$. Due to the fact that in 2D and particularly in 3D such pair states are rare and therefore, no significant singularity at $q = 2k_F$ is observable. [69] However, in 1D there are exactly two points at the Fermi contour, which are always connected, and the Fermi surface is completely nested by q . Thus, the singularity of $\chi(\vec{q})$ in a 1D electron gas corresponds to the periodic modulation of Fermi contours with a wave vector $q_{||} = 2k_F$ along chains. In case the adjacent chains separated by distance b , this modulation appears with $q_{\perp} = \pi/b$ perpendicular to the chains (see Fig. 2.1). The scenario mentioned above implies that an external perturbation (or external potential) causes a divergent charge redistribution in the 1D electronic system. Within self-consistency, at $T=0$, the electron gas itself is unstable relative to the formation of periodic spin and charge density waves. This periodicity corresponds to the Fermi wave vector as $\lambda = \pi/k_F$.

The Fermi surface for ideal 1D metals consists of two parallel lines. However, in real quasi-1D metallic systems, the Fermi surface deviates from the ideal 1D character due to interaction with its surroundings. For example, in the case of strong 2D interaction between 1D wires, the Fermi surface tries to form cylindrical or even spherical form depending on coupling strength. However, in a weak 2D coupling

range wiggling of the Fermi surface occurs as illustrated in Fig. 2.1(b). Such wiggling of the Fermi surface has been experimentally observed for all members of the Si(hhk)-Au family and will be discussed in Section 6.1. Fermi surface and Brillouin zone overlap in ideal 1D metals contrary to 2D and 3D cases in which these two have distinct form and size (or volume). Hence, some of the nesting conditions from perfect 1D state can still be filled with the same vector.

2.1.1. Electronic and Structural Correlations

An important case of electron-lattice coupling in 1D metallic systems is the Peierls distortion. [70] A Peierls distortion can generally be classified as a symmetry breaking transition which is physically different from a transition that lifts degeneracy, such as the Hohn-Teller effect. [71]. In this case, only electrons with a wavelength commensurate with the lattice ($k = \pi/a$) feel the periodic potential, and they form a standing wave pattern. According to Peierls, the uniform chain of a one-dimensional wire is formally unstable against any doubling of the unit cell. [7] The reason is symmetry-lowering modulation of nuclear positions and valence-charge density resulting in the opening of energy gap at or near edge of the Fermi distribution. In strictly one-dimensional systems, such a gap opening is expected to occur only at 0K. The simplest example is that with one electron per atom (half-filled band). In that case, the zone boundary is at $\pm\pi/2a$, as shown in Fig.2.2.

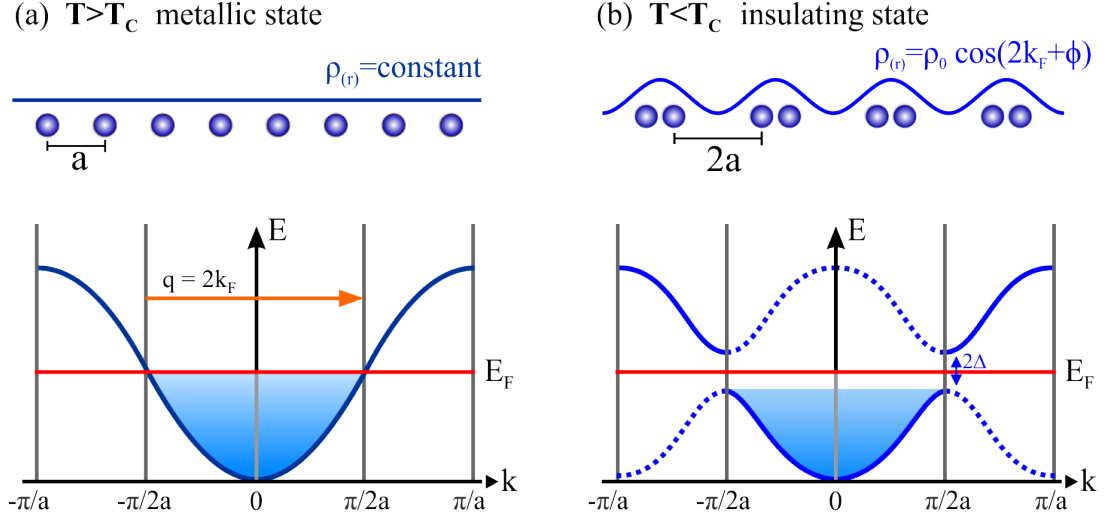


Figure 2.2: Schematic representation of 1D atomic chain and Peierls type periodic lattice distortion and/or CDW transition with corresponding energy dispersion relation. a) Undistorted one-dimensional atomic chain-Metallic phase with equal charge density (ρ_r). This ground state possesses half-filled band in reciprocal space with Fermi vectors k_F separated by the nesting vector $q = 2k_F$. b) Peierls distorted 1D chain DW below T_C due to the periodic modulation by doubling the lattice constant $2a$ along the chain. This phase corresponds to insulator state because of band-gap 2Δ (often regarded as Peierls gap) opening at $2k_F = \pi/2a$.

In the standard treatment of the distortion of linear metallic chains by Peierls, the translational symmetry is subject to periodic displacements in chain direction. The mechanism driving such charge-reordering instability involves a powerful connection between the vibrational modes of the lattice and the electrons close to the Fermi level in 1D. The ground state of the Peierls chain is isolating; by increasing temperature, some electrons are thermally excited to the upper band, the band gap declines, and the system undergoes a second-order transition resulting in restoring of metallicity. Nevertheless, the description just mentioned includes some significant gestures. First of all, this approach disregards entropic fluctuations. In fact, thermal fluctuations always ruin long-range order within the 1D-boundary and avoid phase transition. Therefore, the observation of a Peierls kind transition is much more feasible for real materials in the presence of 2D (3D) inter-chain coupling. [72, 73] Second, Peierls' hypothesis totally ignores the electron-electron correlations in 1D systems. However, in real systems, the Peierls transition may be taken over by other competing many-body ground states such as spin-density waves, Luttinger liquid, superconducting phase, and so on.

2.2. Theoretical Concept of Plasmons

Plasmons are quasiparticle resulting from the quantization of plasma oscillations of the conductive electrons (free electron gas density) with respect to the fixed positive background. In general, the plasmon oscillation relies on the Coulomb interaction between charge carriers and their interaction with the positive ions. Thus, the perturbation of the free carriers by means of external particle generates excited electrons, which are still bound to atoms with a simultaneously emerging Coulomb force tending to re-establish the charge neutrality. Due to inertia, the excited electron exceeds its equilibrium position resulting in plasma oscillation as schematically shown in Fig. 2.3. This excited state preserves its oscillation unless it emits radiation, which can result from different processes such as inter-particle collision and the interaction of collective and single-particle excitation states.

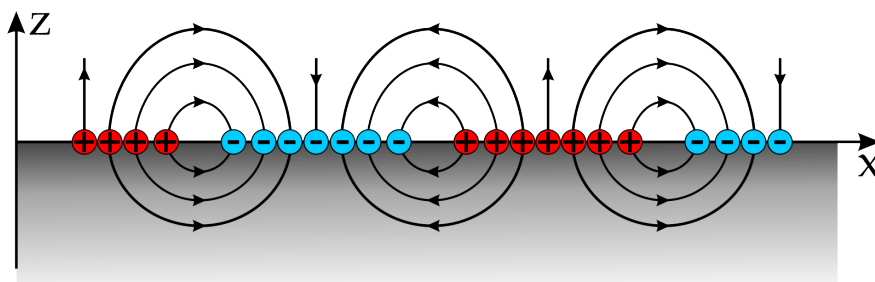


Figure 2.3: Schematic representation of the collective electronic excitation and associated field generated by the displacement of charges.

Plasmon has the following energy for approximation at long wavelengths in a standard quasi-free

electron gas. [74]

$$E_p = \hbar\omega_p = \hbar\sqrt{\frac{ne^2}{\epsilon\epsilon_0m^*}} \quad (2.2)$$

This is the so-called plasma energy. Here, n is the charge density, ϵ -the dielectric constant of media, ϵ_0 -permittivity of vacuum, e -electron charge, m^* is the effective electron mass, and ω_p is the bulk plasma frequency. Eq. 2.2 shows the fundamental relation between plasmon frequency and available charge carrier density in the corresponding system. This square root dependence seems to survive even down to the smallest systems, as measurements on low-dimensional systems showed [75]. However, in the low-D systems, other parameters such as confinement potential, electronic and structural correlation, the form of electronic bands, etc., also come into play. On the other hand, m^* can also be changed considering a parabolic band structure and nonlinear dispersion at E_F . Nevertheless, these small changes have no substantial effect on whole plasmon dispersion and, therefore, have never been taken into account as a flexible parameter in this simplified approach.

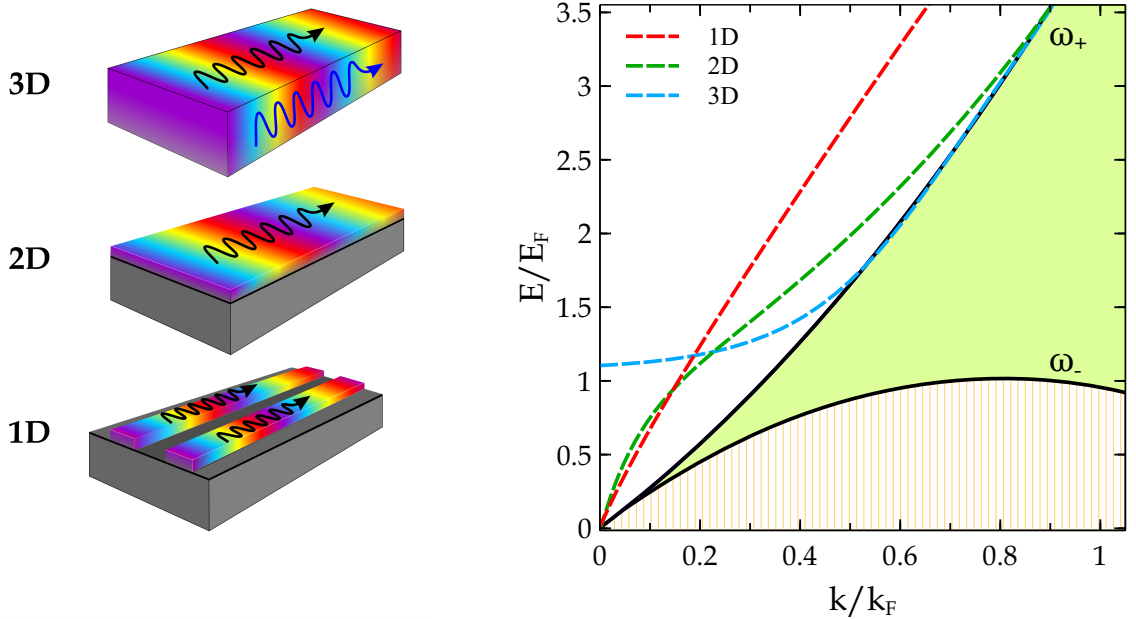


Figure 2.4: Left: schematic representation for the 3D-volume plasmon, 2D-surface and sheet plasmon, 1D-wire plasmon. Right: plasmon dispersion in different dimensions. The green area indicates the single-particle electron-hole continuum excitation regime in 1D with the corresponding upper ω_+ and lower ω_- boundaries. Unlike 2D and 3D systems, which possess only an upper boundary of the electron-hole continuum, 1D systems have the lower boundary due to the existence of the low energy gap between 0 and ω_- . This is due to severe phase-space restrictions imposed by the energy-momentum conservation. The hatched area represents the range of excitations in which the dielectric function is purely imaginary. After Ref. [76].

2.2.1. Plasmons in Nearly Free Electron Gas

Regarding the relation between particle response (or producing wave) and its position, the response of electrons to a wave can be formulated in two ways: 1) The particle response is independent of its position, which considers a well-ordered system. 2) The particle response or phase difference depends on the particle position. Considering a random distribution of particles, the second approach averages the response to zero. This approach is the so-called random phase approximation (RPA). [77] Within the RPA, the elementary excitation spectrum of the 1D electronic system can be formulated in two ways based on the strength of the tunneling between the adjacent quantum wires. Thus, in a strong tunneling limit, the whole system is considered as a 2D patch of 1D wire arrays with a periodic modulation of potential in the higher symmetry direction. If the modulation potential is small, however, it is regarded as a perturbation. In the absence of inter-chain coupling, the electronic distribution of atomic wires can be formulated as electrons free to move in one direction (i.e., x-direction) and strongly confined in other directions (i.e., y and z). [78] The elementary excitation of the free electron density can be described by the dynamical structure factor $S(k, \omega)$. $S(k, \omega)$ is related to dynamical dielectric function $\epsilon(k, \omega)$ via $\text{Im}[\epsilon(k, \omega)^{-1}]$. Within the RPA, the dielectric function is given by:

$$\epsilon(k, \omega) = 1 - V_c(k)\chi_0(k, \omega), \quad (2.3)$$

where $V_c(k)$ is the Coulomb interaction, χ_0 is the noninteracting dynamical polarizability. $\chi_0(k, \omega)$ is so called the Lindhard function or polarizability function of the 1D electron gas. It is well known that the polarizability function of a noninteracting 1D electron gas is logarithmically divergent at $k = 2k_F$, where k_F is the 1D Fermi wave vector. [53] This is a simple consequence of the perfect nesting of the Fermi surface in 1D and is related to the well known Peierls instability (see Section 2.1). This $2k_F$ singularity will be softened by thermal and other broadening mechanisms in a real system. Following Refs. [79,80], the condition for the existence of a plasmon is defined by the real part (\Re) of the dielectric constant as:

$$\Re[\epsilon(k, \omega)] = 0, \quad (2.4)$$

Therefore, the plasmon dispersion and its lifetime or damping are given by the zeros of the complex dielectric function via

$$\epsilon(k, \omega) = 1 - V_c(k)\chi_0(k, \omega) = 0 \quad (2.5)$$

Unlike its higher-dimensional counterparts, the electron density in 1D systems is strictly confined in the transverse plane (i.e., y and z) while its motion is free along the wire (or x) axis. Assuming that the transverse motion is confined by a 2D potential $V_c(y, z)$, which is infinite in x axis and restricts the electron distribution to the lowest sub-band. Then the one-electron wave function can be written as:

$$\Psi(x, y, z) = \frac{e^{ikx}}{\sqrt{L}} \phi(y, z) \quad (2.6)$$

Here, L stands for the macroscopic wire length of a cylindrical symmetric chain (along the x -axis) and $\phi(y, z)$ is the transverse part of the total wave function indicating quantization in the y and z plane. However, using a more realistic finite-width (sufficiently long) 1D chain model, the Fourier transformed Coulomb interaction is expressed by the following equation:

$$V_c(k) = \frac{e^2}{\epsilon_0} \int_{-\infty}^{\infty} d(x-x') e^{ik(x-x')} \times \int \int d(y, z) d(y', z') \frac{|\phi(x, y)|^2 \phi(y', z')}{\sqrt{(x-x')^2 + (|y, z - y', z'|)^2}} \quad (2.7)$$

The actual form of the plasmon dispersion is dependent on the used confinement mode. The following confinement models have been employed in the literature. [81]

- I. Harmonic confinement in the $y - z$ plane for a 1D wire with a cross section of b . Considering the transverse wave function as a Gaussian

$$\phi(R) = \frac{1}{\sqrt{2\pi b^2}} \exp\left(-\frac{y^2 + z^2}{4b^2}\right), \quad (2.8)$$

The electron-electron potential in Eq. 2.7 can be solved for $V_c(k)$ as:

$$V_c(k) = \frac{e^2}{\epsilon_0} \exp(k^2 b^2) E_1(k^2 b^2), \quad (2.9)$$

where $E_1(x) \sim \int_x^{\infty} \frac{e^{-x}}{x} dx$ is the exponential-integral. The asymptotic behavior of Eq. 2.9 in short and long wavelength limit is given via the following relation:

$$V_c(k) \sim \begin{cases} -\ln k & k \rightarrow 0 \\ 1/k^2 & k \rightarrow \infty \end{cases} \quad (2.10)$$

Thus, at large distances, the inter-particle potential is that due to point charges, while at small distances, it is that of parallel planar charge distributions.

- II. Infinite square-well confinement in the $y - z$ direction with the square-well width a .

$$V_c(k) = \frac{2e^2}{\epsilon_0} \int_0^a dy \int_0^a dy' \int_0^a dz \int_0^a dz' |\phi(y, z)|^2 \times |\phi(y', z')|^2 K_0(kR), \quad (2.11)$$

Here, K_0 is the zeroth-order modified Bessel function of the second kind, ϵ_0 is the background lattice dielectric constant. $R = \sqrt{(y - y')^2 + (z - z')^2}$.

$$\phi(y, z) = \left(\frac{2}{a}\right) \sin\left(\frac{\pi y}{a}\right) \sin\left(\frac{\pi z}{a}\right), \quad (2.12)$$

III. Infinite square-well confinement in the y -axis:

$$\phi(y, z) = \sqrt{\frac{2}{a}} \sin\left(\frac{\pi y}{a}\right) \zeta(z) \quad (2.13)$$

Here, a is the width of the 1D wire along the y axis. $\zeta(z)$ is the optimized wave function in the z -direction, which is given by the Stern-Howard [82] variational wave function as following:

$$\zeta(z) = \sqrt{\frac{\beta^3}{2}} z \exp\left(-\frac{\beta z}{2}\right) \quad (2.14)$$

Here, β is a variational parameter and takes into account average wire width in z direction, through $\beta = 3/\langle z_0 \rangle$.

IV. Harmonic confinement in the y direction and $\sqrt{\delta(z)}$ wave function in the z direction. In this case the $V_c(k)$ gets the following form:

$$V_c(k) = \frac{e^2}{\epsilon_0} \exp\left(\frac{kb}{2}\right)^2 K_0\left(\frac{kb}{2}\right)^2. \quad (2.15)$$

where the harmonic confinement in the y direction is defined as following:

$$\phi(y) = \frac{1}{\sqrt[4]{2\pi b^2}} \exp\left(-\frac{y^2}{4b^2}\right) \quad (2.16)$$

V. Infinite square-well potential in the y -axis and $\sqrt{\delta(z)}$ wave function in the z -axis. [83]

$$V_c(k) = \frac{8e^2}{\epsilon_0 a^2} \int_0^a dy \int_0^a dy' \sin^2\left(\frac{\pi y}{a}\right) \times \sin^2\left(\frac{\pi y'}{a}\right) K_0(k|y - y'|). \quad (2.17)$$

$$\phi(y) = \sqrt{\frac{2}{a}} \sin\left(\frac{\pi y}{a}\right) \quad (2.18)$$

Using the above mentioned 1D confinement models, the dependence of the $V_c(k)$ on the wavenumber has been calculated in Ref. [81] for $b = 0.4$ nm and coupling parameter $r_s^* = 0.35$. One of the most widely used description of the electronic properties of metallic systems is by the dielectric response function $\chi(k, \omega)$. The dielectric response function describes the response of electrons to a weak space-time dependent external longitudinal electric potential. The two most significant features of the 1D

dynamical response are: i) the linear (with small logarithmic corrections, depending on the details of the confinement potential) wave vector dispersion of the long wavelength collective charge density excitation plasmon mode, ii) the total suppression of the electron-hole single-particle excitation continuum at low energy (which arises from the severe 1D phase restriction, due to energy-momentum conservation). The 1D plasmon exhausts the f -sum rule up to the second-order in k/k_F . Therefore, the 1D RPA plasmon dispersion is exact not only in the long wavelength limit (as it is trivially in all dimensions) but up to large values of the wave vector ($k/k_F \sim 1$). This has earlier been pointed out in the literature in a somewhat different context. The present detailed RPA treatment of the 1D dynamical response is thus of considerable quantitative validity, as the RPA appears to be a more accurate approximation in 1D than in 2D and 3D systems. This adaptation of the STLS model, which was originally developed for 3D systems by Singwi, Tosi, Land, Sjölander [84] has been employed for 1D electronic systems in literature. [85] Importantly, the electron correlation effect, which is highly essential for 1D systems, can also be considered in the STLS formalism. [84] Although its exact solution is not possible due to many-body effects, $\chi(k, \omega)$ can still be calculated within the framework of linear response theory by employing the generalized mean-field approximation. [81, 86] In this case, the response of electron density to a weak space-time dependent external longitudinal electric potential is given by the density response function, which is also called the Lindhard function:

$$\chi(k, \omega) = \frac{\chi_0(k, \omega)}{1 - V_c(k)[1 - G(k)]\chi_0(k, \omega)}, \quad (2.19)$$

Here, $\chi_0(k, \omega)$ is the zero temperature free electron density response function, which is given in the following form:

$$\chi_0(k, \omega) = \frac{m^* g_s}{2\pi k} \ln \left\{ \frac{\omega^2 - (kk_F/m^* - k^2/2m^*)^2}{\omega^2 + (kk_F/m^* + k^2/2m^*)^2} \right\}, \quad (2.20)$$

Here, $G(k)$ is the local-field correction (LFC) factor that describes the modification of $V_c(k)$ due to exchange-correlation effects. g_s is the spin-degeneracy factor. It can get either 1 or 2 depending on how many spin component is present in each of the two spin-orbit split bands. k_F is the 1D Fermi wave vector defined via $k_F = \pi n/g_s$. Within this approach $G(k)$ is given by the following equation by taking into account the static structure factor $S(k)$ [87]:

$$G(k) = -\frac{1}{n} \int_{-\infty}^{\infty} \frac{dk'}{2\pi} \frac{k'V(k')}{kV_c(k)} [S(|k - k'|) - 1]. \quad (2.21)$$

Consecutively, $S(k)$ is determined by using the density response function (Eq. 2.19) through the fluctuation-dissipation theorem. [88]

$$S(k) = -\frac{1}{\pi n} \int_0^{\infty} \text{Im} \chi(k, \omega) d\omega. \quad (2.22)$$

Here, $n = N/L$ is the electron density. Now the plasmon dispersion can be described by solving the pole of Eq. 2.19.

Recently the true potential of plasmon spectroscopy as a tool for the analysis of 1D systems has been demonstrated. [27, 31] In this context, the investigation of the collective excitations of low-dimensional electron gases on the scale of a few nanometers becomes partially feasible. The analysis of 1D plasmonic quasi-linear dispersion, measured for example, for regular arrays of atomic wires on insulating and semiconductor substrates, yields information about the form of the occupied as well as the unoccupied band structure in the vicinity of the Fermi level. Without any damping (i.e., when $\alpha = 0$), we find the dispersion relation for an undamped quantum wire plasmon at $T = 0$ as:

$$\omega_p(k) = \sqrt{\frac{\omega_+^2 e^{A(k)} - \omega_-^2}{e^{A(k)} - 1}} \quad (2.23)$$

Here, ω_+ and ω_- are the upper and lower boundary of the single electron-hole pair continuum. $A(k)$ is a function of the Coulomb matrix element $v_c(k)$. Notably, both parameters are related to the electronic band structure and charge distribution as follows:

$$\omega_{\pm} = \frac{\hbar(k^2/2 \pm kk_F)}{m^*}, \quad A(k) = \frac{\hbar^2 2\pi k}{m^* g_s V_c(k)} \times \frac{1}{1 - G_{\text{corr}}(k)} \quad (2.24)$$

In case $g_s = 1$, the other band is considered to be an insulator and for $g_s = 2$ either both bands are degenerated or the band is not subject to spin-orbit splitting. In the latter case, the available electron density is twice the previous one, and therefore the resulting plasmon dispersion also possesses a slightly higher slope for $g_s = 2$. For the present calculations, the local field correction factor $G_{\text{corr}}(k)$ has been derived from self-consistent mean-field approximation (STLS), which considers long-range electronic correlations. [84] The input wire parameters are as following: $m^* = 0.52m_e$, $k_F = 4.1 \text{ nm}^{-1}$, $\bar{\epsilon} = (\epsilon_{Si} + 1)/2$ with $\epsilon_{Si} = 11.5$, $b = 0.4 \text{ nm}$, and $g_s = 2$ or 1 . These parameters are taken for the single atomic Au chain superstructure on the Si(557) surface, and no other coupling than inter-chain interaction was considered. The results of this calculation are given in Fig. 2.5(b). According to the results, the plasmon frequency shows a strong dependence on the structure of the 1D band (i.e., g_s , m^*), and on the form and type of confinement potential. One should note that the best match between experimental and theoretical results was obtained for $g_s = 1$, where $g_s = 2$ matches the experimental dispersion only in the low k region. The dependence of plasmon frequency on the effective electron-density parameter r_s^* is shown in Fig. 2.5(a). r_s^* is related to the electron density n and the effective mass m^* in 1D via the following relation:

$$r_s^* = \frac{1}{2na_0^*} = \frac{1}{2n} \times \frac{m^* e^2}{4\pi\bar{\epsilon}\epsilon_0\hbar^2} \quad (2.25)$$

Here, the second term accounts the effective Bohr radius given by $a_0^* = \epsilon(m_0/m^*)a_B$ with $a_B = 0.0529 \text{ nm}$. The relation mentioned above implies that the increase of coupling in the 1D electronic

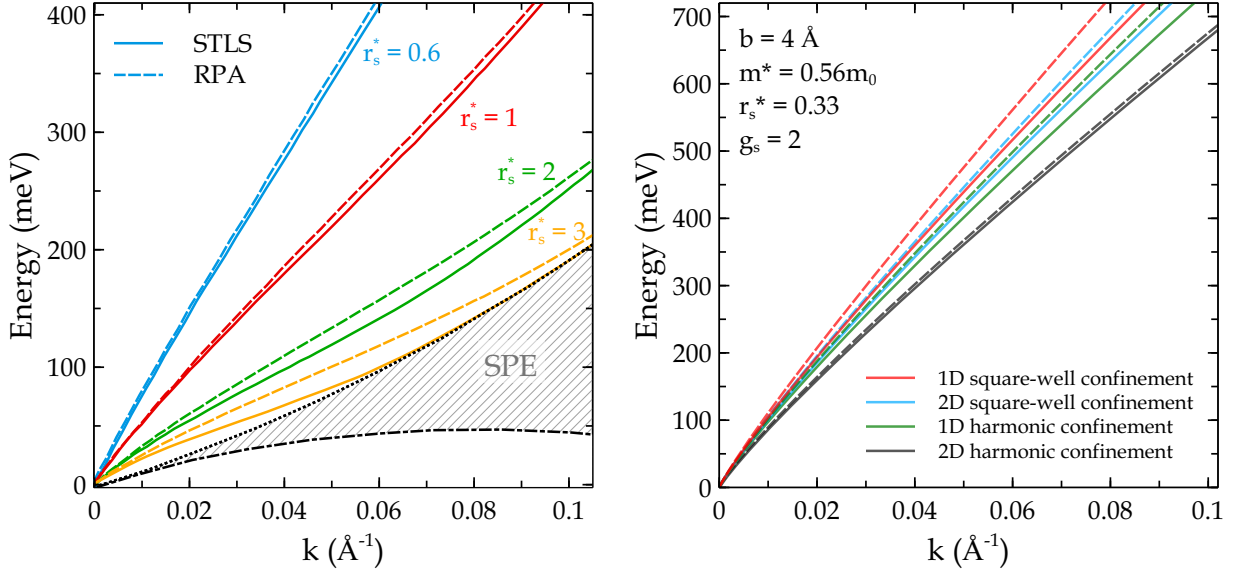


Figure 2.5: Effect of the coupling parameter r_s^* (left) and confinement model (right) on the 1D-plasmon dispersion. The solid and dashed lines represent the dispersions calculated using the STLS and RPA theories, respectively. In the left graph, the shaded area corresponds to the electron-hole pair continuum for this particular system derived for $r_s^* = 3$. The upper and lower boundaries for the SPE zone is given by the dotted and dashed-dotted line, respectively. In the right graph, the black, blue, green and red curves correspond to the confinement models I, II, IV and V, respectively. Adapted from Ref. [81] with permission. Copyright 2010 by IOP Publishing.

system results in a blueshift of plasmon frequency. In other words, the same electron density can now be excited with comparably less energy (see Fig. 2.5(a)). Moreover, in the strong coupling regime (i.e., $r_s^* = 3$), the plasmon dispersion deviates from linearity, mainly at low k (see also Fig. 2.6). However, plasmon dispersion shows a weak response to the change of b within the harmonic confinement model. This has been tested from $b = 0.4$ nm (width of the single atomic wire) up to $b = 1.9$ nm (the terrace width or the maximum width of the electronic distribution for this system), revealing a weak blueshift of plasmon frequency at small b due to increased confinement. This blueshift becomes more pronounced by decreasing b/r_s^* (which accounts for the effective electronic distribution) in RPA. This is because the e-correlations, which are ignored completely in RPA, build up with decreasing b/r_s^* and reduce the plasmon frequency in the STLS model. In turn, the latter compensates for the confinement-induced blueshift. This also explains the weak dependence of plasmon frequency on the confinement in the STLS model while the exchange-correlation effects grow in strength with increasing r_s^* in compared RPA (see Fig. 2.5). Moreover, at fixed k_F the plasmon dispersion reveals higher frequency for RPA in comparison with STLS revealing the essence of e-e correlation. Thus, the plasmon frequency shows a redshift as the effective electron-electron interaction becomes weaker due to decreased transverse confinement. Therefore, transverse confinement is an important parameter for the description of 1D

electron systems. Moreover, the effect of exchange-correlation on plasmon dispersion and, therefore, the difference between plasmon dispersion from RPA and STLS increases as a function of momentum. In a similar way, the exchange-correlation shows a stronger effect for the case of $g_s = 1$ than $g_s = 2$. Using the parameters mentioned above, the m^* was fitted to $m^* = 0.52m_e$, which is comparable to the $m^* = 0.45m_e$ from experimental ARPES. [89] The slight discrepancy between calculated and ARPES effective mass might be due to the experimental uncertainty and contribution of e-e correlation in theoretical determination.

The plasmon-pole approximation assumes that the excitation spectrum consists of no particle-hole excitations but solely of a collective mode, which exists for all values of wave vectors and possesses unit oscillator strength. In fact, the one-dimensional phase-space restriction of the particle-hole excitations increases the spectral weight of the plasmon excitation over a wide range of wave vectors. Therefore, the plasmon-pole approximation works well in such 1D systems. For the support of this statement, the oscillatory strength of plasmon excitation for 1D-quantum wire and 2D electronic systems have been calculated by D. Sarma et al. [79] There, the authors showed that the oscillator strength of the plasmons in a quantum wire shows almost no k dependence, only a slight decrease was observed at large- k . On the other hand, the oscillator strength of plasmons in a quantum-well (or in 2D electron gas) drops rapidly to zero at a critical wave-vector.

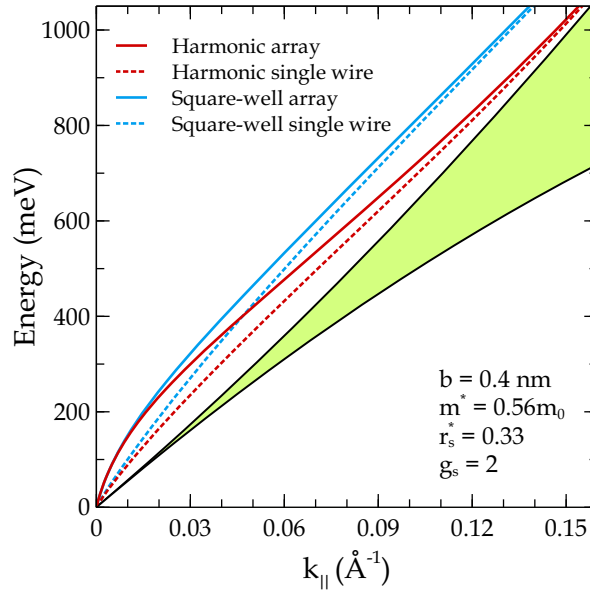


Figure 2.6: Plasmon dispersion curves obtained numerically for the single and laterally placed wires within the harmonic (model IV) and square-well (model V) confinement. Regardless of the choice of the confinement potential, by switching from single wire to array, plasmon dispersion manifests a blueshift, mainly at lower k due to lateral interaction of adjacent electron density. For modeling, 13 wires, 6 left and 6 right from the central wire were employed.

2.2.2. Plasmons in 1D Wire Arrays

In fact, the growth of a single isolated atomic (quantum) wire is not possible in experiments where it ends up with lateral arrays of 1D chains. Notably, their lateral interaction can be reduced by changing the step periodicity of the substrate but it can never be fully neglected. Therefore, to have a more realistic match between the theoretical and experimental plasmon dispersion, one should consider the lateral interaction (coupling) of those wires. This additional potential is again formulated in the framework of the self-consistent LFC theory (or STLS). [90]

$$V_c^{\text{eff}}(k) = V_c(k) + V_c^{\text{array}}(k) \quad (2.26)$$

Here, the first term accounts for intra-wire potential, while the second term considers the additional potential applied by inter-wire interaction. This additional Coulomb interaction can be described by the following integral [53]:

$$V_c(k)^{\text{array}} = \frac{e^2}{\bar{\epsilon}\epsilon_0} \int_0^a dy \int_0^a dy' \int_0^a dz \int_0^a dz' |\phi^{\text{array}}(y, z)|^2 \times |\phi(y', z')|^2 K_0(kR). \quad (2.27)$$

The relation mentioned above takes into account the interaction between electron density in the central wire $\phi(y, z)$ with the adjacent electron density $\phi^{\text{array}}(y', z')$. Where the electron density of the surrounding wire arrays is given with the following relation:

$$\phi^{\text{array}}(y, z) = \sum_{l \neq 0} \phi(y - ld, z) \quad (2.28)$$

Similar to the plasmon in an isolated wire (Eq. 2.3), the plasmon dispersion for 2D wire arrays is also given by the zeros of dielectric function in the low k region. [53]

$$\epsilon(k, \omega) = 1 - \chi_0 \sum_{l'} V_{l-l'}(k) e^{ik(l-l')d} = 0 \quad (2.29)$$

This mode assumes the following form in the low k regime.

$$\omega(k) = \hbar\omega_0 ka \times \sqrt{K_0(ka) + 2 \sum_{l=1}^n K_0(kld)} \quad (2.30)$$

where d is the wire separation, a is the width of each wire in y direction. ω_0 is a system-specific constant, which considers the bulk plasmon frequency and is given as:

$$\omega_0 = \frac{e}{2a} \sqrt{\frac{2n}{\pi\bar{\epsilon}\epsilon_0 m^*}}. \quad (2.31)$$

In the strong 2D interaction case, Eq. 2.30 yields plasmon dispersion identical to the plasmon dis-

persion of 2D metallic system with the form of $k^{1/2}$ at $k \rightarrow 0$. However, switching off the coupling by increasing d/a , plasmon dispersion shows a linear 1D behavior starting from $k = 0$. This underlines the strong dependence of the 1D plasmon dispersion on the wire dimension or electronic distribution. [53] Using the methodology mentioned above, the effect of lateral interaction of wire arrays has been numerically obtained and is shown in Fig. 2.6. For this, the above-mentioned wire parameters and IV and V type confinement models have been employed.

From these results, the plasmon dispersion shows a blueshift when switching from a single wire to a wire array. This is because the additional electron density increases the lateral interaction and therefore increases the 2D character of the plasmon dispersion. It is a common feature on all measured dispersion for atomic wire plasmon. [31] The results show a strong response of plasmon dispersion to the form of confinement potential mainly at low k . Besides, as discussed above, the plasmon dispersion calculated for the harmonic confinement yields lower energy slope compared to the square-well potential (see Fig. 2.6). Consequently, the harmonic confinement yields a more reasonable match to the experimental plasmon dispersion measured for the Si(557)-Au system. [81]

2.2.3. Plasmon Life-Time and Damping

Since Eq. 2.23 implies that ω_p is greater than ω_+ , the RPA plasmon dispersion does not decay to electron-hole pairs for all k points. Accordingly, the imaginary part of the dielectric function vanishes, $\epsilon(k, \omega) = 0$. This situation is very different from higher dimensions where ω_+ becomes larger than ω_p at a critical wave vector, $k_c \approx \omega_p/v_F$. Thus, if $k > k_c$, $\epsilon(k, \omega)$ has a large imaginary part, since ω_p penetrates into the electron-hole continuum and damps according to Landau damping mechanism. [91] Inside the Landau damping region, the plasmon decays by emitting electron-hole pairs, which is allowed by energy-momentum conservation. This damping rate can be determined at small k by taking $Im[\epsilon(k, \omega)] = \omega(k) - i\alpha(k)$ in Eq. 2.3. Another decay channel of the plasmon oscillation is due to impurity scattering. The critical wave vector, k_c , below which the plasmon does not exist due to impurity scattering effects, depends on the density of scatterers and the scattering rate. Thus, the inclusion of impurity scattering (γ) causes collisional damping of the plasmon mode resulting in further spectral broadening in addition to the Landau damping.

It is worth noting that the STLS approach (RPA) does not account for the damping of plasmons for $k < k_c$. This is due to the structure factor, which relies on the absorption of a photon with energy ω and momentum k . Without any interaction, the absorbed energy gives rise to electron-hole pair formation. The energy of these pairs lies within the interval of $\omega_- < \omega < \omega_+$ for $k < 2k_F$. If ω is outside this interval, the energy and momentum conservation laws cannot be satisfied, and the structure factor vanishes. [92]

In the experiment, the collective participation of a large number of charges in plasmonic excitations gives them an intense optical response. However, rapid damping via scattering among the charge carriers contributes to femtosecond lifetimes and broad resonances that have been experimentally mea-

sured. [93, 94] In general, three following types of electron-involved interaction leading to plasmon decay can be distinguished based on the interacting quasi-particles.

electron-electron scattering — Electron-electron scattering results in the simultaneous creation of an electron-hole pair and leads to decay into bulk or surface states at lower energy. Electron-electron interaction covers the creation or excitation of other quasi-particles such as plasmons and exciton. The nature of such quasi-particles can be manipulated by changing the wave vector and the primary energy of the impinging electrons. This is the main mechanism for plasmonic excitation that has been studied in this thesis.

electron-phonon scattering — Electron-phonon scattering mainly refers to the interaction between excited electrons (such as plasmons) and lattice vibrations, and changes the electron wave vector. The energy loss during this process is rather small compared to the previous example. As a result, the most probable decay happens within the surface state bands. It is noteworthy that owing to their low energy, phonon modes can easily be thermally excited. Therefore, electron (plasmon)-phonon interaction is a feasible process at finite temperature.

electron-defect scattering — Since real surfaces contain a nonnegligible number of defects associated with lattice distortion, adatoms, stacking faults, kinks, steps, impurities, etc., electron-defect scattering is one of the most facing challenges in surface electron dynamics and other related processes. The primary process here is the change of electron momentum by conserving the energy. This process is one of the basic principles for the excitation of standing waves in a quantum wire with a photon. Since the end states for shorter wires (or other kinds of defects) act as momentum sources, there is no additional momentum required for plasmonic excitation in shorter wire sections.

Chapter 3

Surface Studies with Low Energy Electrons

The present chapter gives a comprehensive insight into the basic principle of low energy electron interaction and scattering from the surface. The details of electron diffraction from flat and stepped surfaces will be described. Moreover, scattering conditions and possible mechanisms of elastic and inelastic scattering of low-energy electrons will be discussed. The actual experimental setups, working based on presented principles, will be presented in Chapter 4.

3.1. Low Energy Electron Diffraction

Due to the principles of wave-particle duality, the beam of electrons might be equally regarded as an electron wave incident on the sample, which is scattered by regions of high localized electron density (i.e., the surface atoms) and therefore can be utilized to probe atomic positions or generally surface periodicity. After the discovery of electron diffraction by Davison and Germer in 1927 [95], it became a useful tool for surface investigation with high sensitivity. Its adjustable high energy sensitivity enables us to study vertical and horizontal roughnesses and defects (e.g., kinks, step bunching, etc.) of crystal surfaces. Generally, the scattering cross section of low energy electrons (typically at 100 eV) is 4 to 6 orders of magnitude larger than x-rays, ensuring their usefulness for surface studies. The required surface sensitivity is achieved because of the small mean free path of low energy (10 to 100 eV) electrons within the solids of only a few Å (see Fig. 3.1). [96] For fixed energy, electrons are described by their de Broglie wavelength as follows:

$$\lambda_{\text{el}} = \sqrt{\frac{h^2}{2m_e E}} \quad \Rightarrow \quad \lambda_{\text{el}}(\text{\AA}) = \sqrt{\frac{150.4}{E(\text{eV})}} \quad (3.1)$$

Here, h , m_e and E is the Planck's constant, electron mass, and primary electron energy, respectively.

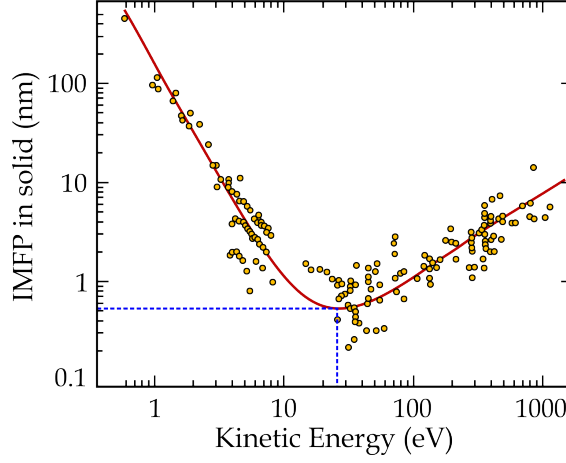


Figure 3.1: Compilation of the inelastic mean free path (IMFP) of electrons in the solid as a function of the kinetic energy according to Ref. [96]. IMFP is material independent and can be described by universal curve (red line), which exhibits a minimum at $E_{kin} \approx 30$ eV.

In this energy range, the wavelength of electrons lies in the range of the inter-atomic distance; therefore, probing of the atomic arrangement at crystal surfaces becomes possible. In this method, structural information is evaluated from the elastically scattered electrons. By evaluating the position and (integrated) intensity of the diffracted electrons, different kinds of information can be obtained from the LEED pattern of the crystal surface. There are three specific methods to evaluate diffraction patterns, such as Geometric LEED theory, Kinematic approach, and dynamic LEED theory. In the first two methods, only a single scattering event is considered, while the last one deals with the multiple scattering case. Generally, the diffraction pattern represents the reciprocal lattice of the real space lattice formed by taking the Fourier transform of the real space lattice vectors. In the 2D surface, the relationship between reciprocal and real space (a, b) and the reciprocal lattice (a^*, b^*) vectors can be stated via the following simplified form:

$$a^* = 2\pi \frac{b \times n}{a \cdot (b \times n)} \quad b^* = 2\pi \frac{a \times n}{a \cdot (b \times n)} \quad (3.2)$$

Eq. 3.2 is the so-called Laue conditions. If the wave vector of the incident electron is $k_0 = 2\pi/\lambda_0$ and scattered wave vector is $k = 2\pi/\lambda$, the condition for constructive interference, and therefore diffraction of scattered electrons from the 2D surface is given by the Laue condition.

$$\vec{K}_{\parallel} = \vec{k}_{\parallel,f} - \vec{k}_{\parallel,i} = \vec{G}_{\parallel} = ha^* + kb^* \quad (3.3)$$

where $\vec{k}_{\parallel,i}$ and $\vec{k}_{\parallel,f}$ is the incident and final scattering vector, G_{\parallel} is the reciprocal lattice vector, and h, k are integers. Since only the elastically scattered electrons are considered, the magnitude of wave vectors remains unchanged (i.e., $|\vec{k}_0| = |\vec{k}|$). The Laue condition can be visualized by using the Ewald

sphere construction (an example is shown in Fig. 3.2). Thus, the wave vector \vec{k}_0 is drawn starting from the center of the incident wave vector up to the intersection point ($\vec{G}_{||}$) with the reciprocal lattice point. And then, Ewald's sphere is drawn with a radius of $|\vec{k}_0|$ and centered at the incident wave vector. This way, at the intersection of a scattering vector parallel to the surface ($\vec{k}_{||}$) and reciprocal lattice vector ($\vec{G}_{||}$), the Brag peak appears. Due to the limited penetration depth of low-energy electrons, no diffraction perpendicular to the sample surface occurs. Therefore, the 2D surface mesh's reciprocal lattice appears as the Ewald's-rods extending perpendicular to the surface in reciprocal space.

3.1.1. Kinematic Approximation

For a further simplification within the kinematic approximation, the individual structure factors $f(\vec{r}_i, \vec{k}, \vec{k}_i)$ can be replaced by a single factor as $f(\vec{k}, \vec{k}_i)$ by assuming that the surface consists of identical unit cells (see Fig. 3.2(c)). Thus, the determination of surface structure is simplified to a single scattering process instead of multiple scattering events. Generally, the diffraction from a crystal surface can be described as the sum of the final wave vectors of scattered electrons (\vec{k}_f) from surface atoms with \vec{r}_n spatial position in respect to the incident electrons (\vec{k}_i). Then, the following relation gives the amplitude of the resulting wave function.

$$\phi(\vec{K}, \vec{k}_i) = \sum_n f_n(\vec{K}, \vec{k}_i) e^{i\vec{K}\vec{r}_n} \quad (3.4)$$

Here, $\vec{K} = \vec{k}_i - \vec{k}_f$ and $f_n(\vec{r}_i, \vec{K}, \vec{k}_i)$ are the scattering vector and structure factor, respectively. The structure factor refers to the electron waves scattered from atom locates at \vec{r}_n and all underlying atoms at a deeper surface (see Fig. 3.2). Subsequently, the total intensity of the diffracted electrons is expressed as follows:

$$I(\vec{K}, \vec{k}_i) = |\phi(\vec{K}, \vec{k}_i)|^2 = \sum_{n,m} f_n(\vec{K}, \vec{k}_i) f_m^*(\vec{K}, \vec{k}_i) e^{i\vec{K}(\vec{r}_n - \vec{r}_m)} \quad (3.5)$$

Since within the kinematic approximation, all atoms are considered to be placed at perfect lattice sites, the \vec{r}_n can further be written for all surface atoms as:

$$\vec{r}_n = \vec{r}(n_x, n_y) = \vec{a}_x n_x + \vec{a}_y n_y + \vec{a}_z h_n \quad (3.6)$$

Here, $n = (n_x, n_y)$ is the unit mesh, \vec{a}_x, \vec{a}_y stand for in-plane unit vectors while \vec{a}_z is the unit vector normal to the surface, with absolute value d , and height h_n of the corresponding unit mesh, i.e., $\vec{r}_n = a_0 n + \vec{a}_z h_n$ for square lattice with the lattice parameters a_0 and r_n . For considering the parallel and perpendicular components of the wave vector, \vec{K} can be separated into $\vec{k}_{||}$ and k_{\perp} , and then Eq. 3.5 will have the following form:

$$I(\vec{K}, \vec{k}_i) = \sum_{n,m} \left\langle f_{(n+m)}(\vec{K}, k_i) f_m^*(\vec{K}, \vec{k}_i) e^{idk_\perp(h_{n+m}-h_m)} \right\rangle_m e^{ia\vec{k}_\parallel n} \quad (3.7)$$

With the average structure factors as denoted by $\langle \dots \rangle_m$. Eq. 3.7 implies that the actual intensity of diffraction depends on both the atomic arrangement and their scattering amplitudes. Since the scattering amplitude differs for atoms at the step edge and the flat part of the surface, the kinematic approximation works better for smooth surfaces.

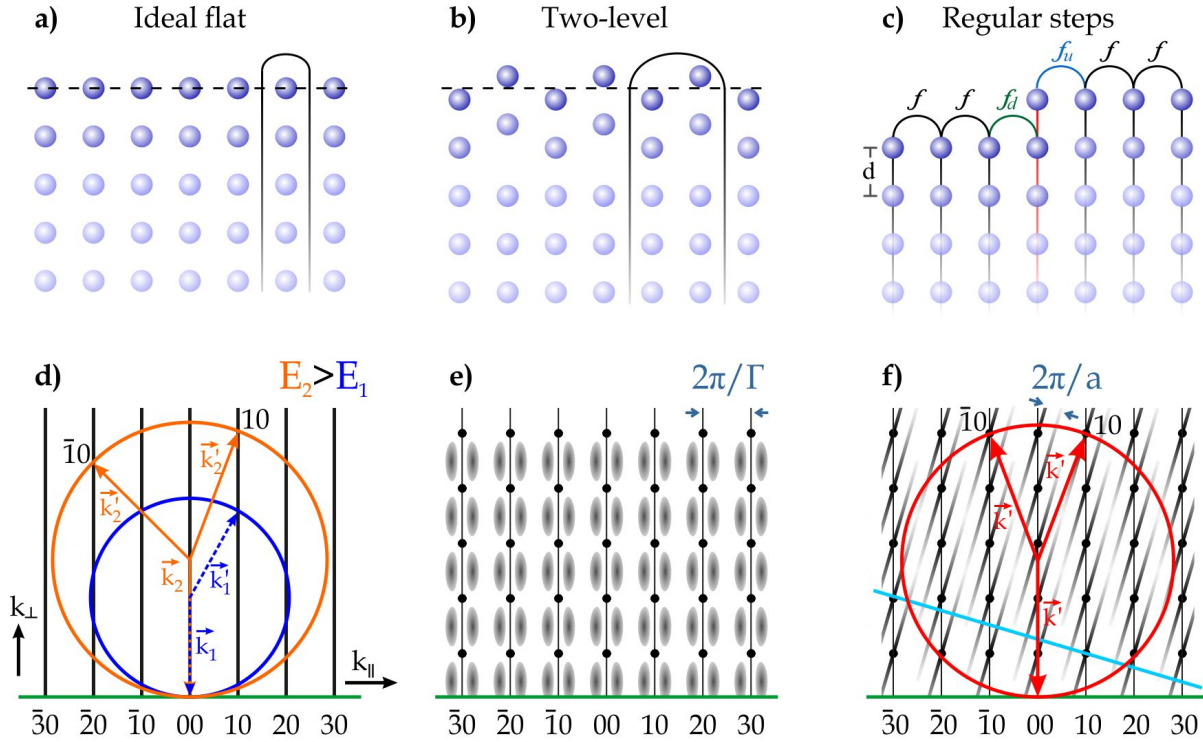


Figure 3.2: The surface unit cell and diffraction rods for (a) ideal atomically flat surface: spot profile does not change as a function of vertical scattering vector k_\perp , it is only subject to the instrumental broadening. (b) two-level superstructure: spot profile shows diffuse intensity with a distinct shoulder at most energies. The diffraction spots are sharp at the in-phase condition ($S = n$, where n is an integer), i.e., the 3D Bragg conditions. (c) a regular stepped (vicinal) surface: spot profile shows a spot splitting due to the linear phase grid of steps. The spots move in accordance with the inclination of the vicinal surface. [97] Determination of the structure factor (f) from a stepped surface is shown in (c). As given with f_u and f_d , the structure factor deviates from its average value at the step edges. The f_u and f_d donate different scattering amplitude resulting in modulation (or changes) of diffraction intensity. The bottom row shows the corresponding Ewald sphere construction, together with seven beams that have experienced back-scattering and resulting diffraction patterns. The green lines in (d-f) show the macroscopic plane, while the blue line in (f) indicates the terrace plane. As given in (d), an increase of the primary electron energy increases the radius of the Ewald sphere and changes the orientation of the diffracted beams as exemplarily indicated by \vec{k}_1 and \vec{k}'_1 .

The intensity (I) of diffracted electron waves (Eq. 3.7) can be split into G (lattice factor) and F (dynamic form factor) by neglecting the small deviation of the scattering amplitude at various structural elements.

$$I(\vec{K}, \vec{k}_i) = F(\vec{K}, \vec{k}_i) \times G(\vec{k}_{\parallel}, k_{\perp}) \quad (3.8)$$

where $F(\vec{K}, \vec{k}_i)$ and $G(\vec{k}_{\parallel}, k_{\perp})$ are given with the following equations:

$$F(K, k_i) = |f(K, k_i)|^2 \quad (3.9)$$

$$G(\vec{k}_{\parallel}, k_{\perp}) = \sum_n \left\langle e^{idk_{\perp}(h_{n+m}-h_m)} \right\rangle_m e^{ia\vec{k}_{\parallel}n} \quad (3.10)$$

Furthermore, considering that the form factor (G) is strongly dependent on the perpendicular component of scattering vector as $k_{\perp} \propto \sqrt{E}$ (E is the electron energy) but weakly on \vec{k}_{\parallel} , the diffraction intensity (Eq. 3.11) can further be simplified to:

$$I(\vec{K}, \vec{k}_i) = F(E) \times G(\vec{k}_{\parallel}, k_{\perp}) \quad (3.11)$$

Here, the form factor $F(E)$ describes the dynamic effects, and the shape of the spot profile can be characterized by using only lattice factor $G(\vec{k}_{\parallel}, k_{\perp})$ in the following equation:

$$G(k_{\parallel}, k_{\perp}) = \sum_n \phi(n, k_{\perp}) e^{ia\vec{k}_{\parallel}n} \quad (3.12)$$

where $\phi(n, k_{\perp})$ stands for the Fourier transform of the phase correlation, and Eq. 3.12 describes the line profile of diffraction spots. The phase correlation can be described using the pair correlation function $C(n, h)$ as Eq. 3.13, which depicts the probability to find the next atom at a distance of na and a vertical distance of dh (h is an integer) from the atom located at $na = 0$ and $dh = 0$. This is only valid for structures with translational symmetry.

$$\phi(n, k_{\perp}) = \sum_{-\infty}^{\infty} C(n, h) e^{ik_{\perp}dh} \quad (3.13)$$

$$C(n, h) = \int_0^{2\pi/d} dk_{\perp} \phi(n, k_{\perp}) e^{ik_{\perp}dh} \quad (3.14)$$

According to Eq. 3.14, the comprehensive information about the surface morphology can be acquired from the series of spot profiles from phase 0 to $2\pi/d$. While structure factor $F(E)$ yields information about the scattering of single atoms, the lattice factor $G(\vec{k}_{\parallel}, k_{\perp})$ is defined by the periodic lattice mesh

and does not modify the integral intensity. However, the intensity distribution in reciprocal space is highly responsive to the structural periodicity. Thus, the spot profile of ideal flat and defect-free surfaces is subject to only instrumental broadening. The latter is commonly called an instrument factor. The pair correlation function on such an ideal surface, coincides with the delta (δ) function as $C(n, h) = \delta(h)$, and therefore the lattice factor $G(\vec{k}_{\parallel}, k_{\perp})$ can also be given as the sum of delta functions as:

$$G_{ideal}(\vec{k}_{\parallel}) = \sum_n \delta(\vec{k}_{\parallel}) - \frac{2\pi}{a}n \quad (3.15)$$

However, in the case of dislocations or surface distortions, the intensity of sharp diffraction spots deviates from the ideal δ function and is scattered as a broad distribution of diffuse intensity. [98, 99] This is visually shown in Fig. 3.2 by comparing the real space surface structure with the resulting diffraction pattern.

As shown there, the ideal round diffraction spots (Fig. 3.2(a)) transform into a diffuse shoulder (Fig. 3.2(b)) by changing the macroscopic surface morphology, from the atomic flat surface to the two-level surface. Moreover, a spot splitting appears for the regularly stepped surfaces (Fig. 3.2(c)).

The latter describes the correlation between arranged (anisotropic) surface elements and/or long-range ordering. Nevertheless, the overall intensity from the central and diffuse parts (i and j) for an individual diffraction spot is always conserved and proportional to the number of surface unit cells (Eq. 3.16). On the other hand, the overall intensity is independent of surface roughness (h_n) and vertical component of wave vector (k_{\perp}). Therefore, it can be normalized to:

$$\int_{BZ} d\vec{k}_{\parallel} G_{ij}(\vec{k}_{\parallel}, k_{\perp}) = 1 \quad (3.16)$$

Here, the lattice factor $G_{ij}(\vec{k}_{\parallel}, k_{\perp})$ corresponds to the Fourier transform of the atomic arrangement of the surface. By considering constant form factor $F(E)$ within the SBZ, the $G(\vec{k}_{\parallel}, k_{\perp})$ can be extracted from the measured diffraction intensity ($I(k_{\parallel}, k_{\perp})$ by normalization to total integrated intensity (I_{total})).

$$\frac{I(\vec{k}_{\parallel}, k_{\perp})}{I_{total}} = \frac{F(\vec{k}, \vec{k}_i) \cdot G(\vec{k}_{\parallel}, k_{\perp})}{\int_{BZ} F(\vec{k}, \vec{k}_i) \cdot G(\vec{k}_{\parallel}, k_{\perp}) d\vec{k}_{\parallel}} \quad (3.17)$$

$$\sim \frac{F(\vec{k}, \vec{k}_i) \cdot G(\vec{k}_{\parallel}, k_{\perp})}{\bar{F}_{BZ} \int_{BZ} G(\vec{k}_{\parallel}, k_{\perp}) d\vec{k}_{\parallel}} \quad (3.18)$$

$$= \frac{F(\vec{k}, \vec{k}_i) \cdot G(\vec{k}_{\parallel}, k_{\perp})}{\bar{F}_{BZ}} \quad (3.19)$$

$$\sim G(\vec{k}_{\parallel}, k_{\perp}) \quad (3.20)$$

In this regard, a small variation of the form factor $F(\vec{k}, \vec{k}_i)$ with \vec{k} affects the spot profile only around the spot as a diffuse intensity or broadening. While lattice factor $G(\vec{k}_{\parallel}, k_{\perp})$ dominates the central intensity. Therefore, the kinematic theory better approximates the large surface structures and/or macro-

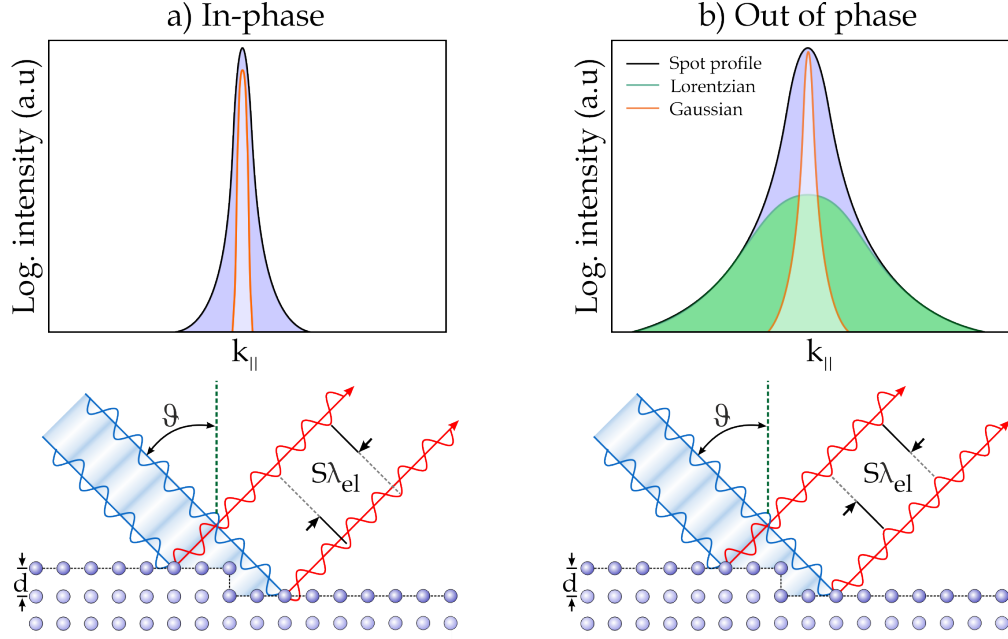


Figure 3.3: Schematic illustration for the phase shift during low-energy electron scattering from a stepped surface. At the step edges, the scattered waves undergo $2\pi S$ phase shift (here S and λ_{el} represent the path difference and electron wavelength, respectively). For integer values of phase S , the scattered waves give rise to constructive interference resulting in sharp diffraction spots (a). At the in-phase condition, electrons are insensitive to the terrace width distribution. However, there is still sensitivity to local deviations from periodicity, etc. In the case of non-integer values of phase S , the scattered waves are subject to destructive interference, where the sharp diffraction spots fade (b). In the latter case, which is the so-called out of phase condition, split diffraction spots appear for a regular array of steps. Split spots are not resolvable for a broad distribution of terrace widths.

scopic roughness.

3.1.2. H(S) and G(S) Analysis

Assuming coherent scattering from the uncorrelated adjacent terraces, the broadening of spot profile $\Psi(\vec{k}_{\parallel}, k_{\perp})$ yields information about the terrace size $\langle \Gamma \rangle$. This corresponds to the Lorentzian shape (broadening) of the measured spot profile at the out-of-phase condition via the following relation [98, 100, 101]:

$$\Psi(\vec{k}_{\parallel}, k_{\perp}) \propto \frac{1}{\left(\frac{2}{\langle \Gamma \rangle}\right)^2 + (a\vec{k}_{\parallel})^2} \quad (3.21)$$

The mean terrace width $\langle \Gamma \rangle$ of a two-level surface can be obtained from the FWHM of the line profile of the diffraction spot as follows:

$$FWHM = \frac{4}{\langle \Gamma \rangle}. \quad (3.22)$$

Scattering Phase — The scattering phase S defines the phase difference between electron wavelength (λ_{el}) when electrons are scattered from the adjacent terraces of a stepped surface.

$$S = \frac{k_{\perp} d}{2\pi}. \quad (3.23)$$

where d is the step height (or interlayer spacing). Following Eq.3.23, the scattering phase depends on the vertical scattering vector k_{\perp} . As shown in Fig. 3.3, integer values of S (i.e., $S = n$, n is an integer number) correspond to constructive interference of waves diffracted from the adjacent terraces ("in-phase" or Brag condition), while half-integer values of S (i.e., $S = n + \frac{1}{2}$) correspond to destructive interference ("out-of-phase" anti-Brag condition). At the out-of-phase condition, the overall intensity is redistributed into the diffuse part around the diffraction spot, which is sensitive to vertical roughness and also yields information on long-range correlation. At the in-phase condition, sharp diffraction spots appear independent of surface roughness (see also Fig. 3.3). For the specular (00) spot, where $k_{\parallel} = 0$, phase S depends on the electron wavelength as following:

$$S = \frac{2d \cos \theta}{\lambda_{el}} \quad (3.24)$$

Here, λ_{el} and θ are the electron wavelength and angle of incidence with respect to the surface, respectively (see Fig. 3.3). θ yields the specular angle of $\cos \theta = 0.997 \approx 1$ for typical SPA-LEED setup. Substituting λ_{el} from Eq. 3.1 into Eq. 3.24, the practical form of the scattering phase can be expressed as:

$$S = 2d \cos \theta \sqrt{\frac{E(eV)}{150.4}} \quad (3.25)$$

Eventually, Eq. 3.25 enables to extract the average step height d using the primary electron energy and scattering phase via Laue condition. Although Eq. 3.22 gives a reasonable result for the two-level surface, it has to be extended for description of multi-level surfaces: The spot profile of the multi-level surface consists of central spike $G_c(k_{\perp})$ and diffuse broadening $\Phi_d(k_{\parallel}, k_{\perp})$ induced by interference from different levels of surface atoms.

$$G(k) = G(k_{\perp})G_c(k_{\parallel}) + [1 - G(k_{\perp})]\Phi_d(k_{\parallel}, k_{\perp}) \quad (3.26)$$

where $\Phi_d(k_{\parallel}, k_{\perp})$ describes the diffuse intensity and it is given by following equation:

$$\Phi_d(k_{\parallel}, k_{\perp}) = \frac{I_d(k_{\parallel}, k_{\perp})}{\int_{BZ} I_d(k_{\parallel}, k_{\perp}) \times dk_{\parallel}} \quad (3.27)$$

The amplitude of both central spike and broadening vary with k_{\perp} . The diffuse part of the scattered intensity varies with scattering phase S by giving the highest intensity at half-integer S . Thus, the spot profile of the multilevel surface (i.e., with randomly distributed terrace widths) should be described by convoluted Lorentzian and Gaussian functions where Lorentzian shape refers to the diffuse part, and Gaussian distribution explains the diffraction spot. In this approach, the FWHM of the Lorentzian distribution directly yields the average terrace width $\langle\Gamma\rangle$ as a function of S . This is the so-called $H(S)$ analysis, and it is given with the following form in the one-dimensional case.

$$H(S) = \frac{1}{\pi\langle\Gamma\rangle} [1 - \cos(2\pi S)]. \quad (3.28)$$

The equation mentioned above can be generalized for multiple step height surfaces by taking the variation of step heights via the following expression:

$$H(S) = \sum_{h \geq 1} \frac{\beta_h}{\pi\langle\Gamma\rangle} [1 - \cos(2\pi Sh)]. \quad (3.29)$$

where β_h comprises the involvement of different step heights $h \times d$. Again if the step morphology is dominated by one step height, the mean width of the terrace can be collected in the out-of-phase condition via the following relationship:

$$\pi\langle\Gamma\rangle = \frac{2}{FWHM_S} \quad (3.30)$$

Here, index S refers to the scattering phase with half-integer values, i.e., $S = n + \frac{1}{2}$. Similar to studies of the lateral surface arrangement (or $H(S)$) analysis, vertical roughness of the 2D surfaces can be studied via $G(S)$ analysis. $G(S)$ analysis employs the integrated peak intensity of the central diffraction spot, which varies as a function of k_{\perp} . The following equation gives the $G(S)$ relation.

$$G(K_{\parallel} = 0, S) = \sum_h C_h \cos(2\pi Sh) = 1 - \sum_{h \geq 1} C_h [1 - \cos(2\pi Sh)]. \quad (3.31)$$

where C_h refers to the vertical height correlation, and it is defined by:

$$C_h = \sum_l p_l p_{h+l} = \frac{1}{2\pi} \int_{-\pi}^{+\pi} dS G(S) \cos(2\pi Sh). \quad (3.32)$$

Here, p_h and p_l is the probability of finding a surface atom in the level h and lateral position l . The calculation of the $G(k_{\parallel} = 0, S)$ as a function of S can be done by the Fourier transformation of the normalized central spike intensity via Eq. 3.17. Now assuming that the lattice factor has the shape of a Gaussian close to the in-phase condition, $G(S)$ is given by:

$$G(S) \approx e^{-\Delta_{\text{RMS}}^2 (2\pi\delta S)^2} \quad (3.33)$$

where Δ_{RMS}^2 is given by the following relation [101–103]:

$$\Delta_{\text{RMS}}^2 = \langle h^2 \rangle - \langle h \rangle^2 = \sum_h C_h h^2. \quad (3.34)$$

One should note that in addition to those LEED theories discussed above that have relevance for the studies in this thesis, there is also the dynamic LEED theory. It is mainly used to study structural information using the variation of intensities of all diffracted spots available as a function of energy at a constant angle of incidence. By employing optical LEED due to easy control of electron beam over huge range on the sample. [104]

3.2. Inelastic Scattering

The interaction of low-energy electrons with the crystal surface relies on two major processes regarding energy conservation. These are the elastic and inelastic scattering events. The elastic scattering process is based on the energy conservation between the initial and final state of the scattering particle. However, in the inelastic scattering process, the scattering particle transfers or gains energy during the interaction event. Since the whole process as *initial state* \rightarrow *collision* \rightarrow *final state* must obey the energy and momentum conservation, the loss energy of the initial particle corresponds to excitation of surface modes (see Eq. 3.35). The resulting excited modes can either be phonon or plasmon (i.e., electronic excitation) kind.

$$\begin{cases} E_i - E_f = \hbar\omega \\ k_i - k_s = q + g \end{cases} \quad (3.35)$$

When the incident electron with wave vector \vec{k}_i scatters from the surface with wave vector \vec{k}_s , two primary scattering processes can be distinguished as described in Fig. 3.4. These will be discussed in the following sections.

3.2.1. Dipole Scattering

The oscillating component of the electric dipole moment creates an oscillating electric field at the sample surface. When the electromagnetic field of the incoming electron waves interacts with these long-range dipole fields scatters. Considering a semi-infinite crystal surface with the ground state charge density $\rho_0(x)$, the total charge density becomes $\rho_0(x) + \rho_1(x, t)$ due to thermal fluctuation. Although the fluctuation rearranges the charge distribution, the charge neutrality of the whole surface is preserved as:

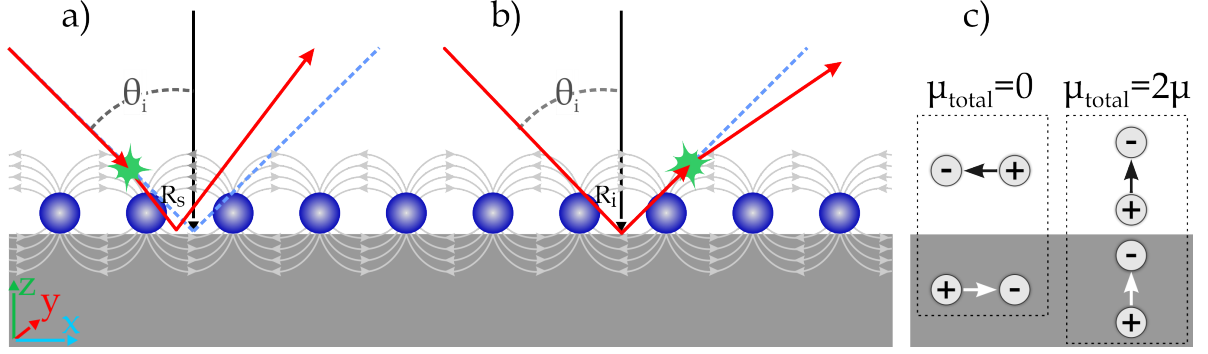


Figure 3.4: Schematic illustration for the most pronounced electron energy loss process through dipole scattering. a) inelastic scattering process (green spark) takes place close to the surface before an elastic scattering, b) inelastic scattering process takes place after an elastic scattering. Both processes happen due to the interaction between impinging electrons and the long-range electric field at the surface (shown with arrows). R_s and R_i are the elastic scattering amplitudes that are not necessarily the same. The blue dashed lines depict the elastic scattering path. c) The selection rule for the dipole scattering on the surface. Depending on dipole-dipole interaction, the resulting dipole moment (μ_{total}) is equal to either sum or difference of the initial dipole moments. The generated electric field by representative image dipoles inside the material tends to increase the dipole effect normal to the surface.

$$\int d^3x \rho_1(x, t) = 0, \quad (3.36)$$

Within this approach, when an electron with charge e approaches the 2D surface with $z < 0$ experiences the electrostatic potential.

$$\phi(x, t) = e \int_{z' < 0+} \frac{d^3x' \rho_1(X', t)}{|X - X'|}, \quad (3.37)$$

where the single interaction event is extended over the whole sample surface with the integral. The integral is extended into the surface in order to consider any contribution from the charge density induced by fluctuation inside the crystal (or deeper surface). The Eq. 3.36 requires that at a large distance from the surface, the main contribution to $\phi(x, t)$ is dipolar in character. Accordingly, retardation effects are ignored in Eq. 3.37. Information from the atom is assumed to be transmitted to the electron on a time scale shorter than excitation itself; it perceives the atomic positions while it is scattered at l_0 above the surface. In Ref. [105] it has been shown that l_0 is related to the two-dimensional wave vector (\vec{K}) as $l_0 \cong \vec{K}^{-1}$. After the corresponding replacement, Eq. 3.37 can be reformulated as:

$$\phi_1(x, t) = 2\pi e \int \frac{d^2\vec{K}_{\parallel}}{\vec{K}_{\parallel}} e^{(i\vec{K}_{\parallel} \cdot x_{\parallel})} \times e^{(-\vec{K}_{\parallel} z)} \int_{z' < 0} \rho_1(\vec{K}_{\parallel} z'; t) e^{+\vec{K}_{\parallel} z'} dz' \quad (3.38)$$

where $\rho_1(\vec{k}, z', t)$ represents the charge density fluctuations and $\vec{K}_{\parallel} = \vec{k}_{\parallel}^i - \vec{k}_{\parallel}^s$ (i and s stand for the incident and scattered electron, respectively). Only components of a wave vector parallel to the surface are conserved. Hence, for a given value of \vec{K}_{\parallel} and energy transfer ω , the direction of the emerging electron can be determined via Eq. 3.35.

The relevant quantity to describe the scattering from the surface is the scattering efficiency Q_{SC} per unit angle $d\Omega(\vec{k}_s)$ and per unit energy $d\hbar\omega$, having the form $d^2Q_{SC}/d\Omega(\vec{k}_s)d\hbar\omega$. This quantity is dimensionless and describes the probability that electron will scatter from its initial state into a final state in the angle $d\Omega(\vec{k}_s)$ and in the energy range $d\hbar\omega$. According to Ref. [106], the scattering efficiency is described as:

$$\frac{d^2Q_{SC}}{d\Omega(\vec{k}_s)d\hbar\omega} = \frac{m^2e^2v_{\perp}^2}{2\pi^2\hbar^5\cos\theta_1} \left(\frac{\vec{k}_s}{\vec{k}_i}\right) \frac{P(\vec{K}_{\parallel}, \omega)}{\vec{K}_{\parallel}^2} \times \frac{|v_{\perp}\vec{K}_{\parallel}(R_s + R_i) + i(R_i - R_s)(\omega - v_{\parallel} \cdot \vec{K}_{\parallel})|^2}{[v_{\perp}\vec{K}_{\parallel}^2 + (\omega - v_{\parallel} \cdot \vec{K}_{\parallel})^2]^2} \quad (3.39)$$

Here, θ_1 is the angle of incidence, v_{\parallel} and v_{\perp} are the magnitude of the incoming electron velocity parallel and normal to the surface. R_i and R_s (also see in Fig. 3.4) are the probability amplitudes that describe the specular reflection of the incoming and scattered electrons from the surface. Thereby, if an incident electron with energy E_i and wave vector \vec{k}_i is considered, the intensity of the specular reflection normalized to the incident intensity is $|R_i|^2$. The processes described in Fig. 3.4(a,b), interfere coherently; their contributions are added to the inelastic scattering amplitude in Eq. 3.39 and are then squared to form the expression for the inelastic intensity $|R_i|^2$ and $|R_s|^2$. Therefore the Eq. 3.39 can be simplified to the following form:

$$\frac{d^2Q_{SC}}{d\Omega(\vec{k}_s)d\hbar\omega} = \frac{2m^2e^2v_{\perp}^4}{\pi\hbar^4\cos\theta_1} \left(\frac{k_s}{k_i}\right) \frac{|R_i|^2P(\vec{K}_{\parallel}, \omega)}{[v_{\perp}^2\vec{K}_{\parallel}^2 + (\omega - v_{\parallel} \cdot \vec{K}_{\parallel})^2]^2} \quad (3.40)$$

According to Eq. 3.39, the inelastic intensity diverges when θ_1 approaches 90° due to the extended interaction time with the surface. This statement is valid for the present model, while it can be removed when the image potential is taken into account. By contribution of \vec{K}_{\parallel} to the potential given in Eq. 3.37, the potential is extended above the surface with a distance roughly \vec{K}_{\parallel}^{-1} . Accordingly, any contribution to the potential with a spatial variation $e^{i\vec{K}_{\parallel} \cdot x_{\parallel}}$ parallel to the surface, regardless of its physical origin, must necessarily decay as $e^{-\vec{K}_{\parallel} z}$ by going away from the surface. Hence, any fluctuation in charge density produces a long-range disturbance in the vacuum that gives rise to small-angle scattering. Likewise, a contribution to the potential proportional to $e^{i\vec{K}_{\parallel} \cdot x_{\parallel}}$ is produced by charge fluctuations that extend into the surface with distance $l_0(\vec{K}_{\parallel}) \approx \vec{K}_{\parallel}^{-1}$ below the surface. Thus, an electron, which suffers scattering that changes its wave vector components parallel to the surface by the amount \vec{K}_{\parallel} , travels into the surface by a distance \vec{K}_{\parallel}^{-1} . $P(\vec{K}_{\parallel}, \omega)$ in Eq. 3.40 is the quantity of response of the system to a particular excitation or probability of scattering from a particular system. Ultimately $P(\vec{K}_{\parallel}, \omega)$ can be related to the dielectric properties of the system. [107]

$$P(\vec{k}_{\parallel}, \omega) = \frac{2\hbar\vec{k}_{\parallel}}{\pi} [1 + n_{BE}(\omega)] \times \Im \left\{ \frac{-1}{\tilde{\epsilon}(\vec{k}_{\parallel}, \omega) + 1} \right\} \quad (3.41)$$

Here, $n_{BE}(\omega)$ is the number of vibration quanta described via the following expression in Bose-Einstein statistics.

$$n_{BE}(\omega) = [e^{\hbar\omega/k_{\beta}T} - 1]^{-1} \quad (3.42)$$

In Eq. 3.41, \Im is the imaginary part of the substrate dielectric constant, and $\tilde{\epsilon}$ is an effective wave vector dependent dielectric function, which the electron sees when it interacts with the surface (or dipole field above surface). In general, $(\tilde{\epsilon}(\vec{k}_{\parallel}, \omega) + 1)^2$ is described as a loss function.

3.2.2. Impact Scattering

One of the approaches describing inelastic impact scattering and the scattering cross section is the quantum-mechanical scattering theory. This approach treats the impact scattering as a scattering of a wave from the crystal lattice, similar to the kinematic diffraction theory. Unlike the kinematic diffraction theory, absorption or emission of energy is necessarily considered. Having an incoming plane wave with wave vector k_i the outgoing wave after scattering from surface atoms (or electron density) is described via $\varphi(k_s, k_i)e^{\frac{ik_s r}{r}}$. Considering a 2D crystal plane with fixed atomic (nuclei) positions $\vec{R}_1, \vec{R}_2, \dots, \vec{R}_n$, the probability amplitude that the scattered electron possesses is given by $\varphi(\vec{k}_s, \vec{k}_i; \{\vec{R}_n\})$. One should note that the scattering amplitude for such a semi-infinite crystal can be given within the kinematic diffraction theory (see Section 3.1.1). Thus, considering a 2D unit cell with the reciprocal lattice vectors \vec{G}_{\parallel} , the scattering amplitude $\varphi(\vec{k}_s, \vec{k}_i) \neq 0$ is satisfied only when $\vec{k}_{\parallel}^s = \vec{k}_{\parallel}^i + \vec{G}_{\parallel}$. This implies the occurrence of only Bragg scattering, which is an elastic event with $E_s = E_i$. In other words, due to the lack of translational symmetry normal to the surface, only wave vector components parallel to the surface are conserved. At finite temperature, the atomic positions are not fixed in their equilibrium positions at each instant of time, but they shift due to thermal vibration with displaced atom j at position $\vec{R}_j = \vec{R}_j^0 + \vec{u}_j$. Here, \vec{R}_j^0 and \vec{u}_j are the vectors to the equilibrium site and displacement from it. In this case, the ideal Bragg condition is altered, while some of the scattered electrons emerge away from the Bragg direction, which gives rise to the thermal diffuse background. Since these off-scattered electrons experience energy absorption or emission, the whole scattering process is inelastic. The scattering amplitude $\varphi(\vec{k}_s, \vec{k}_i; \{\vec{R}\})$ is determined by the atomic positions. Taking into account the only emission of vibrational quanta (ω_s), the cross section for inelastic scattering from the surface is expressed in terms of matrix element as:

$$M(\vec{k}_i, \vec{k}_s; +s) = \langle n_s + 1 | \varphi(\vec{k}_s, \vec{k}_i; \{\vec{R}\}) | n_s \rangle = \sqrt{\frac{(n_s + 1)\hbar}{2N\omega_s}} \times \sum_{i\alpha} \left(\frac{\delta\varphi}{\delta R_{i\alpha}} \right)_0 \left(\frac{\xi_{i\alpha}^s}{\sqrt{M_i}} \right) \quad (3.43)$$

Here, ω_s (vibration frequency) and $\xi_{i\alpha}^s$ (eigenvectors) must be derived numerically. $(\delta\varphi/\delta R_{i\alpha})_0$ is

the derivative of scattering amplitudes. For a given scattering geometry, for electrons that scatter with a particular energy E_s , the difference $(k_{\parallel}^s - k_{\parallel}^i)$ is constant. If G_{\parallel} is the particular reciprocal lattice vector, which, when subtracted from $(k_{\parallel}^s - k_{\parallel}^i)$ yields a vector g_{\parallel} that lies within the first Brillouin zone. Then the vibrational quanta that may scatter the electrons in the direction determined by \vec{k}_s , are only those with a vector g_{\parallel} . This forms the wave vector conservation parallel to the surface. If $(\frac{dS_{\alpha}(k_i, k_s)}{d\Omega})d\Omega$ is the probability that the vibrational quanta ($g_{\parallel}\alpha$) scatters the electron into the solid angle $d\Omega$, one may show that with A the surface area of the crystal:

$$\frac{dS_{\alpha}(k_i, k_s)}{d\Omega} = \frac{mE_1 \cos^2 \theta_s}{2\pi^2 \hbar^2 \cos \theta_i} A |M(k_i, k_s; Q_{\parallel}\alpha)|^2. \quad (3.44)$$

Here, M is a matrix element that describes the formation of a vibrational quantum and is given by the derivative of the scattering amplitude to the nuclear displacement $\delta f / \delta R$. Now, one should assume that the intensity of specular reflection from the surface with fixed atomic positions $|R_i|_0^2$ is subject to reduction by the Debye-Waller factor due to thermal vibrations as:

$$|R_i|^2 = |R_i|_0^2 e^{[-\frac{1}{2}\langle(Q \cdot u)^2\rangle_T]} \quad (3.45)$$

Here, u is the displacement of an atom from its equilibrium position; the thermal average is considered via angular brackets. Scattering of electrons by phonon changes their direction from a specular escape angle and therefore reduces the specular intensity, which adds to the thermal diffuse background. The depletion of the specular beam from one-phonon process is approximated by $\frac{1}{2}\langle(Q \cdot u)_T^2\rangle |R_i|^2$. From this Q^2 is proportional to electron energy E_i and scales with the primary electron energy as $E_i |R_i|$. It must be noted that the dipole excitation cross section is given by $|R|^2$ and decreases as a function of primary electron energy. Now the intensity of losses due to the impact scattering can simply be estimated as:

$$I_{inelastic} \approx \frac{1}{2} (\vec{K} \cdot u)^2 I_{elastic} \quad (3.46)$$

where \vec{K} is the wave vector transfer, which corresponds to the incoming wave vector as $|Q| \cong |k_i|$ at large scattering angles.

Chapter 4

Experimental Technicalities

The first part of this chapter describes the vacuum chamber and gives a brief overview of the experimental techniques and methods used. As the main investigation methods, EELS-LEED and SPA-LEED have been used in the scope of the present thesis. Additionally, to study the oxidation of the Si(553)-Au surface, the infrared absorption measurements were conducted at the Kirchhoff-Institute for Physics, University of Heidelberg. The setup and working principles of the IR-absorption spectroscopy will not be presented here. Therefore, for any further information, please refer to Ref. [108]. In the second section of this chapter, the substrates used and surface preparation will be described.

4.1. UHV Chamber

The ultrahigh vacuum (UHV) chamber is made of stainless steel. The sketch of the UHV vessel with the main parts is shown in Fig. 4.1(a). The UHV vessel is divided into two parts: the main chamber and the load lock. The main chamber is equipped with a high-resolution SPA-LEED and an EELS-LEED, a gold evaporator, a sputter gun, hand-made hydrogen cracker, and a quadrupole mass spectrometer (QMS). The main chamber is connected to a membrane pump (pre-vacuum pump), a Ti-sublimation pump, and an ion-getter pump. Additionally, a getter pump containing a porous ZrVFe alloy is used to reduce residual hydrogen gas. The setup used is capable of achieving a base pressure of 5×10^{-11} mbar. During the measurements, the effort was made to keep the pressure within this range, except during gas exposure experiments. The average pressure is measured by an ion gauge. Additionally, the partial pressure of various gases is examined by the QMS after each baking process and during gas exposures. The load lock was used for sample installation, as well as for initial outgassing. The load lock is connected to a membrane pump and a turbopump. With this combination, a pressure of 10×10^{-9} mbar was achieved in the load lock. In order to establish the desired pressure, the chamber was baked

at a temperature of ~ 170 °C for two days. Baking of the whole setup was also required after switching the gas exposures between H_2 and O_2 .

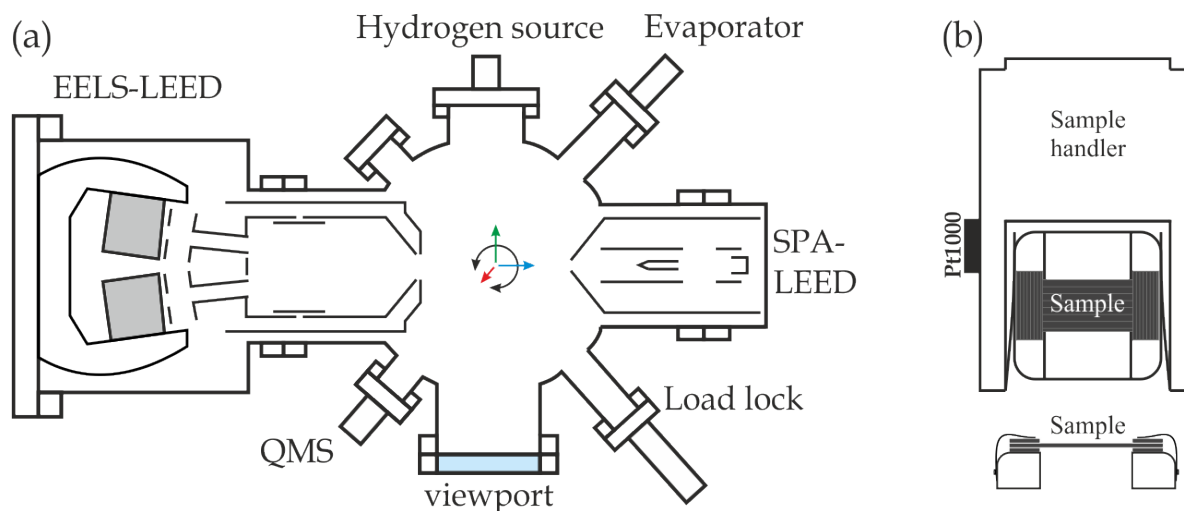


Figure 4.1: (a) Sketch of the UHV chamber with the positioning of the individual components used in this work. The arrows in the center indicate the movable directions of the sample. Sketch adapted from Ref. [109]. (b) Front and side view of the sample handler, which holds the sample. The sample is mounted on the holder using four Si spacers. The Pt1000 temperature sensor located on the side of the sample handler was used for low-temperature measurements.

The sample holder used is made of Molybdenum, which is mounted on the sample handler made out of copper, inside the main chamber. The sample handler can be moved horizontally and vertically as well as rotated for alignment to the various components. The handler can be cooled through a cryostat with liquid nitrogen or liquid helium; however, the heat transfer is not optimal due to spacers and small clamps. The temperatures during cooling were measured by the Si diode located directly on the cryostat near the sample and by the additional Pt1000 resistance located on the side of the handler (see Fig. 4.1). During high-temperature treatment, the sample temperature was measured using the IR pyrometer through the viewport (window). The emissivity is regulated by computer software during the measurement. The sample is mounted on the sample holder with durotherm (CoNiCrMo) clamps. In addition, four Si spacers, cleaned as the main sample, were used to attach the sample to the sample holder (see Fig. 4.1(b)). This configuration helps to absorb (or reduce) extra mechanical stress while heating the sample with direct current. It also prevents contamination of the sample from the metallic sample holder during high-temperature treatment.

4.2. SPA-LEED

Throughout this thesis, a spot profile analysis low-energy electron diffraction (SPA-LEED) was used to qualitatively check the surfaces after each new preparation and quantitative investigation. The sketch of this setup is shown in Fig. 4.2 . [110–112] A prototype of the SPA-LEED device was developed by Prof. Dr. M. Henzler and his group in Hannover, at the same institute as this thesis is realized. [112] This device can be operated in two geometries in reciprocal space: normal geometry of incidence and grazing geometry of incidence. Besides, a real space mode can also be operated, a so-called low-resolution scanning electron microscopy mode. This is used to align the sample in front of the electron beam.

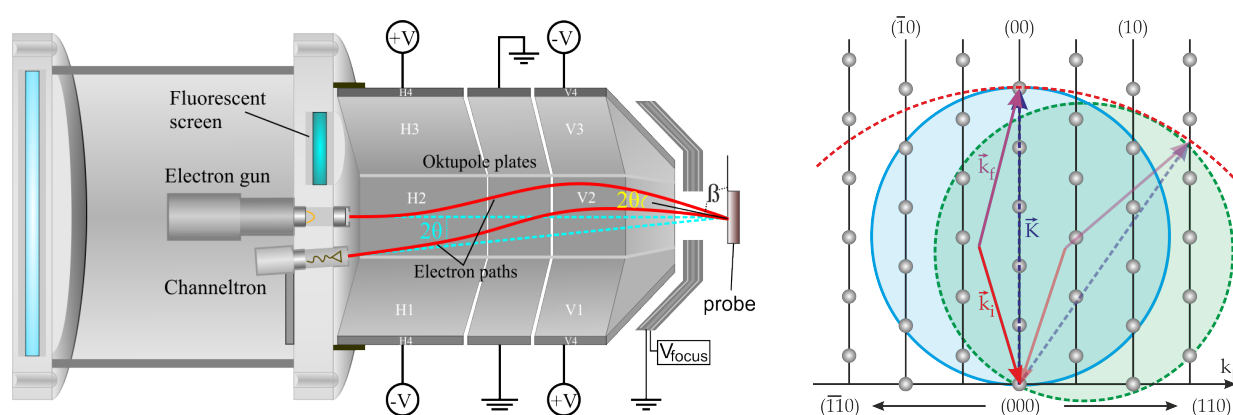


Figure 4.2: Left: Schematic setup of the SPA-LEED system used in this work. Electrons emitted from the hot filament and selected with primary energy directed to the grounded sample using the potential difference between octupole plates. The red lines show the projection of electron paths before and after backscattering from the surface, while the blue dashed lines correspond to the direct vector of the incident and scattered electrons. This setup facilitates H(S) and G(S) analysis of the probed surface by acquiring 1D scans in a predetermined direction. Adapted from Ref. [113]. Right: The Ewald construction, diffraction rods, and resulting diffraction pattern within the given scattering condition. The resulting diffraction pattern is described by the envelope of the rocking Ewald sphere. This sphere (red circle) is centered at the origin of the reciprocal space and has a diameter twice the Ewald sphere. The incident \vec{k}_i and the final wave vector \vec{k}_f are always in the same relative orientation. The regulation of the voltage in the deflection unit results in a change of the scattering vector \vec{K} giving access to the reciprocal space.

The major components of this design include a fine-focus electron gun, an entrance lens close to the specimen, an electrostatic deflection unit, and an opening in front of a channel electron multiplier (CEM) detector. Unlike conventional LEED, the image is not produced on a fluorescent screen. Instead, a CEM analyzes the reflected intensity. The setup also has a phosphorous screen that enables a quick overview of the diffraction pattern. The beam generated by the hot filament is deflected by applying voltages at the octupole plates and finally focused on the entrance slit of the detector. The set of octupole plates is

adjusted in such a way that no voltage is applied in the center, which allows keeping the angle between the incident (\vec{k}_i) and final scattering vector (\vec{k}_f) constant (see Fig. 4.2). Because of this configuration, the scattering condition is changed compared to a conventional LEED. Thus, instead of scanning the margin of the Ewald sphere, a new sphere with a diameter twice the Ewald sphere is generated, which is rotating around the origin at (000) while changing the octupole voltages. This enables scanning a larger area in reciprocal space with increased resolution.

The resolution is given by the size of the spot and the entrance slit in front of the CEM. Small spot size can be obtained by means of a fine-focus electron gun under low current electron beam conditions. Typical existing settings range from 50 pA providing high-resolution images up to 500 nA for low resolution visual inspection. During operation, the electron energy can be varied from 5-500 eV. Moreover, the count rate or intensity can be changed via the primary electron energy, the repeller, and the extractor.

The width of the focused electron beam in the detector plane defines the transfer width of the instrument as:

$$T = \frac{k_{01}}{\Delta k} a_0 \quad (4.1)$$

where Δk is the width of the electron beam, k_{01} is the distance between fundamental spots, and a_0 is the atomic row distance at the surface. A wider transfer width results in a sharper peak. This has the benefit of better statistics in the experimental as well as evaluation of obtained results. Its higher reliability to work with single diffraction spots, as well as recording line profiles even at different energies, makes the SPA-LEED superior to conventional optical LEED. The SPA-LEED is operated with the computer software WinSPA. [114]

4.3. EELS-LEED

Since the energy loss of the electronic excitation is usually measured in fractions of eV, the resulting loss peaks are placed very close to the elastic peak. Therefore, their observation requires a very high energy resolution. On the other hand, the instrumental broadening must be sufficiently low that the lifetime broadening can be extracted from the measured spectrum. To achieve this resolution, monochromators and high-resolution energy analyzers were used to obtain a uniform electron beam and record the spectra of electrons scattered from the sample. An analysis of the surface excitation relies on the investigation of inelastically scattered electrons. Due to its high surface sensitivity, which is given by the primary electron energy (see Fig. 3.1), the surface plasmonic excitation can easily be studied with almost no contribution from bulk electronic states. In addition to the conventional EELS, an implementation of the LEED deflection unit allows high resolution in momentum transfer.

The EELS-LEED used in this work is a home-built setup combined with the Lebold-type 120° cylindrical monochromator and analyzer. The monochromator and analyzer are made of copper, and all the slits are made of copper-beryllium alloy. All the other components are made of non-magnetic materials such as tantalum, molybdenum, and high-purity alumina. Since low voltages (~ 20 V) makes the slow

electrons susceptible to magnetic and electric fields, the whole setup is shielded with permalloy that reduces the magnetic flux density to $< 7\mu\text{T}$ in the spectrometer. [115]

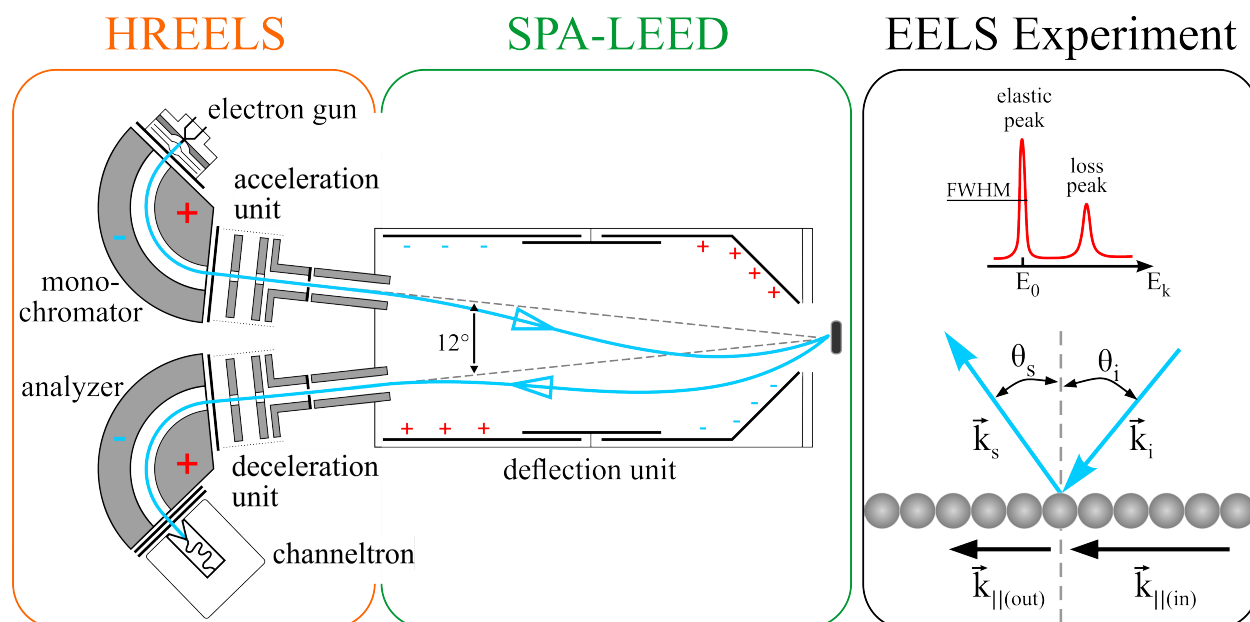


Figure 4.3: Schematic drawing of the EELS-LEED setup used in this thesis. Right part schematic demonstration of EELS experiment. In general scattering geometry and electron primary energy define the momentum transfer direction and magnitude on surface. FWHM of the specular peak related to the angular acceptance of the EEL spectrometer according to Eq.4.5. EELS-LEED sketch adapted from Ref. [116].

The central part of the EELS controller consisted of a combination of high-precision D.C. voltage generators and high-precision potentiometers. All the voltages are tuned and pre-adjusted with respect to the filament voltage. All the electrode voltages are modified by the same value concerning the sample potential to change the electron beam's primary energy. The sample potential is set to the ground level. The EEL spectra are recorded by scanning the offset voltage of the analyzer part with respect to the filament voltage via a programmable D.C. voltage. The voltage generator is controlled by a personal computer. During this thesis, a LaB_6 cathode (filament) was used, which gives well-defined electron emission with a comparably narrower (in comparison with other cathodes) focusing area and energy resolution. The sketch of the EELS-LEED is given in Fig. 4.3. The setup does not allow mechanical movement of the lenses, but the only alignment of the electrons' trajectory by applying voltage differences to the electrostatic lenses.

Historically low-energy EELS was first used in the form inelastic low-energy electron diffraction (ILEED) [117] using a retarding field analyzer to filter out the inelastically scattered electrons from the quasi-elastically scattered electrons, e.g., from the unresolved contributions due to the elastic diffraction and to lattice vibration. The device was also further developed by M. Henzler's group at the University of Hannover [118] to achieve both a high momentum and energy resolution. This device consists of a

127.8° cylinder capacitor. Following Ref. [105, 115], the resolution is approximately given by the pass energy E_p as follows:

$$\frac{\Delta E}{E_p} = \frac{s}{r_c} + \frac{4}{3}\alpha^2, \quad E_p = \frac{1}{2} \frac{\Delta U e}{\ln(r_o/r_i)}. \quad (4.2)$$

Here, $s = 0.3$ mm is the slit width, $r_c = 35$ mm is the radius of the center path, r_o and r_i are the radii of the outer and inner capacitor plates with $r_o/r_i \approx 1.4$, α is the maximum angular aperture of the input electron beam, and ΔU is the difference in voltage between the two plates. In the EELS measurement, the energy and momentum transfer parallel to the surface is conserved that can be expressed as follows:

$$\begin{cases} E_{loss} = E_i - E_s \\ \hbar q_{\parallel} = \hbar(\vec{k}_i \sin \theta_i - \vec{k}_s \sin \theta_s) \end{cases} \quad (4.3)$$

where E_i is the initial (primary) energy of the incident electrons, and E_{loss} is the loss energy after impinging on surface. θ_s and θ_i are the angles in the scattering plane with respect to the surface normal of the sample for incident and scattered electrons. k_i and k_s are the incident and scattered wave vectors normal to the surface, as shown in Fig. 4.3. Here, the parallel component of the wave vector (q_{\parallel}) is expressed via the following relation:

$$q_{\parallel} = \frac{\sqrt{2mE_i}}{\hbar} \left(\sin \theta_i - \sqrt{1 - \frac{E_{loss}}{E_i}} \sin \theta_s \right) \quad (4.4)$$

Thus, the integration window or the resolution in momentum space, Δq_{\parallel} , can be expressed by differentiating Eq.4.4 following Refs. [42, 119].

$$\Delta q_{\parallel} \approx \frac{\sqrt{2mE_i}}{\hbar} \left(\cos \theta_i - \sqrt{1 - \frac{E_{loss}}{E_i}} \cos \theta_s \right) \alpha \quad (4.5)$$

Here, α is the angular acceptance of the instrument, which determines the experimental accuracy. α is translated into an integration over reciprocal space and it can be determined by measuring the FWHM of the specular peak (see Fig. 4.3).

4.4. Gold Evaporator

A home-built gold evaporator has been used during this thesis. The evaporator consists of a gold pearl located on a tungsten spiral surrounded with cooling pipes made of copper (see Fig. 4.4). The whole construction is built on a CF-35 flange. Two 10 MHz Quartz Crystal Microbalances (QCM) were used for calibration of the evaporation rate, one at the sample position, and another on the evaporator. Taking the ratio of frequency changes (by fitting the slope) and the known mass frequency relation of the quartz, the concentration of Au atoms on the sample surface was calculated. The procedure described

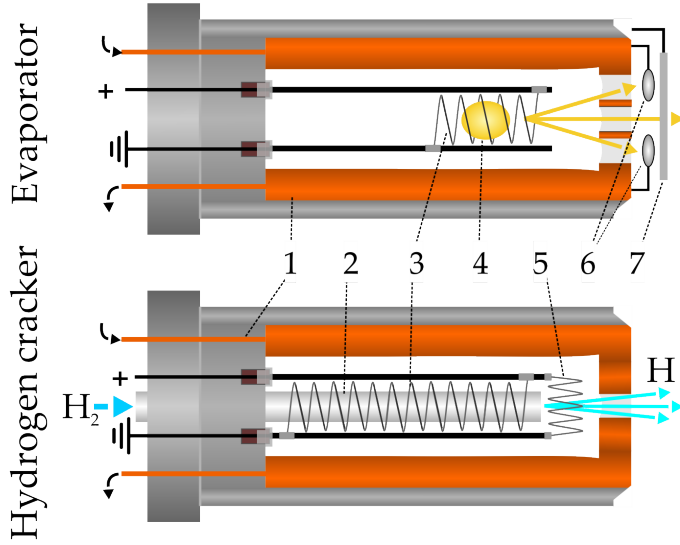


Figure 4.4: Side view of the gold evaporator and hydrogen cracker used in the present thesis. The orange parts in both images represent copper-made cooling sheaths. Rest parts are made of stainless steel. To increase cracking efficiency, two (vertical and lateral) tungsten filaments have been used in the hydrogen cracker. Numbering: 1- Cooling parts, 2- H₂ inlet, 3- vertical tungsten filaments, 4- Au pearl, 5- lateral tungsten filament, 6- QMB, 7- shutter.

in Ref. [120] was applied using the following relationship:

$$\Delta f = \frac{\rho_A \times f_{QCM}^2}{\rho_{QCM} \times N_{QCM}} \quad (4.6)$$

Here, $\rho_{QCM} = 2.65 \text{ g/cm}^3$ is the density of quartz and ρ_A is the additional density (mass) per area. For 1 ML of Au on the Si(111) surface, $\rho_A = 1.71 \times 10^{-10} \text{ g/cm}^{-10}$. $f_{QCM} = 10 \text{ MHz}$ is the ground frequency of the oscillator and $N_{QCM} = 1670 \text{ kHz mm}$ is the eigenfrequency of the thickness shear mode for an AT-cut [121]. From this routine, the frequency change in the sample position was estimated to be: $\Delta f_{Si(111)} = 38.6 \text{ Hz}$. This calibration routine allowed an exact rate of the evaporation of Au onto the sample. It is worth noting that in addition to the discussed pre-calibration of the gold evaporator, SPA-LEED and plasmon spectroscopy were also used as complementary techniques for further optimization of actual surface coverage.

4.5. Hydrogen Cracker

For hydrogen chemisorption experiments, atomic H was produced by dissociation of molecular hydrogen in a homemade hydrogen cracker. [122] The sketch of the hydrogen source used is shown in Fig. 4.4(bottom). The cracker is composed of a tungsten capillary of 3 mm inner diameter that is thermally shielded with a cooling pipe out of copper. The other side of this capillary is connected to a minican of hydrogen gas via a fine control valve. In the cracker, there are two filaments. One is coiled in the direction of the hydrogen flow, the other one is aligned along the cross section of the capillary. The distance between the cracker and sample was estimated to be $\sim 7 \text{ cm}$, which is sufficient to avoid heating of the sample. Therefore, no thermal desorption during hydrogen adsorption experiments is expected.

Hydrogen adsorption experiments were carried at 300 K sample temperature, so only cracked H had to be considered to estimate the adsorbed H amount. The efficiency cannot be precisely determined, but was estimated to $\sim 5\%$ at a filament temperature of 2000 °C. [123] However, experiments with molecular hydrogen showed that a very small fraction of molecular hydrogen could also be simultaneously dissociated at Si step edges (preferable). [33] Since the experiments with H_2 requires extremely high dosage, the disorders induced by hydrogen and water dominates the surface properties. Therefore, all the hydrogen adsorption experiments have been carried out with the atomic hydrogen.

4.6. Definition of Gas Exposure

In this thesis, the adsorbate amount is given in the Langmuir model, so the only chemisorption has been considered as a relative adsorbate coverage.

In the case of gas exposure experiments, the dosage was estimated as a function of exposure time and partial pressure using the following equation:

$$\theta(t) = \frac{1}{Sr_j \cdot 1.33 \cdot 10^{-6}} \int P(t) dt \quad (4.7)$$

Here, Sr_j is the relative sensitivity of ionization gauge to gas species or a correction factor ($1/Sr_j$). Following Ref. [124] that values 0.44 and ~ 0.9 for H_2 and O_2 , respectively. The resulting dose is given by Langmuir (L) as $1L = 1.33 \cdot 10^{-6}$ mbar · sec. It worth noting that this estimation gives only the gas flow that hits the sample surface. In addition, the actual adsorbed gas coverage on the surface is principally dependent on the sticking coefficient and desorption rate. When $P(t) \rightarrow 0$, $\theta(t) \rightarrow 0$, so that at low concentration, adsorption is linearly proportional to P . When $P(t) \rightarrow \infty$, $\theta(t) \rightarrow 1$ the relative adsorbate coverage (Γ) reacts to a monolayer.

Throughout this work, 99.99% clean gases (H_2 and O_2) from Linde have been used. For assurance of cleanness of exposure experiments, the gas lines were baked for several hours before each exposure, and before switching one gas to another, the whole UHV was also baked. Moreover, before and during each gas exposure, mass spectra were recorded.

4.7. Si Substrates and Surface Preparation

Silicon is one of the most used semiconductor materials in technology, as well as for scientific studies. Silicon crystallizes in the diamond structure on a face-centered cubic (fcc) lattice in which each atom covalently binds tetrahedrally with four adjacent atoms equivalently (see Fig. 4.5). The resulting distance and angle between two partner Si atoms are 2.35 Å and 109.5°, respectively. The bulk lattice constant for silicon is 5.43 Å. Si has a direct gap of 3.5 eV and an indirect gap of 1.1 eV, making it an indirect band gap semiconductor. Practically, Si crystal can be cleaved in 3 different directions, such as

[110], [100], [111]. Although the [100] directed Si surfaces are more reliable for technological use¹, the [111] oriented surfaces have been extensively used in scientific experiments. Upon removing the oxide layer, Si(111) surface transforms irreversibly into the lowest energy state of well-known 7×7 reconstructions. According to the DAS (Dimer Adatom Stacking fault) model, this reconstruction forms a non-planar hexagonal unit cell with the 3.84 Å the lattice constant. [126]

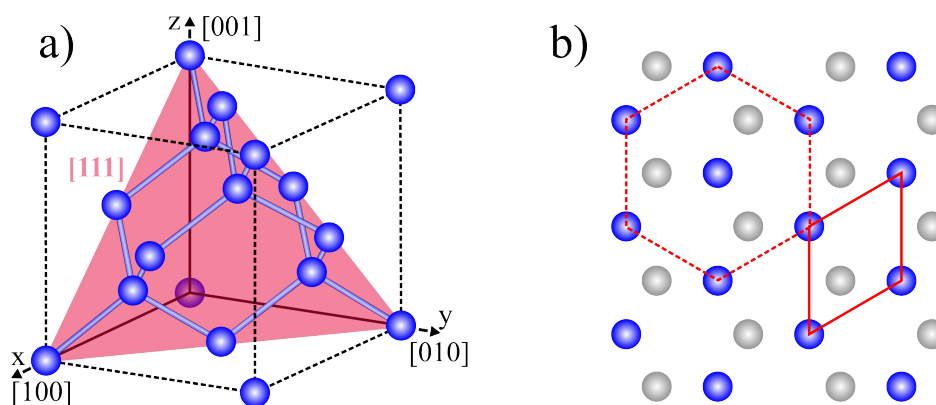


Figure 4.5: Stick and ball model of the diamond crystal structure of bulk Si (a), and Si(111) surface (b). The [111] plane is given in red. The solid and dashed lines show corresponding empirical triangular and hexagonal surface unit cells. Blue and gray balls stand for topmost and second layer Si atoms, respectively.

When a Si(111) crystal is cut at a small angle relative to a low-index orientation, the surface forms steps that separate low-index terraces. These surfaces are called vicinal (or stepped) surfaces. The average distance between steps of a vicinal surface is given by $L = \frac{h}{\sin\theta}$ here, h is the step height, and θ is the angle between the low-index orientation and surface plain. In such miscut Si surfaces, not only the terrace distribution but also the number of free bonds per step edge atoms can be varied. For instance, along $(\bar{1}\bar{1}2)$, each step edge atom possesses two dangling bonds (i.e., (335), (337), (557)) while in the $(11\bar{2})$ direction, every Si step edge atom has one dangling bond orbital (i.e., (110), (553), (775), (995), (13 13 7)). [65] A cross section of the Si(111) surface along the $(11\bar{2})$ direction is given in Fig. 4.6. The step separation and their interaction determine the stable variance for each orientational off-cut. Therefore, although many different inclinations from the nominally flat surfaces have been tested for various purposes, the number of stable orientations are limited to a few. [65, 127] Four members of such inclined Si(111) surfaces have been thoroughly investigated for atomic wire growth. These are Si(hhk) ($h, h, k = h \pm 2n$) indexed surfaces with (553), (557), (775) and (335) orientations, as marked in Fig. 4.6. All known members of the Si(hhk)-Au family share a similar set of recurring structural building blocks. The detailed parameters of Au-decorated Si(hhk) are given in Table 4.1. Upon deposition of the corresponding amount of Au onto these surfaces, Si atoms at the step edges are rearranged into

¹Due to a higher quality of SiO₂ on the [100] Si/SiO₂ interface has a lower Si adatom density (or lower amount of dangling bonds) and therefore minimum interface density compared to others. This results in higher carrier mobilities for functional devices. However, removing such oxide layer is a highly demanding process for fundamental purposes. [125]

a honey-comb like structure with sp^2 -hybridized states. [65] Single, or double Au atomic strands are located approximately in the middle of the terraces, separated by double atomic height Si steps on the regularly arranged surfaces. The surfaces with slightly wider terraces (i.e., Si(557)-Au and Si(775)-Au), contain an additional single Si ad-atom row per terrace. Moreover, the rearrangement of surface atoms in the presence of ad-atoms gives rise to the rest-atom chains, which are located slightly lower than other Si surface atoms. Indeed, each ordered as well as non-periodic (i.e., defects) structural motif has individual effects on the electronic properties of the corresponding surfaces, as discussed in the following chapters.

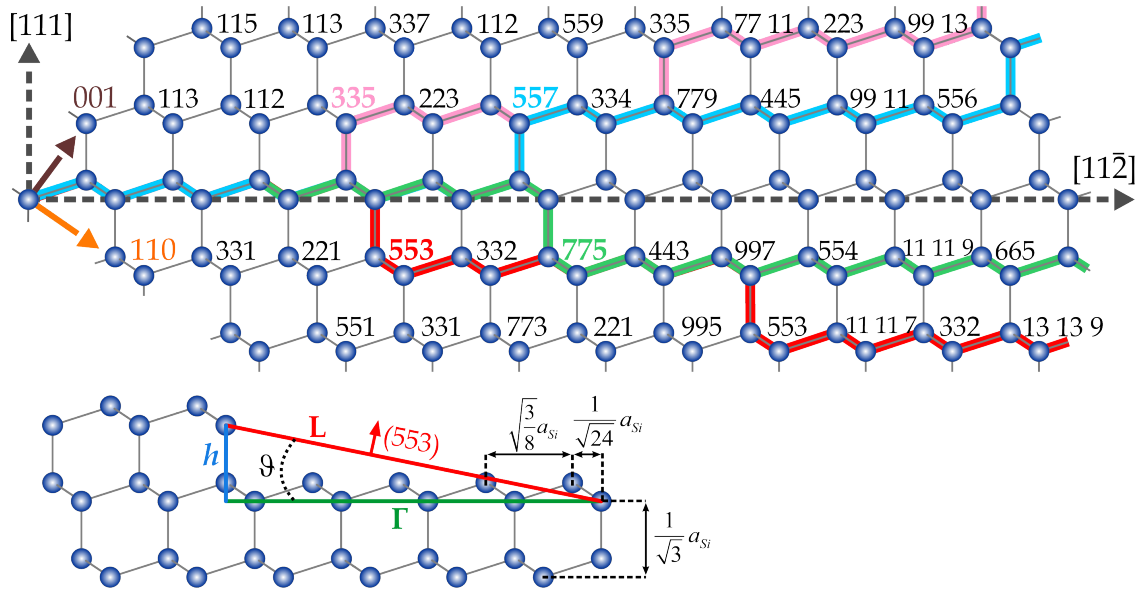


Figure 4.6: Stick and ball model of the Si(hhk) surfaces planes. After Ref. [65]. Colored lines depict the corresponding surface orientation with respect to the (111) plane. The bottom graph is the side view of the Si(553) surface with terrace width Γ , step height h , step-step distance L , and inclination angle ϑ . $a_{Si} = 5.431 \text{ \AA}$ is the bulk Si lattice constant.

4.7.1. Sample Preparation

In earlier studies, [58, 128, 129] no significant dependence of plasmonic excitation on bulk doping concentration was found. However, using highly doped samples simplifies the flashing procedure as an applied small voltage avoids rapid heating of sample and sample holder and, therefore, an uncontrolled increase of UHV pressure. In all measurements presented in this thesis, only highly n-doped (mainly 10^{18} cm^{-3} charge concentration or 0.01-0.03 Ωcm resistivity) samples have been used for all experimental studies. The wafers used have been obtained from CrysTec in Berlin. They were $275 \mu\text{m}$ thick and $5 \times 15 \text{ mm}$ wide with the long side parallel to the step edges. This orientation helps to avoid step bunching during flash annealing with a direct heating current. [130] A recipe for preparation of a well-

Table 4.1: Summary of the known most stable Si(hhk) surfaces that have also been studied in this thesis. The inclination angles are given respect to the [111] surface plane towards the $[11\bar{2}]$ or $[1\bar{1}2]$ direction. Corresponding Au coverage to form stable surface reconstruction and the resulting terrace width are also given.

Sytems	Off-cut angle	Terrace width (Å)	Au coverage (ML)
Si(553)-Au HCWs	-12.5 direct	14.7	0.48
Si(553)-Au LCWs	-12.5	33.2	0.19
Si(775)-Au	-8.5	21.1	0.32
Si(335)-Au	+14.4	12.2	0.27
Si(557)-Au	+9.5	19.1	0.18

defined terrace distribution and kink-free (or with fewer kinks) steps has been applied. Refs. [131–134] The samples were first cleaned ex-situ with acetone, petroleum benzene, and iso-propanol to eliminate grease, dirt, and other residuals from the previous procedures. It was found that cleaning the stepped surfaces in HF solution results in step bunching during annealing, probably due to the etching of steps. Afterward, the sample was mounted on the sample holder (see Fig. 4.1). The sample was outgassed for several hours under UHV condition at a temperature of ≤ 600 °C, below the cracking temperature for the oxide layer. Indeed, the long degassing time helps to keep the base pressure lower than 2×10^{-10} mbar during the flashing procedure. Before every preparation, the sample was flash annealed to 1200 °C several times until a well ordered pristine surface is achieved (see Fig. 4.7). This step reduces surface imperfections by increasing the diffusion rates of surface and bulk atoms. Moreover, it helps to desorb not only weakly bound but also chemisorbed species from the surface. All direct heating procedures have been carried out with the current parallel to the step edges to avoid step bunching due to thermal migration. [134, 135] The surface preparation procedure is summarized in Fig. 4.8.

Pristine Si Surfaces from SPA-LEED — The room temperature SPA-LEED patterns for the pristine 1° Si(111), Si(553), Si(557) and Si(775) surfaces are shown in Fig. 4.7. After removing the oxide layer the nominally flat Si(111) surface shows well defined 7×7 reconstruction (see Fig. 4.7(a)). Although this is a fundamental reconstruction for other stepped surfaces, it appears very faint in the diffraction pattern due to the domination of steps. The round spots in all diffraction patterns originate from the Si step trains; their sharpness and roundness show the regularity of step arrays and step perfection, respectively. They show characteristic splitting, which points out the step separation.

A quantitative analysis of this splitting for Si(553) surface yields ~ 14.7 Å terrace width, separated with bi-atomic height steps, as reported earlier in Refs. [136–138]. The first-order spots form a unit cell consisting of flat (111) terraces as indicated with the side down arrows in Fig. 4.7(b-d). As revealed by LEED, the well-arranged and stable arrays of steps on Si surfaces were achieved by applying appropriate flashing cycles.

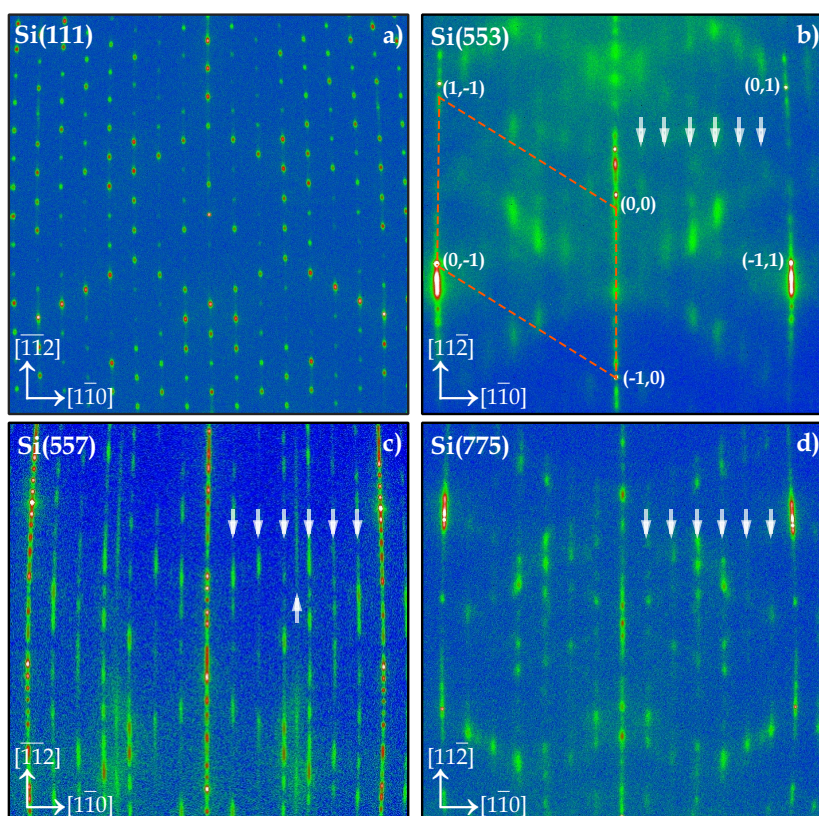


Figure 4.7: SPA-LEED patterns of the pristine Si(553), Si(557) and Si(775) surfaces. Images were recorded at room temperature after several flash annealing cycles. The white down arrows indicate the $\times 7$ periodicities, which are common to all Si(111) surfaces. The first order spots form a 1×1 unit cell, indicated by the dashed orange rhomboid in (b). The arrow pointing upwards in (c) marks the $\times 2$ periodicity due to the dimerized adatom chains.

Si(557) is 9.5° miscut with respect to (111) and inclined towards $(11\bar{2})$. According to earlier studies, bare Si(557) is composed of three facets (111), (112), and (557). [139] Based on the scanning tunneling microscopy (STM) images, Kirakosian et al. reported that for the (557) surface, the period of the staircase is 5.73 nm, which corresponds to 17 atomic rows. [140] The latter appears as 17 diffraction spots between integer-order spots in $(11\bar{2})$ direction, as shown in Fig. 4.7(c). However, following STM studies [141], this surface is oriented along the $(7\ 7\ 10)$ rather than the initially proposed (557). Within their model, the periodically ordered steps have a height of 3 atomic layers, a width of 16 atomic rows, and a periodicity of 5.2 nm. Recently, the precise atomic arrangement of this triple step has been under debate by different authors. [142–145] While macroscopic surface morphology is similar to those at the Si(553)-Au and Si(775)-Au surfaces, the surface energy of Si(557)-Au is higher than them due to the appearance of Si adatom chains (details are given in Section 7.2). [142, 143] It has been previously shown for the Si(557) surface that higher flashing temperature transforms it into larger Si(111) terraces due step bunching. [50, 146] In the present study, all tested surfaces showed 17 atomic rows supporting

the initially proposed macroscopic (557) surface orientation. In addition to the common features, the Si(557) surface exhibits $\times 2$ streaks due to dimerization of adatom chains, which has not been found on other similar surfaces.

4.7.2. Anisotropic Atomic Wire Growth

A sub-monolayer amount of adsorbed gold breaks the three-fold symmetry on flat Si(111). Hence, the lattice match along the long axis of terraces determines the chain direction. However, 2D arrangement (i.e., $\sqrt{3} \times \sqrt{3}$, 6×6) at higher concentrations preserve or restore the three-fold symmetry due to diffusion of metal atoms in all high symmetry direction regardless of the step-like morphology of the small-angle miscut sample. In this regard, the stepped surfaces serve as a much better playground than the flat surfaces for the growth of 1D wires due to the anisotropic stress applied by well-defined steps.

It was previously reported that after appropriate annealing or by deposition of adatoms onto Si(114), a regular reconstruction over a large area could be obtained. [147] Following this study, it was found that perfect step morphology and atomic surface arrangement can be obtained by deposition of a sub-monolayer gold onto high Miller index planes (i.e., Si(hhk)) [148] instead of atomically corrugated low index surfaces, e.g., Si(114). On the other hand, the amount of adsorbed metal atoms is also very important, while excess amounts of metal adatoms introduce disorder to the chain structure. Also, due to individual diffusion pathways as well as chemical interactions between metal adatoms and template surface only particular metals (i.e., In, Au, Gd, Pt [65, 149–151]) tend to form anisotropic 1D chain superstructures, whereas some others (i.e., Ag, Pb, Sn [36, 152, 153]) mainly generate anisotropic 2D surface arrangements. Gold forms anisotropic metallic chains on the flat and stepped Si(111) surfaces with odd Miller indices. The procedure applied for the production of a well-defined wire arrangement in this thesis is described in Fig. 4.8.

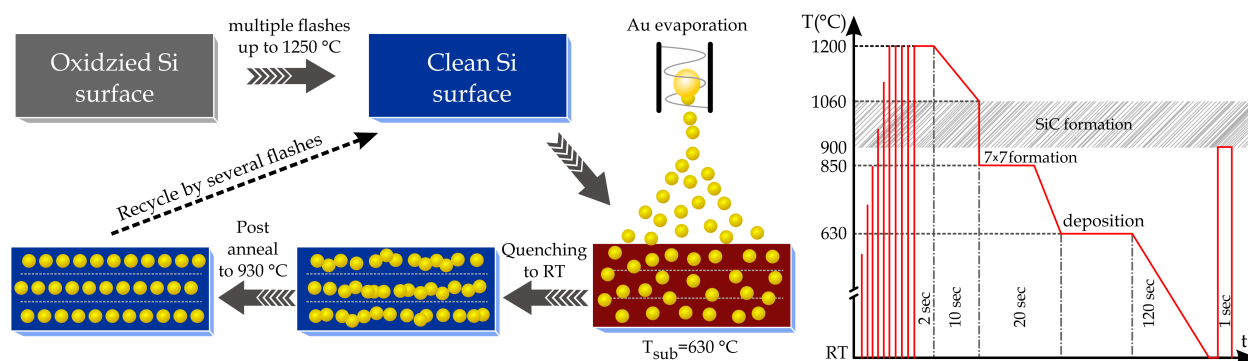


Figure 4.8: Schematic illustration of the surface preparation in the UHV condition following ex-situ chemical cleaning and long time in-situ degassing at 600 °C. The right graph shows the optimized temperature treatment cycles starting from flashing of the pristine surface to post-anneal of Au deposited surface with corresponding time scale.

Formation of anisotropic Au atomic wires and important growth parameters on the Si substrates have

been well documented. [20, 22, 154–159] Nevertheless, most of the time, these parameters need to be optimized for slight differences such as sample doping concentration, UHV condition (i.e., base pressure should be sufficiently low to avoid mainly carbon contamination [160, 161]), etc.

Gold Deposition — Evaporation of Au was conducted at 630 °C sample temperature, for all surfaces reported here. This temperature was found to be the optimal condition for perfect surface preparation. The elevated temperature increases the mobility of surface atoms and, therefore, facilitates superstructure formation. A shutter, positioned on top of the evaporator, was used to start or stop evaporation onto the sample (see Fig. 4.4). After each preparation, the sample was kept at this temperature for ~15 sec. Then, the sample temperature was lowered to RT, and then post-annealing to 930 °C in ~1 sec was applied. In the previous studies, as well as here, it was found that post-annealing helps to get rid of Au atoms from step sites as well as for ordering those on the terraces. This step was skipped only for LCWs on the Si(553) surface and was reduced to 650 °C for the Si(111) surface. Despite the many similarities of the structural motifs, each member of the Si(hhk) family requires a specific amount of Au for the formation of stable reconstruction and long-range periodicity determined by the orientation of the steps and the width of the terrace (see Table 4.1). It has already been reported in the literature and the present investigations that the procedure mentioned above produces anisotropic Au chains on the terraces with low defect density. The main advantage of self-assembly is the long-range ordered and large scale growth of atomically ordered structures that enable investigation with area integrating methods (i.e., LEED, IR, EELS, ARPES, etc.), which usually require a large sampling area. Another advantage of self-assembly is the wide-range thermal stability of the produced structures. Thus, contrary to atom-by-atom manipulation or lithography, self-assembly is usually associated with RT or high-T structural mobilization.

Part II:

Au Decorated Silicon Surfaces

Chapter 5

Gold Atomic Wires on Flat Si(111)

This chapter deals with the structural and electronic properties of gold atomic wires on the flat Si(111) surface. In the beginning, single- and multi-domain Si(111)-(5×2)-Au superstructures will be discussed as studied by SPA-LEED. In this regard, the role of Au coverage and preparation condition to transform the (7×7) to 5×2 periodicity and emerging instabilities is investigated. Then, the plasmonic excitation associated with this surface will be discussed. For detailed studies, the plasmon dispersion is used to investigate the excited-state band structure and then be compared to the available structural models (i.e., KK and EBH). Modification of the metallicity by surplus Au coverage and hydrogen chemisorption will follow this. The chapter ends with a summary of the main findings.

5.1. Surface Structure and Properties

Gold deposition onto the nominal flat Si(111) surface forms triple domains. Significantly, the introduction of a regular array of steps by slight misorientation of the Si(111) surface (1°) leads, upon Au deposition, to the formation of a single (5×2) domain. Although investigations of this system have a long history, the difficulties in determining absolute concentrations of an adsorbed material in the submonolayer regime are exemplarily demonstrated with this system. Consequently, several structural models and optimal concentrations have been suggested for the (5×2) structure over time. [162–166] Although the sequence of ordered Au-induced structures with increasing coverage, (5×2), $\sqrt{3}$ and (6×6), have been shown, their relative and absolute saturation coverages differ widely.

Pioneer works on Si(111)-Au surface employing LEED revealed a (5×2) periodicity where the five-fold symmetry was related to Si, and the two-fold periodicity was then explained as a shift between two adjacent Au atomic rows. [167, 168] Afterwards, several attempts have been made to optimize the surface at a Au coverage of ~ 0.4 - 0.5 ML by employing high-resolution electron microscopy (HREM)

using the heavy-atom holography method on the basis of previous LEED studies. [169] However, the resulting surface models, as well as coverage, appeared to contradict the "Y"-shaped feature observed earlier and protrusions in STM results. [170, 171]

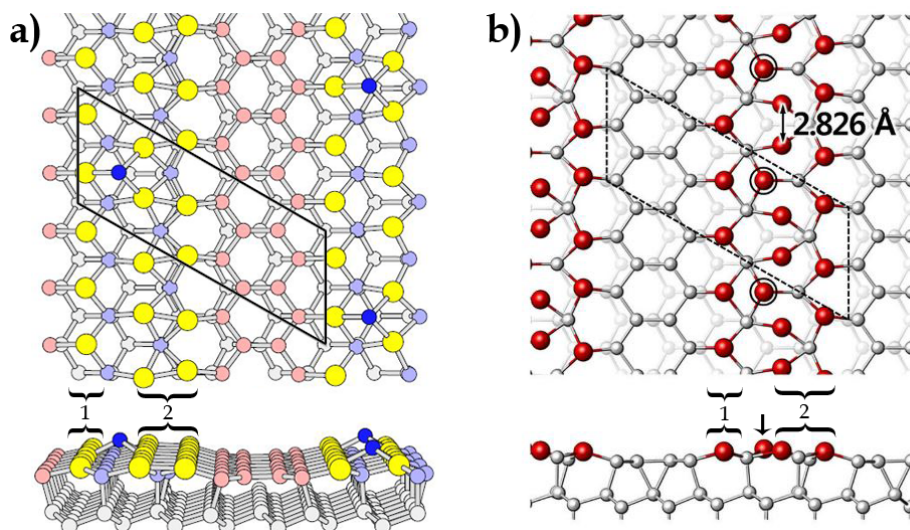


Figure 5.1: The most relevant structural EBH-(a) and KK-(b) models for the Si(111)-(5 \times 2)-Au surface. The rhomboid in both images depicts the (5 \times 2) unit cell with six and seven Au atoms for EBH and KK models, respectively. The bottom panels show a side view of the corresponding model. Single and double Au atomic chains are numbered with 1 and 2, respectively. In (a) the blue balls depict the Si adatoms, In (b), the 7th Au atom is marked with a black circle (arrow). (a) and (b) adapted with permission from Ref. [163] and [164], respectively. Copyright 2009 and 2014 by the American Physical Society.

In 2003, S. Erwin proposed a double gold chain model, which contains 4 Au + 1 Si adatom per 5 \times 2 unit cell and additional Si-HC chains at the step edge. [162] This model was modified to the EBH model by S. Erwin et al. by employing DFT and STM (see Fig. 5.1(a)). [162] The main differences of the EBH model to previous models were 6 Au atoms per 5 \times 2 unit cell forming spatially separated single and dimerized double Au chains in the presence of the Si-HC chains and stabilization of Au chain system by additional Si adatoms. The existence of these Si-adatoms, as well as that of the Si-HC chain, was corroborated by an optical reflection anisotropy spectroscopy (RAS) study and by DFT, [172] that questioned the alternative model suggested by Abukawa et al. [165]. Subsequently, the 0.6 ML coverage was approved by STM and other DFT calculations. [28, 173–175] In contrast, Kwon and Kang proposed a model (henceforth, KK model) with an optimal Au concentration of 0.7 ML, i.e., one Au atom more per unit cell than the EBH model. [164] With this model, a metal-insulator transition, induced by adding additional Au to the optimal concentration could successfully be modeled. [176] Similarly, many structural details seen with tunneling microscopy as well as electronic properties could be reproduced within this model [177]. Nevertheless, the optimal concentration suggested by this model is at variance with the findings of several recent studies that found values for completion of the (5 \times 2) structure

between 0.60 and 0.67 [165, 173, 178–180].

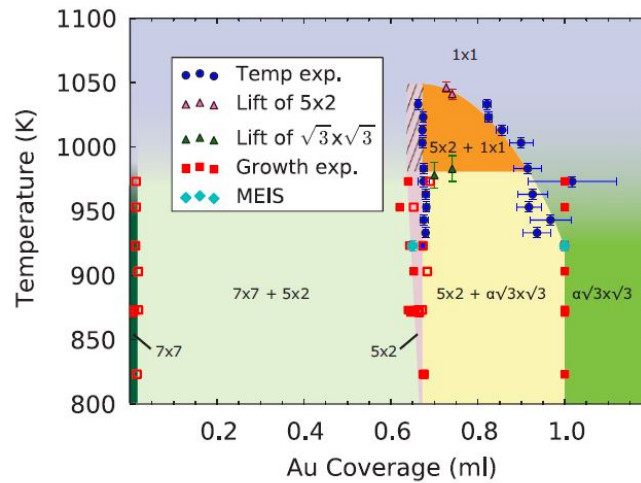


Figure 5.2: Experimental phase diagram for submonolayers of Au on almost flat Si(111) surface. The filled red squares indicate the completion of the 5×2 and $\sqrt{3}$ phases. The open squares represent the first observation of the 5×2 and $\sqrt{3}$ phases, from left to right, respectively. The blue circles are the results of the temperature variation experiments. The green and pink triangles depict the transition of the $\sqrt{3}$ and 5×2 phase, respectively, into a 1×1 phase. The estimated melting temperatures have been depicted as smooth transitions in the phase diagram for the lower and higher coverages. [181] The hatched area represents the continuation of the 5×2 phase with temperature. Reprinted from Ref. [179] with permission. Copyright 2014 by the American Physical Society.

In particular, the study by Kautz et al., using a combination of low energy electron microscopy (LEEM) in combination with medium and high energy ion scattering (MEIS, RBS), fixes this value to 0.65 ± 0.01 ML. [179] The experimental phase diagram from this work is shown in Fig. 5.2.

Both EBH and KK models are shown in Fig. 5.1. In view of these still controversial results, it is obvious that there is no generally accepted structural model for this system yet. While absolute calibrations of surface concentrations are usually very difficult, there may be alternative experimental approaches that are able to discriminate between the various models suggested. Indeed, the combination of a diffraction study with the result of plasmon spectroscopy, which yields valuable information on the unoccupied bandstructure close to the Fermi level, allows such discrimination.

5.1.1. Recalibration of Surface Coverage

Single-Domain Surface — The pure 7×7 structure (see Fig. 5.3 (a)) was produced by flash annealing cycles as described in Section 4.7.1. Upon Au evaporation the 7×7 periodicity transforms into the 5×2 structure along the $[1\bar{1}0]$ direction. [181] The results from SPA-LEED for different domains together with a representation of domain arrangements are given in Fig. 5.3. In several earlier studies, as well

as here, the $\times 2$ periodicity along $[\bar{1}\bar{1}0]$ starts to appear at a Au concentration of 0.2 ML. Its intensity increases up to 0.6 ML Au coverage. On the other hand, the (7×7) structure loses intensity and finally disappears when the Au coverage approaches 0.6 ML. At the latter concentration, the sharpest and most intense (5×2) structure was seen. Especially the $\times 2$ intensity decreases quickly when the surface coverage is increased further. This behavior gives evidence for the formation of (5×2) -ordered islands at Au concentrations above 0.2 ML, presumably with a local Au concentration close to the saturation of 0.60 ML, in coexistence with a low-density lattice gas that does not destroy the (7×7) structure of the clean Si(111) surface. These findings are in close agreement with those published earlier. [179,181,182]

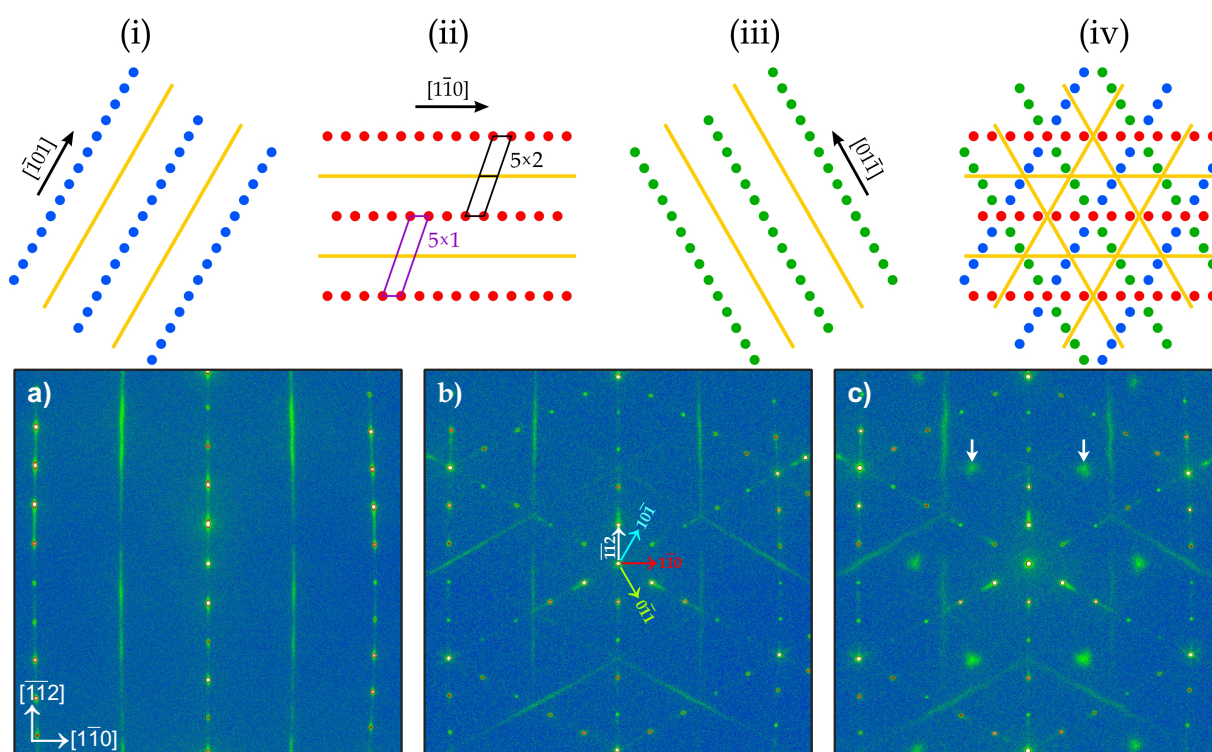


Figure 5.3: Upper panel: i,ii,iii show a schematic LEED pattern of the three 5×2 domains rotated by 120° with respect to each other and (iv) shows the overall pattern containing all three domains. Lower panel: Experimental LEED patterns obtained for a Au coverage of 0.6 ML (a) and 0.65 ML (b) showing single and triple domain 5×2 surfaces, respectively. Fig. (c) shows the Si surface after deposition of 0.70 ML of Au and post-annealing at 650°C . The white arrows in (c) depict the $\sqrt{3}$ periodicity. LEED images were recorded at RT with primary energy of 138 eV.

Au Concentrations Above 0.6 ML — When exceeding the Au concentration of 0.60 ML, the $\times 2$ intensity in LEED is reduced, as already mentioned above. Furthermore, exceeding this optimum coverage induces a gradual reduction of stability of the single-domain structure and the appearance of all three domains along $[\bar{1}0\bar{1}]$, $[\bar{1}\bar{1}0]$ and $[0\bar{1}\bar{1}]$. An example is shown in Fig. 5.3(a) at a concentration of 0.65 ML. Here, the $\times 2$ streaks of all three domains appear with still the original domain having the

highest intensity. The intensity of the other domains becomes more pronounced upon preparation at 630 °C and subsequent postannealing at 650 °C for a few seconds. At this point, the possible reasons for the reduction of structural anisotropy in the formation of the (5×2) domains can only be speculated on as follows. Step decoration of Si steps by the surplus Au atoms (i.e., by Au atoms not needed for the formation of (5×2)) may play a role, but also kinetic effects such as increased mobilities of steps and/or and easier diffusion of Au atoms at these higher Au concentrations. When Au coverage is further increased, the formation of $\sqrt{3} \times \sqrt{3}$ structure is observed, starting at a concentration of 0.68 ML, best seen after subsequent postannealing at 650 °C for 5 sec. An example at a Au concentration of 0.70 ML is shown in Fig. 5.3(c). According to Ref. [183], the latter structure has a local concentration of 1 ML. These results show that there is a second range of coexistence at high Au coverages, now between (5×2) and $(\sqrt{3} \times \sqrt{3})R30^\circ$ phases, which is in agreement with published phase diagrams [179, 181]. There is even quantitative agreement for the critical concentration of phase coexistence between (5×2) and $(\sqrt{3} \times \sqrt{3})R30^\circ$ phases with Ref. [179]. The limit of stability of the pure phase of three domains of the (5×2) structure is at a Au concentration of 0.67 ML. Interestingly, this perfect agreement with the recent phase diagram (see Fig. 5.2) means that the anisotropy introduced by steps plays no role at all for this phase transition, i.e., at this concentration, the single-domain structure is completely destabilized by surplus Au.

For the pure three-domain structure (i.e., without the appearance of $\sqrt{3}$ -islands), the surface coverage to 0.65 ML and a preparation sample temperature of <630 °C turned out to be optimal. While this finding again agrees with previous results, it triggers some intriguing further questions about the role of adsorbed surplus Au atoms, which seem to destabilize the single-domain structure and result in optimal stability of the single (5×2) phase with three domains. They can not be resolved at this point. Noteworthy, this surface calibration is highly correlated with plasmon dispersion. For comprehensive plasmonic investigation, both single and triple domain surfaces were investigated and will be discussed in Section 5.2.

Electronic Structure: Overview — Electronic properties of the Si(111)-(5×2)-Au surface have been studied intensively in the last decade. However, similar to the surface structure, its electronic properties also have not yet been fully understood. Earlier ARPES measurements with 0.4 ML Au coverage revealed a strongly dispersive parabolic band along the Au chains. This band possesses a Fermi surface perpendicular to the Au chains, as expected for 1D metallic surfaces. [184, 185] It has been shown that upon Au adsorption, the Si adatom states at E_F are replaced by Au-induced metallic states. [186] As a result, starting already at 0.3 ML Au coverage, this surface is dominated by metallic properties. This is directly related to the formation of local 5×2 islands, regardless of their small fraction at the surface. It must be noted that the same behavior is highly improbable to happen on the stepped surface due to restriction of the flow of local Au coverage between terraces and requires occupation of the majority of terraces for stable wire array formation. As detected by ARPES, the metallic band stays almost unchanged upon further addition of Au coverage up to 0.7 ML. This band, called S_1 band, has an energetic

minimum at the zone boundary. However, starting from 1.0 ML Au coverage, where the surface is entirely covered by $\sqrt{3} \times \sqrt{3}$ structure, these bands are modified to the bands associated with $\sqrt{3} \times \sqrt{3}$ periodicity. [89] Since the $\sqrt{3} \times \sqrt{3}$ is a 2D arrangement, the minima of the new band are shifted from its origin. Moreover, the pseudogap on (5×2) structure at E_F extends by magnitude of -1.1 eV from E_F for $\sqrt{3} \times \sqrt{3}$ structure, this was preliminary related to quantum-well states. [187] 2D interaction of adjacent electron packets inevitably modulates the Fermi surface. [185] This has been explained as a strong hybridization of Au and Si substrate at higher binding energies. Due to its low symmetry, the Au-modified surface state shows a clear spin polarization that goes beyond the conventional Rashbatype spin-orbit interaction of Au. [188]

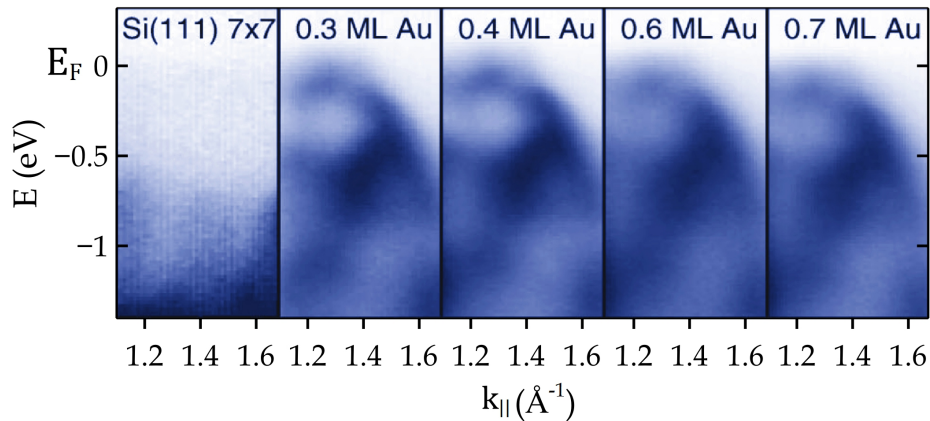


Figure 5.4: Electronic band structure measured with ARPES for various Au coverages on flat Si(111). The observed band is assigned to the Au-induced metallic 5×2 superstructures. Darker regions represent high photoemission intensity. Reprinted from Ref. [89] with permission. Copyright 2001 by the American Physical Society.

No temperature-induced structural and/or electronic phase transition of this system has been observed in the literature down to 20 K. [176] Notably, plasmonic absorption in IR becomes sharper by lowering the sample temperature revealing the role of relaxation and phonon modes in plasmonic excitations. DFT calculations showed that the metallic states are strongly localized in the vicinity of the Au chains, but also slightly hybridize with the Si surface states. [163, 164] Although the most elaborate models, EBH and KK are in good agreement for the structure of occupied states, they differ strongly in the unoccupied band structure. E.g., the EBH model shows higher energy and a steeper slope for the unoccupied part of the metallic band. It should also be noted that the EBH model is basically a 5×1 structure where doubling of the $\times 1$ periodicity opens a band gap at the unoccupied states, which is similar to the KK model. The band gap opening is additionally increased by the number of Si adatoms per unit cell. [163, 164] The compatibility of these theoretical models with the experimental plasmon dispersion will be discussed in Section 5.2.

5.2. Plasmonic Excitations in Si(111)-(5×2)-Au

The electronic properties of the Si(111)-(5×2)-Au surface have been extensively studied experimentally with different methods such as ARPES, STS, IR, and also theoretically. [163–166, 172, 189–192] It is worth noting that none of the experimental results are fully compatible with the calculated band structures. Refinement of models may be possible by more experimental data. Momentum resolved electron energy loss spectra at a Au concentration of 0.60 ML adsorbed on a freshly prepared surface are shown in Fig. 5.5. While a clear dispersing loss is seen in Fig. 5.5(a), i.e., along the $[1\bar{1}0]$ direction parallel to the wires, no dispersion feature was found in the perpendicular direction shown in Fig. 5.5(b). It is worth mentioning that the present and previous reports show that this domain dominates this surface’s metallic properties. The other two domains show the plasmon frequency as the main domain.

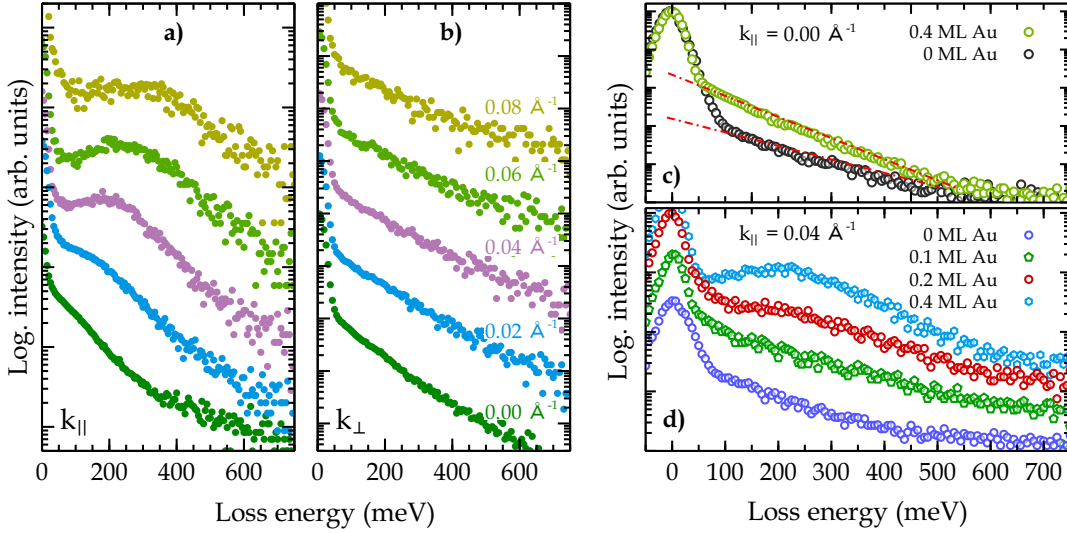


Figure 5.5: Exemplary momentum-resolved loss spectra for Si(111)-(5×2)-Au surface recorded for $\Theta_{Au} = 0.60$ ML in $k_{||}$ (a) and k_{\perp} (b) directions. (c) Change of Drude background from pristine Si(111)-(7×7) to 0.4 ML Au deposited surface at $k_{||} = 0$. The evolution of plasmon loss (or metallicity) as a function of Au deposition recorded at $k_{||} = 0.04 \text{ \AA}^{-1}$ is shown in (d). The spectra were normalized to the elastic intensity and shifted against each other (except (c)) for better visibility.

The anisotropic behavior of the dispersion is very similar to that observed in Au atomic wires on vicinal Si(111) surfaces at higher vicinal angles. Therefore, the dispersing loss observed here can safely be assigned to the quasi-1D plasmonic excitation of the Au wires in the (5×2) structure. Notably, anisotropy is preserved in all Au coverages up to 0.7 ML. The amplitude of the plasmonic excitation vanishes at $k \rightarrow 0$, which shows the longitudinal character of the collective excitation. Only the structureless background increases significantly (please note the semi-log scale) that follows closely an exponential dependence on $k_{||}$. This dependence is characteristic of metallic systems and is due to the continuum of low-energy

electronic excitations. [57] Please note that also the Si(111) surface has a metallic surface state with a low density of states. [193] Plasmon energy goes through a maximum at a finite k_{\parallel} , presumably due to correlation effects and enhanced damping at large k_{\parallel} . [90] However, the extrapolation of the experimental plasmon dispersion to zero energy at $k_{\parallel} = 0$ is not fully compatible with the data due to possible finite-size effects.

The growth mode with large (5×2)-ordered islands is corroborated by the evolution of loss intensities as a function of Au coverage, as shown in Fig. 5.5 (d). The evolution of the plasmonic loss starts already at a Au concentration above 0.2 ML. It is mainly the intensity of this loss that increases as a function of Au concentration with marginal shifts in the energetic position, in agreement with the assumption from above of phase coexistence between large islands of (5×2) and Si(111)-(7×7). These results demonstrate that the metallicity of the Au covered Si(111) surface is fully developed at a Au concentration of 0.4 ML, i.e., at a concentration far below the saturation of (5×2). This is very similar to the observation from ARPES experiments, in which a single nearly parabolic band was reported (see Fig. 5.4). [193] They also agree with the results of Nagao et al. [194] for a nominal Au coverage of 0.44 ML for the same reason.

For a qualitative fit of the plasmon dispersion, the free electron gas model empirically modified from Eq. 5.1 following Ref. [195] as:

$$E(k) = \hbar \sqrt{\frac{4ne^2}{(1+\epsilon)\epsilon_0 m^* a^2}} k_{\parallel} a^* \times \underbrace{\sqrt{K_0\left(\frac{k_{\parallel} a}{1\sqrt{2}}\right)}}_{\text{single wire}} + \underbrace{\sqrt{2 \sum_{l=1}^N K_0(k_{\parallel} l d)}}_{\text{wire array}} \quad (5.1)$$

Here, K_0 is the modified Bessel functions of zeroth order and the second kind, d is the inter-wire distance (or terrace width), a effective wire width, and a^* is the constant for normalization. In a simplified way, $\frac{a^*}{a}$ accounts for the electron distribution around the wire, which is also related to the physical width of the wire. Thus, taking this ratio as a free parameter, the obtained plasmon dispersion was fit using the following input parameters: $n = 1.46 \times 10^7 \text{ cm}^{-1}$, $m^* = 0.36 m_e$, $d = 16$ and $\epsilon = (11.5 + 1)/2$ accounts the mean value of silicon and vacuum dielectric constant. Here, m^* was directly obtained from experimental ARPES band, S_1 [89], and d has been used for the description of this system in Refs. [23, 196]. The resulting fit is given as the solid line in Fig. 5.6(a). n was derived using the same ARPES bands via $n = 2k_F/\pi$ with $k_F = 0.23 \text{ \AA}^{-1}$. This yields confinement of the wire in a parabolic potential with a width of the plasmonic ground state of 6 \AA perpendicular to the wires. Although this model gives a satisfactory fit to the experimental data, it cannot be correct since the plasmon dispersion fully crosses the electron-hole continuum (green part in Fig. 5.6) derived with the same parameters as those used for the plasmonic fit. Most importantly, this fit shows that an extrapolation of plasmon dispersion to zero energy at $k = 0$ is possible for the 0.60 ML surface, while it deviates from this extrapolation for higher coverages. The most pronounced reason is the distortion of wire length. The same fitting procedure was

previously tested for the Si(hhk)-Au surfaces as well. [195] There only the Si(557)-Au surface showed a reasonably small interaction with the single-particle excitation spectrum, while the Si(553)-Au surface showed a similar behavior to the Si(111)-(5×2)-Au surface.

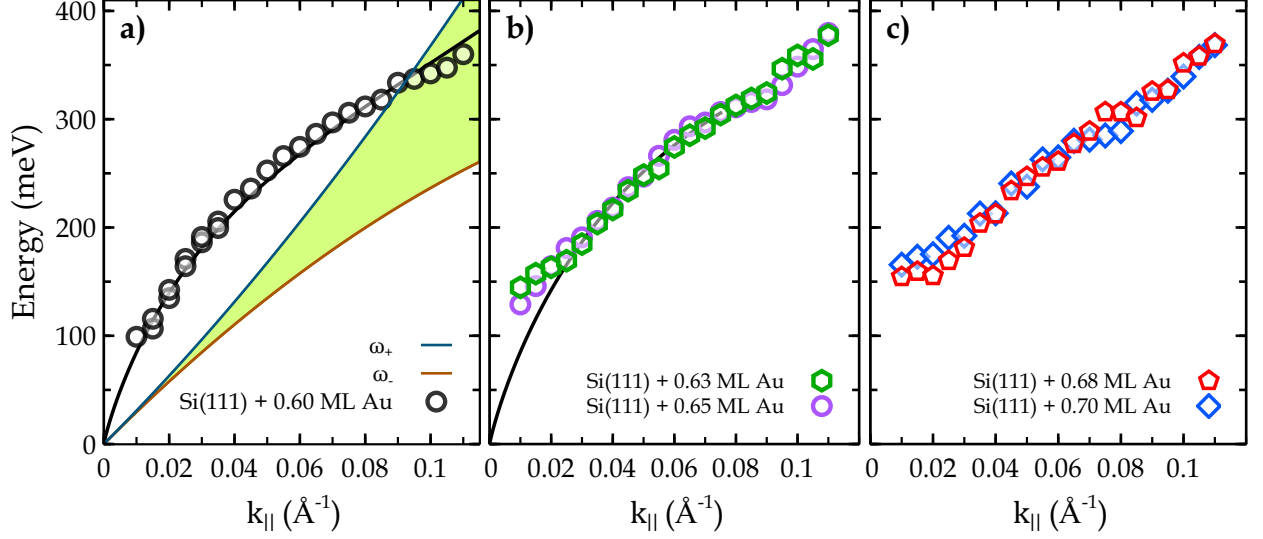


Figure 5.6: Plasmon dispersion obtained for single-domain Si(111)-(5×2)-Au surface (a), triple domain surfaces (b), and other higher Au coverages (c). The dashed line describes the fit from the modified empiric 1D model as described in the text. The green area in (a) corresponds to the electron-hole continuum zone derived particularly for this system; see the text for the parametrization.

For Si(557)-Au, the overlap of the electron-hole continuum with the measured plasmon dispersion, however, is barely outside the scatter of the experimental data so that here a description with the NFEG model may be possible, which was in fact used in literature. [81] However, this coincidence between the excitation spectrum derived from band structure calculations and the NFEG model seems to be unique for Si(557)-Au.

5.2.1. Description within the NFEG: Comparison with the Theoretical Models

For a quantitative comparison between the measured plasmon dispersion and the calculated band structure, the close relationship between the upper edge of the electron-hole continuum and the plasmon dispersion in quasi-1D systems has been employed. As already discussed in Section 2.2.1 in this approach, the quasi-1D array of wires is considered as a 2D electron gas that is confined to wires of finite width by a periodic confining potential. Combining Eq. 2.23 and Eq. 2.24:

$$\omega_+(k_{\parallel}) = \sqrt{\frac{\omega_p^2(k_{\parallel})(e^{A(k_{\parallel})} - 1) + \omega_-^2(k_{\parallel})}{e^{A(k_{\parallel})}}} \quad (5.2)$$

where $A(k_{\parallel})$ contains the Fourier transform of the confinement potential and the 2D wire array (see Eq. 2.24). For this calculation, a harmonic confinement potential, and for modeling 15 wires, 7 left and 7 right from the central wire, were employed. The Fourier transformed Coulomb interaction ($V_c(k)$) was computed with $d = 16 \text{ \AA}$ and $b = 6 \text{ \AA}$. ω_- was obtained from the Au-induced band just below the Fermi level in the calculated band structure of the EBH model with the assumption that this band can be approximated by a parabola close to E_F . This assumption is not critical for the determination of the dispersion of ω_+ , since ω_- has only a significant influence very close to E_F . Therefore, for the single band crossing E_F , ω_+ is expected to closely coincide with the unoccupied part of this band.

In Fig. 5.7, the numerically derived ω_+ , using the experimental plasmon dispersion (ω_p), is compared with the calculated band dispersions of EBH and KK models. Interestingly, an almost quantitative agreement is obtained between the numerically derived ω_+ and the undoped model of a Au-induced (5×1) structure of the EBH model, at a Au coverage of 0.6 ML.

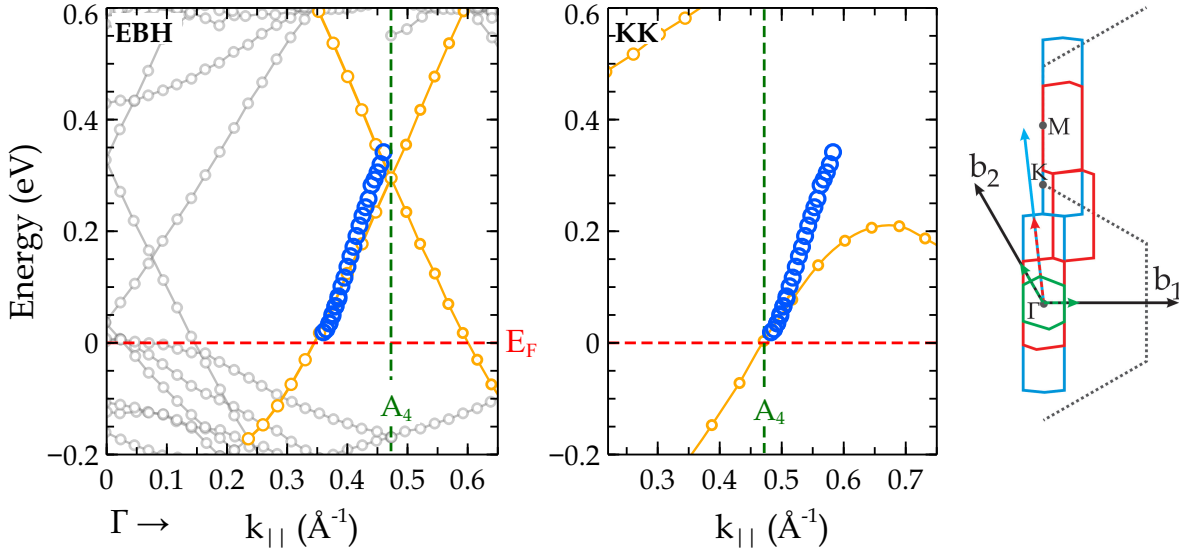


Figure 5.7: DFT calculated electronic band structure for the EBH (left) and KK (middle) models. Numerically derived ω_+ is given in blue circles in both graphs. The rightmost figure depicts the SBZ and reciprocal lattice vectors for (1×1) - dotted hexagon, (5×1) - (blue), (5×2) - (red), and (5×4) - (green) surface unit cells. EBH and KK model band structures adapted with permission from Ref. [163] and [164], respectively. Copyright 2009 and 2014 by the American Physical Society.

Only the experimental slope is slightly higher than in theory. This is somehow expected since the calculations have not been optimized for such approximation. However, one of the main uncertainty might be the 5×1 periodicity, which does not consider dimerization of Au chains. The mentioned, dimerization opens a gap at unoccupied states. In addition, according to the EBH model, the total energy can be lowered by adding Si adatoms (or just two electrons per (5×4) unit cell) onto the gold dimer chain. The existence of such adatoms has been verified by STM. [173, 177] According to the

calculation of Ref. [163], however, this type of doping leads to multiple openings of band gaps that are not compatible with the current data, in which no indication for band gap opening is seen. Assuming that indeed the Si adatoms are necessary for stabilization of the structure, it seems that the effect of band gap opening, if any, is much less drastic than in the simulated EBH model. Alternatively, it may be that the (5×2) was formed without Si adatoms under our conditions of preparation. No systematic variation of preparation parameters has been performed, however, to answer this question.

Within the KK model (see Fig. 5.7) the band gaps in the unoccupied band structure are even larger than those calculated with the EBH model, which do not match the current data. Since also the slope of the dispersion of the unoccupied band structure close to E_F is far off the experimental data points (see Fig. 5.7), this model is clearly not able to describe the experimental findings (namely plasmon dispersion). While various mechanisms (lifetime broadening, finite k -resolution, etc.) may make small band gaps invisible in plasmon spectroscopy, the trend within the EBH model to form a set of very flat bands with corresponding band gaps at large dimerizations allows to conclude that the dimerization leading to the ×2 modulation must be significantly smaller than that postulated by the model calculations [163, 164], but this model is definitely compatible with the present estimation of the optimal Au concentration (see Section 5.1).

Although the ideal filling of a (5×2) can only be realized by an integer number of adatoms per unit cell, several experimental studies mentioned above obtained optimum coverages that correspond to non-integer numbers for ideal filling, [178, 179] indicating that there may be an important role to adatoms, as suggested theoretically. [163] Therefore, the role of additional Au exceeding the coverage of 0.60 ML up to 0.70 ML was investigated.

Au Concentrations Above 0.6 ML — The experimental plasmon dispersion for Au coverages higher than 0.60 ML are given in Fig. 5.6(b) and (c). The dependence of plasmon dispersion on Au coverage turns out to be small but significant. When looking at Fig. 5.6(b), the increase of Au concentration from 0.60 to 0.63 and 0.65 ML leaves the dispersion curve virtually unchanged. Only in the limit $k_{\parallel} \rightarrow 0$ there is a tendency for an increase of the energy values, as seen by the direct comparison with the 0.60 ML dispersion curve. This behavior is characteristic of the increased disorder caused by the excess Au concentration, as seen in LEED. Disorder generally enhances scattering probabilities, also for plasmons, and can lead to the formation of standing waves with a finite wavelength. In the simplest picture, this means that there is a maximum wavelength plasmons cannot exceed, i.e., dispersion ends at finite average k -value with a finite excitation energy. This finite k value increases with the density of defects. In agreement with this interpretation, the deviation from the 0.60 ML dispersion curve gets larger at small k_{\parallel} with increasing surplus Au concentration (see also Fig. 5.6(c)). This interpretation of enhanced scattering probabilities is also supported by the observation of an increased half-width of the plasmon loss as a function of Au coverage, as shown in Fig. 5.8(a). An increased density of defects is expected to reduce the plasmonic lifetime, thereby increasing the linewidth of the plasmonic loss, as observed.

The relative increase of the FWHMs amounts to about 30 % and with a slight tendency to get bigger at large k_{\parallel} . At k_{\parallel} values above 0.03 \AA^{-1} the dispersion curves seem to be unchanged by excess Au apart from a small kink in the dispersion curve at a k_{\parallel} value of 0.09 \AA^{-1} (see Fig. 5.6(b)) that was not visible in the dispersion curve at 0.60 ML (cf. Fig. 5.6(a)). This kink may indeed be an indication for the opening of a small gap, which, contrary to the model with adsorbed Si atoms [163], is now caused by the adsorption of additional Au atoms. This kink cannot be resolved any more when the Au concentration is increased into the range of appearance of $\sqrt{3}$ -ordered islands (Fig. 5.6(c)), possibly again due to the influence of enhanced disorder. These comparatively small changes of dispersion by increasing excess Au concentration indicate that extended islands with prevailing (5×2) order still exist, as also seen in LEED. The intensity of the plasmon loss, however, is reduced both by enhanced diffuse scattering due to disorder and by the formation of three domains. Both effects lead to enhanced uncertainties and an increased scatter of data. No signs of an extra loss due to the $\sqrt{3}$ -ordered islands was ever seen. Since also these islands form a 2D phase before at total coverages above 1 ML 3D islands can be formed [183] they are expected to exhibit a low-energy plasmon, if they were conducting. The absence of such a plasmon indicates that they are insulating.

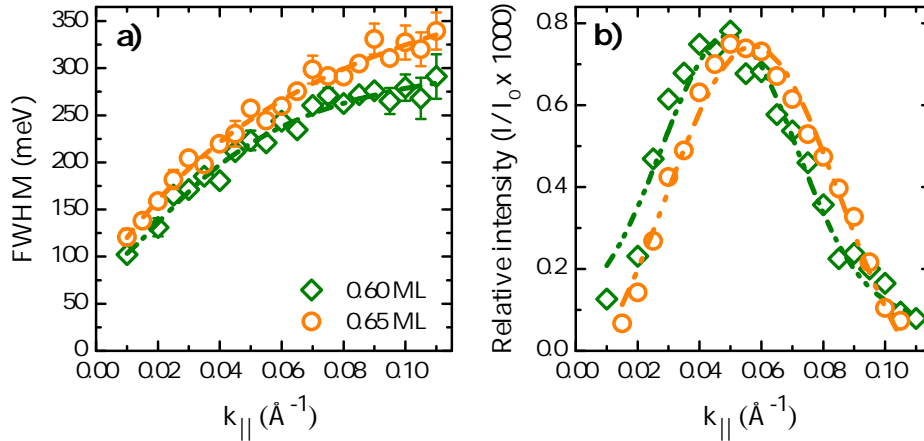


Figure 5.8: FWHM (a) and intensities (b) of plasmonic losses, both plotted as a function of k_{\parallel} for Au coverages of 0.6 and 0.65 ML. Plasmon loss intensity was normalized to the elastic peak at $k_{\parallel} = 0$.

Coming back to (5×2) , the formation of three domains in a system with very limited order may also lead to crosstalk between the domains so that there is a possibility for crossover from quasi-1D to 2D. Although no plasmonic excitation was detected in the present work in k_{\perp} direction for Au concentrations up to 0.65 ML, interestingly, a weak absorption feature for the polarization perpendicular to chains was observed in IR experiments. [196] Similarly, crossover from 1D to 2D was reported from ARPES experiments. [89] Some indication for such a behavior is the shift of the intensity maximum to higher k_{\parallel} values, which corresponds to a redistribution of intensity in k -space, and the widening of this maximum, as seen in Fig. 5.8. Also, there an influence of disorder cannot be ruled out.

5.3. Doping-Induced Metal-Insulator Transition in Si(111)-(5×2)-Au

The Si(111)-(5×2)-Au surface shows some extraordinary features, which were partially addressed in Sections 5.1 and 5.2. Another peculiar property of this surface is the high sensitivity to change of carrier concentration. This was first observed in DFT calculations due to Si adatom doping, which drives a metal-semiconductor transition. [162] According to that study, one additional Si adatom transforms the parent 5×1 unit cell into 5×2, and the additional 0.5 elementary charges in the 5×2 band structure results in multiple band gap openings above E_F . Further increase of the concentration to one Si adatom per 5×4 unit cell opens >100 meV energy gap at the Fermi level. Similar behavior was also observed by IR spectroscopy, but after a surplus of Au onto the 5×2 surface. [196] There, the observed MIT was explained as being connected with the structural transformation when increasing the Au concentration from 7 Au atoms 5×2 unit cell to 8 atoms. Although the employed model is still under intense debate (see Section 5.1), the observed redshift of the absorption maximum shows a clear signature of reduced metallicity. However, due to the restriction of optical excitation to $k_{||} = 0$, no experimental evidence for modification of plasmon bands was discussed in those studies. Considering the underlying question, plasmon spectroscopy has been used as a complementary tool to study the modification of plasmonic excitation by surplus Au atoms on this surface. Also, it is believed that further insight from plasmon spectroscopy would enlighten the existing issues with an optimum Au concentration and related band structure.

In this study, a significant dependence of MIT on the initial Au coverage was not observed. Starting at 0.6 ML Au coverage, we end up with a nonmetallic state following doping with surplus gold atoms. This supports the idea that the band filling and the general form of the Au-induced metallic bands, mainly in the occupied state, is the same for Au coverage of 0.6-0.7 ML. Therefore, the main factor of the MIT is the amount of required additional charge to fill the empty states and opening of an energy gap at E_F . In Ref. [196], the opening of 300 meV energy gap after 0.1 ML surplus Au deposition was observed, resulting in an insulating state. As shown in Fig. 5.9, the plasmonic excitation vanishes already after 0.07 ML surplus Au deposition. Notably, the existence of the Drude background for this coverage manifests the residual of metallicity [193, 197].

Since the 5×2 structure (or the main Au related band) loses its metallicity, the visible Drude background might be due to available free charge carrier from Si surface states, that was observed on the pristine surface as well (see Fig. 5.5). However, annealing this nonmetallic state at 650 °C brings back the metallicity. This proves that the additional Au atoms are not incorporated into the metallic chains, while they can migrate to form the $\sqrt{3}$ structure, which seems to be insulating. The applied temperature is not enough for the diffusion of Au into the deeper surface. This finding is in accordance with the result of diffraction studies, as shown in Fig. 5.10. The deposition of surplus 0.05 ML gold onto this surface at RT slightly reduces the ×2 intensity or presumably increases background scattering. Subsequent annealing brings about $(\sqrt{3} \times \sqrt{3})R30^\circ$ spots and almost recovers the ×2 intensity and therefore plas-

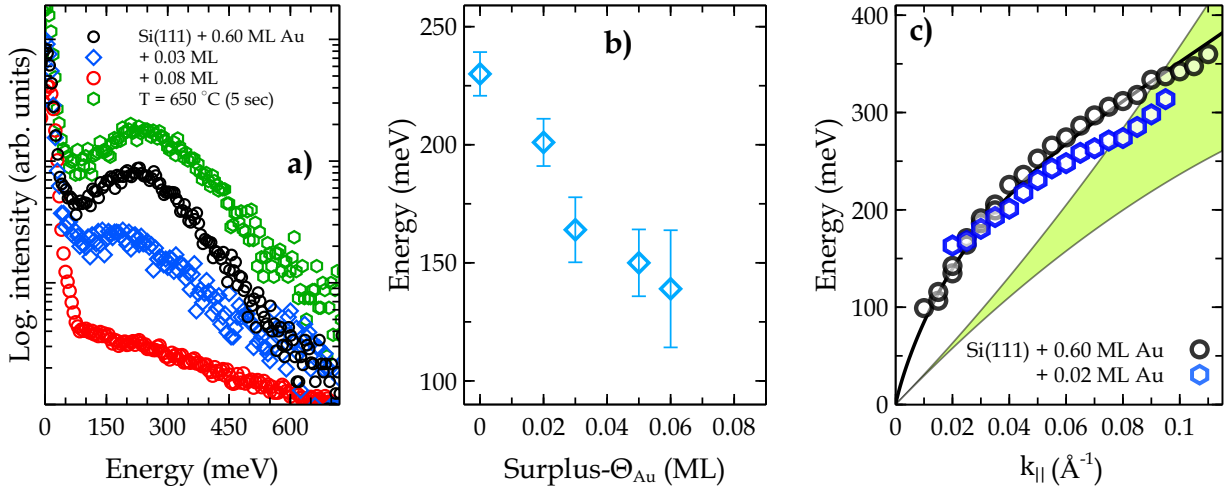


Figure 5.9: (a) EEL spectra from the Si(111)-(5 \times 2)-Au surface showing the redshift of plasmon frequency at fixed $k_{||} = 0.05 \text{ \AA}^{-1}$ as a function of surplus Au coverage. The starting gold coverage was $\Theta = 0.60 \text{ ML}$. (b) shows the plasmon dispersion for 0.6 ML Au surface (black circles) together with 0.02 ML surplus Au coverage (blue \circ).

mon loss is also recovered. Another notable finding is the coalescing of surplus Au atoms into the $\sqrt{3}$ structure instead of transforming the surface to a multidomain structure. As discussed in Section 5.1, at total 0.65 ML Au coverage destabilizes the single-domain surface into three domains. Meanwhile, the present finding shows that the multidomain formation is also a well-defined procedure and is evidently determined by the initial wire formation condition as same as a single-domain surface. As shown in Fig. 5.9, the plasmon loss energy decreases almost linearly as a function of surplus Au coverage. Extrapolation of the obtained data to $E = 0$ results in a critical surplus Au coverage of $\sim 0.11 \text{ ML}$, which is in accordance with the previous report [176].

Besides, plasmon loss intensity in long wire sections is highly sensitive to induced disorder and, therefore, drops drastically following surplus Au deposition. Such disorder again appears as a finite size effect on the plasmon dispersion after surplus Au deposition. Plasmon dispersion for optimum 0.60 ML Au surface together with 0.02 ML surplus Au is shown in Fig. 5.9(c). The higher part of the plasmon dispersion is reduced by $\sim 10\%$ after 0.02 ML surplus Au deposition. Interestingly, short leveling off at $\sim 250 \text{ meV}$, which was observed for 0.63 ML, is also reproduced after surplus Au coverage, i.e., it depends only on the total Au amount.

The formation of the small kink in Fig. 5.9(c) might be due to a small indirect energy gap between the bands. On the other hand, such band gap is also highly sensitive to additional charges (or surplus Au atoms). This might be a reason that it does not appear on the 0.60 ML optimal surface. The present study shows that the plasmon loss on this surface can completely be vanished after 0.1 ML surplus Au deposition up to the total gold coverage of 0.7 ML and does not require an additional Au atom incorporation into the unit cell of 5 \times 2 structure. To test this statement, additional doping experiments were

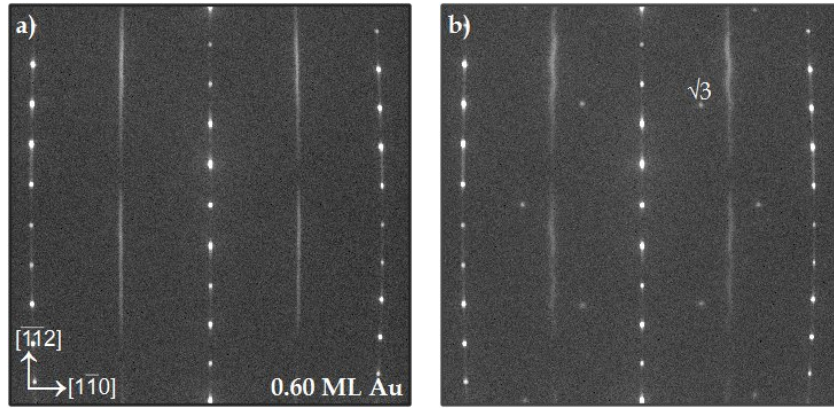


Figure 5.10: SPA-LEED patterns of the Si(111) surface with optimal 0.60 ML of Au coverage (a), after deposition of 0.05 ML surplus of Au at RT and subsequent annealing at 650 °C for 5 sec (b). Images were recorded at RT with primary energy of 138 eV.

conducted, this time with atomic hydrogen. These results are summarized in Fig. 5.11. It is apparent that hydrogen doping also drives such a kind of MIT on this surface, even though ordered integration of hydrogen atoms into atomic arrays and altering the atomic arrangement is highly unlikely. Therefore the effect here can easily be related to charge doping. Noteworthy, the Si(111)-Au surface requires half of the hydrogen exposure in comparison to the Si(553)-Au surface. [32] This can be explained with higher adatom density and higher chemical reactivity of the present system. Although the doped charge concentration is difficult to compare directly with Au doping, the observed redshift of plasmon frequency is qualitatively the same. Moreover, as known from the previous studies ([32, 33, 198]), the direct interaction of H with Au chains is not favorable for Si(hhk)-Au surface. Considering the almost same structural motifs, the same might hold for the Si(111)-(5×2)-Au surface. This is another indication that there may be no need for modification of atomic arrangement for MIT.

In Ref. [176], the metal to insulator transition was explained as a shift of the Fermi level from the valence band maximum (50 meV) upward with a magnitude of 210 meV due to increased (or even complete) band filling. This results in a ~ 300 meV wide indirect energy gap at E_F lying in between the VMB (valence band maximum) and the CBM (conduction band minimum) of bulk Si. Although this large band gap explains the reduction of the plasmon frequency, it is not enough to judge the insulating state. A similar band gap opening was also observed for doping of this surface with surplus Si adatoms. [199] There, the ARPES mapping of the occupied state showed such a gap opening at Si adatom coverage close to 100%, which rendered the final semiconducting state. Interestingly, doping with Si, Au, and H shows almost the same result, regardless of different interaction possibilities, and most probably, the charge transfer mechanism is also different. Notably, the effect of Au is much severe, especially in comparison to Si. It also worth noting that the EBH 5×1 model as its present form (see Fig. 5.7) cannot reproduce such an electronic band gap where 300 meV shift of E_F might be required for such transition. It should also be mentioned that experimental plasmon dispersion undermines the KK

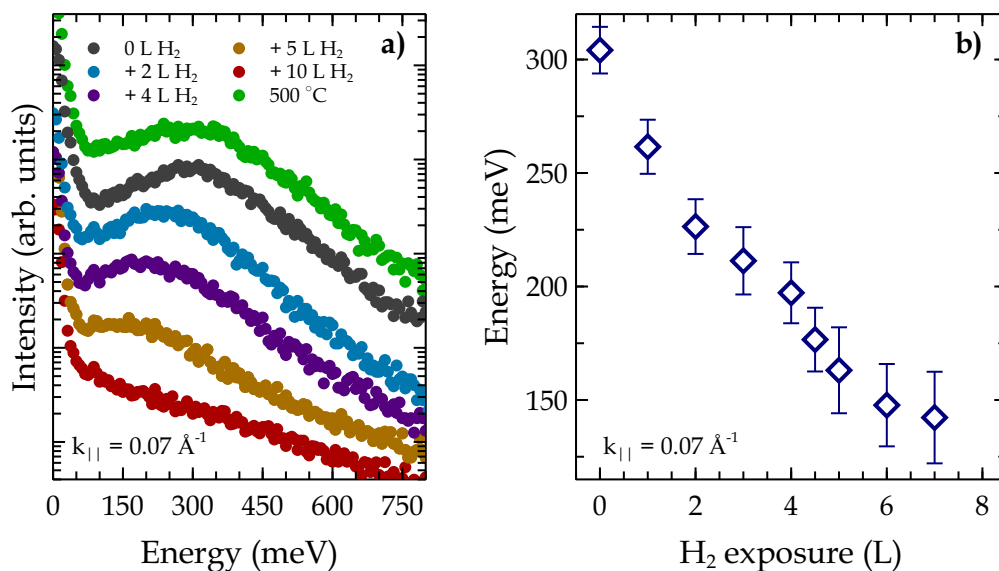


Figure 5.11: Exemplary EEL spectra from the Si(111)-(5×2)-Au surface showing the redshift and reversibility of plasmon frequency recorded at defined $k_{||} = 0.07 \text{ \AA}^{-1}$ for different hydrogen exposures (a). The spectra were normalized to the elastic intensity and shifted against each other for better visibility. The results were obtained for the Au coverage of 0.60 ML. (b) Change of plasmon energy as a function of hydrogen adsorption.

model, which has an extremely lower slope of the unoccupied metallic band for the clean surface. This finding might be another standing point for further optimization of Si(111)-(5×2)-Au surface structure and electronic properties.

5.4. Summary and Conclusion

In summary, the present chapter investigated the low energy electronic excitations of the (5×2) phase formed by Au wires on the Si(111) surface using plasmon spectroscopy. A slight miscut by 1° allowed the observation of a single-domain surface, a necessary prerequisite for these detailed investigations. It turns out that the whole range of Au concentrations from 0.2 ML up to 1 ML is governed mostly by phase coexistence of the (5×2) with either the clean Si(111)- (7×7) or with the $(\sqrt{3} \times \sqrt{3})R30^\circ$ phases, in agreement with earlier results on the phase diagram [179]. Only in a small concentration range around 0.60 ML, a single (5×2) phase exists. In addition to previous studies, the transition from a single to multi-domain surface and the resulting change in the electronic properties were also investigated. While no new plasmonic excitation associated with the $\sqrt{3}$ structures was detected, the plasmon dispersion of the remaining (5×2) structure provides evidence of increased disorder above 0.60 ML and an opening of a small band gap. The precise role of Au atoms at concentrations exceeding 0.60 ML that seem to stabilize formation of three domains, however, can not be explained with the obtained results.

As this study shows, we can gain valuable information about the unoccupied part of the bandstructure close to the Fermi level by studying plasmon dispersion. This part of the bandstructure, accessible to plasmon spectroscopy, turned out to be much more sensitive to differences between various structural models proposed for this system than spectroscopies of the occupied bands such as ARPES. Hence, the presented study corroborated the validity of the EBH model that suggests a saturation coverage of 0.60 ML of Au, in agreement with the new coverage calibration and LEED investigations in Section 5.1.

In the second part of this chapter, the effect of doping on the electronic properties of this surface was investigated employing surplus Au and H adsorption. The main effect of both adsorbates is charge doping, which results in a redshift of the plasmon frequency. These results support the metal-insulator transition in this system earlier reported [196], which required modification of the unit cell by adding an extra Au atom per (5×2) unit cell. However, the present study shows that such a transition does not necessarily require structural modification but can be rendered by just charge donation. This statement was proven by atomic hydrogen doping. The latter showed almost the same trend of reducing plasmon frequency even though such a small amount of hydrogen cannot drive any structural rearrangement, which was also not observed by diffraction studies.

Considering that this system's geometric structure and electronic properties are still under debate, the discussions presented here strongly suggest the optimum Au concentration for stable surface structure. On the other hand, a slight discrepancy between the calculated ω_+ and band structure poses a question about the correctness of the EBH model itself. Therefore, this study gives valuable insights into this surface, which is highly essential for further optimization and understanding.

Chapter 6

Gold-Induced Atomic Wires on Stepped Si(hhk) Surfaces

This chapter focuses on the structural and electronic properties of Si(hhk)-Au surfaces. At the beginning, the surface structures will be verified using SPA-LEED and available DFT calculated structural models. The extended SPA-LEED investigations are applied to study different Au concentrations on the Si(775)-Au. In this regard, the crucial role of adsorbed Au atoms on the final structural properties will be discussed. This will be followed by a detailed discussion on the plasmons on these surfaces. Since a general overview of plasmonic excitations on the clean Si(hhk)-Au surfaces have already been given in the recent literature [27,31], here only new findings and further insights are discussed. For this, Au-induced low coverage wires (LCWs) and high coverage wires (HCWs) phases on the Si(553)-Au surface have been considered as particular systems, and their excited-state band structures are compared with the atomistic DFT calculations. Subsequently, plasmonic excitations on the Si(775)-Au surface will be presented as a result of different Au concentrations. Before summarizing the findings from this chapter, the effect of temperature on the plasmonic excitation will be briefly discussed.

6.1. Surface Structures and Properties

Unlike the slightly inclined Si(111) surface, the periodically stepped structure of Si(hhk) surfaces imposed by the off-cut are stabilized by the presence of metal adsorbates. Most importantly, the use of stable vicinal substrates inhibits the formation of multiple domains in chain growth. The remaining important challenges are the increase in defects caused by excess or lack of metal coverage and/or the emergence of bunched steps due to inaccurate heating procedures. Fundamentally, the number of Au atoms

involved in the unit cell is the most relevant parameter for constructing a suitable structural model. The widely accepted models for the frequently used Si(hhk) surfaces were first proposed by Crain et al. [65] These models are still gaining updates following new experimental outcomes. [24, 25, 30, 200, 201] Notably, all these models contain a common structural building block, a graphitic sp^2 hybridized Si-HC chain at step edges, which emerges upon Au evaporation. It has also been proposed that it is a main structural block that drives the anisotropic surface reconstructions even on the nominally flat Si(111) surface. [158] In the following subsections, the most relevant structural models, together with their electronic structure, will be discussed.

Electronic Properties: Overview — Deposition of Au onto Si surfaces form metallic states that dominate the whole electronic properties of the surface. The states near E_F are particularly interesting because they determine most electronic properties, such as conductivity, superconductivity, magnetism, charge density waves. The surface state band is absent at the central Γ point, which is common to the 1×1 and $\sqrt{3} \times \sqrt{3}$ lattice. In particular, this concerns the fine splitting of the Au-induced 1D conduction band seen in ARPES, which was initially mistaken as the signature of the spin-charge separation in the TLL. [17]

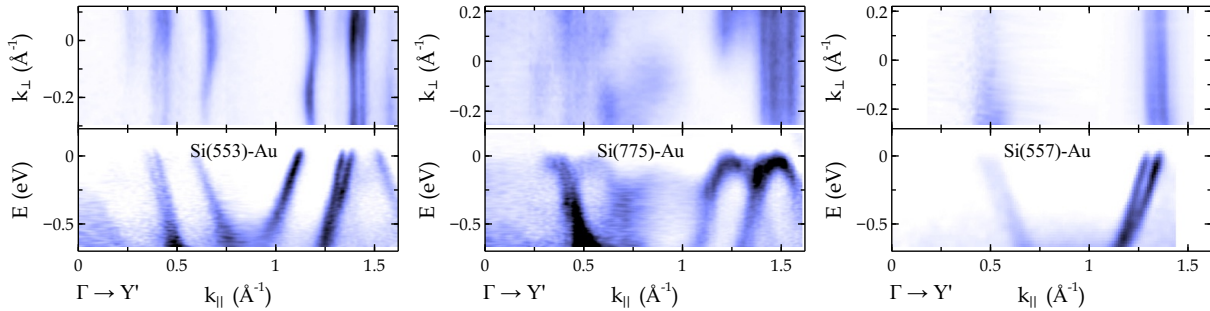


Figure 6.1: Experimental ARPES maps of the electronic band dispersion for the most pronounced members of the Si(hhk)-Au surfaces. The dispersions obtained with momentum transfer parallel to the wires in the first SBZ, in the $\Gamma \rightarrow Y'$ direction. All bands possess an energetic minimum at the zone boundary. Additionally, they (only the outer band for double chain systems) show extra band splitting close to E_F ($E = 0$). The Fermi surfaces are given on top of the corresponding band dispersion. All surfaces exhibit almost linear Fermi surfaces as expected for highly confined 1D metals. The minor undulations are the signature of 2D coupling perpendicular to chains. The dark area in all figures corresponds to high photoemission intensity. Adapted from Ref. [65] with permission. Copyright 2004 by the American Physical Society.

However, with an improved experimental resolution, it could soon be shown that split bands do not merge at the Fermi level, thus excluding the interpretation as spinon and holon branch of the TLL. [89] In fact, all members of the Si(hhk)-Au family are characterized by split parabolic bands. [65] This splitting was recently assigned to Rashba-type spin-orbit coupling caused by the strong spin-orbit interaction of

Au. [24–26, 202–205] One of the main resemblances of Si(hhk)-Au systems is the number of atomic stripes per terrace and the number of metallic bands in the vicinity of the Fermi level (see Fig. 6.1). While for double Au chains, two bands have been observed, for the systems with a single Au chain, one band lies at the Fermi level. However, in both cases, only a single band has been observed to cross the Fermi level that gives rise to single plasmonic excitation on all surfaces have been investigated here. Although the photoemission data for the Si(hhk)-Au systems suggest that the Au-induced bands are located in the band gap of Si and show free-electron-like dispersion, atomistic calculations, using the geometries derived from STM, consistently show that in none of these systems a free-electron-like behavior should be expected. [26, 31, 33, 65] In all systems, there is a strong hybridization of the Au-induced band(s) with the Si surface states. Consequently, band gaps of 0.1 to 0.2 eV open, which have also been observed in experimental studies [202, 206].

6.1.1. Si(553)-Au: Double Atomic Chain

The Si(553)–Au system is one of the most investigated 1D systems and a paradigmatic example of fine engineering of self-assembled atomic-scale wires. [25, 27, 30, 93, 200, 207] The most reasonable structural model the so-called dimerized Au-rows was proposed by M. Krawiec in 2010 [24], which replaced the single Au-chain model at the coverage of 0.25 ML proposed by J. Crain et al. in 2003 [22]. The Krawiec model explained several ground state properties of this surface, such as the coupling of the band gap with dimerization parameters. This model was soon replaced by S. Erwin’s spin-chain model, which was structurally almost the same, while it was accounting for spin chains formed at the step edge Si atoms. This model, which is shown in Fig. 6.2, predicted that every third Si step edge atom possesses a half-filled electron orbital while others are filled completely. The half-filled bands are fully spin-polarized, and their coupling across terraces and along the step edges was originally predicted to form a ferromagnetic and antiferromagnetic ordering, respectively. [25] As evidence of these half-filled orbitals, distinct unoccupied electronic states above the Fermi level were found in STS studies. [208, 209] The double Au chain model, which is formed at a Au coverage of 0.48 ML was strongly supported by STM [208, 210] and diffraction [211, 212] studies. Previously, a gradual energy gap opening at low-T was revealed by STS and ARPES measurements, which was consequently interpreted as a Peierls-type metal-insulator transition associated with a periodic doubling of the Au atomic periodicity along the terraces. [20, 213] However, the following studies eliminated this Peierls transition while a similar transition was observed under different conditions. For example, a reversible transition between the $\times 3$ ground state and the $\times 2$ excited state periodicity due to tip-induced transient doping was found in STM studies. [210] At a temperature lower than 80 K, the $\times 3$ periodicity was also observed, which is associated with the step edge Si atoms. [20, 204, 211] While the $\times 2$ periodicity exists at RT and persists at elevated T, the $\times 3$ periodicity undergoes an order-disorder transition at $T = 100$ K. [201] Based on the diffraction studies, the spin-chain model was also updated by revealing a centered structure at low-T. [201] Subsequently, the rehybridized model was proposed. [214] However, the last two models

have not put substantial changes in the previous models, so electronic band structure and strength of hybridization is not modified. Spin ordering was found to be relevant only for the ground-state spin pairing, which is not accessible with experimental techniques because the thermal fluctuation destroys this ordering. Therefore, and considering that plasmon spectroscopy is not sensitive to spin ordering, the Krawiec model [24] is accepted as a basis for the interpretation of plasmonic excitation in this thesis.

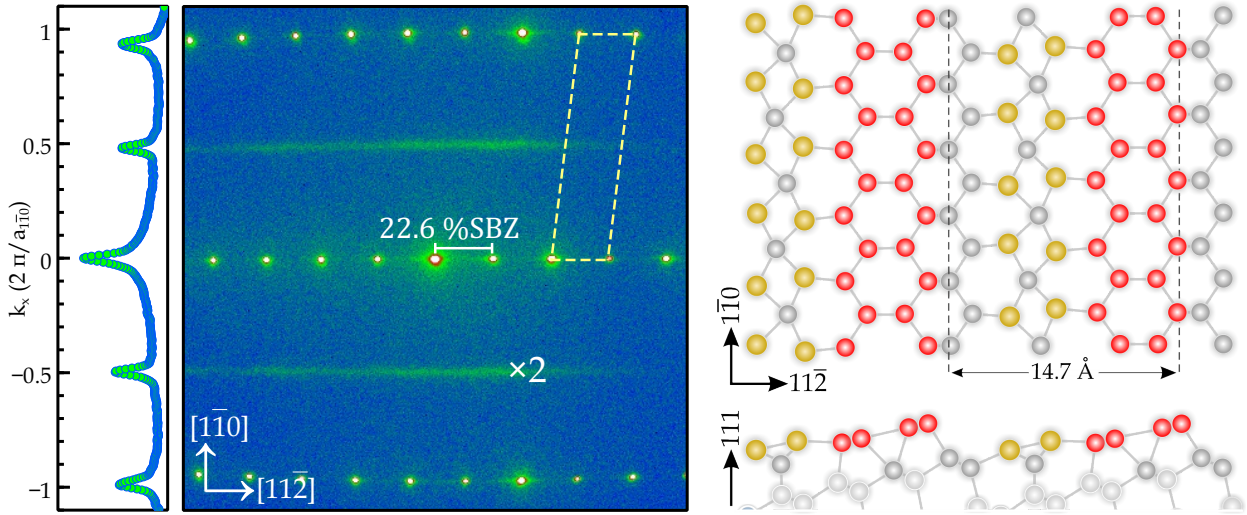


Figure 6.2: SPA-LEED pattern and DFT calculated structural model for Si(553)-Au surface. The SPA-LEED image was recorded at room temperature after 0.48 ML Au deposition at 630 °C. The dashed yellow rhomboid depicts the 1×1 Si surface reconstruction that involves flat (111) terraces with double atomic height steps. The 1D spot profile recorded through the 0,0 spot in step direction is shown on the left side of the diffraction image. The right graph is the energetically most stable model with a double atomic Au chain per terrace separated by 14.7 Å. In the right graph, yellow, red, gray, and light gray balls stand for the gold, Si-HC chains, Si surface, and bulk atoms, respectively.

Fig. 6.2 shows a SPA-LEED pattern of the (553)-Au surface with 0.48 ML gold deposited. This is the so-called high coverage wires (HCWs) phase. The diffraction pattern of the corresponding surface is dominated by round and sharp spots related to the Si step train. The sharpness of spots is an indication of well-ordered surfaces. These spots form an oblique 1×1 surface unit cell with the corresponding dimension as:

$$\underbrace{2\pi/14.7}_{a_{112}} \times \underbrace{2\pi/3.84}_{a_{110}}$$

The spot splitting of 22.6% SBZ (surface Brillouin zone) for the HCWs phase corresponds to the following periodicity:

$$4\frac{1}{3}a_{112} / \cos 12.5^\circ = 14.7 \text{ \AA} \quad (6.1)$$

Here, $a_{\perp} = 3.32 \text{ \AA}$ is the substrate unit cell along the $[11\bar{2}]$ -direction. The terraces are separated by steps with a height of 3.14 \AA . The first order spots are interlaced by the two-fold periodicity of Au atoms. These so-called $\times 2$ streaks, which reflect the dimerization of the Au double-chains along the $[1\bar{1}0]$ direction. Since $\times 2$ is composed of metallic atoms they determine the metallicity of the surface. Moreover, its intensity and width are highly responsive to small deviation from 0.48 ML coverage as well as to changes in the preparation condition. Depending on the preparation (namely temperature treatment), several facets such as (111) and (331), were previously observed on the Si(553) surface [156]. Nevertheless, in the scope of this thesis, only a $(\sqrt{3} \times \sqrt{3})R30^{\circ}$ periodicity associated with large (111) terraces was observed for $>10\%$ additional Au coverage (see Section 8.1.2).

The double gold chain produces two metallic bands that are strongly dispersing in the direction parallel to the gold chains with minima at the boundary of the 1×1 Brillouin zone, as observed in photoemission (see Fig. 6.1). Only one of them seems to cross the Fermi level and gives rise to quasi-1D metallicity. [25] This band is historically numbered as a $S_{1,2}$ band while it is slightly split by the spin-orbit interaction. [25, 89, 206] Moreover, an antiferromagnetic ground state is predicted theoretically along the step edge Si-HC chains. [25] Contrary to an earlier model with a single Au strand, the dimerized double Au chain model reproduced the band structure better and showed that the $S_{1,2}$ and S_3 bands are all related to Au-induced surface bands. [24] The origin of the Rashba split $S_{1,2}$ bands was also supported within this model. [163] At the step edge, Si atoms are packed into a graphene-like honeycomb chain with a pair of dangling bonds per sp^2 hybridized Si step edge atom, which shows at low temperature intrinsic magnetic ordering with $\times 3$ periodicity. [25] The latter has also been interpreted as a consequence of a diamagnetic $sp^2 + p$ hybridization. [214] The well defined Fermi surface and band dispersion, as shown in Fig. 6.1, prove its comparatively high stability and anisotropic metallicity. The slight modulation of the Fermi contours was assigned to lateral interaction of wire arrays similar to Si(111)-(5 \times 2)-Au. The relation of the aforementioned electronic bands with the plasmon dispersion will be discussed in Section 6.3.

Crucial Role of Gold Coverage — The effect of Au concentration on the resulting surface structure has been tested using SPA-LEED by slightly varying the Au coverage. It was found that only 0.03 ML deviation from the optimum (0.48 ML) gold coverage is already enough to see minor changes in the diffraction pattern. Surface preparation with the same procedure but now with 0.44 ML Au coverage, resulted in streaky step train spots in the $(11\bar{2})$ direction. Also, the intensity and width of the $\times 2$ streaks are highly sensitive to the Au coverage, as shown in Fig. 6.3(a). As a result, lower intensities and broader half-width suggest less wire quality and shorter length of correlation due to inadequate Au coverage. Furthermore, the $\times 2$ streaks appear as wiggled for slightly less Au coverage, as shown in Fig. 6.3(e-c). Increasing the Au amount to a surplus coverage deposited at the same elevated temperature eliminates the intensity modulation and increases the $\times 2$ intensity. 1D line profiles of $\times 2$ streaks along $(1\bar{1}0)$ direction were recorded with small steps in the $(11\bar{2})$ direction. These line profiles are illustrated in

Fig. 6.3(f), which show the left and right maxima of the wiggled $\times 2$ periodicity. Interestingly, this wiggling shows a periodicity of the step distribution. This implies a short range correlation between the adjacent chains in the lack of Au atoms. On the other hand, correlation along the chains, which is more important for the present case, is reduced at lower Au concentration. Although exact reason of this increased lateral correlation cannot be given here, it can be speculated as following: A slight deviation from the required amount results in lasting stacking faults in chain structure due to a missing atom. In the lack of Au atoms the formed chains might exchange their periodicity to compensate the energy cost. Although surplus Au atoms increase integrated intensity the observed phase shift is not recovered. Further increase of Au coverage results in a $(\sqrt{3} \times \sqrt{3})R30^\circ$ structure, as shown with the red circles in Fig. 6.3(d). Moreover, at insufficient coverage the faint $\times 3$ streaks also appear. Noteworthy, such apparent sensitivity of Si(553) to Au coverage makes it highly unique for using it as a model surface for further surface optimization. Not only are the structural changes observed for these tiny changes of Au coverage, but plasmon frequency also shows particular sensitivity to the Au concentration (See Fig. B.5).

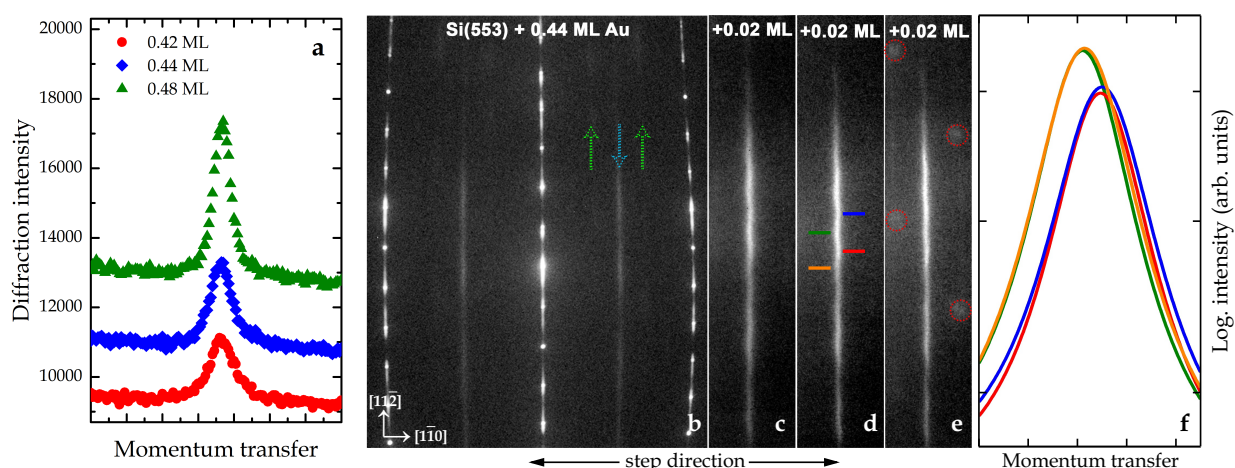


Figure 6.3: 1D line profiles for the $\times 2$ streaks measured parallel to the steps at Au coverages of 0.42, 0.44 and 0.48 ML (a). SPA-LEED patterns for different Au coverages on Si(553) recorded at RT (b-e). In (a), the surfaces were prepared with the same procedure; only the Au concentration was different. In (b-e), the surfaces were prepared by adding surplus coverage at 630°C . In (b), blue and green arrows stand for the $\times 2$ and $\times 3$ periodicity, respectively. Red circles show the $(\sqrt{3} \times \sqrt{3})R30^\circ$ structure. (f) shows four line scans recorded for the wiggled sections indicated by the lines of the same colors in (d). Please note that images (b) and (c-e) have been recorded with different interaction time.

LCWs Phase on Si(553)-Au — Deposition of 0.19 ML Au onto a well annealed Si(553) surface forms a new metastable surface, the so-called the low coverage wires (LCWs) phase. Although its coverage is similar to that which was primarily estimated to be optimum (0.24 ML, [22]) for a single wire structure on the Si(553) surface, its surface structure and properties are rather different. First of all, Au atoms

still form double Au chains (as in the HCWs phase) instead of single chains. However, due to the lack of Au atoms, the surface forms Au-free terraces with a width of $5\frac{1}{3}a_{\perp}$ and only every second terrace is occupied by double Au strands forms $4\frac{2}{3}a_{\perp}$ wide terraces. The latter is the same as on the HCWs phase. These two different terraces result in spot splitting of diffraction spots of 10% of SBZ (see Fig. 6.4). This corresponds to the following periodicity.

$$9\frac{2}{3}a_{11\bar{2}} / \cos 11.3^{\circ} = 32.7 \text{ \AA} \quad (6.2)$$

The Au-free terraces exhibit a $\times 5$ modulation of Si(111) terraces, while the dimerized Au chains at the occupied terraces give rise to the half order streaks ($\times 2$) in the diffraction pattern, Fig. 6.4. In order to maintain the macroscopic (553) orientation, either steps in opposite direction or wider (111) terraces must be inserted. While opposite steps will not be visible in LEED, there is no indication for long (111) terraces. The resulting surface is (11 11 7), which has a slightly wider terrace width than the (553) orientation. Although this macroscopic change might induce step bunching, the Au-induced atomic chains still show long-range ordering, which was proven by plasmon spectroscopy. [27, 215]

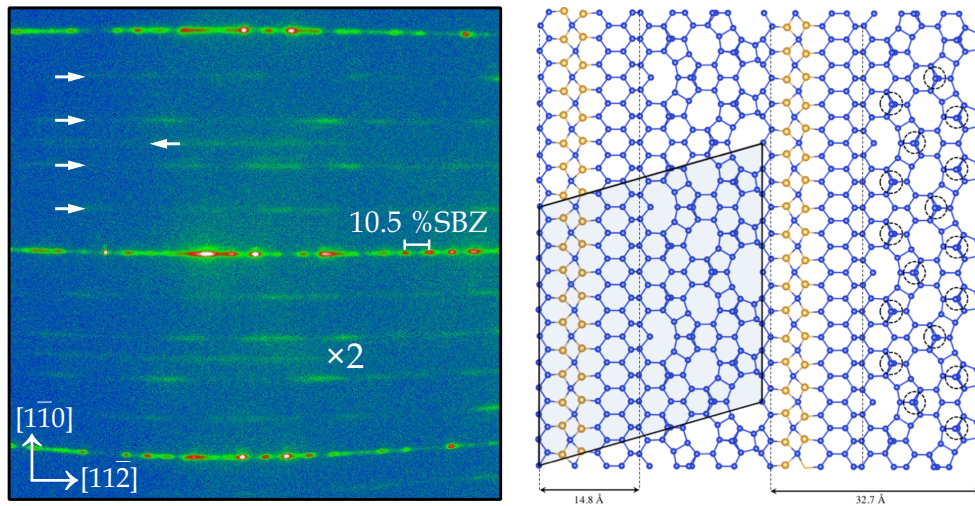


Figure 6.4: Left: SPA-LEED pattern of the LCWs phase recorded at RT. The rightwards and leftwards arrows depict the $\times 5$ and $\times 2$ periodicity, respectively. Right: Structural model of the top-most atomic layer of the same surface. Yellow and blue balls correspond to Au and Si atoms, respectively. The (11×10) surface unit cell and the terrace width are highlighted with a rectangle and dashed lines, respectively. Dotted circles indicate the position of the Si adatoms.

The structural model for the LCWs phase was first proposed by Song et al. [216] and later on successfully used to describe the plasmonic excitation on this surface. [27] There, the formation of double Au chains instead of single Au chains by leaving every second terrace uncovered was explained as a strain-induced effect. In fact, surface stress is much more sensitive to surface relaxation than to surface energy. [217] Notably, the formation of two different kinds of terraces in the LCWs structure underlines the importance of surface stress for the whole surface geometry. Similar to the HCWs phase, on the LCWs surface the

occupied terraces possess undistorted Si-HC chains while the empty terraces have three different kinds of holes with the Si atoms in the three-fold coordination (depicted by dashed circles in Fig. 6.4). The position of these Si-adatoms in the 5×5 structure is the same as in the dimer-adatom-stacking-fault (DAS) structure. [126] The latter brings higher chemical reactivity to this surface (see Section 7.3.4).

The experimental ARPES bands of this surface together with the calculated ones are shown in Fig. 6.5. Comparing the LCWs and HCWs band structures, the $S_{1,2}$ and S_3 states of the HCWs phase can be identified in the LCWs phase as well. However, it becomes evident that because of the five-fold folding and hybridization with the Si atoms, some rearrangement occurs. This behavior is the same as observed in other calculations. [206] Similar to HCWs surface here also Au bands are hybridized mainly with Si step edge states (S_4 band in Fig. 6.5).

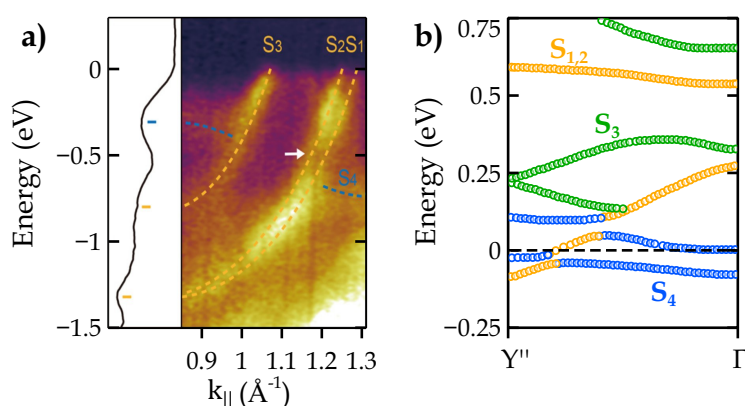


Figure 6.5: (a) Experimental electronic band structure for the LCWs phase on the Si(553)-Au surface obtained from experimental ARPES. (b) The DFT–PBE band structure was calculated for the LCWs system in a smaller energy window close to the Fermi energy (black dashed line). In (b), the $\Gamma \rightarrow Y''$ direction in the LCWs system is roughly parallel to the Au chains. Figure (a) adapted from Ref. [216] with permission.

6.1.2. Si(775)-Au: Double Atomic Chain

The (775)-Au surface is also one of the most known members of the Si(hhk) family. However, its structural and electronic properties have been addressed only in a few studies and require substantial verification. Considering this issue, a detailed structural investigation has been conducted by employing SPA-LEED. The Si(775) surface is 8.5° inclined from the Si(111) surface towards the $[11\bar{2}]$ direction. Previously, a Au coverage of 0.24 ± 0.03 ML was determined for stabilization of Si(775) reconstruction. [218] This coverage produces large regions of (775)-Au with an intermittent minority of the (443) facets. The (443) facets are approximately 1° off the (775) orientation (see Fig. 4.6), which stabilizes to the (775) facet with increasing Au coverage. [219] Following this work, it was revealed that the deposition of 0.32 ML of gold onto the annealed surface forms the most stable structure [65], the so-called optimum coverage wires (OCWs). 2D LEED pattern for this coverage, together with the corresponding

surface structure, is presented in Fig. 6.6. The diffraction pattern is dominated by equally separated sharp and round spots originating from the Si step train.

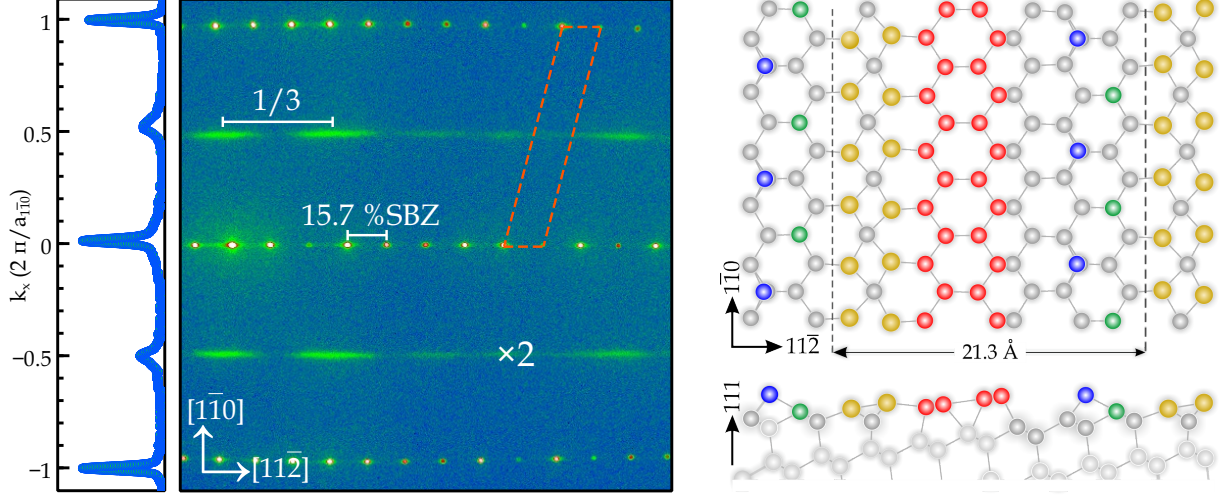


Figure 6.6: SPA-LEED pattern (left) and structural model (right) for the Si(775)-Au surface at the Au coverage of 0.32 ML. The SPA-LEED image was recorded at room temperature. The 1D spot profile recorded through the (0,0) spot along the terrace is shown on the left side of the diffraction image. The dashed orange rhomboid indicates the 1×1 unit cell that involves flat (111) terraces separated by steps of double atomic height. In the right graph, yellow, red, blue, and green balls stand for the gold, Si-HC chains, Si-adatom, and Si-restatoms, respectively. Other Si surface and bulk atoms are shown with the dark and light gray balls, respectively. While this model does not replicate the $1/3$ periodicity observed in electron diffraction, it is a generally accepted model that almost explains the plasmon dispersion (see Section 6.4) and other electronic properties [30].

Similar to the previous surfaces, these spots form an oblique 1×1 unit cell with dimensions of:

$$\underbrace{2\pi/21.3}_{a_{11\bar{2}}} \times \underbrace{2\pi/3.84}_{a_{1\bar{1}0}}$$

Their splitting in the $(11\bar{2})$ direction yields 15.7% of the SBZ, which corresponds to a step-step distance of:

$$6\frac{1}{3}a_{11\bar{2}} \cos 8.5^\circ = 21.3 \text{ \AA} \quad (6.3)$$

It should be noted that its atomic structure originally was adapted from the Si(553)-Au surface with one double-Au strand per terrace and a graphitic Si-HC chain at the step edge. The terraces on Si(775)-Au are wider, 21.3 Å, 1.5 times as wide as on Si(553)-Au. This additional space is equivalent to two additional silicon unit cells and hence opens the door to structural motifs not found on the Si(553)-Au. This comprises the adatom and rest atom chains with $2 \times a_{1\bar{1}0}$ periodicity along the terraces. The latter

makes this surface similar to the Si(557)-Au surface, while on Si(775), the Si adatom chains appear only after Au deposition, see Section 4.7.1. Their exact contribution to the diffraction pattern cannot be resolved here since they also form $\times 2$ periodicity as the dimerized Au chains.

On the other hand, the weak correlation across terraces results in the streak-like appearance of the $\times 2$ periodicity, which adds up another difficulty to that issue. The presence of the Si adatoms on this surface was also confirmed by STM studies. [30] Another interesting feature of this diffraction pattern is the modulation of the $\times 2$ streaks perpendicular to the terraces. This periodicity corresponds to $1/3$ of the terrace width. The construction of this periodicity in real space requires three spatially separated Au-induced periodicities at a single terrace. However, no such periodicity has been reproduced in the DFT calculations [220]. As shown in Fig. 6.10, upon adsorption of surplus Au at RT and subsequent annealing the step periodicity changes by formation of a new facet. Interestingly, the modulation of $\times 2$ normal to the terraces remains unaltered even after modification of the step periodicity. Although it is quite an interesting feature, it has to remain unsolved at this stage. Investigation of this surface in the temperature range between 5-300 K revealed no new periodicity and/or phase transition. [30]

Similar to Si(553)-Au, Si(775)-Au also possesses two parabolic electronic states below E_F . [65] From the mentioned photoemission data, which is shown in Fig. 6.1, it was not clear whether the system is indeed metallic, since both bands do not seem to cross the Fermi level, but to hybridize with Si surface states just below the Fermi level. However, recent plasmon studies, together with DFT calculations, proved the metallicity of this surface. [31] Moreover, the observation of only a single plasmon loss in energy loss spectra (i.e., see Fig. 6.17) supports that only one of those bands crosses the Fermi level. DFT calculations showed that both the quasi parabolic Au-induced bands ($S_{1,2}$ and S_3) strongly hybridize with the Si surface states localized mainly at the Si-HC and the restatoms (see Fig. 6.18). This hybridization leads to band gap opening in the occupied states and to the result that the S_3 band hybridizes with the honeycomb chain in the middle of the BZ around -0.4 eV. $S_{1,2}$ band mixes at slightly higher energy with this state close to the BZ boundary and forms a very small band gap. [31] As a common feature for Au-induced superstructures on Si surfaces, this surface also exhibits a spin-orbit coupling showing Rashba type splitting in photoemission spectra. The details about DFT calculated bands and their relevance to plasmon dispersion, mainly with respect to modification of plasmon bands, will be given in Section 7.5.

6.1.3. Spot Profile Analysis of Si(775)-Au

For a detailed investigation of the 0.32 ML Au adsorbed Si(775) system, spot profiles were recorded for different scattering phase S values, as shown in Fig. 6.7(left). The shown different energy scans were recorded with the momentum transfer perpendicular to wires for studying the lateral terrace distribution. From this measurement, no other facets are visible. Knowing the sensitivity of SPA-LEED to long-range correlation, this implies that the only macroscopically arranged orientation is (775). The observed diffraction rods show only a minor intensity modulation, which indicates very good surface

quality. The slight bending of the Ewald rods at the edge of the image is due to the imperfect alignment of the electron beam over a broad energy range (i.e., $35 \text{ eV} \div 245 \text{ eV}$) and to the typical pillow distortion in SPA-LEED geometry. Beyond this, the straightness of these rods proves the perfect cut direction or inclination of the bare surface.

In order to obtain more information, the line profiles in the $(11\bar{2})$ direction were extracted for the central five diffraction rods as numbered in Fig. 6.7. For data extraction, these line profiles were fit with Voigt functions. In this fit routine, the instrumental broadening is taken into account by the Gaussian function, where the FWHM and intensity of the Lorentzian part yield information on the lateral arrangement and vertical roughness, respectively. This fit procedure is exemplary shown for $S = 5.6$ in Fig. 6.8(right). From this fit, FWHMs of the Lorentzian part are collected and illustrated in Fig. 6.8. The presented data is after subtraction of the instrumental broadening that was estimated to be $\sim 0.01 \text{ \AA}^{-1}$. Based on this data, the minimum range of the lateral ordering was evaluated using Eq. 3.22, which considers a multi-level surface arrangement. This estimation yields $\geq 270 \text{ \AA}$, which is very similar to the value obtained for Si(553)-Au in Ref. [221].

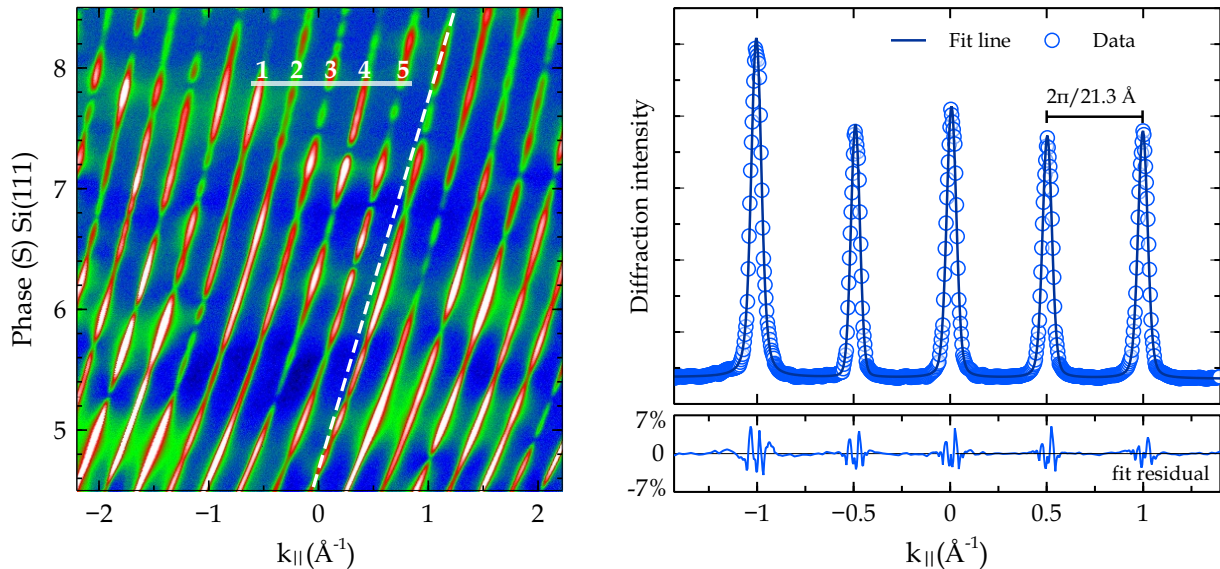


Figure 6.7: Left: Reciprocal space map for the Si(775) + 0.32 ML Au obtained using SPA-LEED at phase $S = 4.5 \div 8.5$ ($E = 77 \div 276 \text{ eV}$). The inclined Ewald rods correspond to the (775) orientation. The direction and position of the extracted line profiles are shown with white line and numbers. The white dashed line approximates the expected Ewald rods. Right: Exemplary 1D spot profile extracted from the different energy scan for $S = 5.9$. The fit line corresponds to the fit procedure, as shown in Fig. 6.8(right).

The FWHM of diffraction spots does not show well-defined sine oscillation or any other systematic variation as a function of the scattering phase S . This behavior also closely resembles the observation on the Si(553)-Au surface showing a nonhomogeneous terraces distribution. Although the estimation of the terrace width is not straight forward, the diffraction pattern shows that the step-step correlation

on the Si(775) surface preserves its periodicity upon 0.32 ML Au evaporation. Moreover, Au shows a healing effect resulting in a better step periodicity. The same procedure was applied to extract the correlation of wire structures along the terraces. Since in this direction, the diffraction appears only at the in-phase condition or integer values for phase S , only these line profiles are shown in Fig. 6.8(middle).

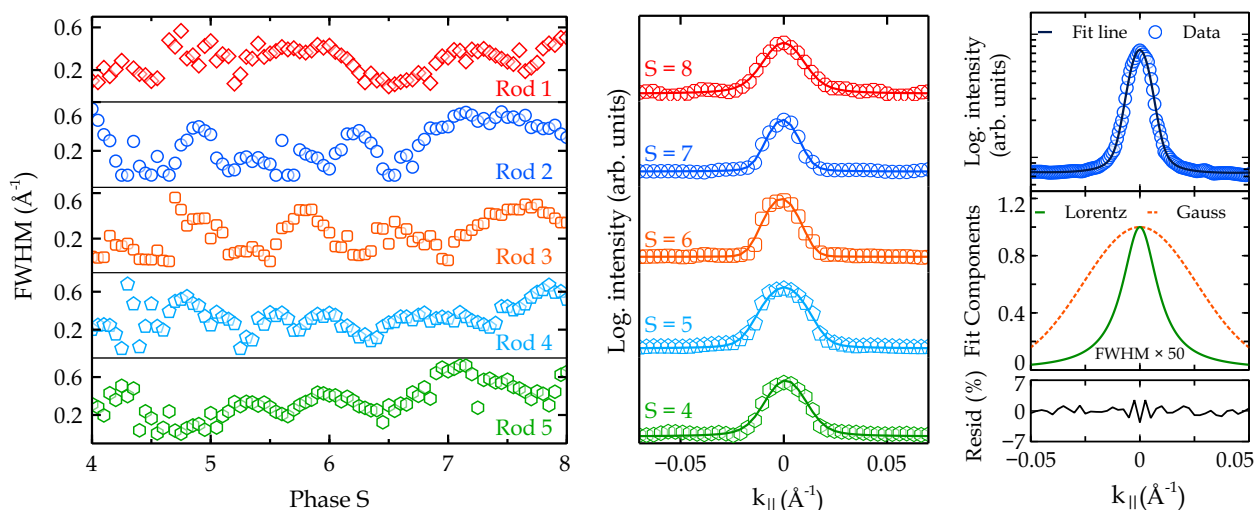


Figure 6.8: Left: Variation of the FWHMs of Lorentzian part as a function of the scattering phase S , shown for $S = 4 \div 8$. Middle: 1D line scans through the central spot recorded in the direction parallel to the steps for various phase S . Right: The fitting routine applied to extract parameters from the 1D spot profiles.

Au Concentrations Above 0.32 ML — Now turning to the effect of Au coverage on the resulting surface structure, several surface coverages have been tested following Ref. [220]. There, more than 100 different Au coverages were optimized, revealing a phase diagram of Au-induced wire structures on this surface. According to the calculated structural models, the dimerized Au strands persist up to 0.56 ML surface. The following coverage, however, dislocates the dimerized Au atoms on the terraces. As a result, the whole surface becomes structurally isotropic. Thus, the excess Au atoms adsorbed on different terraces nearly connects the neighboring terraces by lifting off the Si-HC chains at the step edges. The latter suggests that the almost full coverage surface at a concentration of 0.96 ML Au may show isotropic electronic properties. However, it turns out that the full coverage surface is highly misoriented in both directions. In addition, the first principle calculations show that even at 1 ML Au concentration, the step separation does not produce different variations.

In order to test the Au concentrations proposed by theory, the surfaces were prepared in the same condition, but only the Au amount deposited is different. Exemplary SPA-LEED patterns for 0.56 ML and 0.65 ML coverage are shown in Fig. 6.9. Diffraction patterns for other tested surfaces are given in Fig. B.1. The diffraction elements explained in the previous section were also observed for all higher coverages, though, with different quality. First of all, by increasing the Au coverage, the $1/3$ periodicity (normal to terraces) fades out and completely disappears at 0.56 ML Au concentration. The $\times 2$ streaks

gain more intensity up to a Au concentration of 0.40 ML, then it declines again for higher coverages. This trend was previously observed in RHEED experiments as well. [222] Moreover, the 0.56 ML surface shows continuous $\times 2$ streaks similar to those found on Si(553)-Au. The non-periodic intensity modulation of the $\times 2$ streaks along the $[11\bar{2}]$ direction might be attributed to the random terrace distribution, which was also seen for other coverages and exemplary discussed for the OCWs surface. Moreover, by going away from the 0.32 ML Au coverage, the Si step train spots elongate in the $[11\bar{2}]$ direction, which shows the distortion of step edges. This might be due to the adsorption of an excess amount of Au atoms at the step edges. Preliminary calculations have also shown that the step edges are the most favorable side for adsorption of additional Au atoms on OCWs. Although post-annealing the $\Theta_{Au} > 0.56$ ML surfaces at 800 °C, helps for the accumulation of excess Au atoms in the $\sqrt{3}$ structure, the distortion (elongation) of step train and step bunching are not fully reversed.

Among others, the most interesting coverage is the 0.56 ML surface. This coverage is between the OCWs and higher coverage surfaces with the presence of $\sqrt{3}$. The calculations predicted that at this Au concentration, the surface hosts Si-HC, adatom, and restatom chains and double and single Au strands, which occupy almost the whole terrace. Due to the spatially separated two Au chains, two distinguished diffraction elements or at least a modulation of the original $\times 2$ streaks were expected, but were not observed. This indicates that, contrary to the theoretical modeling, in reality, in the presence of excess Au coverage, the refaceting of (775) orientation and the generation of new terraces are energetically more favorable than a new periodic structure formation.

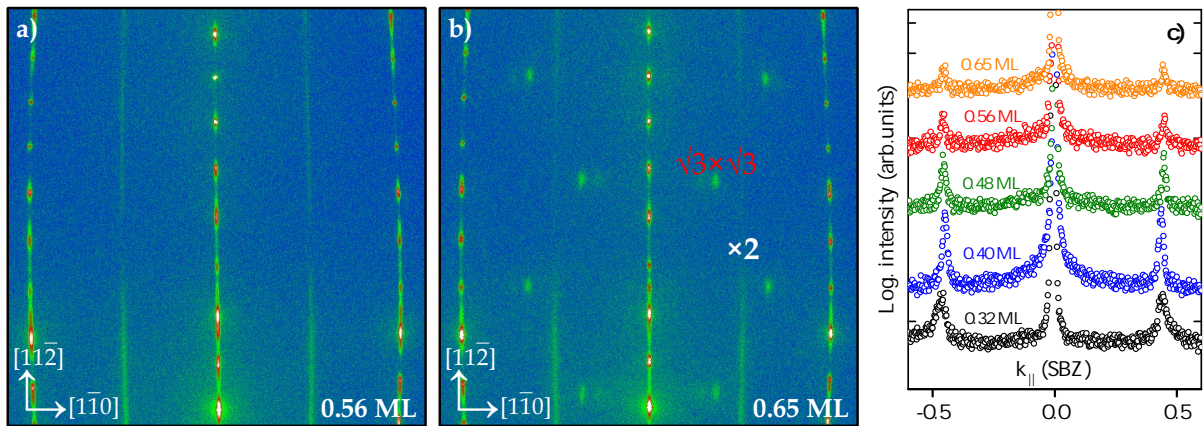


Figure 6.9: SPA-LEED patterns of the Si(775)-Au surface at a Au concentration of 0.56 (a) and 0.65 ML (b). Images were recorded at RT with 138 eV primary energy. (c) 1D spot profiles of the $\times 2$ streaks recorded for different Au coverages along the terraces.

Another interesting additional structural motif is the $\times 3$ periodicity that appears for 0.96 ML Au deposited surface. In a simple approach, occurrence of the faint $\times 3$ streaks might be due to accommodation of non-registered Au atoms at narrow (111) terraces and/or directly at the step edges. These streaks disappear upon subsequent annealing at 800 °C. This might be due to either desorption of ad-

ditional Au atoms and/or again accumulation into $\sqrt{3}$ structure. On the other hand, the correlation of $\sqrt{3}$ spots is also destroyed by this annealing step. It was found that at the Au concentration of 0.96 ML, the regular step structure undergoes step bunching before the postanneal step. Annealing 0.96 ML surface at 800 °C for a few second intensifies and triangulates the appearance of $\sqrt{3}$ spots (see Fig. B.1), which shows the formation of ordered islands. The $\sqrt{3}$ spots show a characteristic splitting in the $[1\bar{1}0]$ direction, which is more visible at the Au coverage of 0.65 ML (see Fig. 6.9(b)). Their separation yields $\sim 6.5\%$ of the SBZ resulting in $\sim 50 \text{ \AA}$ correlation length along terrace. No long-range correlation of $\sqrt{3} \times \sqrt{3}$ perpendicular to terraces was observed. The formation of $\sqrt{3}$ islands require large terraces. In this particular case, increase of the intensity of the first order spots up to 0.56 ML Au deposition implies additional narrower terrace formation, therefore, the formation of a large terrace could be possible. On the other hand, the 1×1 spots lose intensity for the > 0.56 ML surface, most probably due to random adsorption of Au atoms at steps.

Close inspection of the spot splitting show that the terrace width of 21.3 \AA for the 0.32 ML Au coverage contentiously decreases as a function of increasing Au coverage. The tendency of this reduction displays the following trend.

$$\underbrace{21.3 \text{ \AA}}_{0.32 \text{ ML}} \longrightarrow \underbrace{19.8 \text{ \AA}}_{0.40 \text{ ML}} \longrightarrow \underbrace{17.55 \text{ \AA}}_{0.48 \text{ ML}} \longrightarrow \underbrace{14.8 \text{ \AA}}_{0.56 \text{ ML}} \longrightarrow \underbrace{14.54 \text{ \AA}}_{0.65 \text{ ML}} \longrightarrow \underbrace{14.48 \text{ \AA}}_{0.96 \text{ ML}}$$

Evidently, the terrace width decreases quickly up to 0.56 ML coverage from where it stays almost unaltered for the further coverages. The obtained value of 14.8 \AA at 0.56 ML, is the same as the terrace width of the Si(553)+0.48 ML Au surface. These findings show the metastability of the Si(775) against Au coverage, which seems has a strong effect on the restabilization of this orientation. These results are similar to the previous reports. [223, 224] There, the authors showed that the (775) facet is stable up to a Au concentration of 0.40 ML, then refacets to the (553) and (111)- 5×2 periodicity. The latter also transforms into the large (111) terraces in the presence of the $\sqrt{3} \times \sqrt{3}$ structure and residual (553) orientation upon further Au deposition. However, no 5×2 was found in the present study. Similar metal-induced refacetting of stepped surfaces have also been reported in literature. [219, 225, 226]

Refacetting and distortions of this surface were also found after deposition and annealing of a surplus Au coverages, as shown in Fig. 6.10. The deposition of additional Au at RT reduces the $\times 2$ intensity, which is accelerated by annealing at 700 °C. This shows that additional Au atoms have low mobility at RT, so that they cannot form a new ordered structure, but are mainly randomly adsorbed and reduces surface perfections. The subsequent annealing also introduces a clear diffuse background to the first order spots. Moreover, increased background, as shown in Fig. 6.10(inset), is also evidence of random adsorption. On the other hand, increased mobility at high temperatures leads to the destruction of step periodicity and a new facet formation, as shown in Fig. 6.10(b). The spot splitting for the new periodicity again indicates the (553) orientation in addition to the large (111) terraces. Although no enhancement of the structural ordering after doping with surplus Au has been observed, doping at RT

does not significantly alter the long-range correlation along the wires (see Fig. 6.10(a)). Such enhancement was seen in experiments and supported by DFT modeling on Si(553)-Au [227], which also has dimerized Au chains, and will be discussed in Section 8.1.1. The only feature that remains unchanged after the annealing step is the $1/3$ modulation of the $\times 2$ streaks, as shown in Fig. 6.10(c). This shows the still existence of the (775) terraces and proves higher stability of Au-induced structures on those terraces.

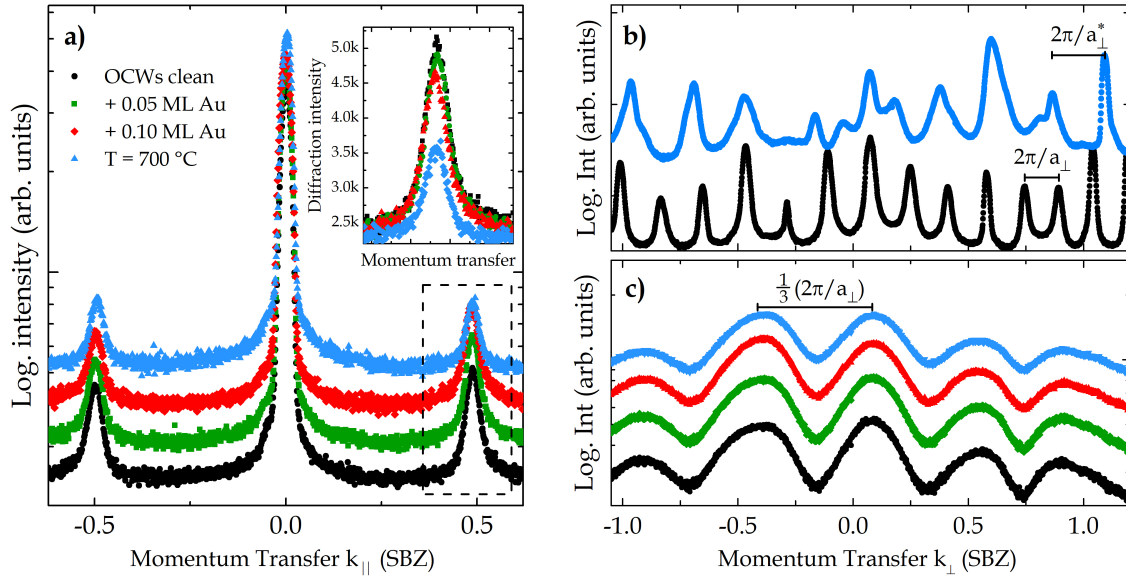


Figure 6.10: Set of 1D diffraction profiles for the Si(775)-Au OCWs surface. (a) Line profiles of the $\times 2$ streaks along $(1\bar{1}0)$ as a function of surplus Au coverage. The inset shows a direct comparison of $\times 2$ peaks, marked by the dashed rectangle, in a linear scale. (b) Line scans in the $(11\bar{2})$ direction for the clean and 0.1 ML surplus gold deposited and subsequently annealed surface. $a_{\perp} = 21.3 \text{ \AA}$ and $a_{\perp}^* \approx 14.7 \text{ \AA}$. (c) Line profiles recorded along the $\times 2$ streaks for the clean surface and after surplus Au deposition and annealing. The color coding is the same in all graphs.

6.1.4. Si(557)-Au: Single Atomic Chain

The Si(557)-Au surface is among the most studied stepped Si surfaces. Its atomic structure has been thoroughly proven by x-ray diffraction and supported by theoretical studies. [65,228,229] Adsorption of 0.18 ML Au onto freshly annealed Si(557) surface generates a LEED pattern characteristic of a regularly and singly stepped Si(557)-Au surface with considerably improved order compared to the clean surface mainly by a pairing of the Si atoms in the adatom row, which generates sharp $\times 2$ streaks in the LEED pattern. [228,230] The lack of phase coherence between adjacent adatom rows gives rise to a streak like view instead of diffraction spots. The resulting SPA-LEED pattern and the structural model are given in Fig. 6.11. The sharp and round spots represent the Si step train. These spots form an oblique unit cell

for the underlying Si substrate, which has the following size:

$$\underbrace{2\pi/18.9}_{a_{\bar{1}\bar{1}2}} \times \underbrace{2\pi/3.84}_{a_{\bar{1}10}}$$

The splitting of the step train spots in the $(\bar{1}\bar{1}2)$ direction is equal to $\sim 18\%$ of the SBZ, which corresponds to the following step periodicity:

$$5\frac{2}{3}a_{\bar{1}\bar{1}2}/\cos 9.5^\circ = 18.9 \text{ \AA} \quad (6.4)$$

This estimation is in accordance with previous studies on Si(557)-Au. [23, 231] The right part of Fig. 6.11 presents the commonly accepted structural model of Si(557)-Au that has also been used for electronic calculations in this thesis.

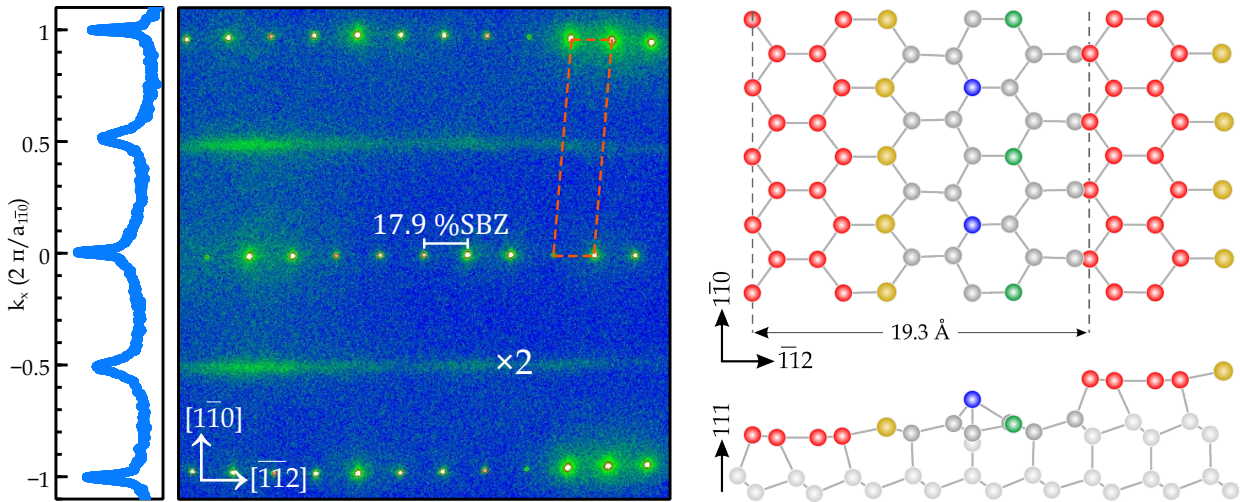


Figure 6.11: SPA-LEED pattern and DFT calculated structural model of the Si(557)-Au surface. SPA-LEED image was recorded at RT after several flash annealing and corresponding Au coverage deposition at 630°C . 1D spot profile recorded through 0,0 spot along the terraces shown in the left side of diffraction image. The dashed orange rhomboid indicates the (1×1) surface unit cell that involves flat (111) terraces separated with single atomic height steps. In the right graph, the yellow, red, blue, and green balls stand for the gold, Si-HC chains, Si-adatom, and Si-restatoms, respectively. Other Si surface and bulk atoms are shown with the gray and light gray balls, respectively.

As all Si(hhk) surfaces, Si(557) also forms Si honeycomb-like chains at the step edges. Additionally, only every second dangling bond at the step edge is fully occupied. [65] Furthermore, Si adatom/restatom rows with a single dangling bond per atom run on the terraces parallel to the Au wires. The latter exists on the pristine surface as well. These free bonds make this surface chemically more reactive with respect to other similar surfaces. [65] Additionally, it has also been shown that increasing the Au coverage a structural transition to the admixture of Si(111)- (5×2) -Au and Si(335)-Au happens along with the de-

velopment of a new metallic band. [185, 199] Further increase of Au coverage ends up with fully covered Si(111)-(5×2)-Au exhibiting a new energy band, which shows a maximum photoemission intensity at Au coverage of 0.39 ML. [173] The electronic properties of this surface were preliminarily studied by Segovia et al. using ARPES. [17] There, the authors observed a half-filled band dispersion only along the atomic chains, crossing E_F with a strong anisotropic 1D metallic character. Since the pristine Si surface is a semiconductor, the observed single band was assigned to Au involving 6s electrons. As shown in Fig. 6.1, the observed single band splits into two branches (here and after S_1 and S_2), which was initially taken as a signature of collective excitation of spinon and holon of a Luttinger liquid. It was also found that these two bands show slightly different band filling, 0.49 for S_1 , and 0.42 for S_2 . [65] However, subsequent high-resolution photoemission data revealed no merging of these two branches at the Fermi level; instead, they cross E_F at two individual points close to the BZ boundary. [29, 65, 232] This latter observation undermined its possible explanation as a Luttinger liquid. Moreover, in a few preliminary studies, this system was found to undergo at LT a Peierls transition, associated with a periodic lattice distortion due to electron-phonon interaction. [232–234] Later on, Nagao et al. measured a single almost linear plasmon dispersion on this surface, which is accessible only with the momentum transfer parallel to the steps proving the anisotropic nature of this surface. [23] Although the authors revealed a strong impact of the exchange-correlation function on plasmon dispersion, the origin of metallic states hosting plasmonic excitation could not be determined. The latter question will specifically be addressed in Section 7.4.3. Moreover, the Fermi surface of this system also exhibits slight wiggling (see Fig. 6.1) that can be interpreted as weak 2D inter-wire coupling and interaction of Au and Si surface states. The band structure of the Si(557)–Au surface is characterized by two states that cross the Fermi level. [235] A gold–adatom hybrid band crosses the Fermi level close to the Brillouin zone boundary. A restatom band crosses the Fermi level with an extremely flat slope close to the Γ point and is thus less relevant in plasmon spectroscopy. Otherwise, this surface remains metallic at low-T, i.e., no metal-insulator transition and/or periodic lattice distortion have been observed as a function of temperature. [236] This finding also eliminated the discussions about periodic lattice distortion and/or the MIT at LT.

6.2. Quasi-1D Plasmons in Si(hhk)-Au

Sample EEL spectra of plasmon dispersion measured for the HCWs surface are shown in Fig. 6.12. In all systems investigated in this thesis, the dispersing loss was only observed along the Au wires. This anisotropy persists under all conditions, i.e., gas adsorption, higher Au concentration. Only faint dispersionless losses have been observed at k_{\perp} , which appears at 200 meV for all systems (see dashed line in Fig. 6.12(b)). Since their intensity drops for $k \rightarrow \infty$ and shows no dispersion, they can easily be assigned to localized states (standing waves) associated with quantum-wells formed perpendicular to metallic chains. An exemplary fit routine to extract data from the loss spectra is shown in Fig. 6.12(c). The exponential decay of background intensity as a function of energy is known as the Drude tail

and is characteristic of the metallicity of these systems. This is mainly due to the multiple inelastic scattering of electrons within the metallic layer and, therefore, proportional to the available charge carrier density at the surface. [237] The Drude tail is also visible in IR absorption spectra. [40,238] The higher dispersion slope and relatively broad line-width of the plasmon loss exclude the possibility of an inter-band excitation. Moreover, its comparatively lower energy excludes an effective contribution from Si bulk. The observed excitation is assigned to the quasi-1D plasmonic excitation confined in the Au atomic wires by noting that similar loss peaks have been observed in several atom-scale metal sheets and wires on silicon substrates. [31, 49, 90, 239, 240] These low-dimensional plasmons should not be confused with edge plasmons of a 3D solid, usually called surface plasmons or surface plasmon polaritons [42, 241, 242], which have finite energy in the limit of long wavelengths, e.g., $k = 2\pi\lambda^{-1} \rightarrow 0$. This starts at $E_p/\sqrt{2}$ for a NFEG and extends to either negative or positive slope as a function of momentum transfer. [241] The strong 1D character of the observed plasmons demonstrates that they cannot emerge from the space-charge layer of the Si substrate. Indeed, in the scope of this thesis, as well as previous works, no dependence of the plasmon energy on the doping concentration (in the range of resistivity of 0.01-1500 Ωcm) was observed.

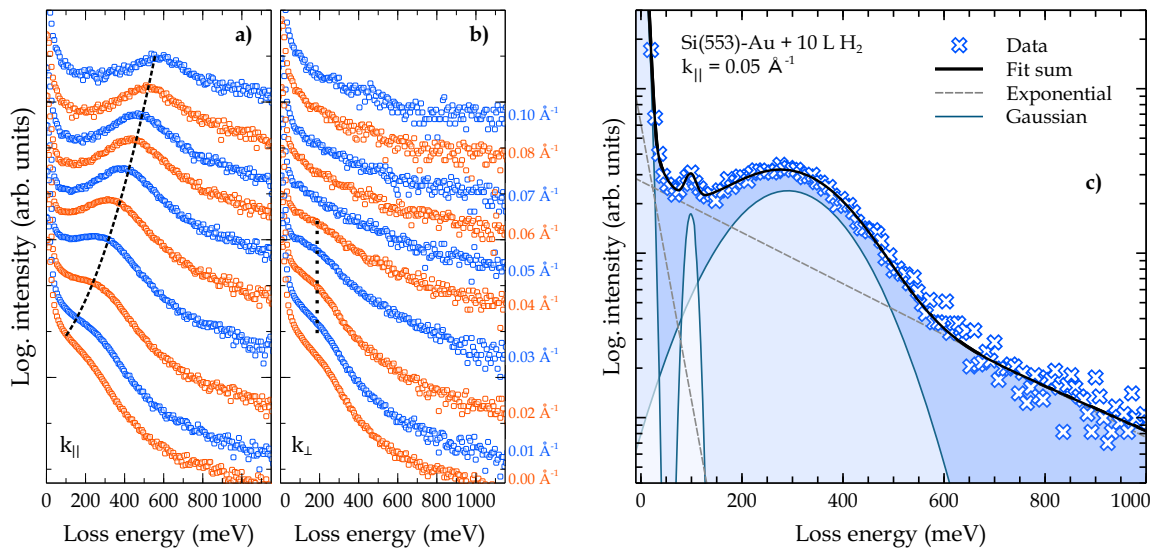


Figure 6.12: Exemplary loss spectra for the HCWs phase on Si(553)-Au recorded at k_{\parallel} (a) and k_{\perp} (b). The spectra were normalized to the elastic intensity and shifted against each other for better visibility. The dashed line in (a) approximates the plasmon dispersion, which could be identified exclusively in the direction parallel to the Au wires. (c) Fitting procedure exemplarily shown for the loss spectrum of Si(553)-Au + 10 L H₂. The plasmon dispersions illustrated in this thesis obtained with the same fit routine. In this particular case, an additional Gaussian function was put to take into account the new loss feature at ~ 100 meV appears after hydrogenation or oxidation. The latter was skipped for the clean surface spectra, where this mode does not exist. Corresponding fit functions are given in the label.

However, the increase in doping concentration has been shown to develop the contribution of the layer of space charge to surface transport. [160] Here, the main difference between surface transport measurements and plasmon spectroscopy plays a crucial role as following: Thus, plasmon spectroscopy turns out to be a valuable tool to get information about the excited state (unoccupied part) of the band structure. Electrical surface transport measurements, on the other hand, probe the detailed electronic properties close to the Fermi level, where contributions from impurity states or space charge layer are inevitable, to which plasmon spectroscopy has little sensitivity, underlining the complementarity of both experimental approaches. To extract the plasmon energy and other parameters, the experimental electron energy loss spectra were fitted with a set of Gaussian functions. Moreover, the Drude background was also considered as an exponential decay. Additionally, the background was subtracted by using an analytical form following Ref. [75].

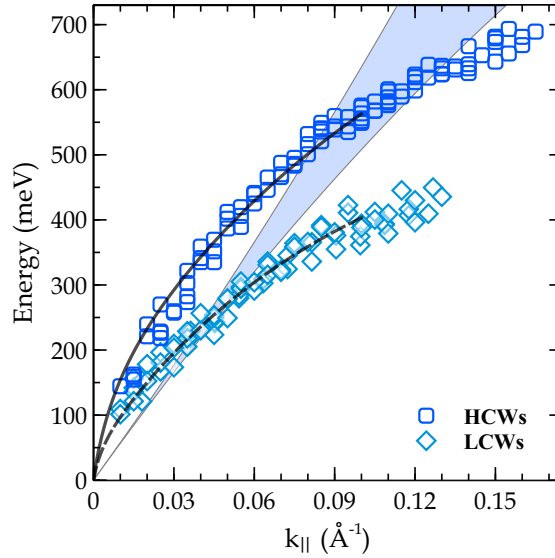


Figure 6.13: Plasmon dispersions for the Au-induced HCWs and LCWs phases on Si(553)-Au. Dispersion curves were partially adapted from Ref. [27]. The blue area shows the electron-hole continuum zone derived from ARPES bands for HCWs phase [65, 206] within the NFEG model (see Section 2.2.1 for the computational details). Plasmon dispersion curves cross the electron-hole continuum, which would generally lead to strong damping of the collective mode due to an electron-hole pair creation.

The measured plasmon dispersion is plotted for both Si(553)-Au systems in Fig. 6.13. Following Ref. [195] the plasmon dispersion of both HCWs and LCWs phases can be qualitatively described by a confined NFEG model of coupled wires. This qualitative fit result is given solid and dashed lines in Fig. 6.13. However, this model fails to describe the fact that the measured plasmon dispersion crosses the electron-hole continuum derived with the same parameters used for the same empiric fit. Obviously, at the highest k_{\parallel} point measured, the plasmon dispersion is even below the electron-hole continuum. In fact, this is impossible, otherwise, no plasmon propagation could be measured because penetration into

the electron-hole continuum leads to strong Landau damping and even to an imaginary solution below this region. This situation is very similar to Si(111)-(5×2)-Au and also to other Si(hhk)-Au surfaces. [31] This discrepancy demonstrates the breakdown of the free electron model. This anomalous behavior of plasmon dispersion can be well understood with the direct comparison between plasmon dispersion and calculated band structure, which will be discussed in the next section.

6.3. Hybridization of Au and Si States: Evidence from Plasmon Spectroscopy

Plasmons excited in a single 1D metallic systems have been predicted to exhibit a linear dispersion at relatively small momentum. [76] However, in reality, Au atomic wires are periodically aligned in an array on the substrate so that coupling to the embedding environment and adjacent chains have to be considered. That requires a multi-wire model constructed by periodically arranged wires with an inter-wire distance of several Angstroms, as investigated in this thesis. Using the single wire model, by switching off the inter-wire interactions, a linear plasmon dispersion can be obtained, as shown by the dashed line in Fig. 2.6. However, it completely deviates from the experimental results. Moreover, as already discussed in the previous section, even a close match between plasmon dispersion and fit curve turns out not to be sufficient to elucidate the electronic properties of such atomic wire systems. Thus, a comprehensive understanding of such systems requires knowledge about the contribution of all surface bands. Such a comprehensive study has been carried for HCWs and LCWs phases on Si(553)-Au surface.

6.3.1. Comparison of the Plasmon Dispersion and Band Structure of Si(553)-Au

For band structure calculations, the double Au chain model suggested by Krawiec [24] was employed for dimerized and nondimerized Au chains (see Fig. 6.15). Details of the band structure calculations were discussed in Ref. [27]. In fact, the calculated band structure without dimerization of Au chains agrees well with previous theoretical works. [24] Additionally, DFT calculations reveal the Si step edge bands (S_4 in Fig. 6.14), which is not visible in photoemission. Moreover, the S_4 bands hybridize strongly with Au bands, $S_{1,2}$, S_3 bands in Fig. 6.14. This hybridization opens up electronic gaps at unoccupied states; the electronic landscape deviates from the free-electron character, which means the parabolic bands observed in ARPES are no longer free-electron like in origin. The absence of S_4 bands in photoemission might be due to intensity overlap between individual bands, which might be related to rapid fluctuations between polarized and unpolarized Si states. [206] Nevertheless, these hybridization result in opening up band gaps of about 0.1 eV, which partly have been observed in some experimental studies. [202,206] One of these gaps is located right at E_F and prevents the S_3 band from crossing the E_F . This is the reason that the metallicity of this surface is dominated by $S_{1,2}$ band. The other gap is opened up between Au bands at about 0.6 eV above E_F . This band is more pronounced in the LCWs phase than HCWs.

Moreover, the position of the S_3 band is different for LCWs and HCWs phase. While it starts at about 0.5 eV above E_F on HCWs, it is found at lower energies for LCWs. [206] This might be due to electron transfer from alternate (5×5) terraces to the Au chains. [27] In addition, the magnitude of the second band depends strongly on the dimerization parameters between Au atoms. [33, 35] The magnitude of the Au dimerization is estimated as $d = (a_1 - a_0)/a_0$, here a_0 is the surface lattice constant and a_1 is the longest Au-Au distance along chains. [25] Thus, the band gap develops by increase of a_1 and/or d . Moreover, the magnitude of band gap is also sensitive to the choice of the XC functional, even without considering spin (see Fig. 8.1). This dependence will be discussed in more detail on the basis of experimental structural results in Section 8. Experimental and calculated band structures are shown in Fig. 6.5.

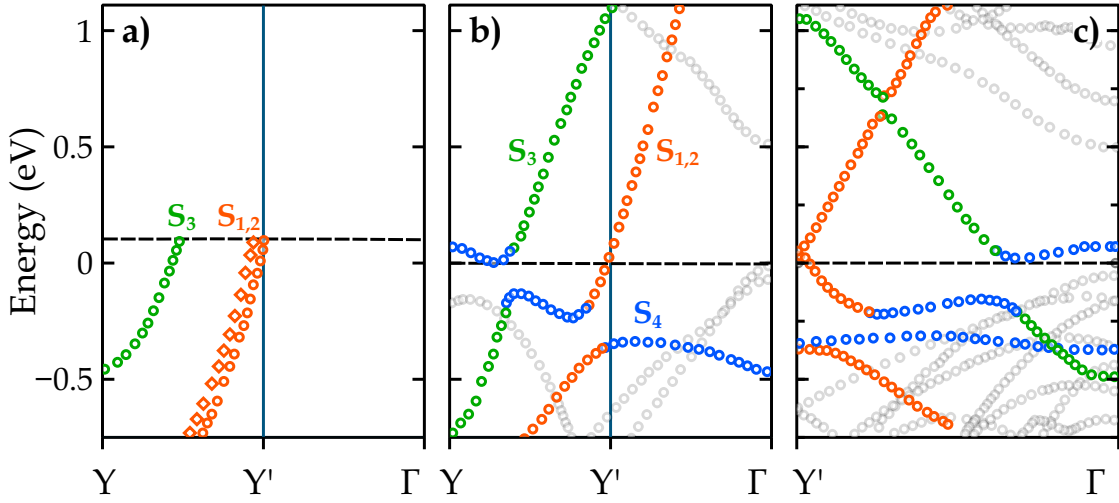


Figure 6.14: Schematic representation of the electronic band structure of Si(553)-Au. (a) as measured by ARPES, for example, in Refs. [65, 206]. Following Ref. [206], the entire measured bands were shifted by approximately 0.15 eV to facilitate the comparison between theory and experiment. The electronic states are labeled as $S_{1,2}$ (orange) and S_3 (green), according to Refs. [65] and [206]. The Rashba split state $S_{1,2}$ is represented by the circle and diamond symbols. The DFT-PBE band structure calculated for the HCWs system is shown in both the extended (b) and conventional (c) Brillouin zone representation. For the sake of clarity, only bands with strong Au character and the Si step edge state S_4 (blue) are labeled. Surface-projected bulk Si bands are in gray. The $\Gamma \rightarrow Y'$ direction is roughly parallel to the Au chains.

DFT calculated band structures for the clean surface with and without dimerization of Au chains are given in Fig. 6.15. The relevance of this hybridization on metallicity has been investigated by means of plasmon dispersion. As already discussed in Section 2.2.1, the close relation of plasmon dispersion with the upper boundary of the electron-hole continuum is relevant for describing the unoccupied part of metallic bands. This was already applied to the Si(111)-(5 \times 2)-Au surface in the previous section. Previously, this description was also employed to other similar systems in Ref. [31], here the same

definition is extended for Si(553)-Au based on new theoretical outcomes mentioned above.

The direct comparison between the plasmon dispersion and calculated band structure has been made by employing Eq. 5.2, as derived in Section 2.2.1. For calculation of ω_+ , the $\omega_-(k_{\parallel})$ has been taken from the band just below E_F , whose k dependence deviates from free electron model due to hybridization with mainly Si (S_4) bands (see Fig. 6.16 as well). In addition, a Gaussian distribution of the electrons in the system with a full width at half-maximum of 6.5 \AA is assumed. This width corresponds to a parabolic confinement with a ground-state width of 2.8 \AA or, approximately, to a square-well confinement of 13 \AA . As tested, the results depend very little on the exact wire width (see Fig. 2.6 in Section 2.2.1). Even changes of the form of the confining potential to a square well yields a correction that amounts to a maximum change of slope of 10% at most at small k_{\parallel} , in agreement with Ref. [81]. The results of these calculations are shown in Fig. 6.15 for both phases.

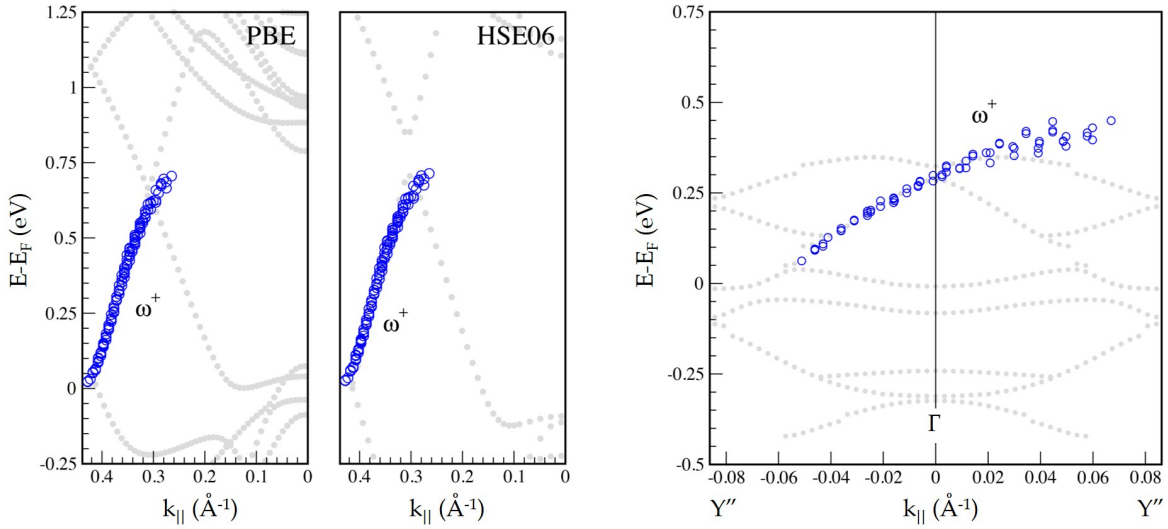


Figure 6.15: DFT calculated electronic band structure (gray dots) calculated without considering spin-orbit (SO) interaction for the Si(553)-Au HCWs phase. The blue circles show the positions of ω_+ calculated from the plasmon dispersion with the procedure described in the text. Left: DFT-PBE calculations without Au-Au dimerization. Middle panel: DFT-HSE06 (Heydt-Scuseria-Ernzerhof hybrid functionals) calculations with Au-Au dimerization. Right: DFT-PBE band structure calculated without SO interaction (gray dots) and ω_+ (blue balls) for the LCWs phase. Adapted from Ref. [27].

As derived in Section 2.2.1, the plasmon dispersion merges into ω_+ , which yields a better match for the HCWs phase than LCWs in the case of the excitation from the Fermi level to the first Au-induced unoccupied band. Moreover, considering the dimerization-induced energy gap at around $\sim 700 \text{ meV}$ above E_F where measured plasmon dispersion also ends, this match becomes even more quantitative. Here, within the HSE calculation, $d = 0.005$ equal to $\sim 150 \text{ meV}$ band gap is considered. This gap was also measured by STS. [208] In fact, the magnitude of the present energy gap nicely fits the flattening

of the plasmon dispersion. The strong curvature at small k_{\parallel} is a clear indication of lateral interactions of wire arrays, as already discussed in Section 2.2.2. This feature also coincides with the interaction with the substrate. Inevitably, finite-size effects in a real system make extrapolation to $E = 0$ at $k_{\parallel} = 0$ impossible. According to the result of the ω_+ calculation, the plasmon can exist up to $k_{\parallel} = 0.15 \text{ \AA}^{-1}$ before decaying into electron-hole pairs. As explicitly shown in Fig. 6.16, the electronic properties of this surface are less or more related to all surface atoms. Although the electron density is mainly confined at the Au-induced superstructure, it is intermixed with all other bands. This delocalized picture of the electron density can be related to other similar atomic wire systems as well.

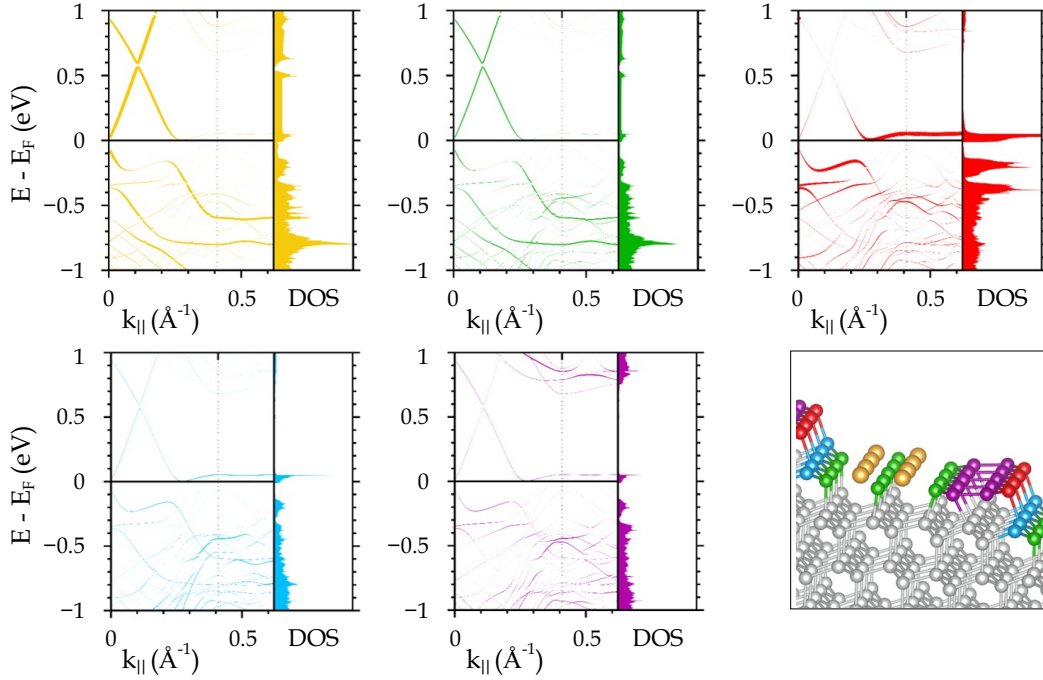


Figure 6.16: Electronic band structure and DOS of the clean Si(553)-Au system. Projections of the bands onto different structural motifs are colored following the lower rightmost panel. The line width corresponds to how strongly the bands are located at the corresponding atom groups. Data was provided by S. Sanna [227].

The same procedure has now been applied to predict the upper boundary of the electron-hole continuum for the LCWs phase. As shown in Fig. 6.15, the extrapolated plasmon dispersion is very similar with those of the HCWs phase, however, with a lower slope. The main difference between these two phases appears in the unoccupied band structure. As shown in Fig. 6.15, in case of LCWs phase, the band crossing at E_F is significantly more curved in the unoccupied section and levels off at a lower energy than HCWs bands. This reduces the dispersion of this band as a whole. As a reason for such low dispersion, the “spill-out” effect, which was originally postulated in Ref. [206] due to unoccupied adjacent terraces, can now be pinned down to a shift of E_F coupled with slight modifications of the

electronic interaction with the ionic potentials. As a result, small changes in the band structure, mainly in the unoccupied part, become obvious, resulting in reduced plasmon frequency. As shown in Fig. 6.15, this result is in satisfactory agreement with the calculated band structure, even though small band gaps of the calculations seem to be ignored. There are several possibilities to rationalize this result. First, there are not only excitations from E_F to the unoccupied states at a given k_F , but also excitations from occupied states to E_F have to be considered.

According to the present band structure calculations, this possibility can be ruled out in the energy range under consideration. Second, the finite lifetime of excited states could smear out the visibility of small band gaps, together with a limited instrumental resolution, both in energy and k -space. Because the band gaps under consideration here are fundamental gaps, k -space resolution plays no role, and energy resolution was much better than the size of the calculated band gaps. Third, there can be a real plasmonic effect in the sense that a sheet plasmon as a collective excitation cannot be formed by strongly localized electrons or by electronic hybrids that localize electrons. In other words, such a hybridization is “ignored” by plasmonic excitations, that is, the projection of a wave function on the nonhybridized delocalized contributions is much more strongly weighted for plasmonic excitations than those more localized. This behavior is observed only for weak hybridization and small band gaps.

6.4. Plasmons on the Si(775)-Au Surface

Sample EEL spectra of the 0.32 ML Au deposited Si(775) surface are given in Fig. 6.17(a,b). Similar to the previous systems, this system also exhibits plasmonic loss only along the chains, which possesses the same features (i.e., exponential decay, broad line width, etc.) as observed for the previous surfaces (see Section 6.2). However, it has lower intensity compared to the Si(553)-Au system, which might be due to the less surface ordering. Plasmonic excitation on this surface has been the subject of recent research. [31] Plasmon dispersion from this surface is given in Fig. 6.17(c). This surface shows a comparable lower dispersion slope. This can be due to the ~ 0.2 eV indirect energy gap at 0.35 eV above E_F as found in DFT calculations (see Fig. 6.18). Nevertheless, the experimental plasmon dispersion is not limited to the end of this band but propagates 150 meV into the band gap.

Its calculated electronic band structure presented in Fig. 6.18. The calculations reveal that similar to Si(553)-Au, the electronic structure of Si(775)-Au is strongly dependent on the structural features. Thus, both the quasiparabolic Au-induced Rashba split $S_{1,2}$ and the S_3 bands strongly hybridize with the Si surface states localized preferentially at the honeycomb chain and the restatoms (see Fig. 6.18). This hybridization leads to a band gap opening in the occupied states and to the result that the S_3 Au-induced band hybridizes with the honeycomb chain in the middle of the BZ around -0.4 eV, whereas $S_{1,2}$ band mixes at slightly higher energy with this state close to the BZ boundary and forms a very small band gap.

In particular, there is a correlation between the Au dimerization and the electronic band gap. The

dimerization shifts the Au related bands upwards by opening a band gap. This hybridization between Au and Si structural elements leads to several weakly dispersing bands also in the unoccupied band structure, which can clearly be identified as those localized at the adatom and restatom Si chains. These hybridizations and the deviations from free electron gas behavior associated with them are the main reason for the inconsistencies using the NFEG model for the description of the electron-hole continuum and the associated plasmon (see Fig. 6.17).

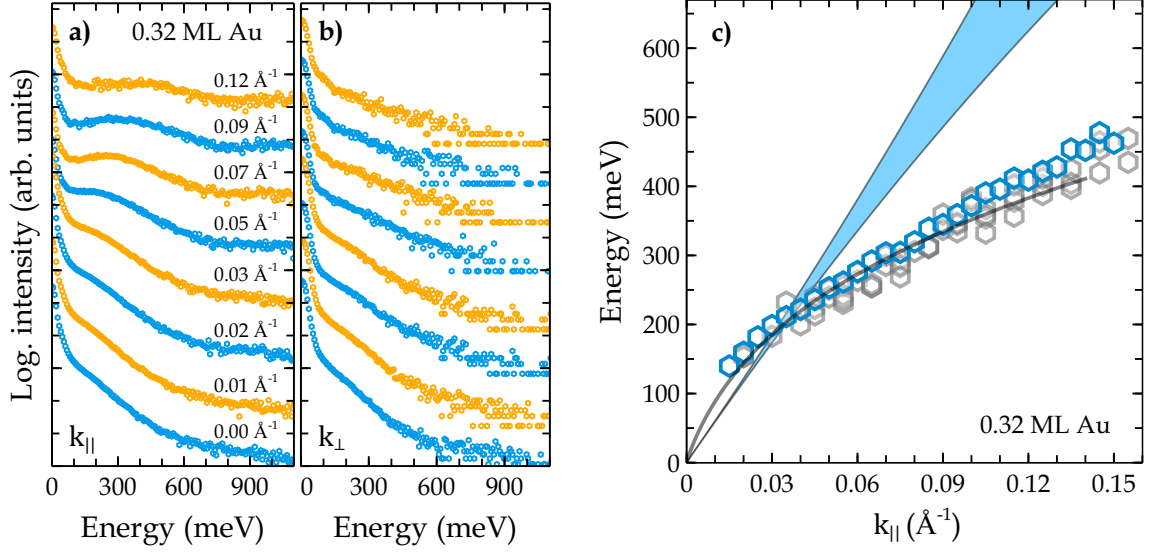


Figure 6.17: Exemplary momentum resolved EEL spectra for the Si(775)-Au OCWs surface measured with a momentum transfer parallel (a) and perpendicular (b) to the wires. The spectra were normalized to the elastic intensity and shifted against each other for better visibility. (c) Plasmon dispersion for the same surface collected from the loss maxima by applying the fit the routine given in Fig. 6.12. The blue area indicates the electron-hole continuum zone derived using the NFEG model, as discussed in Section 2.2.1. The gray data points in (c) are taken from Ref. [31] for comparison.

With these assignments, the crossing relevant for the observed plasmon loss can only be that at $k_F = 0.365 \text{ \AA}^{-1}$. It is also the location where one of the quasiparabolic gold-induced bands should cross. The other crossings may be relevant for further plasmonic excitations, which, due to the small dispersion of the adjacent bands, should have much lower energy and are not observable in the present experiments. For a direct comparison of the plasmon dispersion and calculated band structure, the ω_+ was calculated. For this, the calculated nearly parabolic band close to the BZ was taken as ω_- (i.e., by neglecting the small band gap at the BZ boundary). An effective mass was calculated to $m^* = 0.08m_e$. $V_c(k)$ was derived numerically for a Gaussian periodic distribution of electron density with a width of 6.6 \AA and a wire separation of 21.7 \AA , which corresponds to the average terrace width. Due to the small effective mass and the correspondingly large $A(k)$, ω_+ is almost completely determined by the experimental plasmon dispersion, indicated by black circles in Fig. 6.18. The calculated ω_+ levels off close to 0.5 eV and thus

clearly deviates from the NFEG expectations.

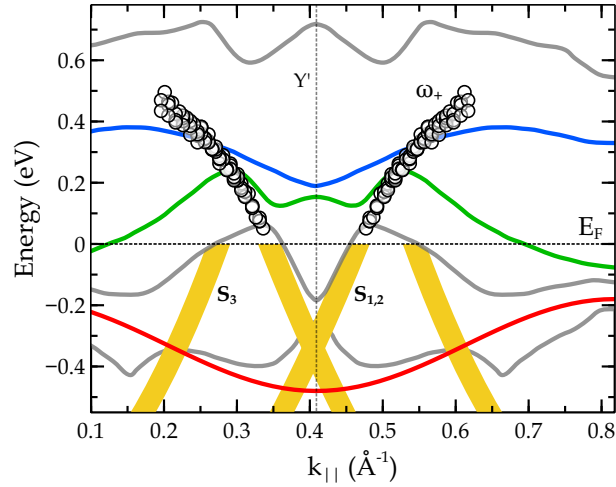


Figure 6.18: Calculated electronic band structure for the Si(775) + 0.32 ML Au surface. Blue, green, red, and gray lines stand for Si-adatom, restatom, Si-HC, and other Si bands, respectively. The yellow bands are fit to experimental ARPES data following Ref. [65]. The black balls represent the ω_+ derived from the experimental plasmon dispersion (details are given in the text). Adapted from Ref. [31].

Comparing with the calculated band structure, this upper edge of the electron-hole continuum determined from Eq.5.2 runs through two band gaps caused by the hybridization described above. Still, it levels off at the lower boundary of the large band gap between the two uppermost bands shown in Fig. 6.18. This behavior is qualitatively similar to the Si(557)-Au system described in Ref. [31], including the tangential approach to the unoccupied band structure in those parts where the group velocities are comparable. Interestingly, the topmost band gap is not crossed, indicating that this gap is likely to interrupt the electron-hole continuum. While there is some uncertainty in the exact location of unoccupied bands as calculated by DFT with (semi-)local potentials, it should be noted that almost quantitative agreement between experiment and simulation for the unoccupied band structure is obtained. However, contrary to the Si(553)-Au surface here, a significant deviation of ω_+ from the calculated electronic band structure was seen. As an example, multiple band crossings of E_F exist for Si(775)-Au and it is not easy to single out the precise contribution of each of these bands because of multiple hybridizations. Nevertheless, most of the associated plasmons are expected to be so low in energy that may not be observed with the actual experimental resolution. The observed discrepancy might have some origin in the calculated model as well: As discussed in Section 6.1.2, the current model fails to explain 1/3 periodicity revealed by diffraction experiments. Moreover, a higher extrapolation of plasmon dispersion at $k \rightarrow 0$ in comparison with the similar surfaces indicates a possible band gap at the Fermi level. However, no such band gap was observed in the calculations. Indeed, a clear sign of such band gap opening was observed after oxidizing this surface (see Section 7.5.2). Therefore, the electronic and structural

properties of Si(775)-Au require further theoretical optimization.

6.4.1. Effect of Au Coverage on Plasmonic Excitation

Following the different Au coverages studied by SPA-LEED, plasmonic excitations at higher Au concentrations have also been investigated. Exemplary EEL spectra obtained for the 0.56 ML gold deposited surface are shown in Fig. 6.19(c,d), which displays the same characteristics as the OCWs surface. Plasmon loss gains 30% more intensity for 0.4, 0.48, 0.56 and 0.64 ML coverage in comparison with the 0.32 ML surface. Up to 0.40 ML, this increase is correlated with the development of the $\times 2$ intensity. A further increase of Au coverage results in a decrease in the loss intensity. Similarly, the decline of $\times 2$ streaks was also observed for Au coverage of >0.56 ML. Noteworthy, plasmonic excitation maintains its anisotropy in all the Au coverages studied. Due to its nearly 2D arrangement (evidenced from DFT calculation in Ref. [214]) at Au coverage of 0.96 ML, plasmon loss in the direction normal to the steps was also expected. However, it turns out that this surface is highly miss-oriented in both directions. This strong anisotropy is also associated with the stepped structure, which is preserved under all conditions investigated (i.e., see Section 6.1.3). Nevertheless, with a momentum transfer parallel to the wires, a comparable weak plasmon loss is still visible (see Fig. B.2 in Appendix). Considering that the $\sqrt{3}$ islands are not metallic (i.e., no loss associated with them was observed), the remaining plasmon can be assigned to a residual from the Au-induced $\times 2$ structures. Additionally, compared to lower coverage surfaces, plasmons on the nearly full coverage surface show higher energy at $k \rightarrow 0$ limit, indicating shorter propagation length. At the k_{\perp} direction, only the dispersionless loss feature at ~ 200 meV was observed, similar to other investigated systems. This loss was observed for different surfaces and assigned to quantum-well states. For hosting plasmon standing waves, they must be ordered metallic structures. Additionally, the spectra recorded at $k_{\parallel} = 0 \text{ \AA}^{-1}$ also shows a faint loss feature at similar energy, which cannot be resolved from the plasmon loss at $k_{\parallel} \neq 0$. This can be related to their quasi-two-dimensional nature.

Although there is no clear description of these structures, it is obvious that additional Au atoms increase their ordering and/or density. This continuously develops up to 0.56 ML. At even higher Au concentrations, change of step density might be the main reason for the destruction of these states and sudden decrease of the loss intensity associated with them (see Fig. B.3 in Appendix). Such distortion of step train was observed in diffraction experiments. Besides, distortion of wire periodicity and/or quality is also manifested as a finite size effect on plasmon dispersion (see Fig. 6.19). Beyond all the effects mentioned above, plasmon dispersion changes significantly as a function of Au coverage. The plasmon dispersion remains almost the same up to Au coverage of 0.40 ML, and it develops rapidly for the following coverage. In general, considering the inverse dependence of plasmon dispersion from effective wire width, the decrease in plasmon dispersion was expected upon an increase in the occupation of the terraces. First of all, this implies that the interaction of electron gas in the adjacent terraces might be developed, which is strengthened by the decoration of steps with Au atoms. However, as revealed

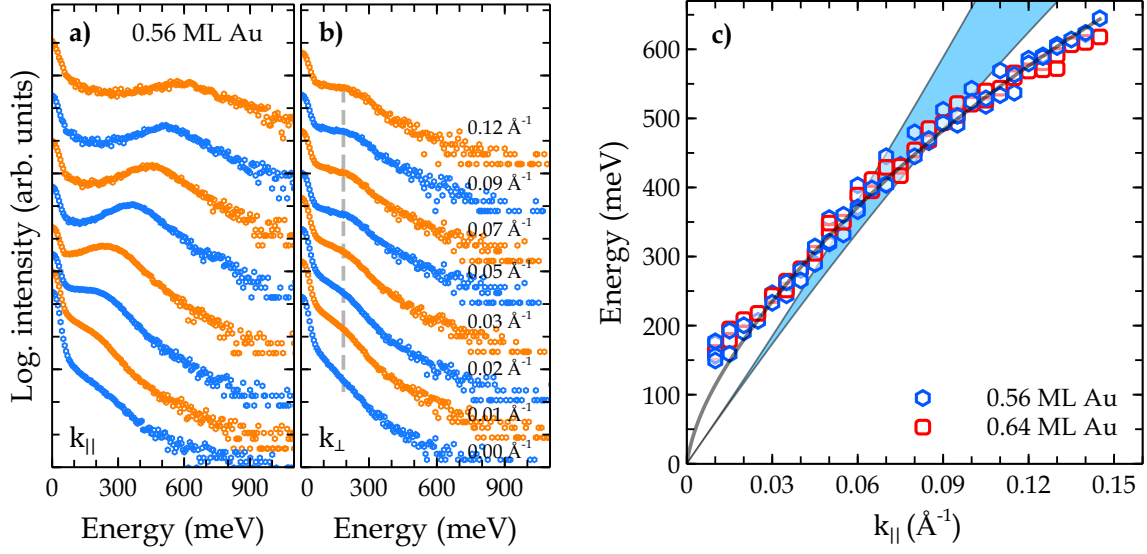


Figure 6.19: Sample momentum resolved EEL spectra for Si(775)-Au measured at a Au concentration of 0.56 ML with k_{\parallel} (a) and k_{\perp} (b) to the wires. The spectra were normalized to the elastic intensity and shifted against each other for better visibility. (c) Plasmon dispersion for the 0.56 and 0.65 ML Au coverages. The blue area depicts the electron-hole continuum zone derived for 0.32 ML surface using the NFE model as discussed in Section 2.2.1. The plasmon dispersions for other high coverage surfaces are given in Fig. B.4.

from the diffraction studies refacetting to the (553) orientation reduces such expectations. The 0.56 ML Au surface shows the plasmon dispersion very similar to the Si(553)-Au surface, however, with higher extrapolation at lower k_{\parallel} , as shown in Fig. 6.19. Its dispersion has 30% higher slope in comparison with the 0.32 ML Au surface. Using Eq. 5.1, the line shape was fitted for obtained dispersion curves. For this again parameters obtained for 0.32 ML surface were used: $n = 3 \times 10^7 \text{ cm}^{-1}$, $m^* = 0.6m_e$. This empirically modified model enables a satisfactory comparison of the effective wire width following Eq. 5.1, as $\omega \propto \frac{a_0}{a} \sqrt{n/m^*}$, where a_0 is a constant for normalization, and a is the effective wire width. This fit yields the following ratio for 0.32 and 0.56 ML Au surfaces: $\omega_{0.32ML} \propto 0.522 \times \sqrt{n/m^*}$, $\omega_{0.56ML} \propto 0.536 \times \sqrt{n/m^*}$. Almost same ratio was achieved for the Si(775)-Au (OCWs) and Si(553)-Au (HCWs) surfaces in Ref. [195]. Although this fit is indirectly consistent with diffraction experiments that support the transformation to the Si(553) facet, plasmon dispersion itself can not be significantly explained. First of all, plasmon dispersion still penetrates the electron-hole continuum. This behavior contradicts the plasmon dispersion described by the theory (i.e., see Section 2.2.1), which predicts that the plasmon dispersion should always be above the upper boundary (ω_+) of the electron-hole continuum. Otherwise, the plasmon decays by emitting electron-hole pair excitations. Correspondingly, the existence of the measured plasmon dispersion requires modification of the electron-hole continuum or band structure itself, which has not been studied for this coverage.

6.5. Temperature Dependence of Plasmonic Excitations

The coupling between electrons (plasmon) and crystal lattice vibrations (phonons) inevitably affects the properties of atomic wires. The electron-phonon scattering establishes the most prominent decay channels for the dissipation of plasmon energy, which is the so-called non-radiative decay. [243, 244] This effect becomes more relevant when discussing finite (nonzero) temperature electronic properties of solid surfaces, which inescapable possess thermally excited lattice vibrations. Surface phonons on Si(hhk)-Au have only recently begun to investigate. [245, 246] The obtained phonons show a comparable lower energy scale than that of plasmon modes, which thoroughly phases out their direct interaction. [247] However, the phonon modes associated directly with the metallic chains might have some relevance. To test such possibilities, low-T measurements were conducted for the Si(553)-Au and Si(557)-Au surfaces. The results are shown in Fig. 6.20.

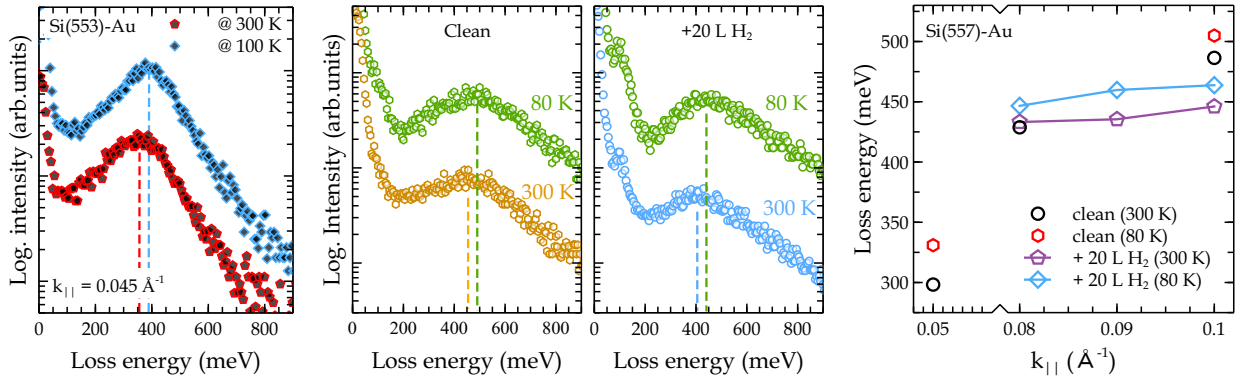


Figure 6.20: Exemplary spectra for the temperature dependence of plasmonic excitation on the clean Si(553)-Au (leftmost), clean and hydrogenated Si(557)-Au surface (middle) recorded at RT and 80 K cooled with l He. All spectra for Si(557)-Au were recorded for the same surface preparation at $k_{||} = 0.09 \text{ \AA}^{-1}$ with the same interaction time (10 min per spectra). To avoid the residual gas (mainly hydrogen) accumulation, the surface was heated up to $500 \text{ }^\circ\text{C}$ before H exposure. The rightmost graph shows several $k_{||}$ points obtained for the clean and hydrogenated Si(557)-Au surface at RT and LT. In this graph, $0.6\text{-}0.8 \text{ \AA}^{-1}$ area is extracted from the x -axis for better visibility.

Both surfaces manifest a slight increase of plasmon frequency and shrinking of FWHM by lowering the sample temperature down to 80 K. Comparing these outcomes with LEED results, it can be concluded that the observed effect is mainly due to the relaxation of surface vibrational modes. Since the observed effect is not so strong and was totally expected, no further experimental studies were continued on this topic. Moreover, the same measurements were conducted for the hydrogenated Si(557)-Au surface. As shown in Fig. 6.20, the blueshift at low-T is visible for the hydrogenated surface as well. This might be due to either the H could not saturate all phonon modes or the phonon modes saturated have no energetic interaction with the plasmon. Some more results from these experiments are given in

Fig. 6.20(rightmost). These results also show that blueshift due to lowering of temperature for the clean and hydrogenated systems has an almost same magnitude, ~ 25 meV in all k_{\parallel} range. This suggests that the observed effect is not due to any change in plasmon bands but must be related to surface relaxation as predicted.

6.6. Summary and Conclusion

In the first part of this chapter, the surface structures of the Si(hhk)-Au systems were verified by using SPA-LEED and compared with structural models. Indeed, the surface structure has an essential role in understanding the whole surface properties, as shown in the rest of the chapter. For example, the adsorbed Au concentration was found to be highly effective in the correlation along and between the adjacent double atomic chains on the Si(553)-Au surface. The extended SPA-LEED investigations on the Si(775)-Au surface also showed the crucial role of the Au concentration in the resulting surface ordering and stability. Thus, on both surfaces, the excess Au coverage deposited at elevated temperature destroys the wire periodicity by introducing a $\sqrt{3}$ structure. Although the (553) orientation is stable at even higher Au concentrations, the (775) surface refacets into the more stable (553) facet. Interestingly, the new (553) facet shows plasmon dispersion identical to the HCWs phase of Si(553)-Au. This finding emphasizes the strong relation between the electronic properties and surface structure (i.e., structural motifs, ordering, periodicity, etc.).

In the second part, plasmon spectroscopy and atomistic DFT calculations were combined to study the origin and nature of metallicity on the Si(hhk)-Au systems. It was revealed that, while the electron density available for plasmonic excitation is mainly confined to the Au-induced chains, the whole surface bands are either placed or hybridized in such a way that each structural motif plays a key role in surface metallicity. The DFT calculations strongly supported this delocalized nature of electron density for the Si(553)-Au surface, as presented in Fig. 6.16. Moreover, the Au related electron wave packets strongly overlap with adjacent Si atoms. The detailed investigation revealed that these interactions of Au-induced and Si surface states are the main reasons that the obtained plasmon dispersions are not compatible with the free electron model. Noteworthy, with the most recent methodology (see Section 2.2.1), which uses the relationship between the upper boundary of the electron-hole continuum and plasmon dispersion, the experimental findings could be reasonably described. Together with the calculated band structures, this formulation revealed a substantial modification of the 1D metallicity on Si(553)-Au due to the hybridization of the metallic Au with the semiconducting Si states. However, its application to the Si(775)-Au system showed a discrepancy between the band structures calculated and the experimental plasmon dispersion. Since the structural model of this system was also found to contradict the experimental diffraction pattern, the observed discrepancy might have an origin in the structural model itself, which requires further optimization.

At the end of the chapter, the effect of temperature on the plasmonic excitation was briefly discussed. Although no strong dependence of plasmon frequency on the temperature was found, a slight blueshift and increased loss intensity reveal the importance of surface relaxation in plasmonic excitation. The information obtained in this chapter will be applied to study the modification of the plasmonic excitation and electronic band structure in the following chapters.

Part III:

Modification of Structural and Electronic
Properties

Chapter 7

Tuning Metallicity by Selective Chemisorption

The present chapter gives insight into the tunability of quasi-1D plasmons in Au-induced atomic wires on Si(hhk) surfaces. Beyond electronic properties, the structural modification upon selective chemisorption will be comprehensively discussed. Following a brief description of the interaction of Si surfaces with additional adsorbates, the oxygen-induced modification of electronic properties will be discussed. The standing wave formation upon oxidation of the Si(553)-Au surface will follow this. The next section will address the extrinsic doping of Au atomic wires with atomic Hydrogen. Before the summary, the H and O-induced modification of the Si(775)-Au surface will be discussed.

7.1. Chemical Modification of the Si Environment

As it is obvious from the previous chapters, the properties of metal-induced wires are strongly related to the coupling between the ultimate chains and the embedded environment. The interaction of Si surfaces with different adsorbates have been studied in many theoretical and experimental works [248–251]. Due to the technological application of Si, most of these studies address oxidation and/or hydrogenation of Si surface either for stabilizing or terminating for further application. In this regard, this study has some significance since oxidation is the first modification that will take place when such samples are brought into the ambient condition. On the other hand, it has also been proven that adsorption of oxygen and hydrogen on the Si surface modifies its electronic properties. The latter mostly shows up as a band bending and/or changes of the energy gap due to charge localization or doping. Indeed, the number of dangling bonds per unit cell makes the Si different surfaces less or more chemically active,

affecting the strength of chemical modification. Therefore, the surface arrangement plays a crucial role in site-specific adsorption and patterned surface functionalization. Regarding this, the Si(hhk) surfaces provide an excellent playground with their highly ordered steps and other atomically ordered preferential adsorption sites. Indeed, the results obtained in this thesis show that all the parameters mentioned above can be beneficial for manipulating the properties of atomic wires on the Si surfaces.

7.2. Robust Metallicity of Gold Atomic Wires on Si(557)

A reconstructed Si(557) surface and anisotropic Au wires were fabricated, as already discussed in Section 4.7.2. Prior to the plasmonic studies, the changes in the surface structure were monitored using a SPA-LEED. Diffraction images for the clean, oxidized, and after annealing of the Si(557)-Au surface are presented in Fig. 7.1. The clean surface diffraction pattern was comprehensively discussed in Section 6.1.4. Notably, oxygen does not change the surface structure or periodicity but mainly increases the background intensity, and the $\times 2$ structure is only barely visible after 25 L O₂ dosage. Please note that a direct link between the $\times 2$ streaks and the plasmon loss cannot easily be constructed since the former originates from the Si adatom chains. Nevertheless, its quality can still be accepted as a reference for the surface quality as a whole. This qualitative change is fully recovered upon annealing the oxidized surface at 900 °C. This surface shows a clear low energy plasmonic excitation whose dispersion is in good agreement with previously published results [23, 31]. A set of sample spectra from the clean and oxidized surfaces are shown in Fig. 7.2. The nearly exponential decay of the structureless background at low k_{\parallel} , known as Drude tail, is a clear indication of metallicity, i.e., of the low-energy continuum excitations within the conduction band(s).

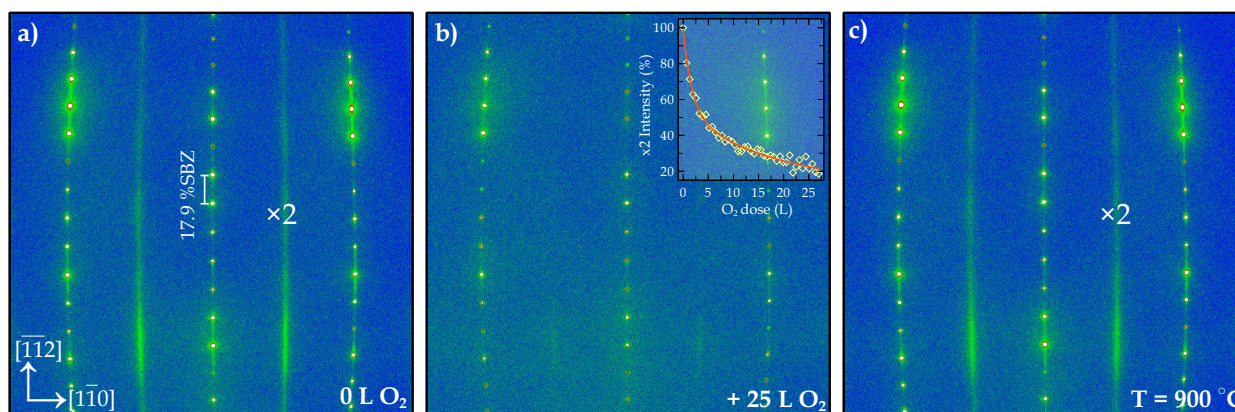


Figure 7.1: SPA-LEED images of the Si(557)-Au surface, freshly prepared (a), upon 25 L O₂ exposure (b), after thermal desorption of oxygen at 930 °C (c). Images were recorded at RT with $E_0 = 138$ eV. The inset in (b) shows reduction of the $\times 2$ intensity as a function of O₂ dose.

The spontaneous dissociation of oxygen is evident from the appearing loss peak at ~ 100 meV, which is due to the formation of Si-O bonds and their vibrational excitation. This peak does not disperse as a

function of momentum transfer and. It also does not react to the direction of momentum transfer (i.e., k_{\parallel} or k_{\perp}). These prove their local vibrational character. This mode has been studied in the literature for the oxygen, as well as water adsorbed Si surfaces. [249, 252, 253] This peak was also observed with infrared spectroscopy (see Fig. 7.8). Because IR transmittance at normal incidence of light is sensitive only to vibrational dipoles parallel to the surface, the Si–O bonds should have an oblique orientation on the surface. It has to be noted that the angular acceptance and energy resolution of the EELS used does not allow to investigate its exact response to minor changes of experimental conditions and to discriminate oxygen and OH related modes or resolve the individual peaks if several peaks are merged. Identification of H and O species on surface was realized using their different desorption temperature, which is $\sim 300^{\circ}\text{C}$ for hydrogen and $> 800^{\circ}\text{C}$ for oxygen (see Fig. 7.17 and 7.2). It was found that this peak can thoroughly be assigned to the H or O-induced modes in the corresponding exposure. Though gas with 99.9% purity has been used in both cases, and special effort was put to assure cleanliness of the gas lines and the UHV chamber. A comprehensive study of this mode is even not required for this work; otherwise, it will go beyond the electronic and structural properties of atomic wires.

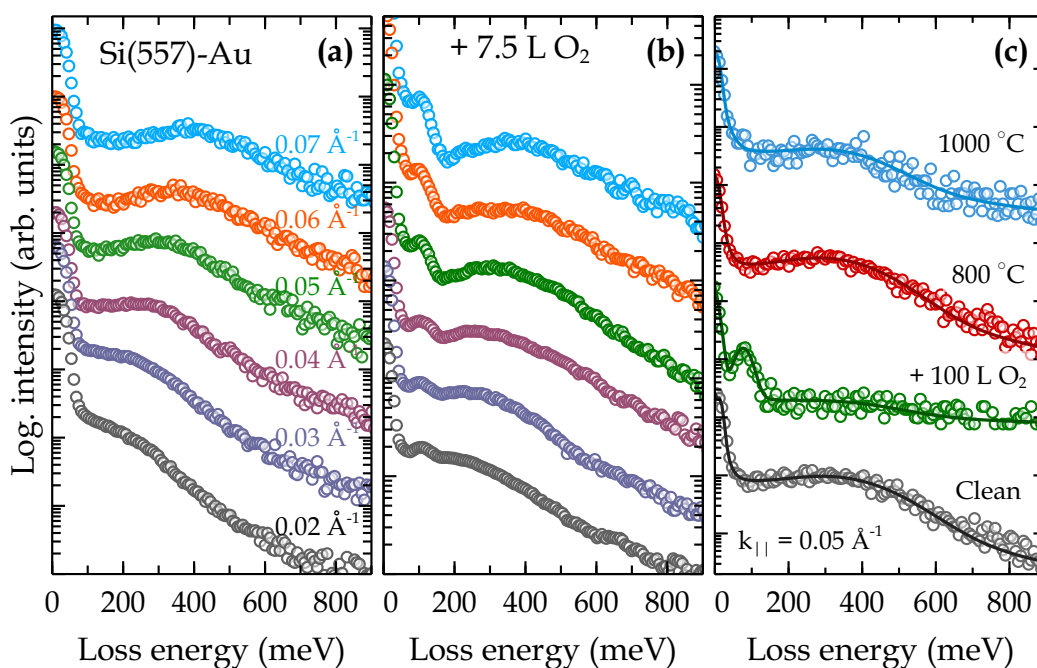


Figure 7.2: EEL spectra of the Si(557)-Au surface, clean (a) and after oxidation with 7.5 L O_2 (b). (c) shows the temperature-driven reversibility of plasmonic excitations on the heavily oxidized surface. In fig (c), the balls stand for experimental data while solid lines show the resulting fit. All spectra were recorded with 20 eV primary energy at RT. The spectra were normalized to the elastic intensity and shifted against each other for better visibility.

Although the increasing oxygen exposure introduces disorder into the surface layer, the plasmonic loss seems to be almost unaffected for the given dosage, as discussed in the following. As illustrated

in Fig. 7.2(c) plasmon loss intensity vanishes after heavy oxidation with 100 L O_2 . Here, collapsing of the surface structure due to disorder induced by oxygen adsorption is a more pronounced effect. The effect of oxygen adsorption is reversible by heating the sample to 800 °C (~ 3 sec), i.e., to a temperature that is still far below the temperature necessary for the destruction of Au-induced superstructures. The oxygen-induced loss at ~ 100 meV vanishes entirely after this annealing step. Furthermore, the blue balls in Fig. 7.2(c) show that a further increase of the annealing temperature to 1000 °C destroys the metallic surface structure as it introduces more scattering.

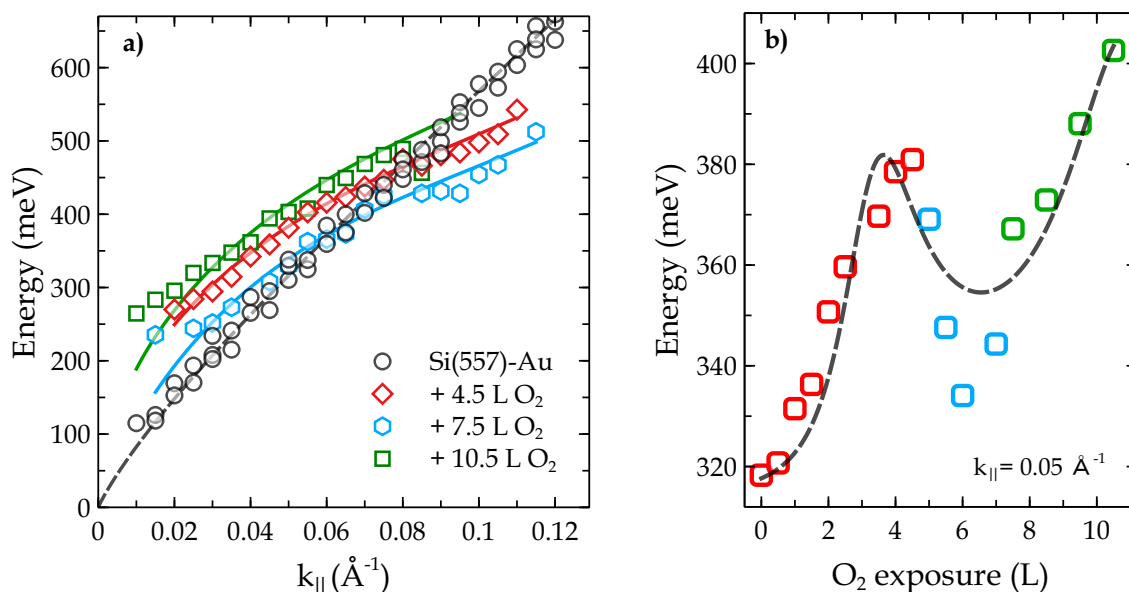


Figure 7.3: Plasmon dispersion for the clean and oxygen adsorbed Si(557)-Au surface (a). (b) Changes in the plasmon energy as a function of oxygen exposure measured at fixed $k_{||} = 0.05 \text{ \AA}^{-1}$. The solid and dashed lines in both graphs have no physical meaning but only serve as an eye guide.

As shown in Fig. 7.3, this surface manifests the most 1D-like plasmon dispersion that barely deviates from extrapolation to zero energy at the $k_{||} = 0$. This well-defined plasmon dispersion makes it highly unique to study the effect of individual bands on the plasmonic excitation or metallicity. Previous surface conductance measurements showed that conductance in the direction along the wires decreases by about 20 % within the first 10 L of oxygen exposure [231], followed by a slow reduction of an additional 10 % up to an exposure of 35 L. Thus, metallicity is not lost by oxygen exposure, but a clear decrease of the plasmon loss energy upon exposure to oxygen was expected. Oxygen adsorption at room temperature, however, turned out to partly even increase the plasmon loss energy. Oxygen adsorption showed a rather nonmonotonic effect on plasmon frequency. These results are summarized in the measured dispersion curves shown in Fig. 7.3. Compared to the pristine system, the curves obtained after various doses of oxygen are less dispersive. Thus, the data points after oxygen exposure are below those of the pure system at high $k_{||}$ and above them at low $k_{||}$.

Furthermore, the nonmonotonic shift of the dispersion curves as a function of oxygen exposure is remarkable and needs to be explained. While this overall change of slope can only be caused by significant changes in the band structure (see below), oxygen dissociation and adsorption also introduces an increasing degree of disorder into the system, as already mentioned. Hence, scattering probabilities of plasmonic waves are increased up to the limit of total reflection and the formation of standing waves. Consequently, deviations from the "ideal" curve, particularly at low k_{\parallel} , are expected, leading to finite loss energies in the limit of $k_{\parallel} = 2\pi\lambda^{-1} \rightarrow 0$. This behavior can clearly be demonstrated for the two higher (7.5 L and 10.5 L) concentrations of oxygen. Almost ideal behavior is indeed seen for the pure Si(557)-Au system, in which dispersion goes to zero in the long wavelength limit within experimental uncertainties (dashed line in Fig. 7.3(a)). For the oxygen covered surface, however, extrapolations of the data to $k = 0$ always end at finite energies. In order to visualize the deviations from the system without disorder, the solid lines were inserted schematically through the data points at various stages of oxidation, assuming that the curves have to start at the origin.

7.2.1. Oxygen-Induced Electronic Modifications

For a quantitative analysis of the plasmon dispersion as a function of oxygen adsorption, the close relationship between the plasmon dispersion and upper boundary of the electron-hole continuum is exploited, which for quasi-1D systems turns out to be particularly simple as demonstrated in Section 2.2.1. As discussed there, if the quasi-1D array of wires is considered as a 2D electron gas that is confined to wires of finite width by an appropriate potential, the plasmon dispersion for a single isolated wire can be expressed as a function of the upper and lower boundary of the electron-hole continuum of excitations ω_{+} and ω_{-} , respectively, following Eq. 5.2. As shown below, this relation sets important boundaries to the validity of certain models regarding the modification of the electronic band structure. In order to get an idea of the modifications of the band structure by dissociative oxygen adsorption, band structures for the stable adsorption geometries determined in Refs. [35, 231] have been calculated by the group of S. Sanna. The optimized structural model is shown in Fig. 7.4 has been used for band structure calculations. A complete row of oxygen adatoms has been adsorbed in all cases. As shown there, O adsorption at the Au sites is unfavorable, whereas Si-adatom and the Si-HC sites are strongly preferred with binding energies up to 8 eV. This site-specific adsorption behavior for oxygen already explains the changes of the LEED patterns and disappearance of the $\times 2$ diffraction spots upon adsorption since it destroys adatom pairing. There are several sites with comparable binding energies: Initially, the Si-HC site is less favorable by only about ~ 250 meV compared to Si-adatoms, which leaves it to kinetics which sites are occupied first with high preference. This statement remains valid for higher average concentrations of oxygen, as tested, e.g., by comparing oxidation of restatoms and HC sites after complete oxidation of the adatom row. The band structures of the Si(557)-Au after oxidation of various structural motifs are shown in Fig. 7.5 in an extended zone scheme, but only those bands with clear contributions from the Au chain, adatoms, rest atoms, and the HC chain. In Fig. 7.5(a) the complete adatom row has

been oxidized. As expected, modifications of the bands associated with the adatoms and the restatoms were observed due to the admixture of oxygen orbitals, but changes to the band with preferential Au character are surprisingly small, as obvious by the comparison with the bands of the pure Si(557)-Au system, which is shown as thin lines in Fig. 7.5. There is still only this one band crossing the Fermi level, and the Fermi wave vector slightly changes from 0.35 \AA^{-1} to $k_F = 0.37 \text{ \AA}^{-1}$. These changes get stronger with increasing oxygen concentration, as seen in Fig. 7.5(b). Although the configuration of Fig. 7.4(c) is energetically not very favorable, i.e., these sites will only be filled after those shown in Figs. 7.4(a) and (b), it was used to test the effect of oxidation of Si atoms in the immediate vicinity of the Au chain. As seen in Fig. 7.5 (c), even under these conditions the system remains metallic.

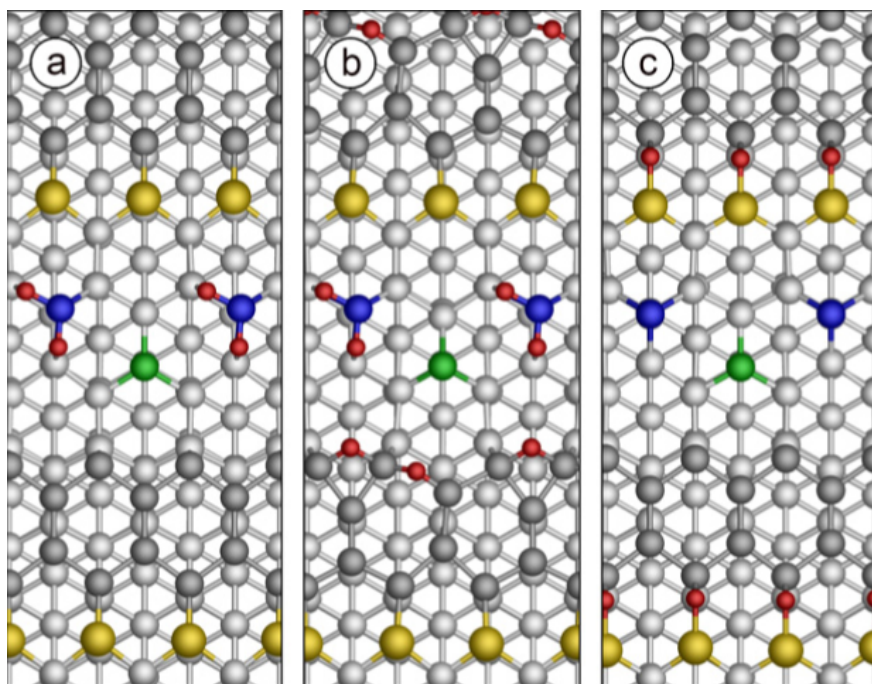


Figure 7.4: Geometrical models of the oxidized Si(557)-Au system. (a)–(c) Oxygen adsorbed at the Si-adatom, adatom and honeycomb chain, and between the honeycomb and Au chain, respectively. Yellow: gold chain, gray: topmost Si atom layer, dark gray: Si honeycomb chain (upper edge corresponds to step edge), blue: Si adatom row, green: Si rest atom row, red: oxygen atoms.

Turning now to the analysis of the plasmon dispersion and its relation to the boundaries of the electron-hole continuum, ω_+ and ω_- , the analysis is similar to the pure system and unique since only one band is crossing the Fermi level in each Brillouin zone. Here, the lowest possible excitations from the occupied bands to the Fermi level, which corresponds to ω_- , were determined from the calculated band structures shown in color in Fig. 7.5. In this case, ω_- corresponds to the excitations from the band marked by a thick dashed line at negative energies to the Fermi level. ω_+ is determined by using these values of ω_- together with the experimental dispersion ω_p obtained as the average values of the exper-

imentally determined plasmon dispersion curve at each k_{\parallel} point. Furthermore, for calculating $A(k_{\parallel})$, a Gaussian distribution of the electrons in the system with a FWHM of 3.3 \AA was assumed, corresponding to a single atomic wire. This width corresponds to parabolic confinement with a ground state width of 1.4 \AA or, approximately, to square-well confinement of 6.6 \AA . These parameters, together with an effective mass m^* at E_F , determine $A(k_{\parallel})$. As tested, the results depend very little on the exact wire width (i.e., see Fig. 2.6). The effective mass close to E_F was determined by approximating the band for ω_- by a parabola near E_F . For example, an effective mass of $m^* = 0.23 m_e$, for the case of adatom oxidation. The calculated ω_+ is shown in Fig. 7.5 as yellow lines. Thus, ω_+ , indicated by the thick dashed line above E_F , closely coincides with ω_p except near E_F . As already seen for the unoxidized system [31], the small band gaps found in the calculations due to hybridization of the Au-induced band with the various structural elements of the Si surface are integrated over in ω_+ , and the dashed line resembles that of a free electron-like band, similar to the clean surface. Only the average slope in the quasi-linear section above E_F is about 15 % lower than in the pure system, as indicated by the thin dashed line in Fig. 7.5(a). The lower average slope at larger k_{\parallel} reflects the lowering mainly of ω_+ , as just discussed. However, there is also a slight change of curvature in this calculated dispersion. A more detailed comparison between clean and oxidized surfaces is shown in Fig. 7.5(d). For adatom oxidation, it is marked as a blue line. As shown in Fig. 7.5(d), the crossing of the oxidized surface plasmon dispersion of the clean surface is also reproduced in these calculations.

Similar procedures have been applied to the other models for the oxidation of this system, i.e., oxidation of the HC chain near the Au chain (Fig. 7.5(c)) and the simultaneous oxidation of adatoms and the HC chain (Fig. 7.5(b)). While the band structure exhibits significant changes, depending on the location of Si oxidation, there is also a varying net charge transfer, which results in up and downshifts of the Fermi level. This seen as shifts of the whole band structures relative to the unoxidized band structure in Fig. 7.5. Nevertheless, the overall behavior of the upper edge of the excitation spectrum changes remarkably little and is still determined by the metallicity of the Au channel. An exception in this respect is the opening of a small gap at E_F when both adatoms and HC chains are oxidized. However, this gap opening is highly sensitive to the model geometries. Therefore, it is quite unclear to what extent such a gap opening will be relevant in experiment. The gap, indeed, may further be smeared out by disorder in the system. The band structures of Figs. 7.5(b), and (c) have the opposite effect on the plasmon dispersion compared with the oxidation of the adatoms alone, as shown in Fig. 7.5(d). A tendency to increase plasmon frequency at low k_{\parallel} is observed, yet the curves for the oxidized systems intersect that of the pure system at $k_{\parallel} = 0.1 \text{ \AA}^{-1}$. Comparing these simulated results with the measured plasmon dispersions as a whole, apparently, the nonmonotonic overall shift is qualitatively reproduced in the calculations, assuming that the Si HC chain first oxidizes together with the adatoms, but with a preference of adatom oxidation, while further elements of the surface follow at a later stage. Due to the limitations of the atomistic models, the semiquantitative agreement between simulations and experiments can be considered as satisfactory. Due to the periodic boundary conditions, a complete and ordered array of oxygen

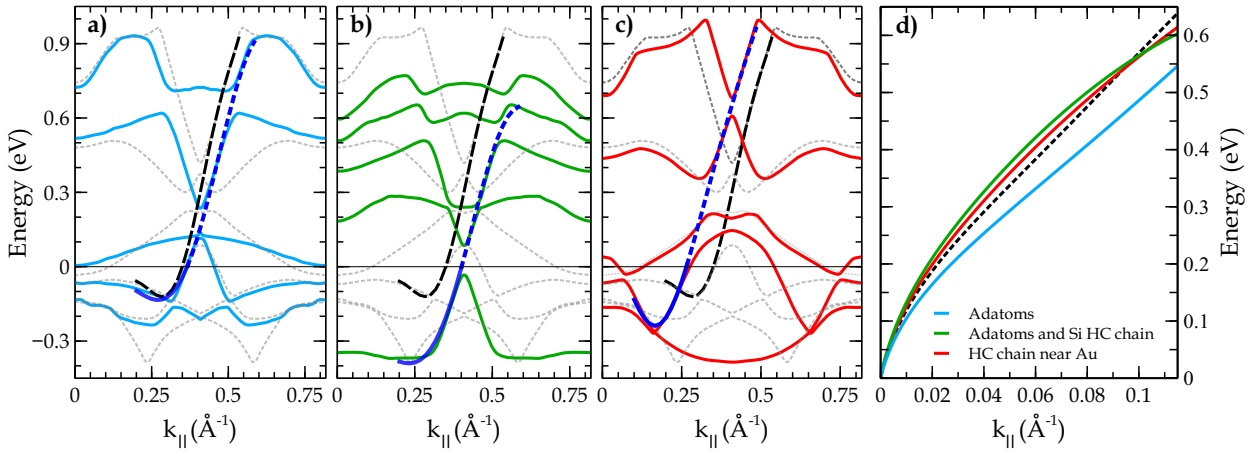


Figure 7.5: Band structures calculated in an extended zone scheme along $\bar{\Gamma}\bar{Y}$ (\bar{Y} at 0.82 \AA^{-1}) according to the structural models shown in Figs. 7.4(a-c). Thin lines correspond to the band structure without oxygen, and thick lines depict the modified bands after oxidizing the corresponding structural motif. a) Adatom row oxidized, b) adatoms, and Si HC chain oxidized, c) Si HC chain near Au chain oxidized. Solid blue lines below E_F in all graphs correspond to the assumed ω_- . The dashed black lines (same in all graphs) show the projection of the metallic band for the clean surface, and dotted blue lines show the same bands after corresponding oxidation. Fig.(c) shows the modifications of plasmon dispersion, as predicted from band structure calculations and the theory according to Eq. 5.2 after local adsorption of atomic oxygen at the various sites, indicated in the legend of (d). The black dashed line represents the clean surface plasmon dispersion.

adatoms is simulated. Thus, this model neither considers the mixture of adsorption sites that will necessarily happen in the experiment nor the disorder introduced by (more or less) random adsorption. The simulations, however, describe nicely the observed robustness of metallicity in the system. The presented plasmon spectroscopy results complement measurements of dc conductance in this system [231]. A reduction of conductance as a function of oxygen dose and the transition from anisotropic to isotropic conductance was found, while total conductance was only reduced by about 20% within the range of oxygen exposure considered here. These results, which at first sight seem to partially contradict those presented here, mainly illustrate the complementarity of plasmon spectroscopy and dc conductance measurements for several reasons: DC conductance mainly probes electronic states very close to the Fermi level, typically in the energy range of $k_B T$ set by the sample temperature, since electric fields are normally very weak. [160] It is also very sensitive to changes in charge transfer and band filling close to E_F . Furthermore, charge carrier mobility enters directly dc conductance that is strongly influenced by disorder. Therefore, dc conductance is highly sensitive to disorder in the system. In addition, the contribution of space charge layers to the overall conductance cannot be excluded. The situation is very different when plasmons are used to probe conductance. The unoccupied states accessible to plasmon spectroscopy experimentally are above 100 meV up to 1 eV. The position of plasmon losses is thus quite

insensitive to small changes of the Fermi level, in contrast to dc conductance. Second, disorder changes plasmon frequencies only at small k_{\parallel} , which can be treated as a correction. Furthermore, the plasmons studied here are derived from surface states. Thus, there cannot be any contribution from space charge layers. Both methods found that metallicity is altered in this system, but it is not destroyed by oxidation. The degree of measured changes, however, is specific to the method used.

7.3. Oxidation of the Si(553)-Au Surface

The room temperature SPA-LEED patterns from the freshly prepared and oxidized HCWs surface are shown in Fig. 7.6. Contrary to the effect of hydrogenation (see Section 7.4.2), oxygen adsorption occurs in a random fashion and inevitably induces disorder in the system. Interestingly, no qualitative changes of diffraction patterns are observed by adsorption of oxygen, even at an exposure of 200 L, as shown in Fig. 7.6. Only the intensity of the $\times 2$ streaks is reduced, and their FWHM in the $[1\bar{1}0]$ direction increases, as shown in more detail in Fig. 7.6. In other words, oxygen adsorption distorts the long-range order of the Au chains and breaks them into smaller sections. The reduction of the average chain length is evident from the FWHM of $\times 2$ streaks (see Fig. 7.6(c)). The average correlation length in chain direction was estimated from the inverse half-width, which is reduced from $\sim 180 \text{ \AA}$ to $\sim 70 \text{ \AA}$ after 3 L O_2 exposure.

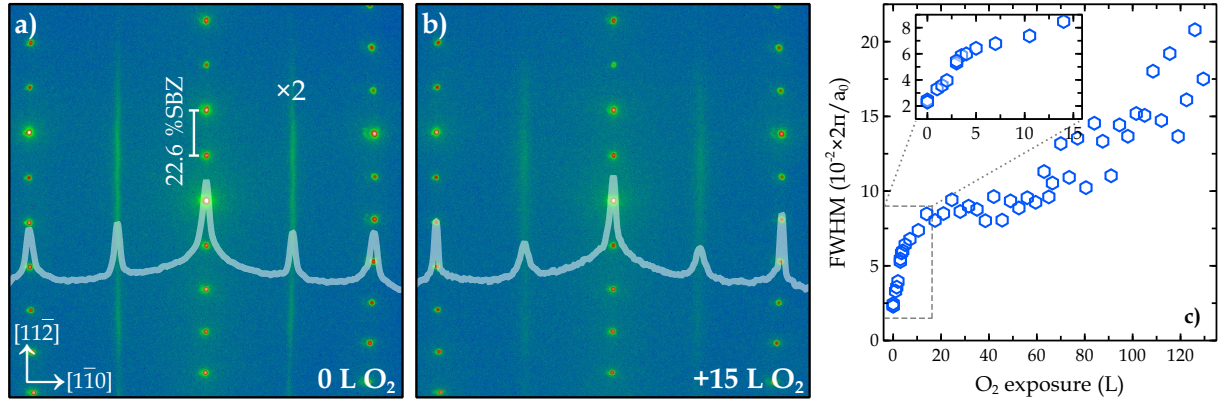


Figure 7.6: SPA-LEED patterns of the HCWs phase of Si(553)-Au and after oxidation. Primary energy: 138 eV. Line scans (white lines) were generated by integrating the intensities along $[11\bar{2}]$ for each k point along the $[1\bar{1}0]$ direction and normalization to the central intensity. c) Dependence of the full widths at half maximum of the $\times 2$ streaks along the $[1\bar{1}0]$ direction on oxygen exposure. Inset: magnification of the initial section. FWHMs from 1D scans have been obtained by applying the fit procedure described in Fig. 6.7.

The consequence of such a destruction of metallic chains is an increased scattering rate also for plasmons, which on the wires can only be backscattered. Therefore, standing plasmonic waves on shorter and shorter sections of the Au wires are formed by increasing oxygen concentrations, and dispersing

plasmons can only exist for wavelengths shorter than these limits. As a result, the dispersion close to $k_{\parallel} = 0$ disappears for larger and larger sections.

The typical loss spectra as a function of k_{\parallel} from the HCWs phase are given in Fig. 7.7(a). In both LCWs and HCWs phases, this dispersing loss can only be observed along the Au wires. Similar to the previous systems, the exponential decay of background intensity as a function of energy is known as the Drude tail and is characteristic for the metallicity of these systems. Exemplary loss spectra after oxidation of this surface with 105 L O_2 are shown in Fig. 7.7(b). The broadening of the loss curve after oxidation is obvious from these spectra. Again the appearance of a new dispersionless loss at ~ 100 meV proves the oxygen binding to the surface. Fig. 7.7(c) shows exemplary spectra recorded in the k_{\perp} direction, which proves that the anisotropy of the whole surface is preserved upon oxidation.

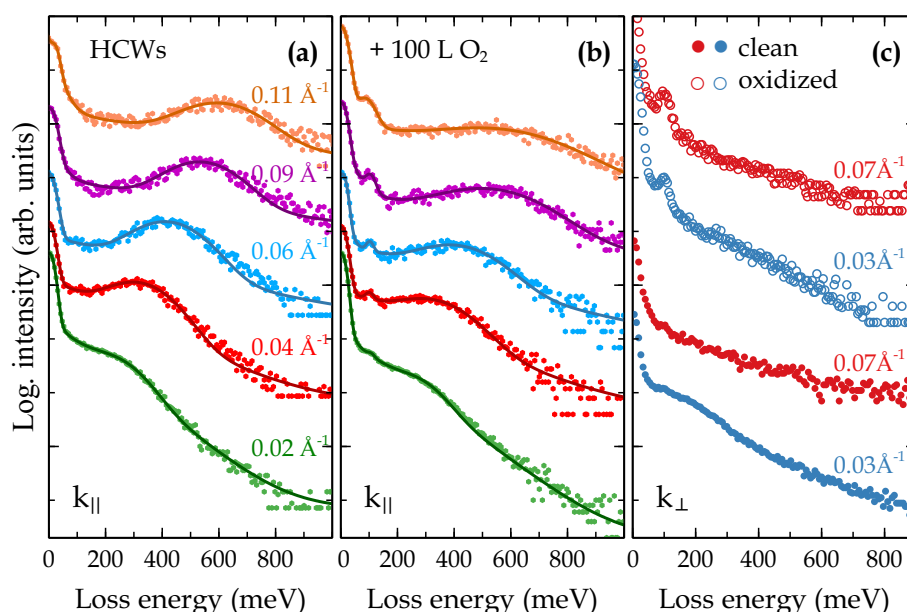


Figure 7.7: Sample electron energy loss spectra from the clean Si(553)-Au HCWs phase (a) and same surface after oxidation with 100 L of O_2 (b). Both data sets were measured with k_{\parallel} along the wires. (c) Comparison of clean (bottom) and oxidized (top) EEL spectra at the two k_{\perp} values indicated. The solid lines are from the fit as depicted in Fig. 6.12. The spectra were normalized to the elastic intensity and shifted against each other for better visibility

An overview of the plasmonic excitations on the clean Si(553)-Au surface, demonstrating their close relation to the unoccupied band structure, was given in Section 6.3. The plasmon dispersions for the clean HCWs surface and after oxidation with various amounts of oxygen are shown in Fig. 7.9. However, upon oxidation, the plasmon dispersion deviates from this extrapolation at $k_{\parallel} \rightarrow 0$, and the onset of deviation shifts to higher k_{\parallel} with increasing O_2 dosage. For $k_{\parallel} > 0.05 \text{ \AA}^{-1}$, the dispersion is insensitive to oxidation up to an exposure of 100 L within error margins characterized by the scatter of data points in Fig. 7.9. A general reduction of the plasmon dispersion was only observed above the dosage of 100 L,

but even at exposure to 200 L, it was only around 15 % with respect to the clean surface. Previous DFT studies of the oxidized Si(557)-Au system showed that the adsorption of oxygen molecules at Au sites is highly unfavorable. [35, 231, 254] Even direct binding of oxygen atoms with the Au chains is very unfavorable so that only the Si surface atoms are oxidized. Since the local structure of Si(557)-Au, apart from the Si adatom/restatom chains, is quite similar, this result should also hold qualitatively for the Si(553)-Au system. Thus, electronic changes of the wire properties should only occur by indirect interaction, similar to the Si(557)-Au surface. However, contrary to Si(557)-Au, oxygen-induced disordering is much more pronounced in Si(553)-Au than indirect modification of plasmon dispersion due to charge transfer and/or localization. Therefore, this effect on plasmon dispersion has been studied in more detail.

7.3.1. Plasmon Standing Waves by Oxidation of Si(553)-Au

As already discussed in the previous section, exposing atomic wire systems to oxygen inevitably distorts the chain order resulting in finite-size formation. This behavior is reflected by an increase of plasmon loss energy as a function of oxygen exposure at small k_{\parallel} , as shown in Fig. 7.9(b) for $k_{\parallel} = 0.02 \text{ \AA}^{-1}$. This is in contrast to the behavior at large k_{\parallel} , where the plasmon loss was found to be constant over a wide range of exposures and finally decreases above 100 L of O_2 exposure as exemplarily shown in Fig. 7.9(c) for $k_{\parallel} = 0.09 \text{ \AA}^{-1}$. The interpretation of the EELS data at small k_{\parallel} is supported by the infrared transmittance experiments.

Plasmonic Excitations with IR-Spectroscopy — While plasmonic excitations in the long wire sections can be investigated via EELS, plasmons resonance in shorter wire sections can be studied by IR spectroscopy. The shortening of the chain length further limits the electron motion in the chain direction and forms standing waves. This kind of standing wave is classified as localized surface plasmon (LSP). Due to the anisotropic nature of the atomic wires under investigation, the localized mode maintains its longitudinal fashion with the polarization parallel to the wires. The plasmon frequency can be tuned by varying the wire length and spatial distribution in a 2D array. Thus, depending on the wire length, plasmon resonance can be optically detectable due to strong electromagnetic field enhancement. Besides, the ends of the short chains serve as an additional momentum source. Previously, IR spectroscopy has been employed to investigate the atomic wire plasmons with a high spatial resolution (8 cm^{-1}) at zero momentum. [40, 93, 255] Fundamentally, the plasmonic excitation for finite length (L) wires can not be formed with wavelength (λ) longer than $2L$ ($\lambda_{max} = 2L$). Namely, the resonance frequency of the optically excited standing waves related to the plasmon energy at the corresponding momentum (q_k) via $q_k = \pi/L$ in the plasmon dispersion. [255] Therefore, the absorption spectra can directly be compared with the plasmon dispersion to estimate the chain length.

In the present work, IR-absorption spectroscopy was used as a complementary method to investigate standing wave formation after oxidation of the Si(553)-Au surface. IR experiments were conducted in

the group of Prof. Dr. Annemarie Pucci at the University of Heidelberg.

The resulting relative transmittance IR spectra from the as-prepared and oxygen-exposed Si(553)–Au surfaces are presented in Fig. 7.8 for HCWs and LCWs phases, respectively. Strong absorption is only seen for polarization parallel to the wires (in the $[1\bar{1}0]$ direction), which reflects the anisotropic metallicity of self-assembled Au wires. The observed absorption feature is associated with the low-energy plasmonic excitation in metal-induced atomic chains, as studied previously by IR-absorption spectroscopy [93,176,255] for different surfaces. The weak absorption signal around 950 cm^{-1} appears upon oxygen adsorption that was observed with EELS as well (see Fig. 7.7). It is attributed to Si–O stretch mode and provides evidence for dissociative adsorption of oxygen [253,256]. As a function of oxygen exposure, a gradual shift of the absorption minimum to higher wavenumbers accompanied by successive broadening is seen in Fig. 7.8(a). As already suggested for the pure system, [93,257] the absorption minimum is mainly sensitive to the average chain length relevant for plasmon propagation. At the same time, the absorption width also reflects changes in the length distribution.

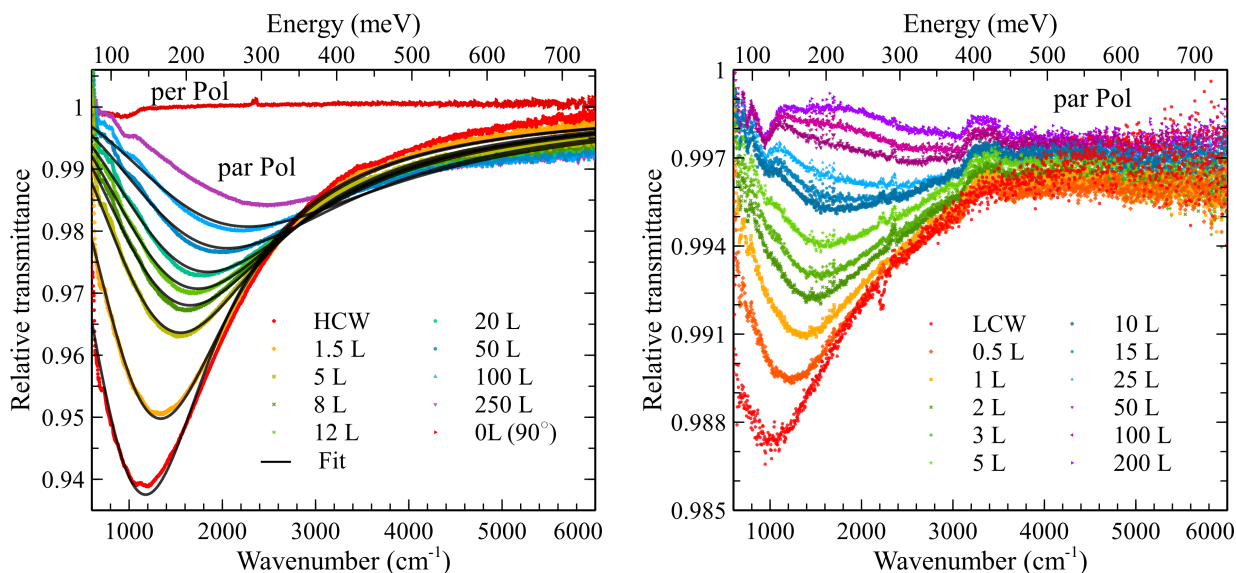


Figure 7.8: Relative transmittance spectra for the oxidation of the HCWs (left) and LCWs (right) phases on Au-Si(553). Relative spectra were obtained by referencing the spectrum to the pristine surface (measured before Au evaporation) from the spectra of Au wires on Si. Solid lines represent the fit from the formula, as described in Appendix A.

Therefore, the observed shift of the absorption minimum indicates successive shortening of the average wire length, while the increasing absorption width is indicative of the widening of the distribution of wire length as a function of O_2 exposure. The spectral shape, especially the plasmonic resonance position of the HCWs wires, was investigated by fitting the data according to Refs. [108,258] (Please see Appendix A for the brief description of the fitting model). With this assumption, the energy of the IR absorption minimum with the energy of the ground state of a plasmon standing wave on wires

with an average length L was identified. As mentioned above, This wavelength ($\lambda_{max} = 2L$) cannot be exceeded at a given oxygen concentration so that no dispersion is possible for smaller k_{\parallel} . Therefore, the energies of the IR absorption minimum corresponds to the plasmon energy at k_{\parallel} values as the intersection of a non-dispersing state of this energy with the actual dispersion shown in Fig. 7.9. For this, it was further assumed that the wavelength at this k_{\parallel} value is that of the plasmonic ground state; that is, the wavelength is twice as long as the average wire. This average wire length is plotted in Fig. 7.10 as half of this maximum wavelength. The initial value of about 31 nm effective length without oxygen is in good agreement with the result obtained in Ref. [93]. Oxidation, which happens mainly on the HC chains at step edges, [35] still has a significant influence also on plasmon scattering by defects, which strongly increases so that the effective wire length for plasmons decreases correspondingly, as shown in this Fig. 7.10.

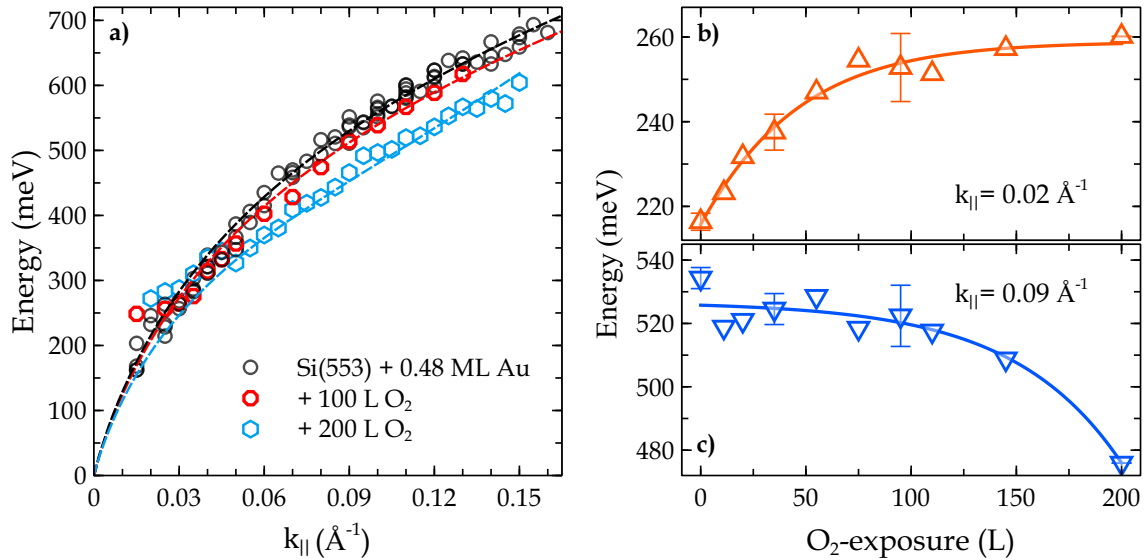


Figure 7.9: Modification of plasmonic excitations on the HCWs phase of Si(553)-Au. (a) Plasmon dispersions for the clean surface and after oxidation with 100 L and 200 L oxygen. The dashed line corresponds to the fit from modified low k approximation Eq. 5.1, as explained in Section 5.2. (b,c) Changes of plasmon frequency as a function of O_2 exposure at two defined values of $k_{\parallel} = 0.025 \text{ \AA}^{-1}$ and $k_{\parallel} = 0.075 \text{ \AA}^{-1}$.

Upon oxidation, plasmon frequency increases gradually at low k but remains almost unchanged up to 150 L oxygen dosage, as shown in Fig. 7.9 (b) and (c). However, plasmon frequency drops at higher k and saturates at low k for the following exposure. Since after such heavy oxidation with 200 L O_2 the wire periodicity barely survives (Fig. 7.6) this might be accepted as saturation for the whole dispersion. Nevertheless, IR spectra could be recorded for a slightly higher dosage, which shows the same trend of the redshift of the plasmon frequency.

A very similar trend is seen when taking the inverse FWHM of the $\times 2$ streaks (shown in Fig. 7.6) along the $[1\bar{1}0]$ direction in LEED (see Fig. 7.10). The reduction of the correlation lengths of $\times 2$ order

along the wires as a function of oxygen exposure is even more pronounced than that in IR and starts at a significantly smaller value, indicating different sensitivities of IR and LEED to various types of disorder introduced by oxygen atoms. It is noteworthy to mention that the small change in the band structure, in this case, is shifting the resonance to a longer wavelength, and thus, the used approximation may deliver a little bit too long lengths.

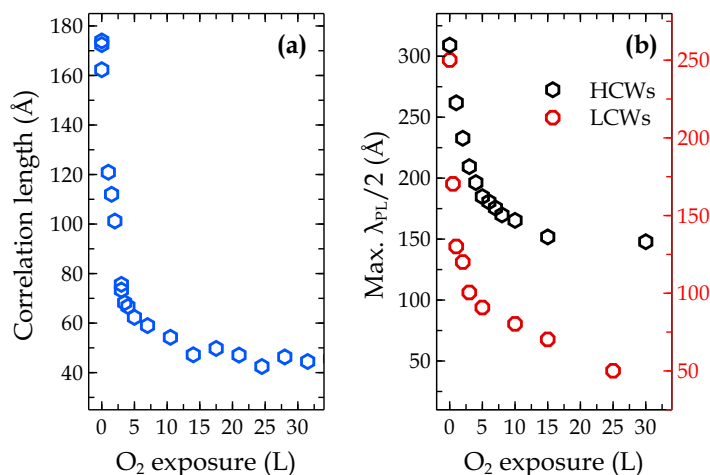


Figure 7.10: a) Correlation lengths along the Au chains determined as the inverse FWHMs of the $\times 2$ streaks as a function of oxygen exposure. b) Maximum plasmon wavelengths divided by 2, determined from the energetic positions of the absorption minimum shown in 7.8 in conjunction with the plasmon dispersion in Fig. 7.9.

These different sensitivities to defects can at least be qualitatively understood. Plasmons generally have wavelengths λ_{pL} much greater than the lattice constant and exhibit a pronounced wavelength dependence [259] that makes the scattering probability at defects of atomic size small at long wavelengths. On the contrary, stacking faults in the dimerization of the Au chains, for example, clearly cause phase changes in LEED and thus limit the correlation length in LEED, whereas they are expected to represent weak scatterers for the plasmons with long wavelengths. Kinks in the Au chains, on the other hand, caused by the roughness of step edges or slight azimuthal misalignment of the sample, should also scatter plasmons more efficiently than stacking faults. Therefore, a higher sensitivity to structural defects in LEED than for plasmons is always expected. This scattering scenario remains essentially unchanged when the system is oxidized: As outlined above, oxidation happens mainly on the Si HC chains; that is, it only indirectly influences the conducting channel by possible local relaxations of the Si atoms involved in oxygen bonding. Thus, it affects the local effective wire width and/or causes distortions of the band structure close to E_F . Again, the geometric distortions by disordered oxygen adsorption seem to be more drastic than the electronic modifications, as concluded from a comparison of the FWHM in LEED with the plasmonic dispersion curve, which turns out to be virtually unchanged up to exposure of ~ 100 L. Therefore, the random geometric disorder reflected in the reduced correlation length due

to O adsorption in LEED shows a similar tendency to the effective wire length for plasmons, but the plasmonic effective wire lengths are larger by a factor of 2.5 to 3. The widening of the IR absorption spectrum, on the other hand, is an indication of electronic damping, which reduces the absorption and also broadens the resonance. The latter is also observed in EELS spectra, as shown in Fig. 7.7. Loss spectra of the oxidized surface show broader curves for a similar reason as IR spectra.

7.3.2. Comparison with the Band Structures

Comparing these results from oxidation of the Si(553)-Au surface with a study on the oxidation of Si(557)-Au, there is a similarity. In both cases, metallicity withstands the adsorption of a very significant amount of oxygen. At first glance, the Si(553)-Au system seems to be less reactive than Si(557)-Au since much higher doses of oxygen are needed to induce any change of dispersion in the former system. However, this statement should be taken with caution since in simulations of the Si(557)-Au + O system the plasmon dispersion turned out to be quite insensitive to oxidation of the Si honeycomb chain, which is the common structural element on both surfaces. In fact, the most extensive changes in plasmon dispersion induced by oxygen adsorption were due to oxidation of the Si adatom chain, which does not exist in Si(553)-Au. Therefore, these results are fully compatible with the assumption that mainly the Si step edge with its local HC structure is oxidized on Si(553)-Au, which then has a small and only indirect effect on the conductive properties of the Au chains, but they do not mean that the reactivity with oxygen is low. This statement is corroborated by theoretical results of complete oxidation of the HC chain on Si(553)-Au (see Fig. 7.11), which even agrees semiquantitatively with the $\sim 15\%$ reduction of the plasmon frequency measured at an oxygen exposure of 200 L. In the simulation, the dispersion of the Au-induced unoccupied band is slightly lowered compared with that of the unoxidized surface. Also, a gap opening at 500 meV above E_F is seen together with possibly a small band gap opening (< 100 meV) close to E_F (see Fig. 7.11(b)).

This opening of a small band gap was found previously to be the reason for the reduction of measurable dc conductivity to essentially the isotropic background level for oxygen exposures around 200 L of O_2 . [231] If the measured plasmon dispersion is extrapolated to $k_{\parallel} = 0$ at the highest oxygen exposure, it ends up at a value of 280 meV, that is, at a much higher value than that expected from such a small band gap. In other words, this high extrapolated value is not dominated by a band gap but is more likely due to disorder induced by oxygen adsorption, as has already been discussed in the previous section. For validation of this suggestion, the measured plasmon dispersion was directly compared with the calculated electronic band structure from Ref. [231] (see Fig. 7.11). Such a comparison for the clean surface has already been presented in Section 6.3.

It should be noted that no dimerization between the Au atoms was considered in the calculation of the oxygen-induced modification of the electronic band structure shown in Fig. 7.11. By comparing this band structure with the oxidized one given in Fig. 7.11(b), the opening of a ~ 200 meV energy gap at 500 meV above E_F is visible. This might be the main reason that the plasmon dispersion of oxidized

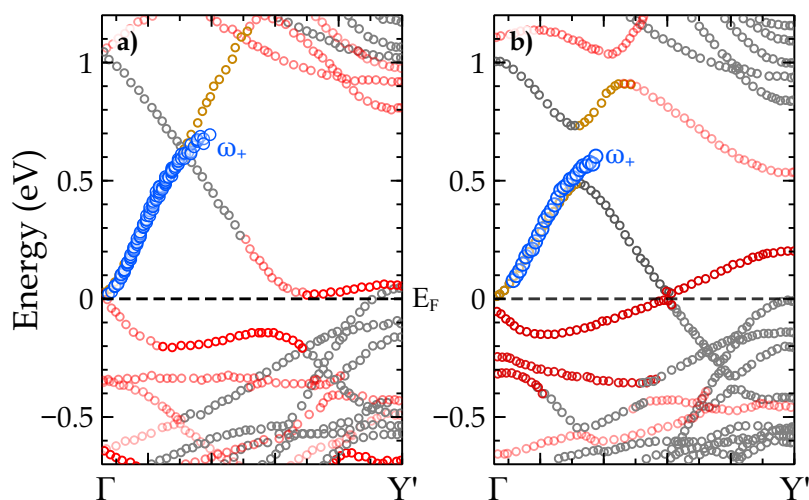


Figure 7.11: DFT-PBE calculated electronic bands for Si(553)-Au and their modification upon oxidation of Si-HC chain. (a) Clean surface bands and upper boundary (ω_+) of the electron-hole continuum. (b) Oxidized surface bands, and ω_+ . The reddish parts of lines correspond to the hybridization of Au bands with Si-HC chains, while the red parts stand for pure Si-HC bands. ω_+ (blue circles) has been calculated considering the experimental plasmon dispersion shown in Fig. 7.9. The metallic $S_{1,2}$ band is given in yellow color. Details of these bands have been discussed in Section 6.3. Band structures adapted from Ref. [231] with permission. Copyright 2017 by the American Physical Society. Please see Section 6.15 for a detailed explanation of the clean surface bands and ω_+ .

surface levels off earlier than that of the clean surface. Moreover, the bands, especially those hybridized with the Au bands (shown in red in Fig. 7.11) are rearranged after oxidation. In the calculations, it was assumed that the energetical minimization is limited to saturation of all dangling bonds. However, this cannot be reached in the EELS experiments, mainly due to the disorders caused by random oxygen adsorption. The latter also limits the observability of redshift as a function of oxidation.

Considering that the dimerization of Au chains opens a band gap at the unoccupied states, employing the non-dimerized chain model makes this medium band gap obvious. However, using such a questionable model enables mainly qualitative conclusions from this calculation. Since the scenario with one band crossing Fermi level does not change after oxygen adsorption, this calculation is very similar to that has been done for the clean surface. Again, for the calculation of ω_+ the ω_- is extracted from the band just below E_F and the measured plasmon dispersion is used for calculation of ω_+ . m^* has been derived from the ω_- band by approximating it with a parabola close to E_F . These input parameters have been used in Eq. 5.2 to derive the upper boundary of electron-hole continuum shown as blue circles in Figs. 7.11(a) and (b) for the clean and oxidized surfaces, respectively. Notably, ω_+ imitates the unoccupied band structure following the band gap openings semi-quantitatively. As a reasonable explanation, charge localization around the O-Si bonds can be shown. Such a band gap opening cannot be explained with finite chain formation. Therefore, it should be concluded that the oxygen-induced

modification on this surface is not limited to the finite-size effects, but the system undergoes slight electronic modifications upon oxidation.

7.3.3. Loss Intensity and Width

The loss intensities and half-widths contain essential information about the wire quality. As discussed in Section 5.2.1, both parameters are quite necessary parameters to yield further insight about plasmonic excitation. The loss intensity and FWHM have been collected for the clean and oxidized Si(553)-Au surfaces and presented in Fig. 7.12. The plasmon loss intensity shows a similar behavior as a function of k_{\parallel} as predicted by the quasi-1D plasmon theory [76]. The extracted plasmon intensities are $\sim 0.1\%$ of the elastic intensity. According to Eq. 3.40, the scattering mechanism itself has a profound impact on loss intensity. The measured scattering probability is three times less after 100 L O_2 exposure. Since the plasmon energy associated with a disordered surface is changed little at higher k_{\parallel} , this change must be due to reduced surface quality more than electronic effects. The FWHM of the plasmon loss for this system has been previously discussed in Ref. [260] and found that only a fraction of the broad line shape contains information about the plasmon lifetime.

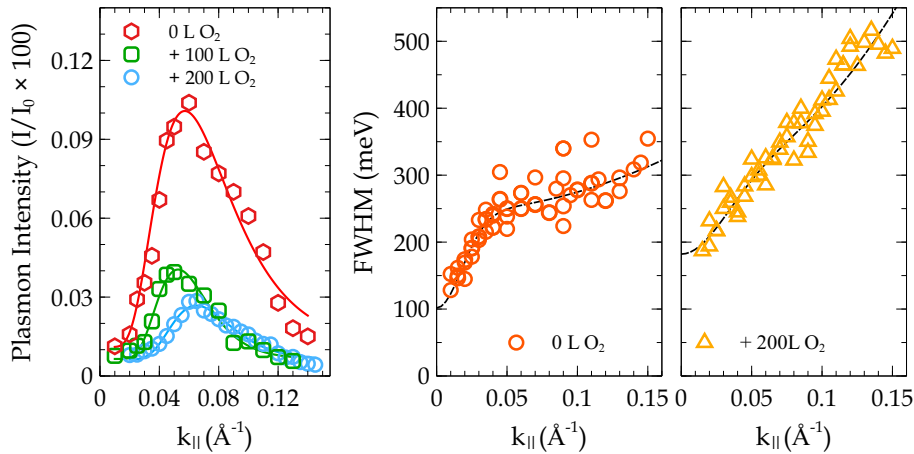


Figure 7.12: The intensity and FWHM of the plasmon loss for the clean and oxidized HWCs phase on Si(553)-Au. The data obtained after fitting the loss spectra with the fit routine described in Fig. 6.12. The loss intensity is given with respect to the elastic intensity at $k = 0$.

The extracted peak widths are shown in Fig. 7.12, which present almost the same behavior as obtained for similar systems. [50, 51] The presented FWHM starts at finite width at $k \rightarrow 0$, which is much higher than the instrumental resolution of $\Delta E = 20$ meV. The plasmon width gradually increases as a function of k_{\parallel} . In a simplified picture, neglecting all side effects (i.e., instrumental broadening, multiple scattering, defect-induced scattering, etc.), this broadening manifests a decrease of the plasmon lifetime. Then taking the width in the limit of $k \rightarrow 0$ would mean a highly over-damped plasmon, which contradicts the findings that the determined plasmon has well-defined energy and a mean free path of several

100 Å. [93, 94, 215] On the other hand, in the $k \rightarrow 0$ limit, the plasmonic excitation energies converge to zero and, therefore, their lifetime must be infinitely long. This shows that the observed broad line width cannot be attributed to plasmon lifetime alone, but defect-induced scattering and instrumental broadening must also be considered.

The actual determination of a plasmon lifetime is subject to larger uncertainty. For example, the linear relation between the short-range electron-electron collisions and plasmon damping was shown for 2D electronic systems. [128, 129] Although there is no such description for a one-dimensional case, it is also ignored in RPA, its true effect on the actual plasmon lifetime can not still be fully ruled out. An additional factor for line broadening is the scattering geometry. Thus, the distance from the atom decreases by increasing the momentum transfer, which results in a more localized scattering event. This increases the uncertainty in momentum and, thus, also in energy resolution. A further influence on the broadening of the loss peak is the order and imperfections of the system. As already discussed in the previous chapter, the obtained atomic wires show finite length and are not free from defects. This observation is corroborated with STM studies on the same surfaces. [261] The latter comprises residual gas adsorption in addition to the local surface imperfections such as kinks and stacking faults. Moreover, as discussed in this section, the electronic properties, mainly plasmonic excitation associated with atomic wires, highly depend on the wire quality. Therefore, it is not surprising that this factor dominates the peak width after oxygen exposure. As shown in Fig. 7.12, the resulting FWHM is two times broader after 200 L O₂ dosage. Similar behavior of loss intensity and half-width have observed as a function of time in the UHV condition at 5×10^{-11} mbar. Therefore, the discussions mentioned above suggest that disordering is a more pronounced effect of oxidation on this surface.

7.3.4. Oxidation of the LCWs Phase

The LCWs phase, in which only every second terrace is covered with a double strand of Au (see Fig. 6.4), behaves qualitatively quite similar but with a higher sensitivity to oxygen because of its higher chemical reactivity on alternate terraces (see Section 6.1.1). The diffraction patterns of the freshly prepared and oxidized LCWs phase are given in Fig. 7.13. The intensity of diffraction features ($\times 2$ and extra $\times 5$ periodicity) on LCWs is extremely reduced in comparison with the HCWs phase. This is already a herald of higher imperfections and disorder on the LCWs surface. Besides, the background intensity increases quickly upon oxygen exposure, which shows random adsorption and enhanced scattering. On the other hand, the 5×2 superstructure is almost disappearing after 10 L O₂ exposure.

As mentioned above, in the presence of the alternate bare Si terraces, this surface possesses higher chemical reactivity than the HCWs surface (see Section 6.1.1). Therefore, the plasmons in the LCWs phase turn out to be more sensitive to oxidation.

The weaker plasmon signal of this phase compared with the HCWs surface (see Fig. 7.7 and 7.8) can easily be understood since only 4/9 of the surface consists of terraces hosting a gold wire. A further loss of intensity is caused by the lower quality of ordering that is obvious from the diffraction profiles (see

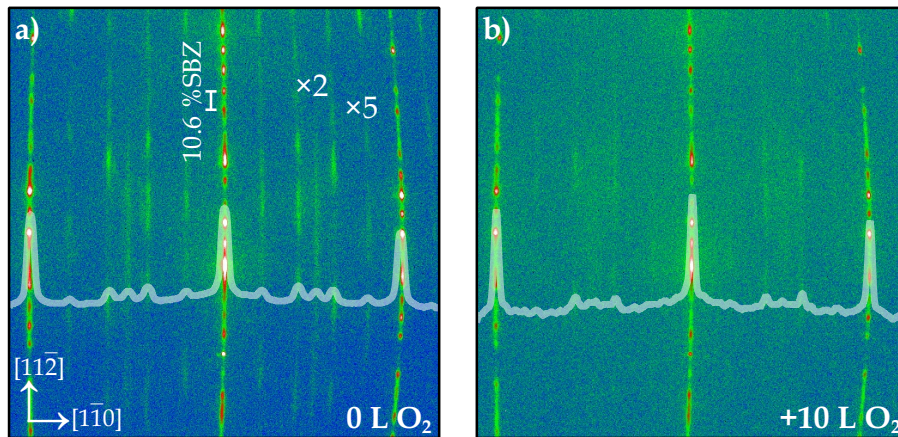


Figure 7.13: SPA-LEED patterns of the clean LCWs phase of Si(553)-Au (a) and after oxidation (b). Primary energy: 138 eV. Line scans (white lines) were generated by integrating the intensities along $[11\bar{2}]$ for each k point along the $[1\bar{1}0]$ direction and normalization to the central intensity.

Fig. 7.13). On the other hand, Si adatoms with unsaturated bonds at the uncovered Si(1×1) terraces make this surface chemically more reactive than the HCWs surface. For these reasons, only 30% of the initial loss intensity remains after an O₂ exposure of 10L, which made it barely detectable at higher exposures. The plasmon dispersion for the clean and oxidized surfaces is shown in Fig. 7.14. At small k_{\parallel} , an increase of plasmon frequency was seen as a function of oxygen exposure (Fig. 7.14(b)) that is very similar to that in the HCWs surface (Fig. 7.8). Therefore, it must have a similar origin.

This higher sensitivity is also reflected in oxygen-induced changes of the plasmon dispersion (Fig. 7.14). Contrary to the HCWs phase, however, O adsorption tends to increase the plasmon dispersion (see Fig. 7.14(b)). While changes in the band structure close to E_F are expected to be very similar in both phases, qualitative differences may be due to the following mechanisms: First, the reduction of the dielectric function upon oxidation should be more significant in the LCWs phase since a much larger fraction of the surface is pure Si, which is primarily oxidized to form SiO_x. Second, the relaxation of surface tension by oxidation in the uncovered terraces may induce additional confinement normal to wires.

The qualitative behavior of IR absorption spectroscopy at normal incidence as a function of oxygen exposure is similar to the HCWs phase (Fig. 7.8) and is in agreement with the interpretation of the small k_{\parallel} behavior given there. Also, in IR, the absorption is significantly smaller than for the HCWs phase for the reasons already discussed above. Compared with EELS, an absorption signal is detectable up to considerably higher oxygen exposures, as given in Fig. 7.8. Interestingly, any plasmonic absorption disappears for exposures above 50L, contrary to the HCWs phase, while the absorption due to the Si–O stretch is still clearly visible. Therefore, it can be concluded that metallicity is in fact destroyed for oxygen exposures above 50L. Whether this finding is due to an extreme disorder or still a band

structure effect has to remain an open question at this point since no numerical studies of the electronic band structure have been done for this purpose.

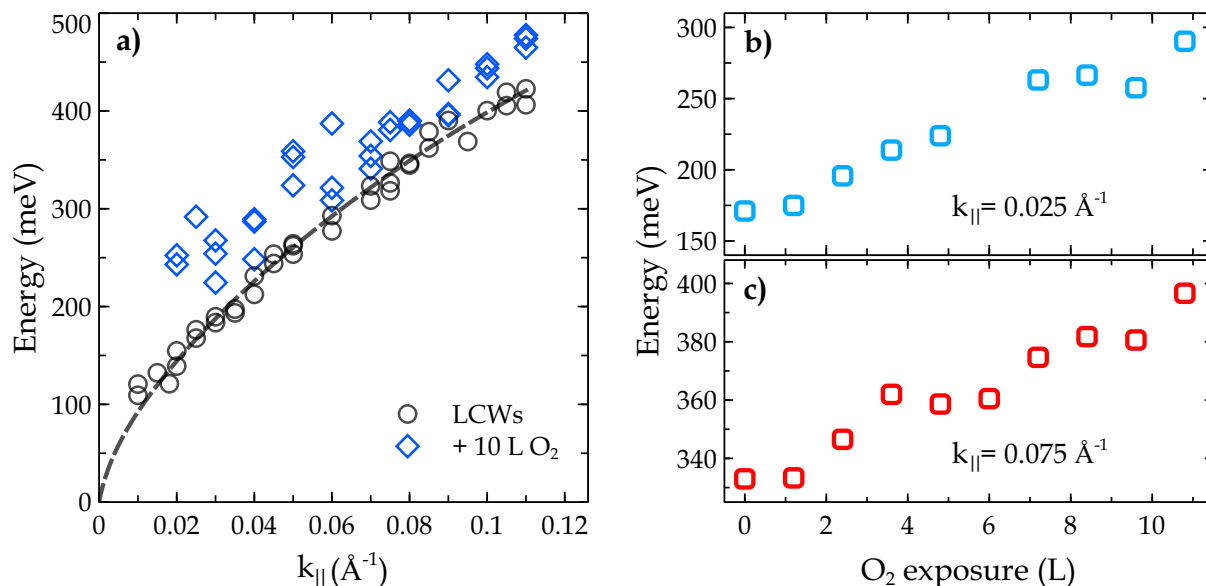


Figure 7.14: Plasmon dispersion for the clean LCWs phase on Si(553)-Au (black circles) and after oxidation with 10 L O_2 (blue diamonds). The dashed line corresponds to the fit from a modified low- k approximation, as explained in Section 2.2.2. (b,c) Change of the plasmon frequency as a function of O_2 exposure at $k_{\parallel} = 0.025 \text{ \AA}^{-1}$ and $k_{\parallel} = 0.075 \text{ \AA}^{-1}$.

7.4. Extrinsic Doping of Au Atomic Wires

Such an ability to control the fundamental electronic properties of low-dimensional systems through doping has been central to the progress in developing active electronic circuits and in many different fields. In fact, due to the higher sensitivity of such wires of ultimate smallness to even small external perturbations, this kind of tunability mechanism should be a well defined and highly controlled process. However, such tunability can also work more naturally by employing the characteristic selectivity of atomic wire systems together with an embedded environment. As an example, site and adsorbate selective response of Au atomic chains can be shown. In the previous section, such a mechanism was shown to be a consequence of oxidation of the Si(557)-Au and Si(553)-Au surfaces. Here, this investigation is extended to the adsorption of atomic hydrogen on these surfaces. Moreover, the last section showed that oxidation of atomic wire systems results in substantial modification of electronic properties. Besides, a high concentration of oxygen introduces defects into the wire order. Considering the strong interaction of oxygen with Si surface, the latter can be reduced by using hydrogen. Thus, the substantial difference between the bond formation of H and O allows studying the charge doping into metallic bands with little structural distortions. The electronic and structural parameters are highly

correlated for Si(hhk)-Au surfaces. Particularly, the Si(553)-Au surface shows electronic properties that are closely connected with a structural phase transition and/or structural rearrangements. [25, 65, 200] Such interrelation can be observed once charge donation to Si surface states (in this case, hybridized with Au bands) happens.

7.4.1. Structural Enhancement on Si(553)-Au by Charge Transfer

Adsorption of atomic hydrogen indeed causes enhanced dimerization of the Au chain, as shown directly by the comparison of SPA-LEED patterns from a freshly prepared and the hydrogenated Si(553)-Au surface, both covered by 0.48 ML of Au (see Fig. 7.15). The sharp spots in both images, separated by $\Delta k = 0.425 \text{ \AA}^{-1}$ indicate a well ordered periodic step structure with (111)-oriented terraces and a terrace width of 14.7 \AA , as expected for the (553) orientation for terraces separated by double steps of 3.14 \AA height. This pattern qualitatively does not change upon H adsorption. Periodic dimerization of Au atoms along the terraces gives rise to $\times 2$ streaks in the diffraction pattern. These streaks become brighter after exposure to atomic hydrogen, independent of electron energy, and the width of the spot profiles decreases along the $[1\bar{1}0]$ direction.

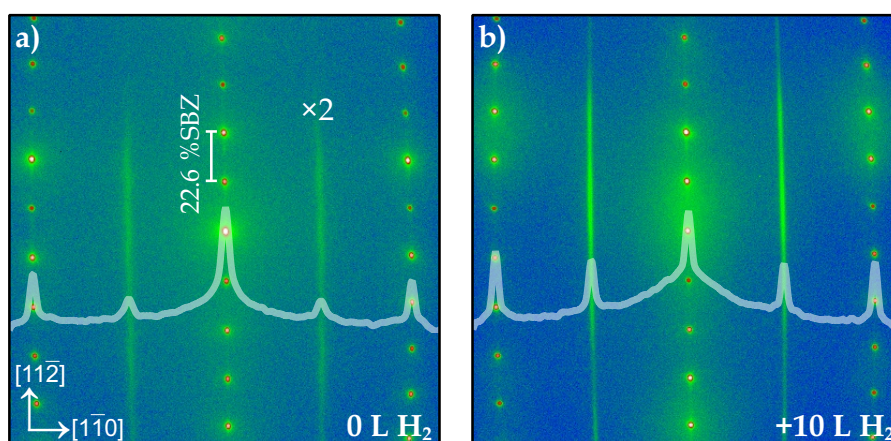


Figure 7.15: LEED patterns of Si(553)-Au at a gold concentration of 0.48 ML (left) and the same surface after adsorption of 10 L H₂ (right). Images were recorded at RT with the same interaction time. Primary energy: 138 eV. The line scans (white lines) were generated by integrating the intensities along $[11\bar{2}]$ for each k point in the $[1\bar{1}0]$ direction and normalization to the central intensity.

These effects indicate an enhanced amplitude of Au dimerization, as well as an increase of the average length of undistorted dimer chains of Au, since this amplitude should be directly proportional to the integrated diffracted intensity (note the log scale in Fig. 7.15). As evident from the more detailed results shown in Fig. 7.16, the structural enhancement of Au chains is a direct result of hydrogen adsorption or doping. These findings are compatible with theoretical models indicating that the adsorption of H at the Si step edge enhances the dimerization parameter of Au chain. [32, 33, 262]

From the combination of experimental results and atomistic DFT, it was found that this enhanced dimerization is strongly coupled to elementary charge donation to surface bands and subsequent band gap opening at unoccupied state or relocation of Fermi level. This will be discussed in Section 7.4.2 in close relation with results from the electronic investigation. At a later stage of hydrogenation, $\times 2$ streaks as well as the whole surface quality decline. This is quantitatively shown in Fig. 7.16, where $\times 2$ intensity, as well as correlation length, decreases almost linearly when a critical H concentration is exceeded critical H dosage.

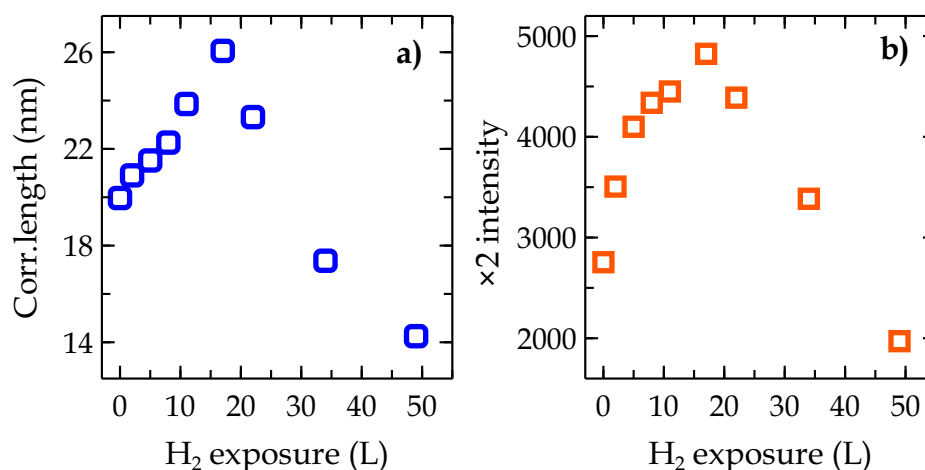


Figure 7.16: Change of correlation along the Au chains determined from the inverse FWHM of the $\times 2$ streaks (a), and intensity of the $\times 2$ streaks as a function of hydrogen exposure (b). Data set were deduced from 1D line scans in the $(1\bar{1}0)$ direction after fitting with convoluted Lorentzian and Gaussian functions, as exemplarily shown in Fig. 7.15.

On the other hand, H adsorption does not induce any new superstructure so that the H atoms must follow the periodicity of the already existing lattice and must be located at well-defined adsorption sites, but there is no long-range order of hydrogen. H adsorption only causes an increase of diffuse background around the central $(0\times)$ spots. Although the following annealing at $\sim 350^\circ\text{C}$ almost recovers surface metallicity, the surface quality is only partially recovered. This can be due to the thermal dissociation of water and oxygen molecules, increasing their chemisorption probability resulting in further structural distortion. Notably, the surface quality can be fully recovered by annealing the hydrogenated surface at $\sim 900^\circ\text{C}$ for a few second.

7.4.2. Modification of Plasmons on Si(553)-Au by Atomic Hydrogen

The exemplary momentum resolved loss spectra for the clean and hydrogenated Si(553)-Au surfaces are shown in Fig. 7.17. Qualitatively, the anisotropic plasmonic excitation is not altered upon hydrogen adsorption (see Fig. 7.17(c,d)). After hydrogenation, the non-dispersive loss feature around 100 meV appears, this might be assigned to the Si-OH stretch modes [249,252]. It is an indication of a very small

amount of water, whereas the hydrogen loss, which has a much smaller cross section [263], is not seen directly.

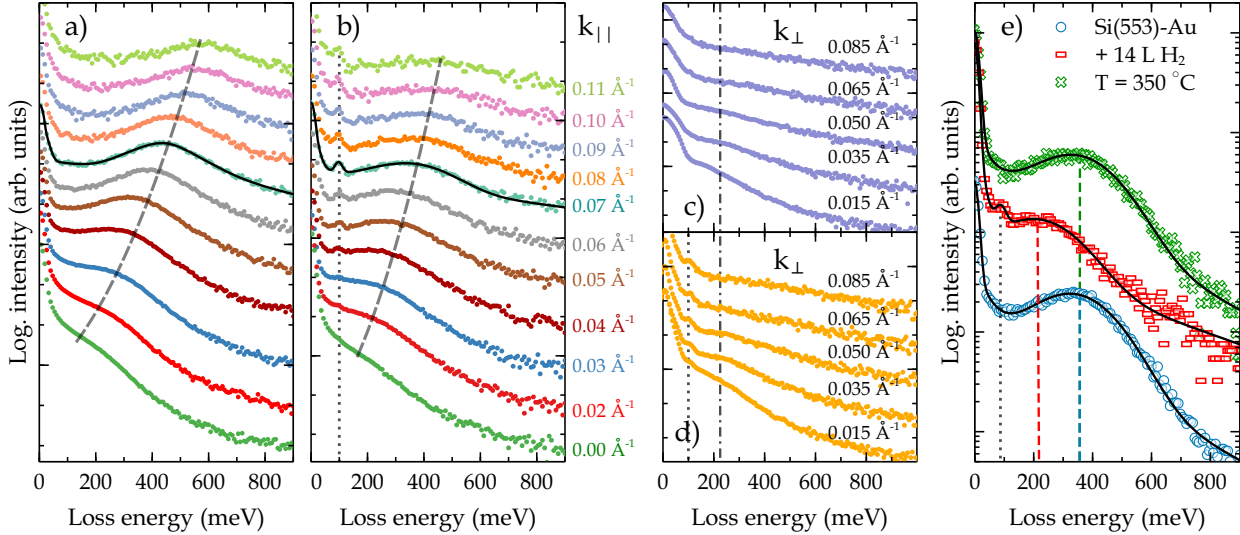


Figure 7.17: Momentum resolved EEL spectra recorded along the $[1\bar{1}0]$ direction for Si(553)-Au: (a) clean and (b) after exposure to 10 L H_2 . The dashed lines approximate the plasmon losses dispersing only in k_{\parallel} along the wires. (c) and (d) show the EEL spectra recorded with momentum transfer perpendicular (k_{\perp}) to the wires for the clean and hydrogenated surfaces, respectively. The dashed-dotted line in (c,d) depicts the nondispersive loss associated presumably with quantum-well states. (e) Reversibility of H-induced redshift of plasmonic frequency measured at fixed $k_{\parallel} = 0.05 \text{ \AA}^{-1}$. The dotted lines in (b,d,e) show the H-induced vibrational mode. The spectra were normalized to the elastic intensity and shifted against each other for better visibility.

Heating the hydrogenated surface to $350 \text{ }^{\circ}\text{C}$ was found to be enough not only for completely remove this peak (i.e., see Fig. 7.17), which is in accordance with the previous report [264]. Contrary to oxidation, hydrogen experiments were conducted with atomic hydrogen. Adsorption experiments with molecular hydrogen showed no effect on plasmon spectroscopy, making the use of atomic hydrogen mandatory.

The plasmon dispersion is reduced gradually by hydrogen exposure, as illustrated in Fig. 7.18(a). The increase of hydrogen exposure is coupled with a reduction of loss intensity (see Fig. 7.17), so that it becomes nondetectable after $\sim 15 \text{ L}$ of H_2 exposure. This behavior indicates that adsorbed H atoms are not ordered. On the contrary, the H-induced disorder is a plausible reason for reducing loss intensity with increasing hydrogen dose. Furthermore, the exponential decay of loss intensity as a function of loss energy, described as Drude tail, indicates that metallicity is mostly preserved under all conditions measured here.

As a function of hydrogen exposure, a significant reduction of plasmon frequency was observed only for exposures above 3.5 L , whereas changes were negligible at smaller exposures. In addition, any elec-

tron beam-induced effects by continuous exposure of the hydrogenated surface to the electron beam over 7 h is excluded, since no detectable change after this procedure was found. The recovery of plasmonic excitation upon heating the hydrogenated sample to 350 °C (see Fig. 7.17(e)) proves that the reduction of metallicity is due to hydrogen adsorption. While thermal desorption of oxygen and recovery of plasmon frequency on these surfaces challenges higher thermal annealing, as an exemplary given for Si(557)-Au surface in Fig. 7.2(c).

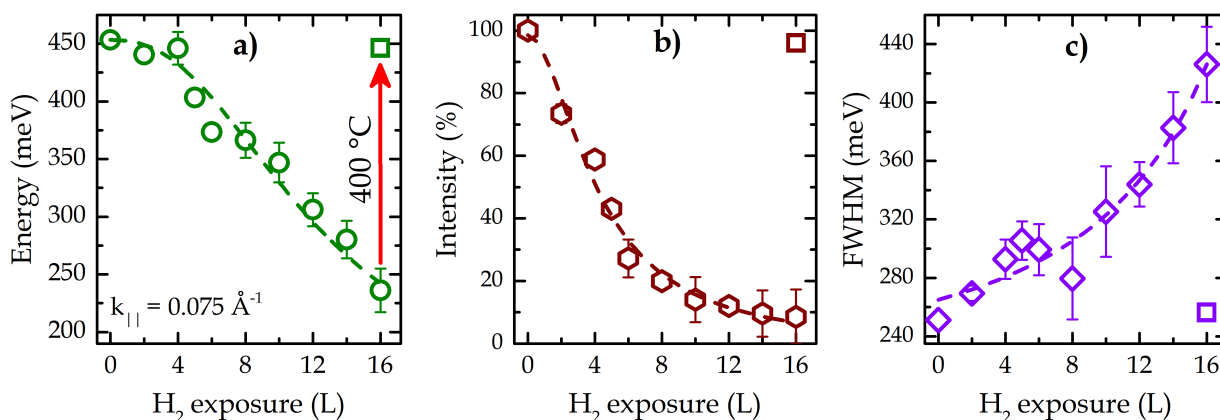


Figure 7.18: Changes of plasmon energy (a), intensity (b) and FWHMs (c) on the Si(553)-Au HCWs surface after adsorption of atomic hydrogen. All data were measured at $k_{\parallel} = 0.075 \text{ \AA}^{-1}$. The dashed lines are guides to the eye. The square data points in all graphs were obtained after subsequent annealing at 400 °C, which show the complete recovery of plasmonic excitation.

The dependence of plasmon frequency on exposure is shown exemplary at a fixed k_{\parallel} of 0.075 \AA^{-1} in Fig. 7.18(a). Evidently, the plasmon frequency remains constant up to 4 L H₂ dose, from where it drops almost linearly. This reduction is in good qualitative agreement with the behavior predicted by the simulations shown in Fig. 7.21. If only a single type of sites at the step edges is occupied, as assumed in the model calculations, this finding implies a strong concentration-dependent reduction also of the sticking probability. This property would partly compensate, but not remove the nonlinear response of plasmonic excitation to H doping found in the simulations. Please note that the observed behavior is not limited to this fixed k point, but it is chosen to guarantee sufficient intensity over the range of hydrogenation as well as to avoid possible finite-size effects on the plasmon frequency. As shown in Fig. 7.18(b) the plasmon loss intensity decreases gradually and almost vanishes 14 L H₂ exposure. Similarly, decline of the $\times 2$ periodicity was also observed in diffraction experiments as well, however, only after 15 L H₂ dose. In addition, the FWHM of the plasmon loss also increases with a similar trend. This observed behavior might be related to an increased scattering rate. It worth noting that the increase of FWHM is most likely associated with a concomitant lifetime broadening due to the interaction of plasmon dispersion with the single-particle excitation.

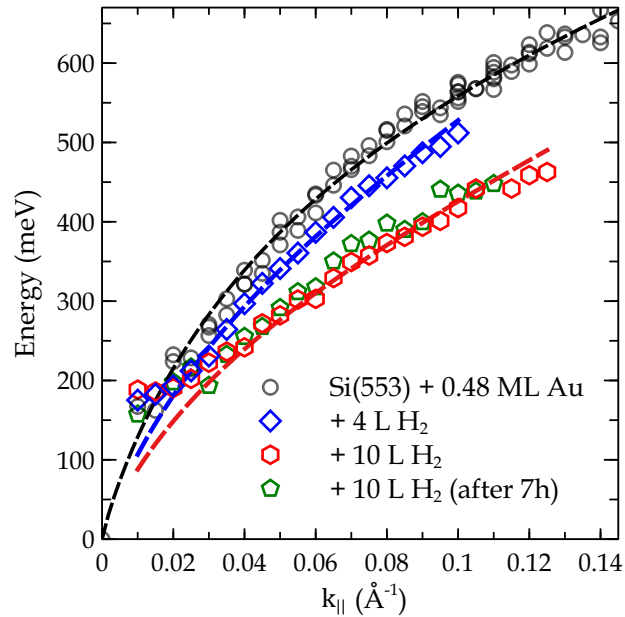


Figure 7.19: Plasmon dispersions of the clean and hydrogenated Si(553)-Au surface. Green data have been obtained from the 10 L H₂ adsorbed surface after 7 hrs to elucidate the negligible effect from the electron beam. The dashed lines stand for an empiric fit, as described in Section 2.2.2, only assuming that the dispersion curves have to start at zero in the long wavelength limit.

From the peak positions of plasmonic losses by applying the fit procedure shown in Fig. 6.12, the plasmon dispersion as a function of k_{\parallel} has been extracted. These are shown for the clean and hydrogenated surfaces in Fig. 7.19. The H-induced reduction of slope in the dispersion is now seen more clearly. While minor changes are already seen at a H dose of 4 L, the slope is about 30 % smaller at 10 L.

Comparing with the band structure calculations shown in Fig. 7.21, the excitation spectrum from E_F to empty states above E_F is virtually unchanged up to an average occupation probability of the Si step edge of about 35 %. This number must be exceeded with the 4 L exposure, while only a relatively small increment up to less than 50 % occupation is necessary to explain the observed changes of slope in dispersion. Furthermore, it is obvious from Fig. 7.19 that the data after H exposure deviate from the extrapolation to zero energy in the long wavelength limit. This finding is compatible with the assumption of H-induced disorder that reduces the possibility of free propagation of plasmonic waves to the limit where only dispersionless standing waves still can exist. Such standing waves allow the excitation of plasmons by infrared radiation (IR), which has been investigated in detail after oxidation of this system, as discussed in Section 7.3.

Site-Specific Adsorption — The present, as well as earlier studies, show that saturation of different chemically reactive sites on vicinal (pristine as well as metal deposited) surfaces has individual effects on electronic properties. Therefore determination of occupation energy of specific adsorption sites

contains fundamental information for subsequent adsorption studies. The PES for adsorption of atomic hydrogen on Si(553)-Au calculated by C. Hogan et al. [33] shown in Fig. 7.20. It shows that the hydrogen chemisorption happens in different stages. Thus, step edge Si atoms leads the favorable adsorption sites with -1.1 eV potential energy shown as the first stage minimum in Fig. 7.20. This is replaced with Si-HC atoms for further H exposure at -0.7 eV. It has been shown that charge redistributes between the step edge and Au chains happen upon H adsorption, while H also changes site reactivity. [265] It was shown that upon step edge hydrogenation, the three-fold periodicity that appears at low temperature is also suppressed. [33] This opens another interesting question for manipulation of spin ordering by selective doping, which is beyond the objective of this thesis.

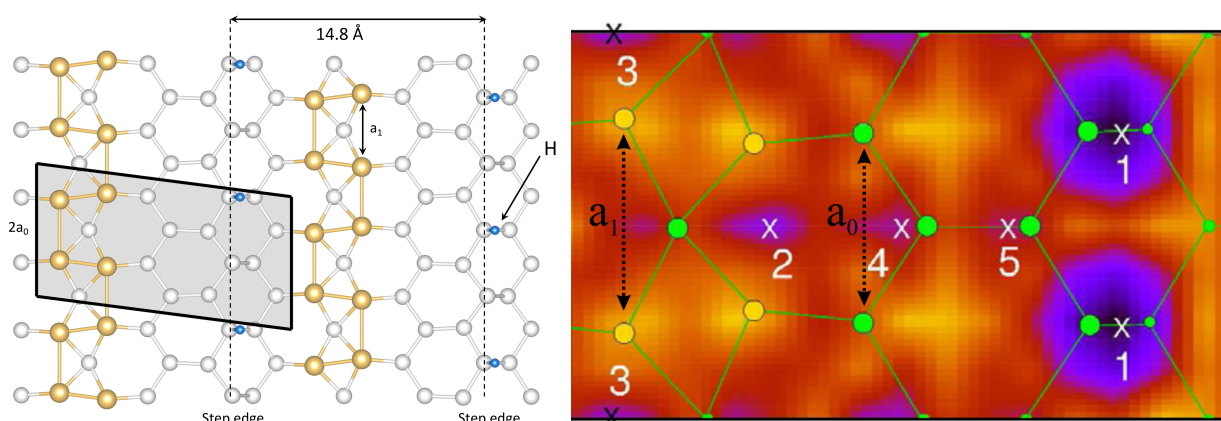


Figure 7.20: Left: Top view of the Si(553)-Au surface with atomic hydrogen atoms (blue balls) adsorbed at the Si step edge. In both figures, Au atoms are given in yellow color others are Si atoms. The coverage shown corresponds to 1H per (5×2) unit cell, which is highlighted in gray. Right: Simulation of the PES for atomic H adsorption on the clean Si(553)-Au surface. Most favorable adsorption sites are numbered in a sequence. Here, yellow, large, and small green circles correspond to the gold, upper edge, and lower step edge Si atoms, respectively. Please note that although the periodic boundary conditions employed in the calculations lead to a regular array of H, adsorbed atoms are most likely not perfectly ordered in experiments. PES adapted from Ref. [33] with permission. Copyright 2018 by the American Physical Society.

Modification of Electronic Bands — For a quantitative analysis of the plasmon dispersion, the close relationship between the upper edge of the electron-hole continuum and the plasmon dispersion has been employed. As discussed in previous sections, for the quasi-1D systems it turns out to be particularly simple. Thus, if the quasi-1D array of wires is considered as a 2D electron gas that is confined to a wire of finite width by an appropriate potential the plasmon dispersion for a single isolated wire is related to single-particle excitation zone via Eq. 5.2. Pure electron donation to the well-defined edge sites, compensated by background charges, was recently found to be sufficient to mimic the influence of H adsorption at the step edges on band structure [33]. Fig. 7.21 shows the effect of additional electronic charge on the Si(553)-Au band structure along the Au chain. The calculations are performed in a (5×2)

unit cell, adding various fractions of an elementary charge. This cell features a full mini-terrace and $\times 2$ periodicity along the chain. It thus allows us to describe the effect of electron doping on the dimerization of the Au chain, too. At low electron doping concentrations, the band structure modification mainly concerns the occupied states and leaves bands close to the Fermi level almost unaltered. This situation drastically changes for electron doping higher than 0.75 e per (5×2) unit cell. From this point, the Au-derived sp band above E_F starts to move downward. The unoccupied bands are rigidly shifted downwards so that no fundamental band gap can open at any concentration.

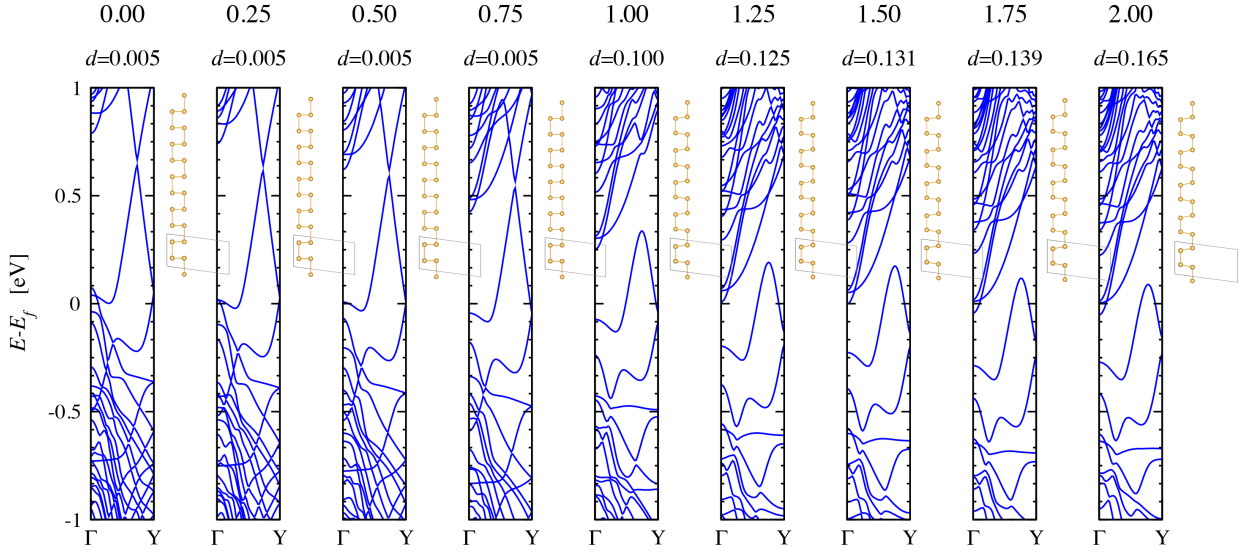


Figure 7.21: Electronic band structure of the Si(553)-Au system calculated by DFT as a function of electron doping. The additional elementary charge per (5×2) unit cell and the Au dimerization, d , (see text) are indicated above each graph. The sidebars depict the change of dimerization between Au chains. The Γ – Y direction is roughly parallel to the Au-chain.

The electron doping by addition of external charge is also coupled, but in a highly nonlinear manner, with both the dimerization parameter d defined as the relative deviation of the Au-Au distance from the Si lattice constant a_0 , $d = (a_1 - a_0)/a_0$ [25], and with the form of the Au-related bands above the Fermi level. Indeed, only after a certain threshold, the Au-related bands are occupied, which leads to the observed enhancement of dimerization. It has been pointed out recently that artificially increasing the chain dimerization results in an opening of the electronic band gap between the Au related bands. This effect confirms the direct and strong coupling between Au-related electronic bands and chain dimerization. Indeed the results of Fig. 7.21 predict an enhancement of the chain dimerization and, in turn, of the $\times 2$ periodicities upon electron doping. The parameter d develops almost linearly as a function of elementary charge donation, as shown in Fig. 8.1. The discussion regarding the coupling of dimerization and band gap opening will be extended in Section 8.1. Nevertheless, as already discussed in Section 7.4.1, H-induced enhancement of dimerization amplitude is limited to a certain dose where structural distortion due to random adsorption takes over the whole surface properties.

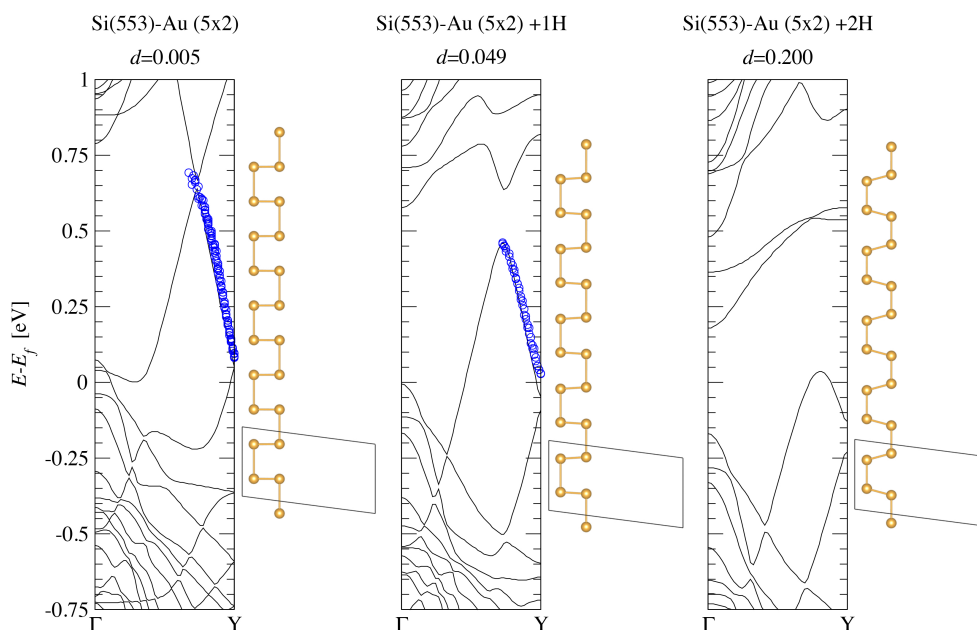


Figure 7.22: Calculated electronic band structures for the clean (left) and the hydrogenated (middle and right) HCWs phase. The dimerization of the clean and after H adsorption is shown schematically at the right side of the respective band structure. For the band structure calculations, the model given in Fig. 7.20 was used. H adsorption was tested as an elementary charge transfer to the 5×2 unit cell. The upper boundary (ω_+) of the electron-hole continuum, derived from the plasmon dispersion by the procedure described in Section 2.2.1, is shown by blue circles as an overlay to the corresponding bands for the clean (left) and the hydrogenated surface (middle).

In order to make a more direct comparison between the measured plasmon dispersion and the calculated band structure, the dispersion of ω_+ was determined from the measured plasmon dispersion ω_p using the assumption discussed in Section 2.2.1. For this, ω_- was obtained from the calculated band structure (shown in Fig. 7.22) with the assumption that the topmost occupied Au-induced metallic band can be approximated by a parabola close to E_F . This even quantitative agreement of the dispersion of ω_+ with the calculated band structure, as derived from plasmon spectroscopy after adsorption of 10 L of H, is remarkable and again proves the usefulness of plasmon spectroscopy for getting quantitative information about the unoccupied part of the band structure close the Fermi level. Furthermore, it gives clear evidence for the H-induced widening of the band gap to about 0.2 eV. This widening is coupled with an increase of the amplitude of dimerization by roughly one order of magnitude. These results are also in qualitative agreement with the calculations by Hogan et al. and corroborate the interconnection between band gap opening and dimerization [33]. This interrelation is caused by the hybridization of Au-related bands with the Si surface bands near the Fermi level. The modification of the unoccupied band structure due to this hybridization and its significant deviation from a parabolic dispersion pre-

vents the plasmon dispersion to enter the electron-hole pair continuum (or Landau damping zone). In other words, the free-electron gas picture turns out not to be adequate for the description of plasmon dispersion in this class of systems.

The disorder introduced by hydrogen adsorption in this system affects strongly its plasmonic properties and limits the range of observability in momentum space. As already shown in Fig. 7.16, doping with hydrogen works almost perfectly up to 15 L H_2 , while the whole surface quality decreases for further exposure. For this reason, the metal-insulator transition predicted from simulations at the DFT-LDA level [33] is experimentally not accessible here. According to the calculations shown in Fig. 7.22(right), the metallic band, as well as hybridized Si states, almost disappear from the unoccupied part resulting in ~ 400 meV wide indirect energy gap after adsorption of 2H atoms per 5×2 unit cell. Also, one should note that no localized states were formed at this surface, which was observed for Si(557)-Au after hydrogen adsorption. As a result of an increased adsorbate-induced disorder in the experiment, it was not possible to achieve a sufficient concentration of doping required to drive a metal-insulator-transition.

7.4.3. Hydrogen-Induced Plasmon Localization on Si(557)-Au

Compared with Si(553)-Au, higher chemical reactivity and interaction complexity are expected, since the terraces are larger and Si adatom and restatom chains with unsaturated dangling bonds exist. The low energy electron diffraction patterns of clean and hydrogen-exposed Si(557)-Au surfaces are shown in Fig. 7.23. Details of the diffraction pattern for the clean surface have been discussed in Section 6.1.

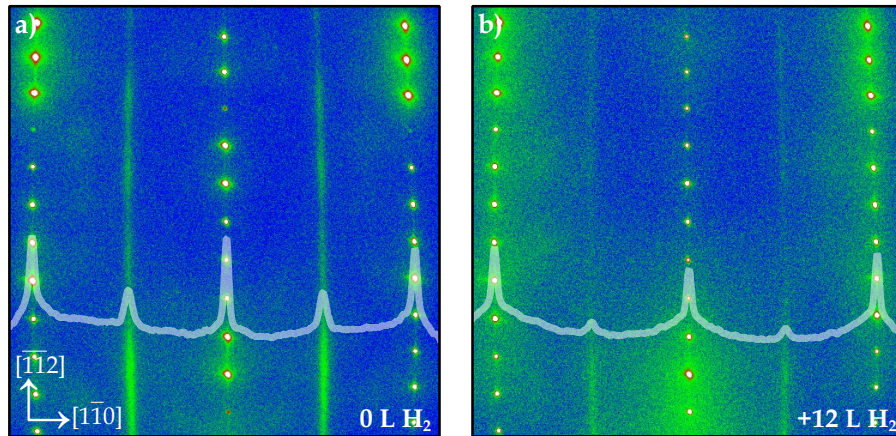


Figure 7.23: SPA-LEED patterns of clean Si(557)-Au (a) and the same surface after adsorption of 12 L of hydrogen (b). Primary energy: 138 eV. The line scans were generated by integrating the intensities along $[11\bar{2}]$ for each k point along the $[1\bar{1}0]$ direction and normalization to the central intensity.

The bright integer order spots in both images are from the Si step train, characteristic of a periodic sequence of (111) oriented nano-terraces separated by double Si steps. As obvious from the diffraction patterns, hydrogenation leaves the overall step structure unperturbed, while it induces disorder, best

seen as an increase of the diffuse intensity around the integer order spots (see Fig. 7.23(b)) and an overall increase of linear background. Moreover, the intensity of the $\times 2$ streaks is reduced upon H adsorption. However, no direct conclusion can be drawn about Au chains, since the $\times 2$ streaks are not due to Au chains. Nevertheless, distortion of whole surface perfections affects metallicity associated with the Au chains in a similar way as on other surfaces. Please note that hydrogen exposures are given for molecular hydrogen, i.e., only about 5% is atomic H (see Section 4.5).

Fig. 7.24 shows a set of EEL spectra from the clean and hydrogenated Si(557)-Au surfaces acquired at room temperature with the momentum transfer parallel to wires. As already discussed in Section 7.2 and also in Ref. [23,31], dispersing plasmons on this surface exist only along the wires. Although dispersion appears only in this direction, it is only apparently compatible with the quasi-1D theory. [31,81]

Similar to Si(553)-Au, here also hydrogen adsorption induces an additional nondispersive loss around 100 meV, which demonstrates the chemical interaction of hydrogen with the surface (see Section 7.1).

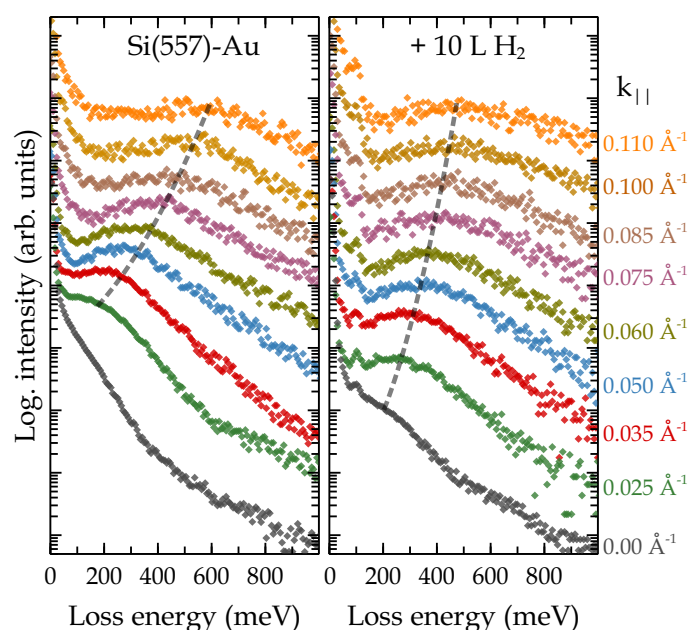


Figure 7.24: Set of EEL spectra as a function of $k_{||}$ from the clean Si(557)-Au surface (left) and after hydrogenation with 10 L of H_2 (right). In both cases, a dispersing of plasmon loss is only seen for a momentum transfer in the $[1\bar{1}0]$ direction or parallel to the wires. The spectra were normalized to the elastic intensity and shifted against each other for better visibility.

The results presented here are completely different from those caused by oxidation of the same surface (see Section 7.2). The observed effects must be mainly driven by atomic hydrogen in the present case. Although the surface keeps its anisotropic metallicity, strong changes of plasmon frequency are observed upon hydrogenation. As shown in Fig. 7.24(b), the loss curves broaden and also the signal-to-noise ratio decreases after hydrogenation. Therefore, the experimental investigation of hydrogen exposure is limited to ~ 20 L in this particular case.

The obtained plasmon dispersions are presented in Fig. 7.25 together with that of the clean surface, which is almost linear due to Au-Si hybridization close to E_F . The dashed line in Fig. 7.25 is a fit from a modified empirical model as described in Section 2.2.2. It takes into account the experimental band structure and density of states. Taking into account the lateral distance $d = 19.2 \text{ \AA}$, electron density $n = 2.45 \times 10^7 \text{ cm}^{-1}$ and the line shape was fitted using the relation given in Eq. 5.1. For this, the 1D electron density $n = 2k_F/\pi$ and m^* were extracted from the S_2 band in ARPES data [65] considering it as a parabolic dispersion in the vicinity of E_F . This fit yielded a wire width of $\sim 5 \text{ \AA}$, compatible with a single atomic chain.

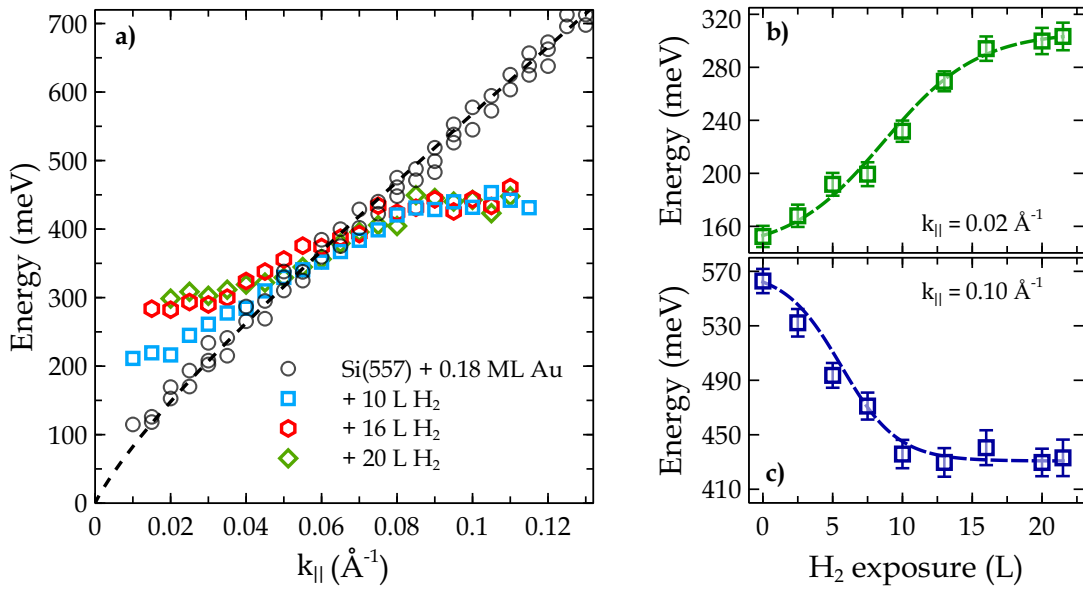


Figure 7.25: Plasmon dispersion for the clean and hydrogen adsorbed Si(557)-Au surfaces (a). The dashed line for the clean surface dispersion is from an empiric model (see Section 2.2.2 for further details). (b) and (c) show the changes of plasmon frequency at defined low k ($k_{\parallel} = 0.02 \text{ \AA}^{-1}$) and high k ($k_{\parallel} = 0.10 \text{ \AA}^{-1}$) region as a function of hydrogen exposure.

Turning now first to the low k part of the dispersion, obviously, the plasmon excitation energy in the long wavelength limit (close to $k_{\parallel} = 0$) continuously raises as a function of hydrogen exposure up to 290 meV after 20 L H₂ exposure (see Fig. 7.25 (a,b)). This effect is quite common for atomic wire systems and can be described as a finite-size effect due to the break-up of the conducting chains into sections of smaller and smaller lengths as a function of increasing hydrogen exposure. On the other hand, this effect is able to hide the possible opening of small band gaps close to E_F . No such band gaps, however, seem to be present up to the hydrogen coverage investigated here, as concluded from the calculated band structures (see following Section 7.4.3). For larger k_{\parallel} values ($k_{\parallel} > 0.05 \text{ \AA}^{-1}$) the dispersion crosses that of the clean Si(557)-Au system and then quickly levels off at constant energy of 0.43 eV. This behavior turned out not to be dependent on H₂ exposure above 10 L, i.e., it saturates there (see Fig. 7.25 (a,c)). Since the plasmon frequency for these k -values is directly coupled with the

upper edge of single-particle excitations close to E_F , this behavior is a clear indication for a band gap opening in the unoccupied part of the band structure that is large enough to be also relevant for plasmon dispersion.

7.4.4. Comparison with the Theoretical Model

The results obtained in the previous section were corroborated by the DFT calculations for a better understanding of the underlying mechanisms. For this, first of all, the preferential adsorption sites for atomic hydrogen were tested. The potential energy surface (PES) for the adsorption of atomic H on the clean Si(557)-Au surface calculated in the group of S. Sanna is plotted in Fig. 7.26 (a). It shows a corrugated energy landscape, with global minima close to the Si step edge atoms and local minima close to the adatom and restatom chains. The PES furthermore suggests that H adsorption on the Au chain is not energetically favorable. Please note that due to the constraints on the atomic relaxation, the PES does not represent the adsorption energy. The latter is obtained starting a structural optimization without any constraint from the minima of the PES.

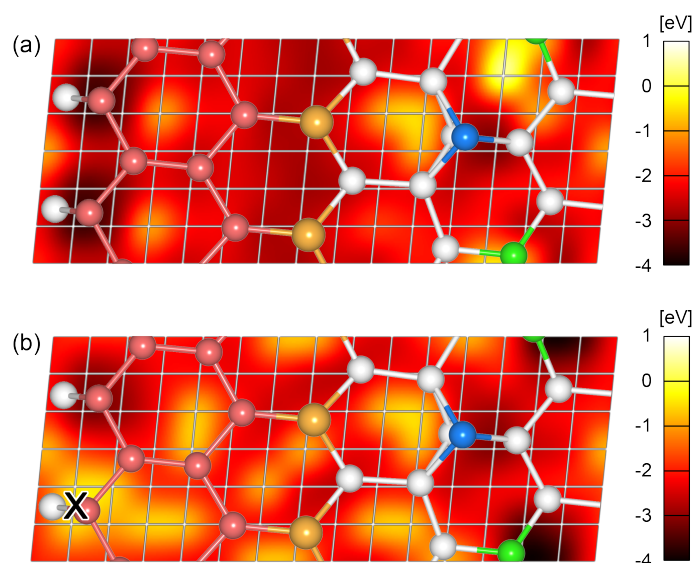


Figure 7.26: PES to define the most preferable adsorption sites for atomic H on Si(557)-Au. (a) PES for the adsorption of atomic H on the clean Si(557)-Au surface. Darker regions mark favorable adsorption sites. The atomic structure of the surface termination is overlaid. Si honeycomb chain atoms are represented in red, Si adatoms in blue, and Si restatoms in green, while other 4-fold coordinated Si atoms are in gray. (b) PES for the adsorption of atomic H, assuming a H atom is already adsorbed at the Si step edge, in the position marked by a cross. The PES was obtained with a fixed surface atoms.

The adsorption energy at the lattice site X is estimated as: $E_{ads} = E_{slab}^{H@Si(557),X} - E_{slab}^{Si(557)} - E_{gas}(H)$. The calculated values are shown in Table. 7.1. Both the adsorption at the Si step edge and the restatom

site are very stable and characterized by very similar energy. H adsorption at the Si adatom also leads to a strong bond with the substrate, although less favorable by about 0.6 eV than in the case of Si step edge atom. Moreover, the H adsorption at the Si step edge changes the global minimum for the adsorption of a second H atom close to the restatom (see Fig. 7.26(b)). Again, the H adsorption on the Au chain is not energetically favorable. In all the configurations investigated, the H adsorption does not significantly modify the morphology of the clean Si(557)-Au surface, which supports the results obtained in diffraction experiments (see Fig. 7.23).

From these calculations, it was concluded that atomic H is adsorbed close to the restatom site and at the Si step edge. However, since adsorption is a random process, and the H adsorption modifies the energy landscape, transient, i.e., metastable occupation of the adatom sites may be occupied with some probability. Adsorption at the gold chain, on the other hand, can be excluded, since the energy difference to the most favorable sites is large.

Table 7.1: The adsorption energy of atomic H adsorbed at different sites of the Si(557)-Au surface. The adsorption energy is given in eV per (5×4) surface unit cell, the bond distance to the closest atom (Si or Au) is given in Å.

Adsorption site	Adsorption energy	Bond distance
Si rest atoms	- 4.65 eV	1.503 Å
Si step edge	- 4.55 eV	1.503 Å
Si adatom	- 3.91 eV	1.507 Å
Au chain	- 3.16 eV	1.823 Å

H-Induced Band Structure Modification — For band structure calculations, a unit cell of (5×4) periodicity was used to model the influence of the H adsorption on the electronic states, as it allows to model more realistic H concentrations. Fig. 7.27(a) shows the band structure of the clean Si(557)-Au surface, calculated for the slab with doubled periodicity in the chain direction. Comparing the band structure with Fig. 7.27(b), both the band folding as well as the origin of the states can be recognized. Again, (now at Γ , due to the folding) the relatively large band gap of 0.33 eV between the Au bands (labeled as (1) and (5) in Fig. 7.27) was observed. With the assumption that not only the plasmonic dispersion is closely related to the unoccupied single-particle band structure, but also that the charge distribution, relevant for plasmonic excitations, closely follows that in these bands, this gap does not allow the plasmon propagation without the presence of the adatom and restatom states (labeled by (2) and (3) in Fig. 7.27) within the gap. Although these states do not close the gap, they reduce it to an extent that the lifetime broadened bands overlap sufficiently to allow a continuous plasmon propagation [27]. In fact, they are also spatially close to the gold states and partially hybridize with them, so that they can act as a “bridge” for the plasmons, and reduce the effective gap to 0.09 eV. To underline these arguments, the squared wave functions at the Brillouin-zone center associated with the bands (1) to (5) were plotted and shown in Fig. 7.29. Now, it can be also observed that the bands labeled as gold

bands (1 and 5 in Fig. 7.27) are indeed a hybrid involving Au and adatom states. However, the band (1) and band (5) have a slightly different degree of hybridization with the adatom states (see Fig. 7.29).

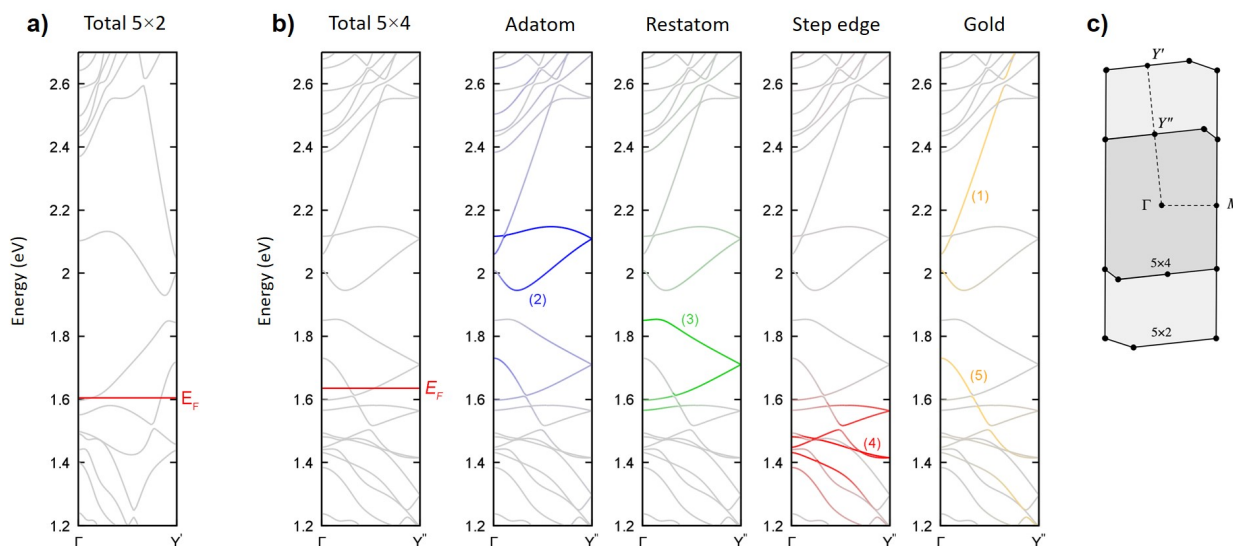


Figure 7.27: (a) Band structures calculated within DFT-PBE for the clean Si(557)-Au surface model with a (5×2) unit cell. (b) shows the band structure calculated for a (5×4) surface unit cell. The left panel of (b) shows the total band structure, while in the remaining panels, the projection of the electronic states into atomic orbitals are represented. The color coding of the surface states denote their localization in real space: bands with strong Si adatom character are blue, bands with strong Si restatom character are green, while states related to Si step edge atoms are red (see Fig. 7.26 for the corresponding structural motifs). (c) illustrates the surface Brillouin zone of the Si(557)-Au surface with (5×2) and (5×4) periodicity.

As seen from Fig. 7.29, the step edge states are localized at a different surface region. Thus, they are not suited to bridge the gap between the Au bands, even if they would have a suitable energy. The H adsorption at all investigated sites modifies the electronic band structure by electron transfer from H to the surface states. This modifies mainly the occupation of states spatially close to the adsorption site. In turn, it has the principal effect of opening (or widening) the band gap between the Au bands in the unoccupied part of the band structure and, most importantly, between adatom and restatom states, in qualitative agreement with the experimental observation. However, the magnitude of this effect is site-specific, since different bands are involved, as shown in detail in Fig. 7.28(b-d). As seen from the energetic considerations described above, the change of restatom and step edge bands by atomic H should play the dominant role on the plasmonic excitation.

The by far largest effect on the band structure is due to H adsorption at the Si step edge atoms, shown in panel Fig. 7.28(b). Moreover, due to charge redistribution, the indirect gap between adatom and restatom states extends to 0.171 eV. The occupation of this site alone, however, cannot explain the experimental finding that plasma frequency is strongly limited at large k_{\parallel} (see Fig. 7.25). H adsorption

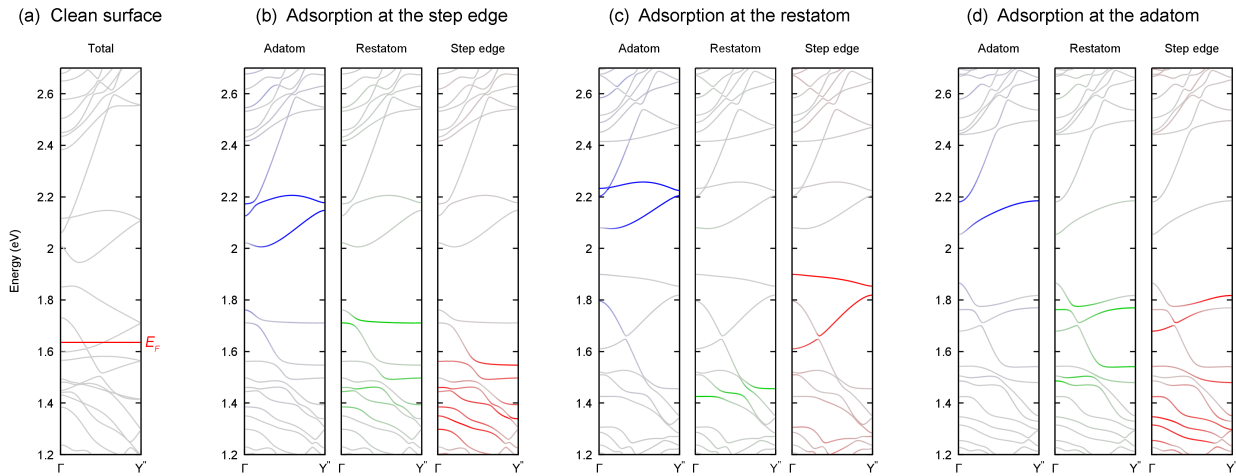


Figure 7.28: (a) Electronic band structure calculated for the clean Si(557)-Au surface using a (5×4) unit cell. (b) Band structure after adsorption of one H atom per (5×4) unit cell at the step edge, together with the projections of the bands onto the individual structural elements, indicated at the top. (c), (d) as in (b), after adsorption of the same amount of H at the restatom and the adatom chains.

close to the restatom, illustrated in panel (c) of Fig. 7.28, has the main effect of shifting downwards the bands related to the restatoms. Before H adsorption, the restatom band is empty and above the Fermi energy. The electron transfer to the restatom bands is counterbalanced by an upward shift of the step edge bands, as the system has to remain charge neutral. This substantially modifies the electronic structure, causing a rearrangement of other bands. As a consequence, upon hydrogenation, the character of the unoccupied band at about 1.9 eV (0.3 eV above E_F at Γ) switches from being mainly located at the restatom to being located at the step edge.

The consequence of the excitation of the plasmons is a frequency cutoff because there is no overlap of this band with the states of the gold chain (see Fig. 7.29). Since the restatom site is the most favorable adsorption site, its occupation by H, together with further upward shifts of other bands, blocks its bridging function of the gap in the unoccupied states. This explains why a clear upper boundary of plasmon excitation appears on the H covered surface. In experiments, it appears at 0.43 eV, slightly higher than the 0.3 eV found in the simulation. Finally, H adsorption at the adatom causes an important electron transfer to an empty adatom band, which is downshifted in the valence band. Correspondingly, as the system has to remain neutrally charged, the filling of the previously occupied bands is reduced, resulting in an upward shift of the bands, as shown in Fig. 7.28 (d). Also, in this case, the widening of the band gap is minor, and amounts to 0.096 eV. Since this state is occupied only to a small fraction, it should not have any dominant influence on the excitation spectrum. Common to all investigated cases is that the strongly dispersive Au bands are not really affected by the H adsorption. This is not surprising, as the adsorption occurs spatially separated from the Au chains.

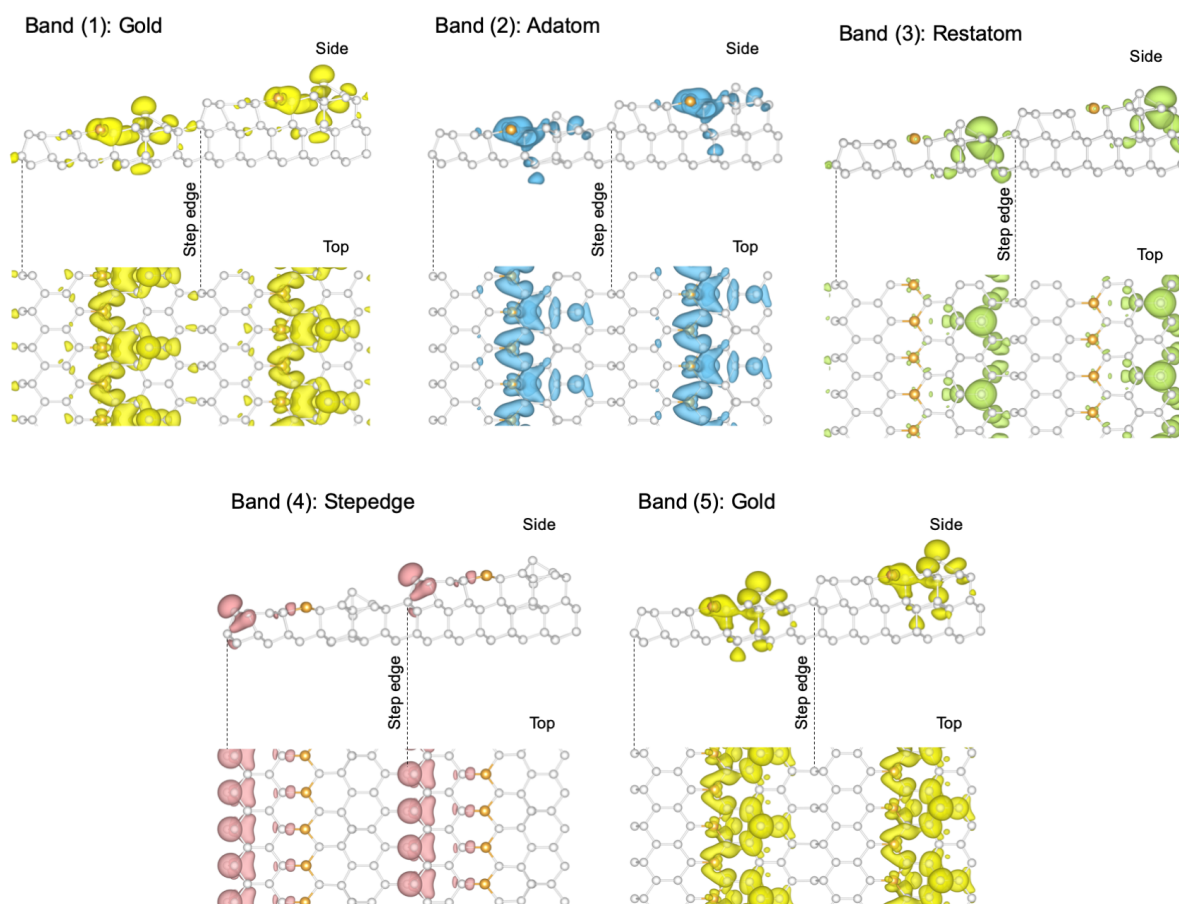


Figure 7.29: Squared wave functions at the Brillouin-zone center associated with the bands shown in Fig.7.27. The corresponds to the electronic bands is depicted with numbering. Color code follows the structural motifs, as given in Fig. 7.26

Increasing the H presence at equivalent surface sites shows that the opening of the band gap is directly proportional to the H coverage. The limiting case is represented by the adsorption of two H atoms per (5×2) unit cell, saturating each band crossing the Fermi energy for the clean surface. Modeling this case, e.g., with one H atom adsorbed at the step edge and one at the restatom, leads to the downward shift of all the half-filled states related to the Si step edge and the restatom. No band crosses the Fermi energy, and the system becomes insulating. This coverage, however, is never reached in the experiments. It was estimated that in the experiments, maximum coverage of 1 H atom per (5×2) unit cell is achieved, which is close to the scenarios described above.

In reality, the adsorption does not necessarily take place in an ordered manner. Fig. 7.26 (b) shows, e.g., that the restatom site is the favored site once an H atom is adsorbed at the Si step edge. In other words, the average and concentration-dependent effect of all the adsorption-induced changes in the band structure discussed so far should be expected in the experiments. It is noteworthy that the

theoretical results discussed above clearly reproduced the band-gap opening, which leads to the plasmon localization in the experiment. This proves the sensitivity of the plasmon spectroscopy to minor changes of the electronic states associated with the whole surface metallicity.

7.5. Modification of the Si(775)-Au Surface

According to the present model, Si(775)-Au possesses structural motifs that exist on both Si(553)-Au and Si(557)-Au surfaces. Therefore, after investigation, the response of those individual systems to additional adsorbates, studying their somewhat combined properties is highly interesting. In this regard, detailed experimental studies for the oxygen and hydrogen adsorbed Si(775)-Au surface have been conducted. Interestingly despite their different nature, the effect of both adsorbates is somewhat similar. This is different in comparison with adsorbate-induced modifications of other similar surfaces (i.e., Si(553)-Au and Si(557)-Au). This behavior shows the unique properties of this system despite several similarities with the mentioned surfaces. These peculiarities were partially discussed in Section 6.4 and will be extended further in this section.

7.5.1. Surface Structure upon Oxygen and Hydrogen Adsorption

First of all, the structural changes after hydrogen and oxygen adsorption were studied by means of SPA-LEED. Diffraction patterns for oxidized and hydrogenated surfaces are shown in Figs. 7.30 and 7.31, respectively. A detailed analysis of this surface was conducted in Section 6.1.2. Like the other systems under investigation, H and O do not alter the periodicity of steps or the macroscopic surface morphology. However, both adsorbates modify the $\times 2$ periodicity, as well as the whole surface quality. Thus, after a specific dose of both adsorbates, the $\times 2$ periodicity is destroyed. Although oxidation destroys the $\times 2$ streaks, the effect of hydrogen is slightly different and increases the $\times 2$ intensity at low concentrations. Interestingly, the results obtained are similar to the response of Si(553)-Au to hydrogenation and oxidation. According to the commonly accepted model, the $\times 2$ streaks originate from dimerized gold chains similar to the Si(553)-Au surface. Therefore, a similar increase of the dimerization parameters is also expected upon the adsorption of atomic hydrogen.

For further insight, the details of the $\times 2$ periodicity as a function of adsorbates were extracted from the 1D line scans along the Au chains. For this convoluted Lorentzian and Gaussian functions were employed after subtraction of a linear background (see Fig. 6.8 for more details about the fit procedure). The results are summarized in Fig. 7.32. The remarkable effect of hydrogenation is the increase of the $\times 2$ intensity up to 20 L H₂ exposure, where it begins to decrease almost linearly (Fig. 7.32(a)). The increase of intensity is similar to the effect of hydrogen on the Si(553)-Au. On the contrary, the correlation length, derived from the FWHM of the $\times 2$ streaks, decreases rapidly and becomes half of its starting value after 5 L H₂ dosage. Therefore, a slight increase in intensity might be caused by the relaxation of the surface upon hydrogen chemisorption. On the other hand, the induced disorder hinders

improvement in the structural parameters. Similar to the other surfaces, oxygen introduces disorder, as seen from the continuous increase of half-width of the $\times 2$ streaks. Thus, after already 3 L O_2 adsorption, $\sim 80\%$ drop of the $\times 2$ intensity is observed. Moreover, an annihilation of step sites is evident from the increased diffuse intensity around the central spike (see Fig. 7.31).

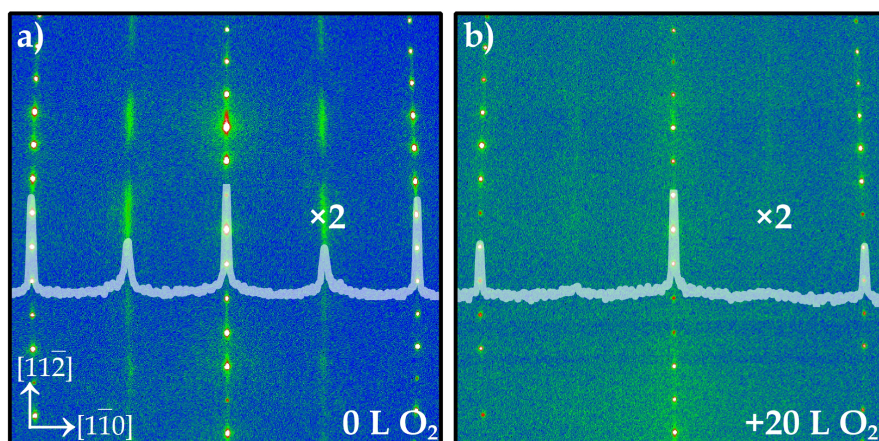


Figure 7.30: SPA-LEED patterns of Si(775)-Au, before (a) and after oxidation (b). Images were recorded at RT with 138 eV primary energy. Line profiles (white lines) were generated by integrating the intensities along $[11\bar{2}]$ for each k point along the $[1\bar{1}0]$ direction and normalization to the central intensity.

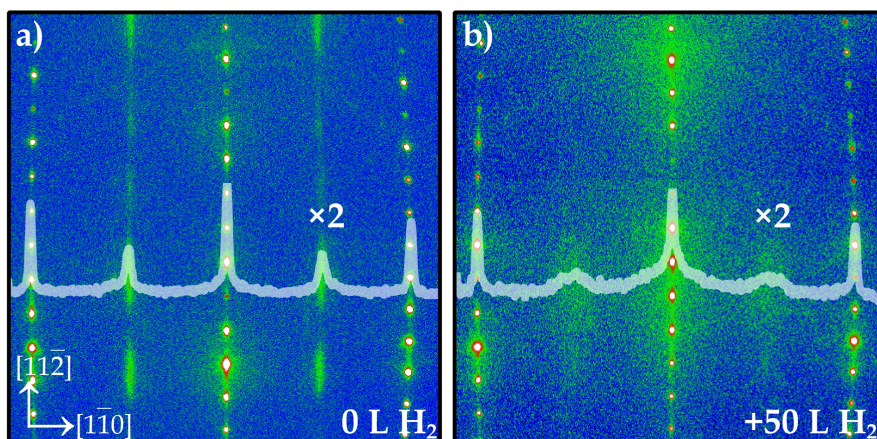


Figure 7.31: SPA-LEED patterns of Si(775)-Au, clean (a) and after 50 L of hydrogen adsorption (b). Images were recorded at RT with 138 eV primary energy. The line scans were generated by integrating the intensities along $[11\bar{2}]$ for each k point along the $[1\bar{1}0]$ direction and normalization to the central intensity.

The correlation length along the Au chains shows an almost linear decrease as a function of oxygen. Interestingly, the observed minimum correlation length (~ 7 nm) after the maximum exposure to O_2 is similar to that obtained after hydrogenation. Here, one should remark that the measured correlation

length from SPA-LEED is susceptible to average imperfections and limited by instrumental broadening.

In general, decreases in intensity and shortening of the correlation lengths are much more severe than other surfaces, in particular the Si(553)-Au. This shows a higher chemical reactivity of this surface in the presence of Si adatoms, which contain two free bonds. The latter was found to be energetically the most preferred site for oxygen adsorption on the Si(557)-Au. In addition, the step edge Si atoms, which contain one unoccupied orbital per atom, are also preferred sites for hydrogen atoms on the Si(557)-Au and Si(553)-Au surfaces. In conclusion, higher chemical reactivity of the Si(775)-Au surface challenges the observation of the structural modifications upon H and O adsorption, which was particularly observed for the hydrogen adsorbed Si(553)-Au (see Section 7.4.1).

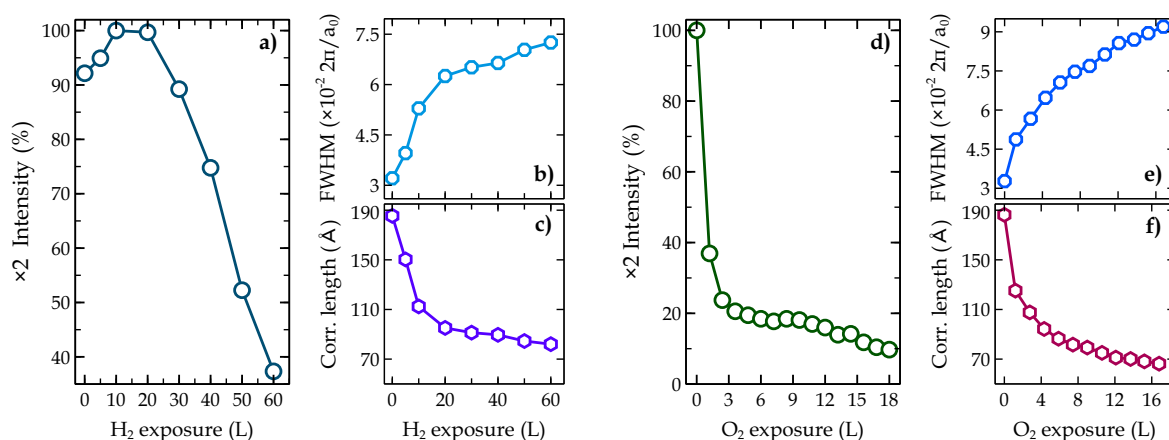


Figure 7.32: Evaluation of the $\times 2$ streaks on Si(775)-Au upon hydrogen (a-c) and oxygen (d-f) adsorption. (a,d) Changes of the $\times 2$ intensity as a function of hydrogen and oxygen adsorption, respectively. (c,f) The inverse of deconvoluted FWHMs, which corresponds to a correlation length along the wires. Parameters have been obtained from individual line scans along the $[1\bar{1}0]$ direction under corresponding exposure after fitting with a set of Lorentz and Gaussian functions, as described in Fig. 6.7.

7.5.2. Plasmon Localization by Adatoms

Exemplary loss spectra for the clean and hydrogen exposed Si(775)-Au surface are shown in Fig. 7.33. This surface shows a well-defined plasmon dispersion, with momentum transfer only parallel to the wires. Plasmonic excitation and dispersion for the clean surface were discussed in Section 6.4. The anisotropy is preserved after oxygen and hydrogen adsorption as well. Due to increased scattering after both exposures, an increase of spectral background and widening of loss curves was observed, in agreement with the diffraction studies (see Figs. 7.30 and 7.31). Moreover, the exponential decay is also reduced upon both exposures. This indicates the saturation of dangling bonds, which leads to a decrease in the available metallic electron density.

The appearance of the vibrational mode at ~ 100 meV proves the chemical interaction between the adsorbate (O or H) and surface atoms. As shown in Fig. 7.33(c,d), the plasmonic signal from the heavily

hydrogenated and oxidized surfaces can be recovered by annealing for a few seconds at 350 °C and 850 °C, respectively.

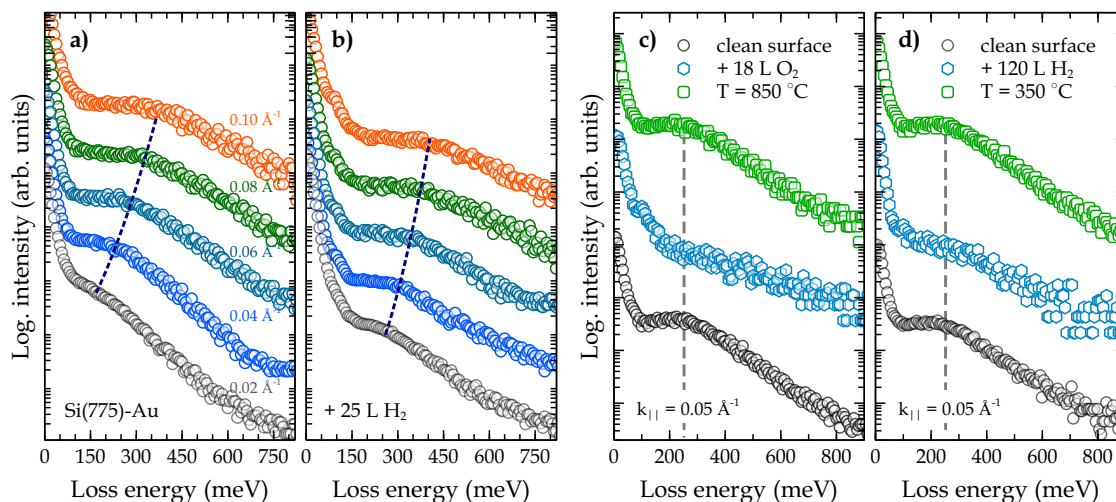


Figure 7.33: Electron energy loss spectra obtained for the clean (a) and hydrogenated (b) Si(775)-Au surface. The dashed lines approximate the plasmon dispersion. (c) and (d) show the temperature-induced recovery of the oxidized and hydrogenated surfaces, respectively. While the hydrogenated surface can be completely recovered by heating to 350 °C, recovery of the oxidized surface requires a much higher temperature, e.g., 850 °C.

The sudden drop of the plasmon intensity, similar to the $\times 2$ intensity upon O_2 exposure, demonstrates the higher reactivity of this surface, especially compared to the Si(553)-Au. As illustrated in Fig. 7.34(c), here only 12 L of O_2 is enough to lose the plasmon signal. This shows that a higher concentration of Si adatoms (or adatom chains) enhances the chemical reactivity of this surface against O_2 by increasing its spontaneous dissociation. Similarly, hydrogenation also broadens the loss width and reduces intensity. In general, changes of the plasmon loss upon gas adsorption is dissimilar to the change of $\times 2$ periodicities in the corresponding gas exposure. Thus, after 3 L O_2 exposure, the $\times 2$ intensity drops by $\sim 80\%$, but the plasmon intensity shows only $\sim 10\%$ decrease. On the contrary, after 20 L H_2 dose, $\times 2$ intensity even increases by 10%. However, at the same dosage, the remaining plasmon loss intensity is only 30% of that on a clean surface. These suggest that the plasmon intensity is sensitive not only to the structural imperfections but also to the electronic modification of the system (i.e., reduced electron density, band gap opening, etc).

As clear from Fig. 7.34(b) and Fig. 7.35(b), plasmon energy at low $k_{||}$ increases rapidly as the exposures start. This can be interpreted as a consequence of two closely related processes. The first is the formation of standing waves in the finite sections of metallic wires, which have been observed for all similar surfaces, discussed in more detail for the Si(553)-Au in Section 7.3. The shortening of correlation length of the $\times 2$ periodicity after H and O adsorption (see Fig. 7.32), as seen in diffraction experiments, directly indicates this effect.

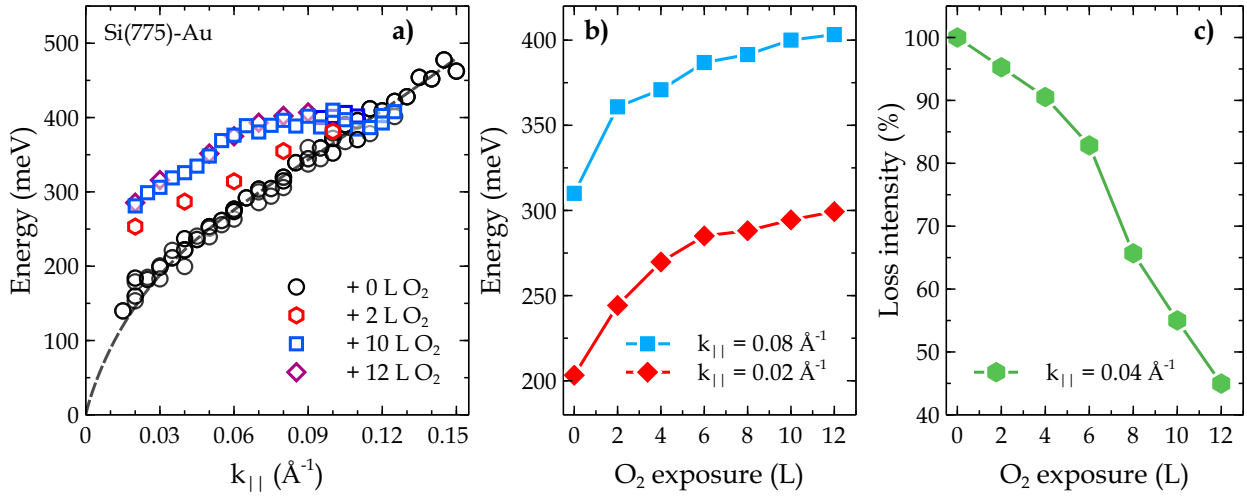


Figure 7.34: Plasmon dispersion for the clean and oxidized Si(775)-Au surface (a). (b) Change of plasmon energy at defined low k ($k_{||} = 0.02 \text{\AA}^{-1}$) and high k ($k_{||} = 0.08 \text{\AA}^{-1}$) points. (c) Change of plasmon loss intensity recorded at $k_{||} = 0.04 \text{\AA}^{-1}$ as a function of oxygen exposure.

However, the wire quality is not the only limiting factor for the extrapolation of plasmon dispersion to $k \rightarrow 0$. There is also the possibility of opening an energy gap in the proximity of the Fermi level. Noteworthy, the increase of plasmon frequency is seen at slightly higher $k_{||}$ values than where the finite-size effect is dominant. Thus, unlike other similar surfaces (i.e., Si(553) and Si(557)), here both adsorbate scale up the plasmon dispersion up to $k_{||} \leq 0.08 \text{\AA}^{-1}$ (see Fig. 7.34 and 7.35). Therefore, the observed increase is most likely due to the band gap opening at E_F . In this case, minimum energy equal to the band gap is required to excite plasmons at $k = 0$. Comparing the oxidized (hydrogenated) and clean surface dispersions, this band gap is estimated to be ~ 100 meV. As seen from Fig. 7.34(b), approximately 6 L O_2 is necessary for the complete opening of this energy gap. However, preliminary band structure calculations have not reproduced this band gap, and therefore its explanation is currently limited to the estimation mentioned above. This question is the subject of ongoing theoretical research.

Now the discussion will continue with the high k ($k_{||} > 0.08 \text{\AA}^{-1}$) region, where a leveling-off of the plasmon dispersion after both adsorbates is observed. This is similar to the hydrogen adsorbed Si(557)-Au surface (see Section 7.4.3). Interestingly, for the present system, this happens after oxygen adsorption as well. Thus, after both adsorption experiments, the plasmon dispersion is leveling off at around 400 meV for $k_{||} \geq 0.08 \text{\AA}^{-1}$. Leveling off at high $k_{||}$ is a clear sign of the plasmon localization, as already clarified for the hydrogenated Si(557)-Au surface in Section 7.4.4. As shown in Fig. 7.34 and Fig 7.35, the leveling off almost saturates after ~ 6 L of O_2 and ~ 45 L H_2 exposures, which indicates the robustness of the localized plasmon mode. This means that the system is highly electronically robust against further modification and survives even after severe structural distortions. According to the current model (i.e., Fig. 6.6), the Si(775)-Au surface shares the same structural motifs as the Si(557)-Au surface but with a double Au strand per terrace. This behavior on Si(557)-Au was explained as

an opening of an energy gap at the unoccupied part due to the occupation of Si adatom and restatom bands. Moreover, the charge redistribution between those surface states reduces the effectiveness of further charge donation.

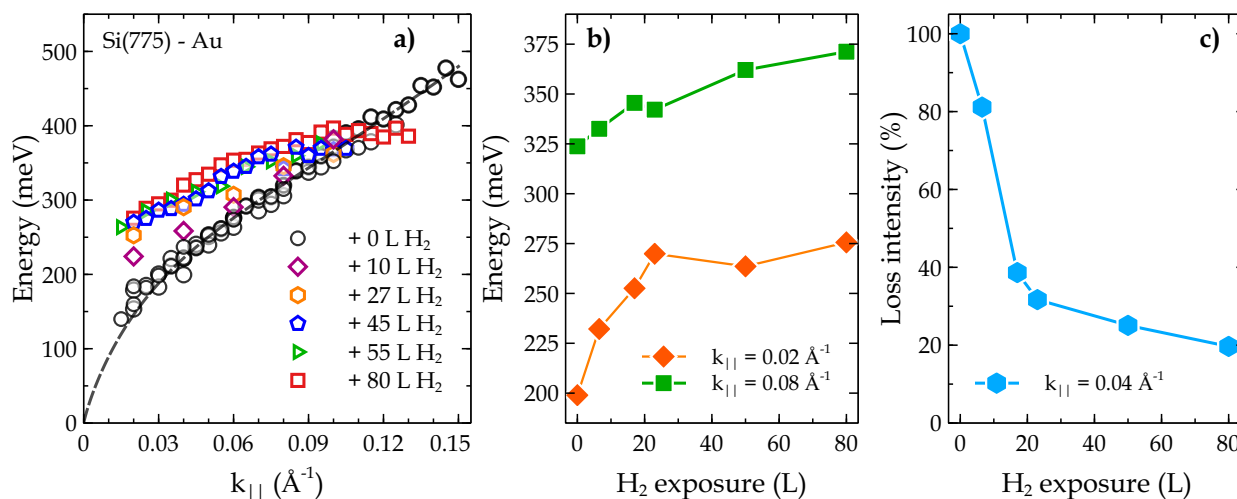


Figure 7.35: Plasmon dispersion of the clean and hydrogenated Si(775)-Au surface (a). (b) shows change of plasmon energy at fixed low k ($k_{\parallel} = 0.02 \text{ \AA}^{-1}$) and high k ($k_{\parallel} = 0.08 \text{ \AA}^{-1}$) points. (c) Change of plasmon loss intensity recorded at $k_{\parallel} = 0.04 \text{ \AA}^{-1}$ as a function of hydrogen exposure.

Comparison with the Theoretical Results — For a detailed analysis of the experimental findings discussed above, theoretical calculations regarding the oxygen and hydrogen adsorption have been conducted in the group of S. Sanna. In the first step, PES was calculated to find the preferable adsorption sites for the H and O atoms. The double-Au chain model (i.e., Fig. 6.6) was used for the calculations. From these calculations, it is concluded that the adsorption of oxygen on the Si-HC chain is energetically the most preferable. It is followed by the Si-adatoms with only 170 meV energy difference. In fact, the small energy difference between these two adsorption sites would not be followed in the experiments. On the other hand, adsorption is a random process, and most likely, adsorption of the first adsorbate atom affects the energetic minimum for the second atom. Adsorption of hydrogen, on the other hand, adsorption above the Si restatom, is the most favorable process. Similar to the other surfaces investigated (i.e., Si(553)-Au and Si(557)-Au), H and O adsorption at the gold chain was found less favorable and can be excluded from further discussions.

To get more insight into the electronic modification, the electronic band structure was calculated for the clean surface and after hydrogen and oxygen adsorption. The results are shown in Fig. 7.36. First of all, the results discussed in Section 6.1.2 were reproduced for the double atomic chain model (see Fig. 6.6). Thus, the individual bands for the Si-adatom, restatom in the unoccupied state are visible at the same energy. Moreover, the gold-related band is strongly hybridized with the band of Si-HC chains close to E_F . In earlier discussions, this hybridization was found to be responsible for a deviation from the

free-electron character. Moreover, the lower energetic situation of the metallic band in comparison to the plasmon dispersion (yellow band in Fig. 7.36) indicates that this band alone can not be responsible for the plasmon dispersion. Therefore, the adatom and restatom bands play an essential bridging function in plasmon propagation within the Si bulk band gap. This scenario is very similar to the Si(557)-Au surface.

After adsorption of one hydrogen atom in the Si-restatom site, its corresponding band vanishes from the band structure (i.e., shifts out of the range of the calculations), as shown in Fig. 7.36(b). On the other hand, the Au-induced band shifts slightly upwards and expands into the band gap. This can be explained as a charge redistribution between the electronic states. Besides, the Si-adatom band moves up ~ 100 meV. However, the Si-HC band changes only a little after hydrogen adsorption. This can be rationalized considering its spatial separation from the adsorption site of H. As a result of the

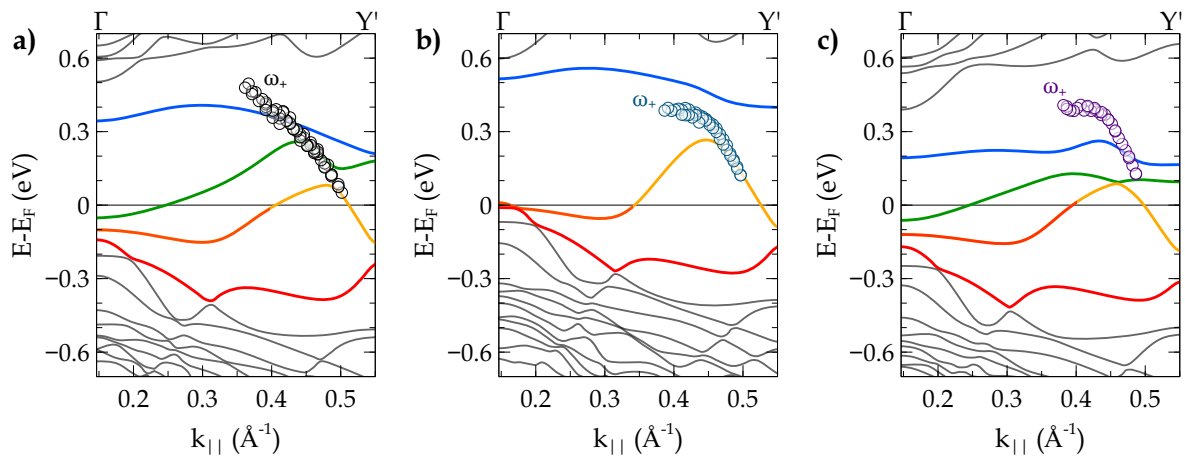


Figure 7.36: Electronic band structure calculated for the clean Si(775)-Au surface (a), after adsorption of one H atom on the Si-restatom (b), and after adsorption of an oxygen atom on the Si-adatom. The Si-restatom band in (a) vanishes after hydrogen adsorption at this site. According to the PES calculations [266], the Si-adatom is the secondary minimum with a small energy difference to the Si-HC. The yellow, red, blue, green and gray bands correspond to the gold, Si-HC, adatom, restatom, and other Si surface states, respectively. For the calculations, the double Au chain model shown in Fig. 6.6 was employed.

changes discussed above, a 150 meV wide electronic gap at ~ 300 meV above the Fermi level is opened. This is partially due to the vanished restatom bands and the resulting renormalization of other bands. Comparing these results with the plasmon dispersion obtained after hydrogenation (see Fig. 7.35), the leveling-off of the plasmon dispersion is semiquantitatively reproduced.

The effect of oxygen adsorption on the electronic bands has also been calculated within this double-Au chain model. [266] Oxygen adsorption on Si-HC is found to be almost ineffective in these calculations. On the other hand, oxygen adsorption close to the Si-adatom, which is the second preferential site, results in a downshift of the Si-adatom, restatom and Au bands (see Fig. 7.36(c)). This rearrangement of

the bands results in the opening of a 300 meV direct band gap in the unoccupied part. Obviously, this huge energy gap is the main reason for the plasmon localization found in experiments (see Fig. 7.34(a)). Nevertheless, the calculated metallic bands after O and H adsorption (yellow bands in Fig. 7.36) show lower dispersion compared to the plasmon dispersion. This is very similar to the clean surface, where plasmon dispersion propagates >100 meV above the calculated bands. Since this energetic difference is reproduced in several calculations, it should be related to the model itself, which is not fully compatible with the experimental results obtained in this thesis (i.e., see Section 6.1.2).

In contrast to H adsorption, there is an apparent discrepancy between the calculated band structure and plasmon dispersion, as shown in Fig. 7.36(c). First of all, the bands associated with the plasmonic excitation can not be identified. In addition, the Si-atom and restatom bands in the unoccupied part are almost flat, and their contribution to the plasma excitation is also questionable. Moreover, there is no indication for a band gap opening close to E_F in these calculations. This finding may be an indication that the model used is incorrect and needs further optimization.

Indeed, this model also contradicted the experimental diffraction pattern (see Section 6.1.2). Moreover, the low k part of the clean dispersion, which shows higher extrapolation, could not be explained within this model. On the other hand, the overall slope of the clean surface dispersion could only be satisfactorily matched to the calculated band structure. [31] Therefore, only a qualitative interpretation of the opening of the band gap in the unoccupied state can be drawn from the current calculations.

Overall, despite sharing the common structural elements (i.e., according to the current double-Au chain model) with other investigated surfaces, this surface shows a different response to H and O adsorption. This proves that the properties of such atomic wire systems should not be restricted to individual structural building blocks. While an interaction, response, and relaxation (or redistribution of charge density) happen as a well-defined mechanism by involving the whole surface atoms.

7.6. Summary and Conclusion

In summary, this chapter reported on the interaction of atomic wire systems with oxygen and hydrogen. The obtained results demonstrated a practical approach for the fine-tuning of atomic wire properties by modifying mainly the substrate regions that are not in close proximity of the ultimate chains. For this, earlier discussed concomitant interactions between the atomic wires and embedded media were extensively studied.

Noteworthy, all tested surfaces preserve metallicity even after heavy oxidation. In this regard, the Si(557)-Au and Si(775)-Au surfaces show unique robustness because of site-specific oxidation, which leads to renormalization and charge redistribution between specific bands. Although calculations and experiments are not strictly comparable due to the assumption of ordered oxygen arrays adsorbed on specific sites, the developed theoretical approach enabled the description of a kinetic sequence of preferential adsorption. On the other hand, oxidation of Si(553)-Au causes mainly the shortening of the chain lengths. However, the shorter wire sections still possess metallicity that is accessible with IR-absorption at $k = 0$. Although the optically excited mode is not propagating, so-called standing wave plasmons still show strong anisotropy, i.e., it can be excited only with the polarization parallel to the wires.

It was found that the systems with Si-atom and restatom chains (i.e., Si(557)-Au and Si(775)-Au surfaces) show metallicity that highly depends on these structural motifs. Although they do not directly interact with the Au-made structures, their saturation leads to a band gap opening and plasmon localization. On the other hand, H doping Si(553)-Au mainly results in the opening of a band gap due to an indirect charge transfer to the Au-related bands. Since the magnitude of the band gap is linearly cross-coupled with dimerization amplitude, charge doping leads to structural improvement of Au chains. By employing the NFEG model with the established methodology, the experimental plasmon dispersion was used to describe the excited-state band structure. It is noteworthy that almost quantitative agreement was achieved between hydrogen-induced modification of plasmon dispersion and calculated band structure for the Si(553)-Au system.

In conclusion, the discussed results showed that the influence of atomic hydrogen goes far beyond the simple charge transfer. Similarly, oxidation does not merely result in a charge localization. In both processes, charge transfer and redistribution, as well as rearrangement of the corresponding bands were observed. Interestingly, despite many similarities of the investigated surfaces, the local structural arrangement of different motifs determines the interaction mechanism with an additional adsorbate. This indeed shows the peculiarity of such atomic wire systems. This chapter showed that the remaining metallicity after interaction with the embedding media can successfully be tuned employing the interaction between the Au chains and the rest of the environment. This tuning is essential for fundamental quantum physics as well, as it brings such systems closer to the use in nanoelectronics. The unexpected effect of doping on metallicity also opens fundamental questions about the diversity of adsorbate-surface interactions.

Chapter 8

Self Doping of Atomic Au Wires

As seen in the previous chapter, the doping of these systems in particular Si(553)-Au, with atomic hydrogen tends to improve the quality of the dimerized Au chains. In order to further analyze such a fundamental relationship, this chapter focuses on the effect of Au doping on the Si(553) surface. In this regard, changes in the surface morphology and/or local structural landscape will be discussed extensively on the basis of the SPA-LEED results. This will be followed by a modification of the plasmon dispersion and its relationship to the electronic band structure. Discussions on electronic and structural cross-coupling will be further enhanced by atomistic DFT calculations.

8.1. Electronic and Structural Cross-Coupling on Si(553)-Au

The cross-coupling and/or correlation of structural and electronic parameters have already been addressed in Sections 6.3 and 7.4.2. Such coupling is more pronounced for Au atomic chains on Si(553). This surface possesses two proximal dispersive electronic bands originating from the Au states, which are characterized by the anticrossing interaction, resulting in the occurrence of an electronic band gap of about 0.1 eV at about $k_{\parallel} = 0.3 \text{ \AA}^{-1}$. This small band gap has been previously predicted by similar calculations [24]. It is worth noting that although there is experimental evidence of this band gap [27, 30] it has not been addressed more precisely yet. To understand the origin of the crossing/anticrossing behavior, DFT calculations were done by S. Sanna, where the opening of this gap was found to be in coherence with a structural feature. Thus, the principal degree of freedom of the double gold chain is the magnitude of the dimerization. Calculating the band structure for differently dimerized chains were found that the value of the band gap is directly related to the dimerization, as shown in Fig. 8.1. These results show that the crossing/anticrossing of the Au bands has a physical origin, which is highly related to structural parameters of the double Au chains. However, its magnitude crucially depends on

the details of the calculation. A pronounced substantially linear dependence of the band gap on the chain dimerization is found. Since the dimerization of the Au chain is directly related to the magnitude of the lattice constant of the substrate, as $d = (a_1 - a_0/a_0)$, it, therefore, depends indirectly on the formulation of the XC functional in DFT modeling. DFT–LDA calculations tend to underestimate the Si lattice constant, resulting in a pronounced dimerization of 0.118. In contrast, DFT–GGA calculations overestimated the Si lattice constant, resulting in a dimerization that is one order of magnitude smaller. [25]

As mentioned above, dimerization and band gap opening in the vicinity of $E = 0.7$ eV above E_F are linearly related, starting from a very small value for the clean system (see Fig. 8.1). This cross-coupling of the structural and electronic properties was discussed for the doping of this system with atomic hydrogen in Section 7.4.2. In this regard, the following results showed that this behavior could be demonstrated more effectively by doping the Si(553)-Au surface with surplus Au coverage. Considering that the metallicity of this system is due to the Au-induced superstructures, this doping is called self-doping.

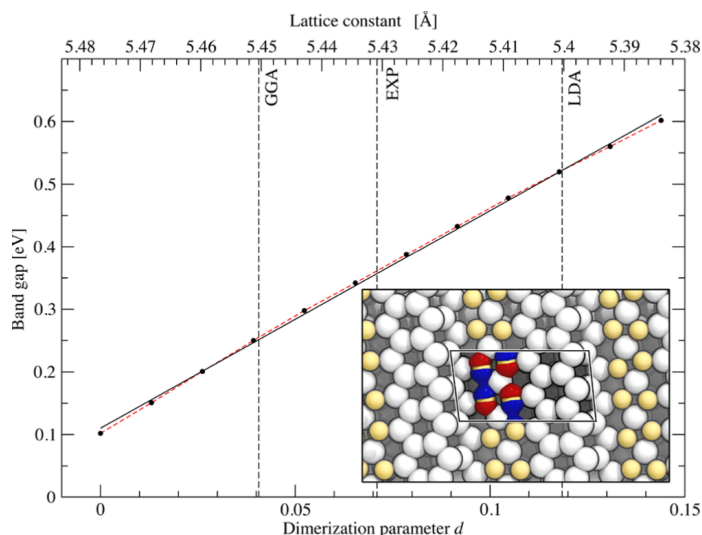


Figure 8.1: The magnitude of the band gap between the Au states as a function of the chain dimerization. Inset shows the electronic charge density difference between the dimerized and nondimerized Au chain. Blue regions indicate charge accumulation, while red regions indicate charge depletion. The isosurfaces ± 0.04 e/Å³ are shown. Si atoms are white, and Au atoms are yellow. The (5×2) surface unit cell is highlighted. Adapted from Ref. [27].

8.1.1. Enforced Long-Range Atomic Ordering

LEED image for the as-prepared Si(553)-Au surface with 0.48 ML of Au is shown in Fig. 8.2(a). The observed diffraction pattern was discussed in Section 6.1.1. The sharp and round integer order spots originate from Si step trains, while the $\times 2$ streaks belong to the dimerized Au chains.

The LEED pattern after deposition of surplus 0.04 ML Au at RT is given in Fig. 8.2(b). It shows no change of step train or its periodicity, but an increase of intensity and narrowing and straightening of the $\times 2$ streaks is noticeable. Similar behavior on this surface was also observed upon hydrogenation (see Fig. 7.15).

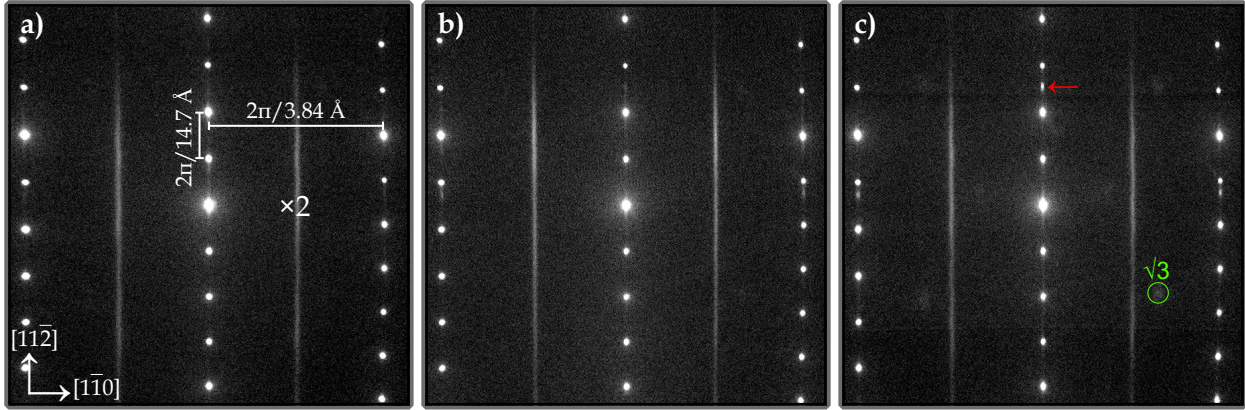


Figure 8.2: SPA-LEED patterns of the Si(553) surface with an optimum 0.48 ML of Au coverage (a), after deposition of 0.04 ML of Au surplus at RT (b) and after subsequent annealing of the latter surface at 650 °C for 1 second (c). The images were recorded at RT with primary energy of 138 eV. The new facet and $\sqrt{3}$ spots are depicted with the red arrow and green circle, respectively.

Similarly, no substantial changes in surface periodicity were observed when the Au concentration was increased further at RT. But heating the surplus Au deposited surface to ≥ 600 °C leads to appearance of a $(\sqrt{3} \times \sqrt{3})R30^\circ$ structure. By a further increase of sample temperature up to 900 °C for a few second, it is possible to desorb (and/or diffuse) small amounts of surplus Au. Annealing at this temperature leads to the disappearance of $\sqrt{3}$ -spots but also brings back the original width and intensity of the $\times 2$ streaks. Noteworthy, such structural recovery works perfectly up to 0.04 ML surplus Au coverage. Although for the higher surplus Au coverages $\times 2$ is still recovered upon annealing, the $\sqrt{3}$ spots gain more intensity and triangular shape, which is the signature of gold islands formation [183,267]. Overall, the discussion presented above shows the instability of this surface due to additional Au concentration. Such instability induced by excess adsorbate atoms can be generalized for the Si(hhk)-Au systems (e.g., see Fig. 6.10). And it underlines the crucial role of the adsorbed Au concentration for stable and perfect wire ordering.

In order to get more insight into the structural modifications of this surface upon surplus Au deposition, the correlation length for the $\times 2$ periodicity was deduced from the 1D line scans along the $[1\bar{1}0]$ direction. For this, the line profiles were fit with the convoluted Lorentzian and Gaussian functions, as described earlier in Fig. 6.7. The results from this fitting routine are shown in Fig. 8.3(b), and (c). Up to 0.04 ML surplus Au coverage, the correlation length increases by a factor of 1.6 to a maximum value of 32 nm, whereas further adsorption of Au leads to a sharp reduction of this quantity. Similar behavior is also seen for the intensity of the $\times 2$ streaks, as shown in Fig. 8.3(c). The enhanced correlation length

and increase of intensity are presumably coupled with a loss of correlation of the $\times 2$ periodicity between the adjacent terraces.

When exceeding the amount of Au, both correlation lengths and intensities drop quickly, meaning that now the effect of disorder introduced by the additional gold atoms dominates over all other effects. This behavior was observed in hydrogen adsorption as well. Hydrogen, however, did not introduce a new facet even at extremely higher concentrations. Moreover, annealing of hydrogenated surface to $T > 350^\circ\text{C}$ resulted in desorption of hydrogen without significant disorders.

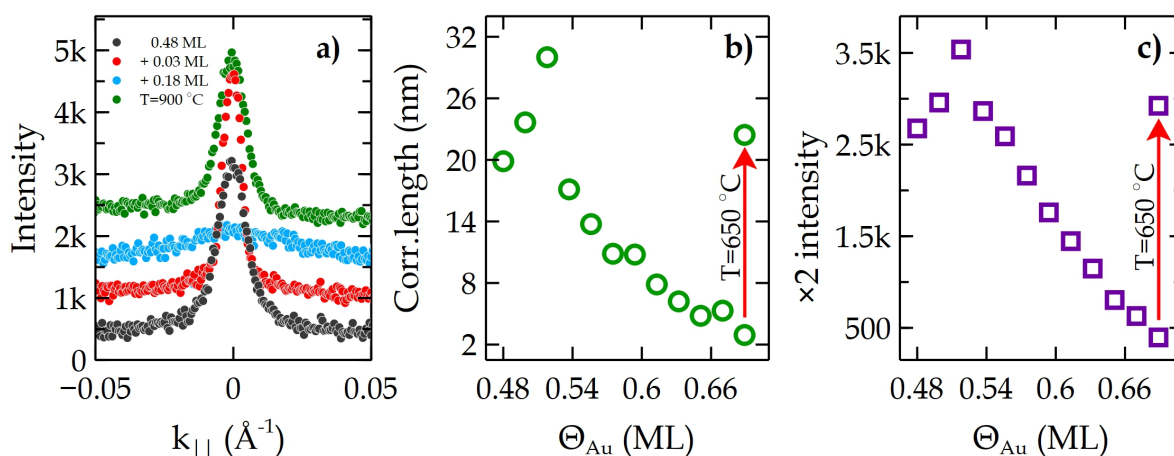


Figure 8.3: Spot profiles (a), correlation length along the Au chains (b), and changes of $\times 2$ intensity (c) as a function of surplus Au deposition. Data set were deduced from line scan in the $(\bar{1}\bar{1}0)$ direction after fitting with convoluted Lorentzian and Gaussian functions. The correlation length is given as the inverse FWHM of the Lorentzian function.

In contrast to the hydrogenation, when annealing a sample with a total Au coverage of 0.52 ML (or more up to 0.68 ML) to 650°C or when directly preparing the Au layer at this temperature, an admixture of $(\sqrt{3} \times \sqrt{3})R30^\circ$ structure was found. Both intensities and half-widths of the $\times 2$ streaks were restored (i.e., they get wider again) by this annealing step (see Fig. 8.3). In other words, the surplus Au atoms phase separate from the atomic wires and coalesce into small islands with $\sqrt{3}$ structure that has a local concentration of 1 ML [183]. This indicates that the surplus Au atoms are not incorporated into the dimerized Au chains, since the destruction of Au chains requires much higher temperature (i.e., $T > 950^\circ\text{C}$). Therefore, the structural improvements upon surplus gold deposition at RT can also be electronically driven due to charge transfer to the surface states, as it was already explained for H adsorption (see Section 7.4.2).

It should be stated that the formation of larger $\sqrt{3}$ -islands is not possible without changing the step morphology. This is clearly seen when annealing a 0.15 ML surplus Au layer to 520°C . New periodicities with wider average terrace widths appear as obvious from the spot profiles recorded perpendicular to the steps shown in Fig. 8.4. These partly disappear after annealing to 930°C due to a loss of Au coverage by partial desorption (and/or diffusion). Followed annealing of surplus surface forms $\sim 3 \times 14.7$

\AA wide larger terraces due to step bunching. Subsequently, the thermal annealing relocates Au atoms from initially random distribution into periodic $(\sqrt{3} \times \sqrt{3})R30^\circ$ structure at the newly formed larger terraces. The $\sqrt{3}$ structures show periodicity of $\sim 20 \times a_{\parallel}$ along terraces. Even after heavy doping and subsequent annealing, the macroscopic (553) orientation still survives (see the orange curve in Fig. 8.4). The subsequent annealing, however, introduces a huge diffuse background that shows the destruction of steps (see the red curve in Fig. 8.4).

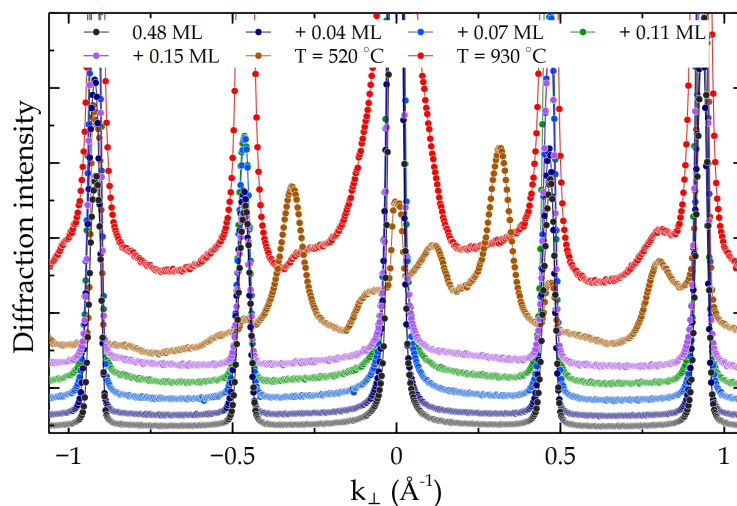


Figure 8.4: 1D diffraction profiles recorded perpendicular to the steps. There is no qualitative change after deposition of surplus gold at RT. Whereas, subsequent annealing gives rise to a new periodicity and introduces a clear diffuse background to the first order spots. The intensity is given on a linear scale. The spectra were shifted upward for better visibility.

Another interesting consequence of this annealing step is the appearance of the $\times 3$ streaks, which has been previously observed at only low temperature for the optimum surface coverage. At low temperature, it is associated with the spin-polarized Si step edge atoms, which are, however, destroyed by thermal fluctuation at finite temperature. Please note that this feature has also been observed for the Si(775)-Au surface at higher Au concentrations (i.e., ≥ 0.65 ML Au) (see Section 6.1.3). Although no detailed investigation has been carried out to find the origin of these streaks, it may be associated with additional Au atoms adsorbed right at the edges of the steps. In fact, this statement is consistent with the results of the total energy calculation, which shows the step edge as the most preferred adsorption site for additional Au atoms.

The experimental results discussed above can be well understood from the structural optimizations, searching for the minimum of the total energy in DFT calculations, after adsorption of one extra gold atom into the (5×2) unit cell. As a first step, and in order to get an overview, the PES for adsorption of an additional gold atom in this unit cell was scanned at different positions, shown with pointed greed leaving the positions of all other atoms in the unit cell fixed. It is shown in Fig. 8.5. A clear preference for adsorption on the distorted Si honeycomb-chain right above the step edge was found. Similar to

hydrogen adsorption, Au sites are less favorable by around 2 eV compared to Si-HC chains.

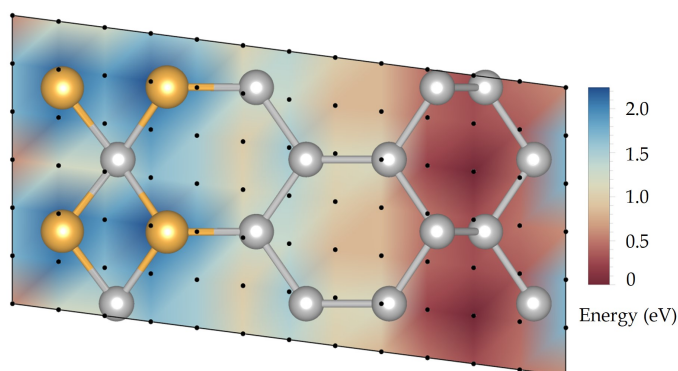


Figure 8.5: Potential energy surface for adsorption of one additional Au atom. The darker areas at the step edge correspond to the most favorable site for the first additional Au atom. The black dots represent the positions tested for an additional Au adsorption.

A complete structural optimization was carried out based on these results, which is shown in Fig. 8.6. The Au adsorption induces a notable structural modification at the honeycomb chain central atoms next to the adsorption site. These two Si atoms (green balls in Fig. 8.6) are moved downwards and towards the Au chain. This rearrangement was not observed with H adsorption. Most likely, the much higher mass and size of the Au atoms in comparison to H play a crucial role in local relaxation. On the other hand, the additional chain of Au atoms at the step edge not only modifies the structure there, but also has a strong influence on the structure of the existing double-chain in the center of the terrace. The now asymmetric dimerization of the double chains is strongly enhanced as illustrated in Fig. 8.6(b). According to the results of this calculation, the increase of the dimerization after Au adsorption is two times stronger than the case of H adsorption. This qualitatively agrees with the experimental results, which also showed strong development of the correlation length after Au adsorption. The scenario just mentioned implies that the structural enhancement upon surplus Au adsorption is not only due to the indirect effect of the charge donation and band gap opening, but structural relaxation induced by heavy Au atoms is also effective. In fact, this is the main difference between Au and H doping of the Si(553)-Au surface. In addition, the asymmetric dimerization of Au chain (e.g., $d_1 \neq d_2$ in Fig. 8.6(b)) after adsorption of additional Au atoms at the step edge also evidences the stronger effect of Au than H.

In the experiment, surplus Au atoms at small concentrations up to 4% ML, seem to have a similar effect, although they reconstruct the surface much more strongly than atomic H, and thus are more efficient than H. Unfortunately, when going to higher Au concentrations, disorder comes into play and finally dominates, since these layers cannot be annealed without inducing structural changes to $\sqrt{3}$ -islands. The same holds for H, but again only at a significantly higher concentration, as visible by a quick drop of correlation lengths and intensities when increasing either H or Au concentration beyond their respective maxima. However, no new periodicity was observed upon H adsorption.

In real samples, stacking faults occur in the Au dimerized chain, which break the long-short sequence

of the Au pairs. Stacking faults lower the structural order and/or long-range correlation by inverting the Au dimerization phase, as schematically represented in Fig. 8.6(c), and cause the smearing of the diffraction spots in electron diffraction. Notably, DFT calculations revealed that the formation energy of a stacking fault rapidly grows with the Au dimerization. Therefore, formation of stacking faults in doped chain (II in Fig. 8.6(c)) is energetically less favorable than the undoped chain (I in Fig. 8.6(c)). Thus, doping of chains, particularly with extra Au, makes them more stable against defects and even recovers the existing ones and improves the chain quality. [227] This finding shows interesting intrinsic cross-coupling of electronic and structural properties, which certainly leads to self-healing and further enhances the structural order as indeed observed experimentally (see Fig. 8.3).

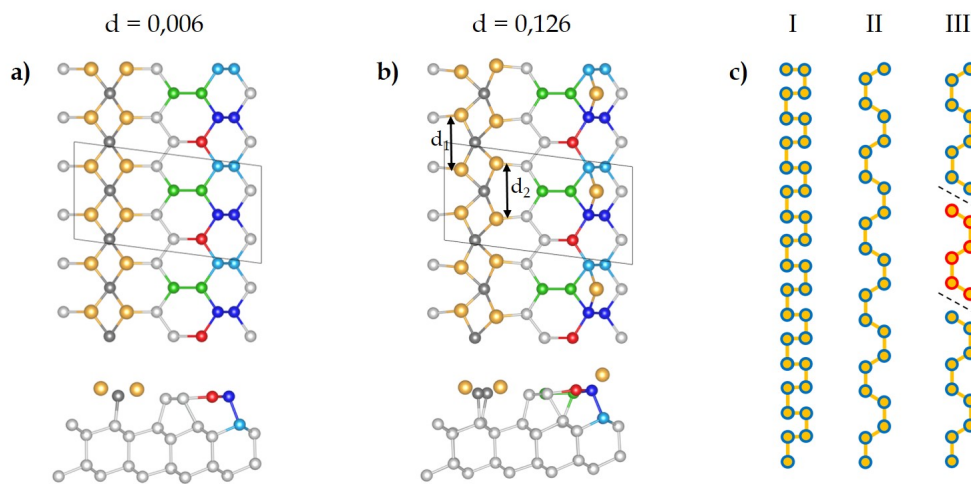


Figure 8.6: Structural model for Si(553)-Au, before (a) and after adsorption of additional Au atom at the step edge (b). The bottom panel displays a side view of the corresponding model. The gray rhomboid depicts the 5×2 unit cell. Atoms are colored in order to make the structural changes visible. The dimerization parameter d (averaged in (b)) is given at top of the corresponding image. With an extra Au atom per 5×2 unit cell, the total surface coverage in (b) corresponds to 0.6 ML. Au atoms are given in yellow, the rest are Si atoms. (c) Schematic representation of the Au chains, before (I), after Au adsorption (II), and with an antiphase segment between two idealized stacking faults (III).

8.1.2. Electronic Modification

The detailed description of the plasmon dispersion of Si(553)-Au has already been discussed in Section 6.3. Here, the effects of doping with additional Au will be discussed, which shows particularly interesting behavior. Electron energy loss spectra from the freshly prepared surface with 0.48 ML of Au is shown in Fig. 8.7(a) together with those after doping with various Au concentrations at room temperature. The increase of Au concentration beyond the optimum 0.48 ML with surplus Au results in a strong redshift of the plasmon frequency as a function of Au surplus concentration. This change of plasmon frequency is quantified at a fixed k_{\parallel} value in more detail in Fig. 8.8. This redshift is not

limited to this selected k_{\parallel} point, but generally reduces the slope of the plasmon dispersion, as shown in Fig. 8.7(b). From Fig. 8.8 (a), it is obvious that already the smallest amount of additional Au leads to a redshift, which increases non-linearly as a function of Au surplus concentration. Interestingly, and similar to the LEED intensity of the $\times 2$ streaks, the plasmon loss intensity (see Fig. 8.8 (b)) goes through a maximum at small surplus Au coverages before it drops quickly so that no quantitative measurements are possible any more above a surplus concentration of 0.12 ML. Also, this maximum in plasmon loss intensity is ascribed to improved ordering as small excess Au concentrations, presumably because of stronger dimerization that makes the Au chains vibrationally more rigid. The reduced intensities at higher Au concentrations also limit the accessible k -range. They are most likely the result of disorder introduced by presumably random adsorption of Au surplus atoms at RT. This was also observed for the H adsorbed surface (see Fig. 7.18).

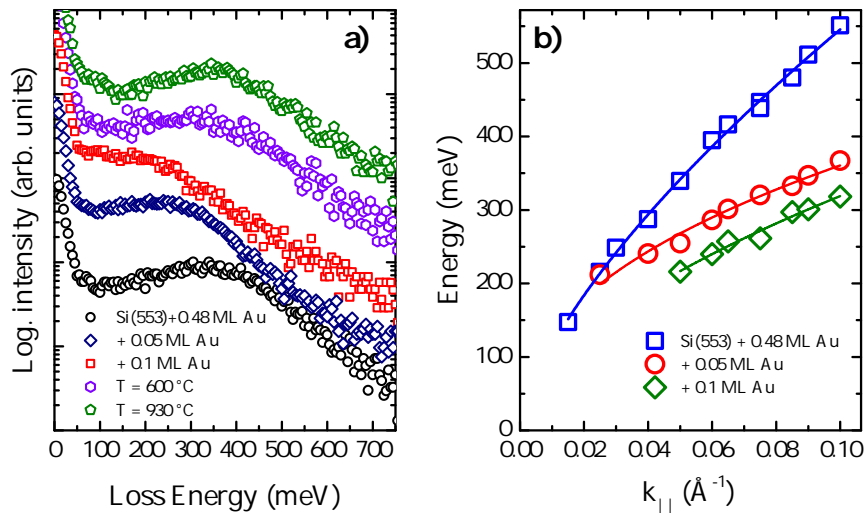


Figure 8.7: (a) Exemplary momentum resolved electron energy loss spectra from the clean Si(553)-Au and as a function of Au doping and annealing. (b) Plasmon dispersion obtained for the clean and after adsorption of surplus Au coverages at RT.

Similarly, the measured FWHMs of the plasmon losses go through a minimum at small excess Au concentrations before they increase (Fig. 8.8(c)), which supports the suggested improved ordering. The increase of FWHM as a function of Au excess coverage above 0.05 ML must then be due to the increasingly dominating effect of disorder, which also leads to an increase of measured plasmon losses in the limit $k_{\parallel} \rightarrow 0$ (see Fig. 8.7). The latter is only indicated in the presented measurements because of too low intensities at small k_{\parallel} and high Au concentrations.

Similar to the LEED observations, annealing of the surplus layers brings back the plasmon intensity, peak width, and the original plasmon dispersion curve measured for a Au concentration of 0.48 ML. Heating to 600 °C already turned out to be sufficient to bring back 90 % of the initial intensity. At these temperatures, no desorption takes place, but thermal diffusion allows the redistribution of the surplus

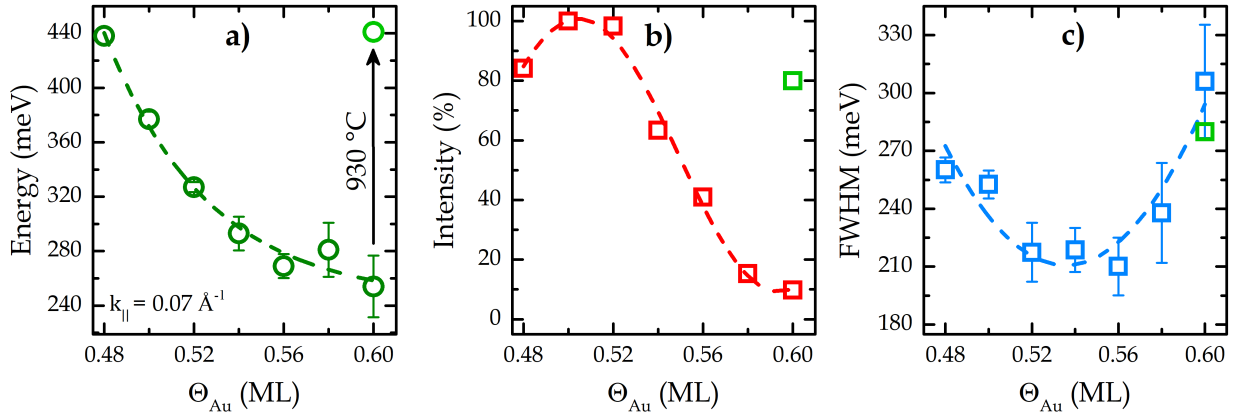


Figure 8.8: Changes of the frequency (a), loss intensity (b) and FWHM (c) of the plasmon loss on Si(553)-Au as a function of surplus Au coverage measured at $k_{\parallel} = 0.07 \text{ \AA}^{-1}$. The light green data points in all graphs were obtained after annealing of the doped surface at 930 °C. Dashed lines are only guide to the eye.

Au atoms. This is consistent with the LEED studies, which showed agglomeration of excess Au atoms into $\sqrt{3}$ structure. The wire plasmons turned out to be ultimately reversible upon annealing at 930 °C. There is no low-energy plasmonic signal detectable from the $\sqrt{3}$ -islands formed during annealing. Since they are still 2D-objects [183], and the plasmon energy for a metallic 2D object has to go to zero in the long wavelength limit, these Au islands have to be insulators. This also supports the fact that the Au atoms adsorbed at the step edges act as a charge reservoir for the metallic states, but their relocation into insulator packs breaks up this charge transfer channel. Therefore, the doping-induced effects (e.g., enhanced dimerization, redshift of plasmon frequency, etc.) are restored by annealing at high temperatures. Additionally, considering the cross-coupling between the electronic gap opening and dimerization amplitude, the results mentioned above indicate the band gap opening. The opening of a band gap is also supported by the reduction of the overall plasmon dispersion curve, as shown in Fig. 8.7(b).

In order to address the electronic modification in more detail, electronic band structures for the clean and one additional Au adsorbed surfaces (shown in Fig. 8.6) were calculated. The resulting band structures are shown in Fig. 8.9. At first glance, charge doping to metallic surface states brings about a band gap opening at the unoccupied electronic band structure and indirectly increases dimerization or wire quality in order to preserve the metallicity. Thus, an additional Au atom extends the energy gap to 350 meV in the unoccupied states, which is 2.5 times larger than 1H atom adsorption in the same unit cell. Due to the linear relation between band gap and dimerization parameter d , the latter also gets $2.5\times$ higher value. This again proves that the structural improvement after Au deposition is an indirect consequence of band gap opening, similar to H. However, the effect of Au adsorption is not limited to the band gap opening but strongly modifies the rest of bands resulting in 100 meV indirect band gap formation. Furthermore, the slope of the metallic band is also reduced. For the direct

comparison of experimental and DFT results, ω_+ is calculated from the plasmon dispersion using the procedure described in Section 2.2.1. As already shown in Section 6.3.1, there is only one unoccupied band ($S_{1,2}$ above E_F in this system, and ω_+ should coincide closely with this band according to the theoretical approach discussed in Section 2.2.1. The upper boundary of the single-particle excitations as extrapolated from the experimental plasmon dispersion of the clean and adsorbed system is shown Fig. 8.9. As shown there, ω_+ is almost quantitatively agrees with the calculated band structure. This again confirms the sensitivity of the plasmon spectroscopy to modification of the electronic bands mainly close to the Fermi level. Noteworthy, the slope of ω_+ indicates the widening of the band gap after surplus Au adsorption. This strong match validates the structural model optimized for Au adsorption and supports the underlying mechanism for reducing metallicity and enhanced structural parameters.

In this scenario, just described, the effect of surplus Au concentration can be interpreted in two steps: At the small surplus concentrations (up to 0.05 ML), the modification of the surface properties is dominated by doping. While at higher concentrations (~ 0.1 ML), modification of the structural parameters goes beyond the doping picture. Besides, calculations revealed that the enhanced dimerization makes the Au chains harder and less prone to stacking faults. This effect can be interpreted as a self-healing of the Au chain.

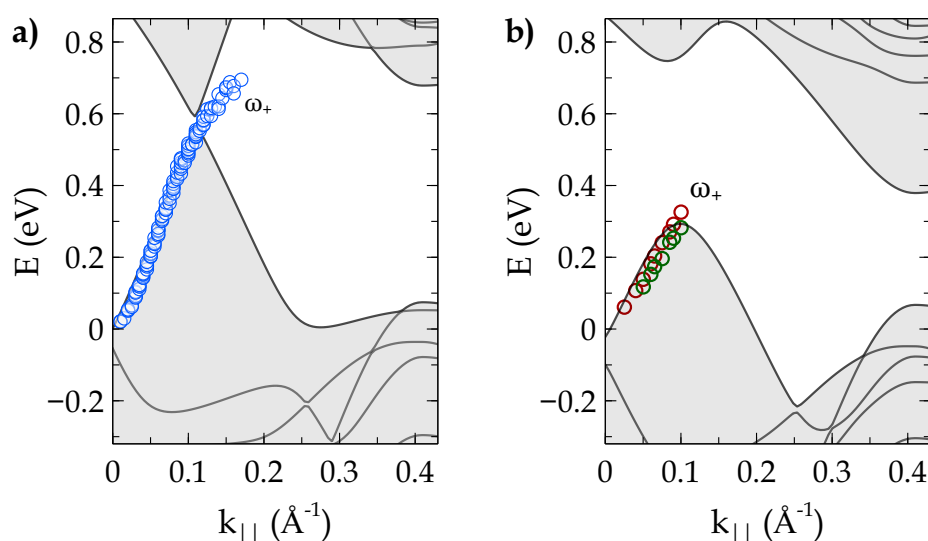


Figure 8.9: Electronic band structures calculated for the HCWs phase on Si(553)-Au. (a) before and (b) after adsorption of an additional Au atom at the step edge. In both graphs, $E = 0$ corresponds to the Fermi energy. The upper boundary of the electron-hole continuum (ω_+) calculated from the plasmon dispersion (Fig. 8.7) for the clean (blue circles), at a surplus 0.05 ML (red circles) and 0.1 ML (green circles) Au deposited surfaces are shown.

8.2. Summary and Conclusion

Doping of the Si(553)-Au system with a surplus Au concentration was discussed in this chapter. It was found that at low surplus Au concentrations, the electronic and structural improvements are similar to the doping with atomic hydrogen. However, Au atoms introduce a structural relaxation that has not been observed upon H adsorption. Hence, this relaxation further improves the dimerization of Au chains, which also strongly increases the energetic cost of defect formation in the chains. This results in a spontaneous self-healing of defects such as stacking faults within the chains, so that long-range order can be enhanced even by random adsorption.

Besides, excess surplus Au concentration destabilizes the stepped orientation of Si(553)-Au by forming large terraces with a presence of $\sqrt{3}$ structures. The structural enhancement at small surplus Au coverage and disorders at higher surplus Au coverage are reversible by annealing at high temperature.

The informational content obtained from the experiments was almost quantitatively supported with the DFT calculations. Furthermore, the calculations showed that surplus Au atoms preferentially make a new single atomic chain at the step edges, with higher mobility compared to the dimerized Au chains in the middle of the terraces. Their less stability was also confirmed by the diffraction studies, which showed that upon annealing at $T > 600$ °C, the surplus Au atoms coalesce into $\sqrt{3}$ structures, while the dimerized chains survive up to ~ 950 °C. Moreover, the upper boundary of the electron-hole continuum derived from the plasmon dispersion validated the enhanced band gap in the unoccupied states.

In conclusion, this study extended our understanding of the cross-coupling between the electronic and structural parameters of the double Au chains on the Si(553)-Au surface. Although a similarity in the doping-induced modification of the electronic and structural parameters is seen, the underlying mechanism and strength of the modification is ultimately determined with the adsorbate-surface interaction. In a general view, an adsorbate atom with a higher electron density and heavier mass has a more substantial effect than H. The interaction mechanism might also depend on the intrinsic properties of the employed surface. As preliminary discussed in the previous chapter, similar structural improvements were also observed upon doping of the Si(775)-Au surface with atomic hydrogen. This shows that such self-healing or structural improvements of atomic wires can be applied to the general class of 1D atomic chain systems, which certainly requires systematic investigation.

Part IV:
Summary and Conclusions

Chapter 9

Summary and Conclusions

This chapter summarizes all significant findings and briefly evaluates the results. The chapter is divided into parts following the major objectives, as discussed in the thesis.

In general, the present thesis investigated the plasmonic excitation in atomic wires in close relation to structural properties and interaction with an embedding Si environment. The achieved results demonstrated that plasmonic excitation in Au-induced atomic wires on Si surfaces is not perfectly restricted to Au made structural building blocks but also highly related to the whole surface properties. Eventually, the plasmon spectroscopy is a powerful tool to investigate such ultimately small metallic objects. Notably, the presented investigations extend the ongoing fundamental studies on atomic wire systems to modify their intrinsic properties by employing the versatile interactions between the wires and the surrounding environment. For this, different scenarios were put into experimental realization in close connection with atomistic DFT calculations.

Plasmons on the Si(111)-(5×2)-Au Surface — In Chapter 5, the Si(111)-(5×2)-Au system was studied with the SPA-LEED and extended potential of plasmon spectroscopy for the first time. The surface structure was investigated for different Au coverages and re-calibrated to 0.6 ML. In addition, it was found that the measured plasmon dispersion is energetically only comparable with the EBH model, which contains 6 Au atoms per the (5×2) unit cell, but contradicted the KK model at the Au coverage of 0.7 ML. In order to gain more insight, the upper boundary of the electron-hole continuum was numerically derived from plasmon dispersion and compared to the calculated band structures. The calculated ω_+ showed an almost quantitative match to the EBH model band structure, while its slope is much higher than the KK model.

A metal-insulator transition (MIT) for this system was investigated by additional Au doping at RT. Contrary to the previous results [196], it was found that the MIT does not depend on the number

of Au atoms involved in the unit cell, but mainly determined with the surplus charge concentration. This finding was further validated by H doping of this system, which showed qualitatively the same behavior, revealing that the MIT is due to the charge donation. However, the exact mechanism of this charge donation cannot be derived from the existing results and require more investigation.

Although the observed features could reasonably well be explained with the EBH model, there are still several discrepancies that need to be clarified for this model. First of all, the EBH model contains a 5×1 unit cell, which is modified to the 5×2 by an additional Si adatom [163]. On the other hand, doubling the periodicity along the Au chains results in a multiple band gap opening above the Fermi level, which makes it incompatible with the presented results. Since previous studies [179] and the present investigation strongly favor the 0.6 ML Au coverage, the observed discrepancies must be related to the structural model itself. The main concern about the EBH model might be the atomic arrangement, dimerization parameters and Si-adatom concentration. In particular, the Si-adatoms, which appear spontaneously, whose concentration can not be quantified in experiments, requires an exact assignment.

Interaction of Gold Atomic Chains with the Environment — One of the primary objectives of this thesis was exploring the informational content of plasmon spectroscopy concerning occupied and unoccupied parts of the quasi-1D band structure. In this regard, valuable new information has obtained about the unoccupied band structure as demonstrated for the Si(hhk)-Au systems in Chapter 6. This investigation showed that the atomic wire systems are characterized by the hybridization of the Au-related electronic states with the less dispersive Si step edge bands. The relevance of hybridization is demonstrated by the complete breakdown of the nearly free electron gas model, as revealed from the plasmon dispersion. Moreover, the combined approach consisting of the plasmon spectroscopy and first-principles calculations allowed for a consistent and almost quantitative description. It further showed that plasmon spectroscopy contains essential information about the excitation spectrum, particularly where a single metallic band dominates the surface metallicity (i.e., Si(hhk)-Au). Thus, using this information, localized modes at $k \rightarrow 0$ and propagating modes at high k_{\parallel} , and their modification under certain circumstances were successfully demonstrated. The results revealed that although the electron density relevant for plasmonic excitation is confined to the Au-induced bands, it is also highly related to the interaction of these bands with other surface states. Because the coupling of the Au wires with higher dimensions through the substrate cannot be neglected, the wires are more appropriately described as an extremely anisotropic 2D object than as purely 1D.

Although the established methodology yielded a reasonable fit to the Si(553)-Au and Si(557)-Au surfaces, there are still several discrepancies with the Si(775)-Au surface. Thus, according to the current double-Au chain model, multiple band crossings of E_F exist for Si(775)-Au. Also, it is not easy to single out the precise contribution of each of these bands because of multiple hybridizations. It must be noted that there can be more than one plasmon if more than one band crosses the Fermi level. Nevertheless, most of the plasmons associated with the bands with a lower dispersion slope are expected to be so low

in energy that they cannot be observed or resolved experimentally, touching one of the limitations of this method. On the other hand, if the metallicity of this surface is due to several bands crossing E_F , it would undermine the present approach to predict the unoccupied band structure for this system. In fact, the determination of ω_+ close to the Fermi level also depends on ω_- , which is determined with the effective mass of the unoccupied band. Conclusions about the occupied band structure are more indirect than for the unoccupied part, and mainly concern hybridizations and band crossings of the Fermi level. However, they affect the excitation spectrum of electron-hole pairs and thus may turn out to be relevant. For example, only when taking hybridization into account do we expect a single plasmon for Si(775)-Au in the energy range observed in the presented experiments.

Although the bands investigated here exhibit only 1D dispersion, the present investigations also show that there is strong 2D coupling, which can be considered as a crossover between 1D and 2D and gives this term a deeper meaning. Therefore, it can be concluded that although these systems are among the narrowest possible quasi-1D objects that can be realized, a pure 1D description is not adequate.

Robust Metallicity of Atomic Wires Upon Oxidation — Oxidation of such metallic atomic wire systems is the main challenge that they would have to meet for any practical utilization. Moreover, the fundamental aspects of oxidation of these systems, which have not been understood yet, possess essential knowledge about the response of the low-D systems. Interestingly, all the tested systems (i.e., Si(hhk)-Au) showed robustness against oxidation. However, it is susceptible to disorder introduced by the adsorption of oxygen, which leads to the formation of standing plasmonic waves.

The robustness of atomic wires, which were generally accepted as susceptible to any external effect, was highly unexpected and raised several interesting questions about the mechanism of interaction between oxygen and these surfaces. These questions were extensively studied for the Si(hhk)-Au systems in Chapter 7. It was found that the surrounding Si surface elements, mainly, are oxidized at room temperature. This oxidation process modifies the metallic channel induced by gold chains, but leaves metallicity almost intact. Moreover, the numerically derived upper edge of the electron-hole continuum together with the calculated band structure made it possible to define the kinetic sequence of preferential adsorption.

However, for the Si(775) surface, the finite energy in the low k region seen in the plasmon dispersion, which is unique to this system, was not reproduced in these calculations, most likely due to the structural model used, which contradicts several experimental observations. These discrepancies with the model cannot be solved here and require more detailed theoretical optimization.

Despite many similarities of the surfaces investigated, oxidation and hydrogenation follow different mechanisms and effects the properties almost differently. This is because the local structural arrangement of different atomic groups determines the interaction mechanism with an additional adsorbate. As an example, the systems with Si-adatom, restatom chains (i.e., Si(557)-Au and Si(775)-Au) show a unique mechanism: after oxidation of the individual band, the rest of the band structure renormalize

itself to compensate the reduced metallicity. Most interestingly, this mechanism compensates for the energy cost of chemical interaction with oxygen so that the structural properties are almost preserved. This indeed shows the peculiarity of such atomic wire systems.

Doping at the Sub-Nanometric Scale — In Chapter 7, doping of the atomic wires with atomic hydrogen was successfully demonstrated. Hydrogen acts as a low-dimensional donor shifting the Fermi level upwards. Since H does not directly interact with the Au chains, the underlying mechanism is not simple doping, but requires concomitant changes in the band structure. Interestingly, while local relaxations at the adsorption sites of H play a marginal role in this context, band filling is coupled directly with the dimerization of the Au chains, i.e., band filling and metallicity can be tuned by changes in Au dimerization and vice versa. This atomic scale effect could be seen in the diffraction experiments as an increase in dimerization strength and correlation along the atomic Au wires. This nice finding opened a specific case regarding cross-coupling between the electronic and structural properties of the atomic wires.

In Chapter 8, it was found that the surplus of Au atoms affects the electronic and structural parameters, similarly. Moreover, the structural improvements were found to be stronger than the effect of hydrogen at a similar concentration of elementary charge transfer. It was revealed that the surplus Au atoms show doping character at low concentration and deviate from simple doping scenario by modifying surface structure itself at higher surplus concentrations.

Interestingly, H-induced changes in the plasmonic excitations on the systems with Si-adatom and restatom chains (i.e., Si(557)-Au and Si(775)-Au) goes far beyond simple charge transfer. Thus, not only an increase of a band filling but also renormalization of the whole bands was observed. As a consequence of this band rearrangement, a huge band gap in the unoccupied part is opened, which blocks plasmon propagation. This results in a plasmon localization, which was observed as a leveling off of the plasmon dispersion at a finite energy.

The presented studies in Chapter 7 and 8 showed that the remaining metallicity after interaction with the Si surface could be successfully tuned employing the interaction between Au chains and the rest of the environment. This tuning is essential for fundamental quantum physics as well, as it brings such systems closer to the use in nanoelectronics. The unexpected effect of doping on metallicity also opens fundamental questions about the diversity of adsorbate-surface interactions.

9.1. Outlook

In general, the present thesis answered several questions regarding the properties of the Au-induced atomic wires on Si surfaces. On the other hand, these findings opened new questions that need to be answered for a comprehensive understanding of such low-dimensional systems.

The possibility of tuning and manipulating the Si(hhk)-Au atomic wire systems on the atomic scale,

which has proven to be successful in the present thesis, enables an exceptional and rather new approach to study 1D quantum phenomena. This will undoubtedly lead to exciting research results in the future. The established knowledge about atomic wire systems and plasmonic excitation in such narrowest possible systems paves the way for scaling plasmon-photon coupling down to atomic sizes. Indeed, the potential of such coupling is not limited to ranging plasmonic devices to THz frequency and increasing their sensitivity but also can be a powerful tool to search new entangled states such as one photon per atom or spin. One feasible way to realize such a coupling might be using a momentum source, such as structured surfaces, quantum dots, antidots, etc., to enhance electromagnetic wave frequency into the plasmon frequency range to produce enough momentum to excite quasi-1D plasmons. In this thesis, such coupling could be realized for the shorter sections of atomic wires, but it still has not been accomplished for long (undistorted) wires.

As discussed in this thesis, one of the interesting systems is the Si(775)-Au system. However, its structural model and electronic properties do not match with the experimental findings and require more experimental evidence and theoretical optimization. For example, the band gap opening at the Fermi level after H and O adsorption has been observed for this system. However, no sign of such an energy gap was reproduced in theory. The existence of an energy gap puts this system into another category by questioning the origin of the observed metallicity.

The studies on the Si(111)-(5×2)-Au surface revealed the optimum Au coverage for the single and multi-domain surfaces. However, the detailed mechanism of instability induced by additional Au atoms is an interesting open question. Moreover, the absence of steps leading to the interaction of different domains and most likely to increase inter-wire couplings makes the Si(111)-(5×2)-Au surface suitable for studying the 2D crossover and the deviation from the one-dimensionality as partially discussed in this thesis.

Another interesting finding was the doping of Au wires with surplus Au concentration. Although its function has been partially addressed for the Si(553)-Au surface, enhanced wire quality and possibly increased stiffness of the dimerized Au chains need a more comprehensive and systematic investigation. For instance, doping of the Si(775)-Au surface with atomic hydrogen showed similar results. However, the precise observation of such small structural changes was challenged mostly by the defects introduced by hydrogen. Likely, using more stable surfaces and gold as a dopant would prevent such disorders enabling a comprehensive analysis of structural and electronic modifications. On the other hand, since plasmon spectroscopy is not sensitive to spin order as proposed for Si(553)-Au, the effect of charge doping in this regard has also not yet been discussed.

Up to now, all experimental research regarding atomic wires has been conducted in a UHV condition. However, a detailed understanding of these systems, mainly against oxidation, would make their utilization much easier. In this regard, one of the main steps forward might be implementing other preparation methods to this field besides UHV compatible methods. Thus, the preparation of atomically arranged surfaces in a chemically stabilized (or in equilibrium) environment would increase the chance

of stabilizing them for the ambient condition. For protection in the ambient condition, another scenario would be covering these surfaces with presumably organic molecules. In this regard, preliminary IR absorption results have been reported for the TAPP-Br (a core brominated tetraazaperopyrene) deposited Si(553)-Au surface in Ref [94]. Although upon TAPP-Br deposition anisotropic surface metallicity was found to survive, disorders in the molecular layer deposited and in the atomic chains lead to the shift of the resonance to higher frequencies and a strong broadening. However, concluding the electronic and structural modification requires systematic and complementary investigations.

Appendix

Chapter A

Plasmon Resonance Studies by IR

In the framework of this thesis, IR spectroscopy was employed as a complementary method to study Si(553)-Au surface after oxygen adsorption. The results from these experiments were discussed in Section 7.3.1. Here, a brief description of the applied fitting model will be presented. The IR-absorption experiments were performed in the group of Prof. Dr. A. Pucci at the Kirschhof Institute for Physics, University of Heidelberg.

Plasmons can be excited by IR radiation in the shorter sections of atomic wires, which results in standing waves of coherently oscillating charges corresponding to oscillating electric dipoles (for the odd orders). Similar to bulky nanorods, the first order plasmonic modes associated with atomic chains manifests a strong IR signal. [268] Following the 1D plasmonic theory [81, 269, 270], the IR resonance frequency can be approximated by the following relationship.

$$\omega_{PL}(q) \approx \left(\frac{eq}{n_0}\right) \sqrt{\frac{n_{1D} \ln(1/bq)}{2\epsilon_0 m^*}}. \quad (\text{A.1})$$

where q is the length of the wave vector, n_{1D} is the 1D electron density, m^* is the effective mass of the electrons, e is the elementary charge, and ϵ_0 is the vacuum permittivity. In Eq. A.1, n_0 is the refractive index, which considers the influence of the substrate and also possible over layers. The confinement of the electron wave functions in the directions normal to the wires is considered by a Gaussian distribution with a width of b . For finite wires with a length of l , the standing wave vector of the fundamental mode can be estimated as $q = \frac{\pi}{l}$. Hence, the IR resonance position follows the following proportionality.

$$\omega_{PL}(l) \propto \sqrt{\frac{n_{1D} \ln(l/b\pi)/m^*}{l \cdot n_0}}. \quad (\text{A.2})$$

The absorption spectrum around that resonance position can be estimated as the classical absorption cross section σ_{abs} of a needle-like object hosting Drude-type metallicity [271, 272], as following.

$$\sigma_{abs} = \frac{n_{1D} l e^2}{m^* \epsilon_0 n_0 c} \frac{\omega^2 \omega_\tau}{\left[(\omega_{PL}^2 - \omega^2)^2 + \omega^2 \omega_\tau^2 \right]}. \quad (\text{A.3})$$

Here, ω , ω_τ , and c is the circular photon frequency, electronic scattering rate, and the vacuum velocity of light, respectively. Considering the absorption cross section in the expression for the transmission of a very thin layer at normal incidence of light [273], the relative IR transmittance (normalized to the transmittance of the non-absorbing substrate with refractive index n_s) is given by the following relation.

$$\frac{T_{Si+Au}}{T_S^i} \approx 1 - \frac{2W}{(1 + n_s) \sqrt{2\pi} \Delta\omega} \times \int_{-\infty}^{\infty} \exp \left\{ -\frac{(x - \omega_{PL})^2}{2\Delta\omega^2} \right\} \frac{\omega^2 \omega_\tau}{\left[(x^2 - \omega^2)^2 + \omega^2 \omega_\tau^2 \right]} dx \quad (\text{A.4})$$

with

$$W = \frac{N}{A} \frac{n_{1D} l e^2}{\epsilon_0 m^* c} \quad (\text{A.5})$$

where $n_{1D} l$ is the number of oscillating electrons in a conductive chain with a length of l . The factor N/A reflects the number of wires N per surface area A . Due to the random distribution of wire lengths, a Gaussian distribution of resonance frequencies with width $\Delta\omega$ is assumed in Eq. A.4. [93, 176, 196, 274] Although the density of wires per area can be different in each preparation, assuming that the resulting conductivity is identical, Eq. A.4 is used as a model function for the spectral fits.

Since the adsorbed molecules change the surface resistivity, changing the electronic scatter rate is also anticipated. Moreover, charge transfer to the surface states changes the $\frac{n_{1D}}{m^*}$ ratio [196, 275]. The quantity $\frac{n_{1D}}{m^*}$ may be considered as 1D analogue to the squared plasma-frequency parameter $\omega_p^2 \propto \frac{n_{3D}}{m^*}$ of the 3D Drude model (with n_{3D} as the free-charge carrier density in the 3D metal). The fit procedure was applied to the measured IR spectra in which the fit parameters W , ω_τ , and the average ω_{PL} depend on the adsorbate coverage, but the parameter $\Delta\omega$ is kept fixed for each of the adsorption experiments.

According to the previous reports with the IR reflection-absorption spectroscopy on metallic surfaces, the adsorbate-induced surface resistance reduces the broadband reflectance. [275–278] In IR transmittance spectra of ultrathin metal layers, surface resistivity changes and charge transfer by adsorbates show up as broadband changes with different frequency-dependent contributions [279]. Fundamentally, the spectral shifts in plasmonic resonances due to the adsorbate-induced effects are different from those of non-resonant metallic surfaces.

The obtained relative transmittance spectra were analyzed within the theoretical framework previously reported in [176, 196, 274]. Consequently, Eq. A.4 was used as the fit model to evaluate the experimental results and derive the effect of the specific adsorbate on the plasmonic excitation associated with the gold-induced atomic wires. The obtained results are summarized in Fig. A.1. The fit

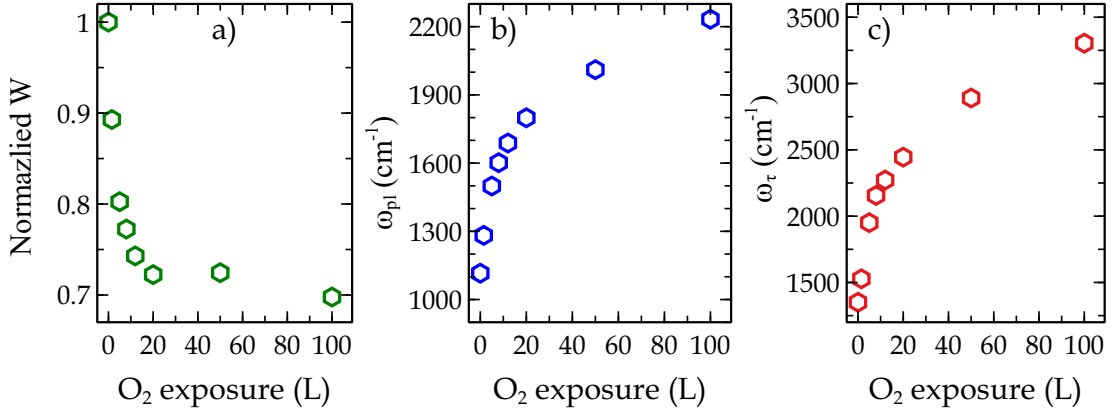


Figure A.1: Fit parameters obtained from the IR-transmittance spectra (given in Fig. 7.8) of the HCWs on Si(553)-Au under different oxygen exposure by employing Eq. A.4. Adapted from Ref. [94].

parameter $\Delta\omega$ describes the resonance broadening due to the length distribution and is characteristic for the preparation of certain superstructures.

Table A.1: Values for the electronic scattering rate ω_τ and the plasmonic resonance frequency ω_{pL} , which are used to normalize the data in Fig. 7.8, as well as the results for the Gaussian broadening $\Delta\omega$.

Parameters	O ₂	H ₂
ω_τ (cm ⁻¹)	1351 ± 47	1087 ± 59
ω_{pL} (cm ⁻¹)	1116 ± 51	560 ± 62
$\Delta\omega$ (cm ⁻¹)	259 ± 13	357 ± 37

Changes in the resonance position ω_{pL} in Fig. A.1(b) indicate a modified average length distribution. In principle, each curve in one experimental data set must be described by its individual Gaussian broadening parameter. However, if the electronic scattering ω_τ is much larger than $\Delta\omega$, the fitting procedure is less susceptible to changes in the non-dominant parameter. As a useful and proven approximation for these systems, the $\Delta\omega$ was used for all spectral fittings for the same initial superstructure preparation, including those that eventually changed the distribution of the chain length.

Chapter B

Supplementary Materials

Higher Au Coverages on Si(775)-Au — As already discussed in Sections 6.1.3 and 6.4.1, in order to search for another Au-induced stable phase on Si(775), several Au-concentrations have been tested. It was found that increasing Au concentration beyond the 0.32 ML destabilizes this surface by forming large (111) terraces. Subsequently, excess Au atoms coalesce into the $\sqrt{3}$ structure at the new formed (111) terraces (see Fig. B.1). Upon further increase of the Au concentration, the (775) surface refacets into the (553) orientation. Besides, it was also found that additional Au atoms induce the $\times 3$ periodicity as seen from Fig. B.1 (a). Although this periodicity is formed at elevated temperature, it is vanished after post-annealing at 930 °C, as shown in Fig. B.1 (b). This shows that additional Au atoms do not form a stable superstructure.

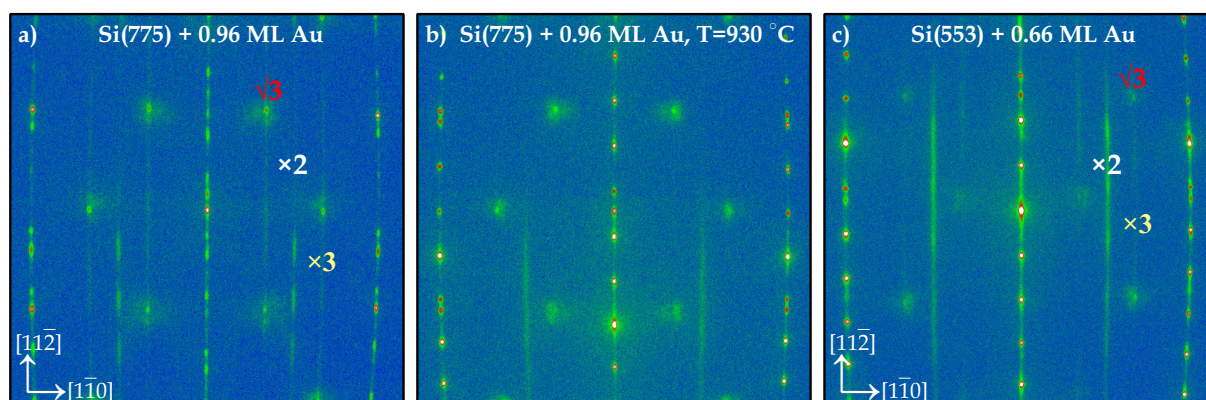


Figure B.1: LEED patterns for the 0.96 ML Au deposited Si(775) surface, before (a) and after post-annealing at 930 °C (b). Images were recorded at RT with 138 eV primary energy. LEED images for the 0.32, 0.56 and 0.65 ML Au deposited Si(775) surfaces are presented in Sections 6.1.2 and 6.1.3, respectively. (c) shows the 0.66 ML Au deposited Si(553) surface.

Similarly, the $\times 3$ streaks associated with additional Au adsorption at the step edges of Si(553)-Au was also observed (see Fig. B.1(c) also Section 8.1.1). The latter was supported with DFT calculations, which revealed new Au-induced single atomic chains at the step edges. In this base, the $\times 3$ structure seen on the Si(775)-Au surface at higher Au concentrations may also be related to the Au-induced superstructures at the step edges. This was supported by preliminary DFT calculations. [266] However, they have higher mobility than the Au chains in the middle of terraces and, therefore, can not survive upon annealing at higher temperatures (e.g., $T > 650$ °C).

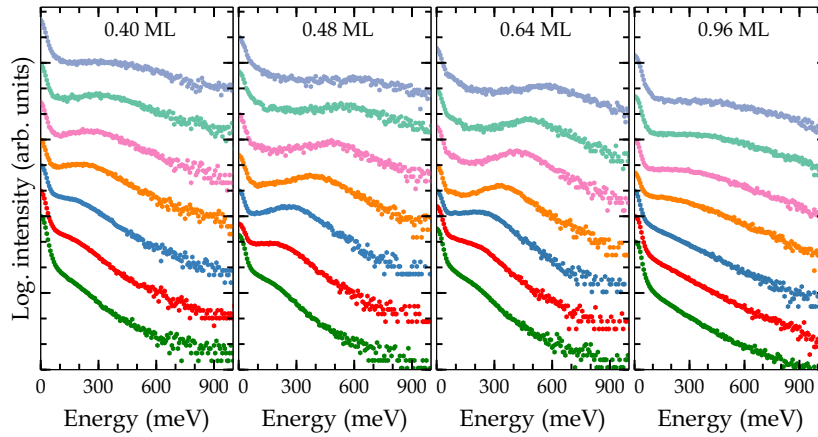


Figure B.2: EEL spectra for the Si(775)-Au surfaces measured for different Au coverages with a momentum transfer parallel to the wires.

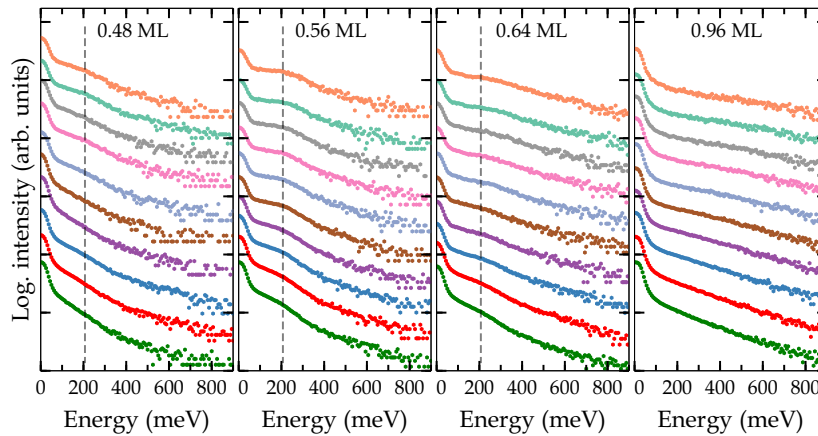


Figure B.3: Exemplary loss spectra for the Si(775)-Au surfaces measured for different Au coverages with k_{\perp} to the wires. The dashed lines show the dispersionless loss feature likely associated with quantum-well states formed perpendicular to the terraces.

The present study showed that this surface preserves its stepped morphology even at a Au concentration close to 1 ML. This may be one of the reasons why this surface exhibits anisotropic metallicity in all Au concentrations tested. This anisotropy was revealed by the plasmonic excitation, which showed

a clear dispersion only with the momentum transfer parallel to the steps, shown in Fig. B.2 and Fig. B.3. As shown there, at the Au concentration of 0.96 ML, the surface gives a very weak plasmonic signal only along the terraces. The less plasmon intensity in comparison with other tested Au coverages might be due to disorders induced by excess Au atoms.

As already discussed in Section 6.1.3 at Au concentration higher than 0.48 ML, the (775) orientation refacets into (553) surface. The metallic superstructures at the new terraces show much higher plasmon dispersion than the OCWs phase. Interestingly, this new plasmon dispersion is very similar to the dispersion measured for the HCWs phase on Si(553)-Au. The new facet and its plasmon dispersion are preserved at even higher Au concentrations. This shows that the newly formed (553) facet is more stable than the (775) (see Section 6.1.3). This is exemplarily shown for 0.48 and 0.96 ML Au deposited surfaces (other coverages were presented in Figs. 6.19 and 6.17).

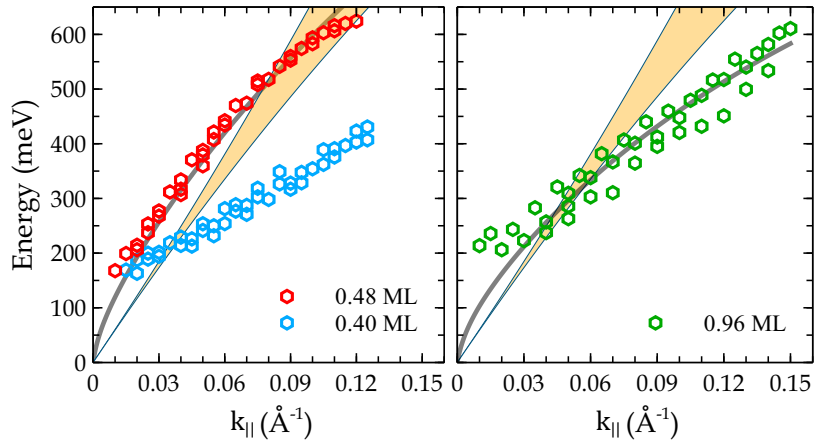


Figure B.4: Plasmon dispersion for the Si(775)-Au surface measured for different Au coverages. The blue area (same in both graphs) represents the SPE zone derived within the NFEG model (as discussed in Section 2.2.1) for the OCWs phase with input parameters of $m^* = 0.08m_e$, $b = 6.6 \text{ \AA}$, $g_s = 1$ and $k_F = 0.351 \text{ \AA}^{-1}$. The solid lines in all graphs represent the fit according to the empirically modified model (see Section 2.2.2). Plasmon dispersion for the 0.32, 0.40 and 0.56 ML Au concentrations are shown in Fig. 6.17 and Fig. 6.19 in Section 6.4.1.

Sensitivity of Plasmon Spectroscopy and Electron Diffraction to Surface Coverage — As discussed in Section 4.4, the gold evaporator used was calibrated using QMBs. The sensitivity of plasmon dispersion and SPA-LEED to the surface order was used for further precision of the deposited Au concentration. For this purpose, the Si(553)-Au surface at the Au concentration of 0.48 ML was employed. It is noteworthy that after only 8 % deviation from this optimum Au coverage, the finite-size effect in the low k_{\parallel} region, and reduction of the plasmon dispersion at higher k_{\parallel} were observed (see Fig. B.5). Also, the diffraction intensity of the $\times 2$ streaks goes through the maximum at this optimum Au coverage, while it is reduced by moving away from it, as shown in Fig. B.5. Similarly, their half-width is narrowed by approaching optimum surface coverage. This noticeable sensitivity of the SPA-LEED and plasmon spectroscopy to the surface order enabled the reproducibility of the surface quality and the direct comparison of the

different surface preparations.

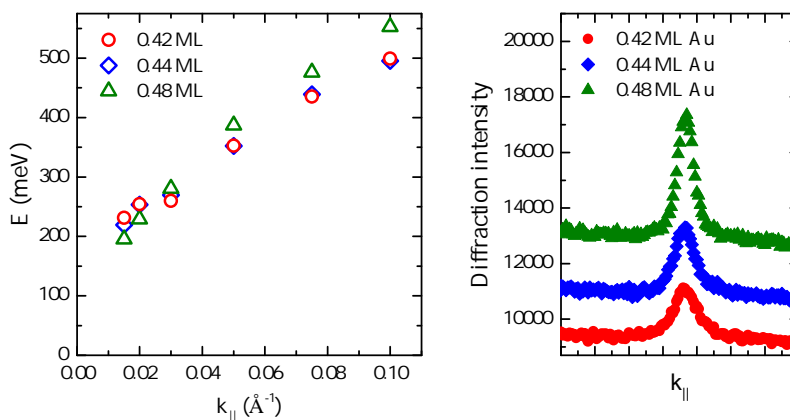


Figure B.5: The plasmon dispersions (left) and 1D diffraction profiles of the $\times 2$ streaks (right) measured along the $(1\bar{1}0)$ direction at Au coverages of 0.42, 0.44, 0.48 ML. Similar measurements were frequently carried for validation of surface calibration. All surface preparations were carried out in the same condition; only Au coverages were different.

The Si(557)-Au Surface at Low-Temperature — The temperature dependence of the plasmonic excitations on the Si(557)-Au and Si(553)-Au surfaces were discussed in Section 6.5. However, no strong temperature dependence was observed. Likewise, the surface structure of this surface changes only qualitatively at low-T, as shown in Fig. B.6. Thus, by lowering the surface temperature, a linear background decreases and the $\times 2$ intensity increases. The latter may be a sign of an increased correlation between the adjacent Si-atom chains due to surface relaxation. On the other hand, the new $\times 3$ periodicity has been seen for the Si(553)-Au surface in this work as well as in the literature [201,208,280]. The $\times 3$ periodicity on the Si(553)-Au system is related to the spin ordering at the Si step edges to which the plasmon spectroscopy is not sensitive. Therefore this has not been discussed in this thesis.

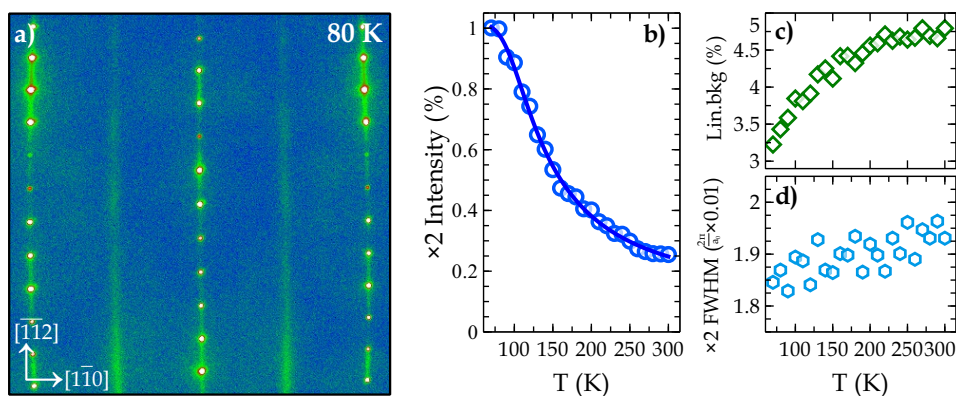


Figure B.6: Diffraction pattern for the Si(557)-Au surface recorded at 80 K (a). The image recorded with $E_0 = 138$ eV. (b-d) Evaluation of the $\times 2$ streaks deduced from 1D spot profiles along the $(1\bar{1}0)$ direction as a function of temperature.

Bibliography

- [1] T. GIAMARCHI, *Quantum Physics in One Dimension*, Clarendon Press, Oxford, 2007.
- [2] R. LANDAUER, *Conductance determined by transmission: probes and quantised constriction resistance*, *Journal of Physics: Condensed Matter* **1**, 43:8099, 1989, doi:10.1088/0953-8984/1/43/011.
- [3] V. V. DESHPANDE, M. BOCKRATH, *The one-dimensional Wigner crystal in carbon nanotubes*, *Nature Physics* **4**, 4:314, 2008, doi:10.1038/nphys895.
- [4] S. KAGOSHIMA, H. NAGASAWA, T. SAMBONGI, *Electron Correlation and Magnetism in Narrow-Band Systems*, volume 72 of *Springer Series in Solid-State Sciences*, Springer Berlin Heidelberg, 1988, doi:10.1007/978-3-642-83179-9.
- [5] G. GRÜNER, *The dynamics of charge-density waves*, *Rev. Mod. Phys.* **60**, 4:1129, 1988, doi:10.1103/RevModPhys.60.1129.
- [6] K. SCHÖNHAMMER, *Luttinger Liquids: basic concepts*, volume 25 of *Physics and Chemistry of Materials with Low-Dimensional Structures*, chapter 4, 93–136, Springer Netherlands, Dordrecht, 2004, doi:10.1007/978-1-4020-3463-3_4, arXiv:cond-mat/0305035v2.
- [7] R. PEIERLS, *Zur Theorie der elektrischen und thermischen Leitfähigkeit von Metallen*, *Ann. Phys.* **396**, 2:121, 1930, doi:10.1002/andp.19303960202.
- [8] L. LANDAU, *On the Theory of the Fermi Liquid*, *J. Exp. Theor. Phys.* **8**, 70, 1959.
- [9] R. MÉLIN, B. DOUÇOT, P. BUTAUD, *Breakdown of the Fermi liquid picture in one dimensional fermion systems: connection with the energy level statistics*, *Journal de Physique I* **4**, 5:737, 1994, doi:10.1051/jp1:1994173.
- [10] J. M. LUTTINGER, *An Exactly Soluble Model of a Many-Fermion System*, *J. Math. Phys.* **4**, 9:1154, 1963, doi:10.1063/1.1704046.

- [11] S.-I. TOMONAGA, *Remarks on Bloch's Method of Sound Waves applied to Many-Fermion Problems*, Prog. Theor. Phys. **5**, 4:544, 1950, doi:10.1143/ptp/5.4.544.
- [12] F. HIMPSEL, K. ALTMANN, R. BENNEWITZ, J. CRAIN, A. KIRAKOSIAN, J. LIN, J. MCCHESENEY, *One-dimensional electronic states at surfaces*, Journal of Physics: Condensed Matter **13**, 49:11097, 2001, doi:10.1088/0953-8984/13/49/301.
- [13] N. ONCEL, *Atomic chains on surfaces*, Journal of Physics: Condensed Matter **20**, 39:3001, 2008, doi:10.1088/0953-8984/20/39/393001.
- [14] P. C. SNIJDERS, H. H. WEITERING, *Electronic instabilities in self-assembled atom wires*, Rev. Mod. Phys. **82**:307, 2010, doi:10.1103/RevModPhys.82.307.
- [15] L. DUDY, J. AULBACH, T. WAGNER, J. SCHAFER, R. CLAESSEN, *One-dimensional quantum matter: gold-induced nanowires on semiconductor surfaces*, J. Phys.: Condens. Matter **29**, 43:433001, 2017, doi:10.1088/1361-648X/aa852a.
- [16] H. PFNÜR, *Atomic wires at surfaces: A perspective on the article: "Peierls instability in Pt chains on Ge (0 0 1)" by A. van Houselt, T. Gnielka, JMJ Aan van de Brugh, N. Oncel, D. Kockmann, R. Heid, K.-P. Bohnen, B. Poelsema and HJW Zandvliet*, SurSc **602**, 10:1727, 2008, doi:10.1016/j.susc.2008.03.021.
- [17] P. SEGOVIA, D. PURDIE, M. HENGESBERGER, Y. BAER, *Observation of spin and charge collective modes in one-dimensional metallic chains*, Nature **402**, 6761:504, 1999, doi:10.1038/990052.
- [18] H. W. YEOM, S. TAKEDA, E. ROTENBERG, I. MATSUDA, K. HORIKOSHI, J. SCHAEFER, C. M. LEE, S. D. KEVAN, T. OHTA, T. NAGAO, S. HASEGAWA, *Instability and Charge Density Wave of Metallic Quantum Chains on a Silicon Surface*, Phys. Rev. Lett. **82**, 24:4898, 1999, doi:10.1103/PhysRevLett.82.4898.
- [19] H. J. W. ZANDVLIET, A. VAN HOUSELT, B. POELSEMA, *Self-lacing atom chains*, Journal of Physics: Condensed Matter **21**, 47:474207, 2009, doi:10.1088/0953-8984/21/47/474207.
- [20] J. R. AHN, P. G. KANG, K. D. RYANG, H. W. YEOM, *Coexistence of Two Different Peierls Distortions within an Atomic Scale Wire: Si(553)-Au*, Phys. Rev. Lett. **95**, 19:196402, 2005, doi:10.1103/PhysRevLett.95.196402.
- [21] J. ORTEGA, F. HIMPSEL, *Atomic Chains at Surfaces*, in *Very High Resolution Photoelectron Spectroscopy*, 147–183, Springer, 2007, doi:10.1007/3-540-68133-7_6.
- [22] J. N. CRAIN, A. KIRAKOSIAN, K. N. ALTMANN, C. BROMBERGER, S. C. ERWIN, J. L. MCCHESENEY, J.-L. LIN, F. J. HIMPSEL, *Fractional Band Filling in an Atomic Chain Structure*, Phys. Rev. Lett. **90**, 17:176805, 2003, doi:10.1103/PhysRevLett.90.176805.

-
- [23] T. NAGAO, S. YAGINUMA, T. INAOKA, T. SAKURAI, *One-Dimensional Plasmon in an Atomic-Scale Metal Wire*, Phys. Rev. Lett. **97**, 11:116802, 2006, doi:10.1103/PhysRevLett.97.116802.
- [24] M. KRAWIEC, *Structural model of the Au-induced Si(553) surface: Double Au rows*, Phys. Rev. B **81**, 11:115436, 2010, doi:10.1103/PhysRevB.81.115436.
- [25] S. C. ERWIN, F. J. HIMPSEL, *Intrinsic magnetism at silicon surfaces.*, Nat. Commun. **1**, 5:58, 2010, doi:10.1038/ncomms1056.
- [26] M. KRAWIEC, M. JAŁOCHOWSKI, *Anisotropic atom diffusion on Si(553)-Au surface*, Phys. Rev. B **87**, 7:075445, 2013, doi:10.1103/PhysRevB.87.075445.
- [27] S. SANNA, T. LICHTENSTEIN, Z. MAMIYEV, C. TEGENKAMP, H. PFNÜR, *How one-dimensional are atomic Au chains on a substrate?*, J. Phys. Chem. C **122**, 44:25580, 2018, doi:10.1021/acs.jpcc.8b08600.
- [28] S. POLEI, P. C. SNIJDERS, S. C. ERWIN, F. J. HIMPSEL, K.-H. MEIWES-BROER, I. BARKE, *Structural Transition in Atomic Chains Driven by Transient Doping*, Phys. Rev. Lett. **111**, 15:156801, 2013, doi:10.1103/PhysRevLett.111.156801.
- [29] R. LOSIO, K. N. ALTMANN, A. KIRAKOSIAN, J. L. LIN, D. Y. PETROVYKH, F. J. HIMPSEL, *Band splitting for Si(557)-Au: Is it spin-charge separation?*, Phys. Rev. Lett. **86**, 20:4632, 2001, doi:10.1103/PhysRevLett.86.4632.
- [30] J. AULBACH, S. C. ERWIN, R. CLAESSEN, J. SCHÄFER, *Spin Chains and Electron Transfer at Stepped Silicon Surfaces*, Nano Lett. **16**, 4:2698, 2016, doi:10.1021/acs.nanolett.6b00354, arXiv:1601.07489.
- [31] T. LICHTENSTEIN, Z. MAMIYEV, S. SANNA, W. G. SCHMIDT, C. TEGENKAMP, H. PFNÜR, *Probing quasi-1D band structures by plasmon spectroscopy*, Phys. Rev. B **97**:165421, 2018, doi:10.1103/PhysRevB.97.165421.
- [32] Z. MAMIYEV, S. SANNA, C. LICHTENSTEIN, T. AND. TEGENKAMP, H. PFNÜR, *Extrinsic doping on the atomic scale: tuning metallicity in atomic Au chains*, Phys. Rev. B **98**, 24:245414, 2018, doi:10.1103/PhysRevB.98.245414.
- [33] C. HOGAN, E. SPEISER, S. CHANDOLA, S. SUCHKOVA, J. AULBACH, J. SCHÄFER, S. MEYER, R. CLAESSEN, N. ESSER, *Controlling the Local Electronic Properties of Si(553)-Au through Hydrogen Doping*, Phys. Rev. Lett. **120**:166801, 2018, doi:10.1103/PhysRevLett.120.166801.
- [34] S. LEE, J. AHN, N. KIM, J. MIN, C. HWANG, J. CHUNG, H. YEOM, S. V. RYJKOV, S. HASEGAWA, *Adsorbate-induced pinning of a charge-density wave in a quasi-1d metallic chains: Na on the In/Si (111)-(4× 1) surface*, Physical review letters **88**, 19:196401, 2002, doi:10.1103/PhysRevLett.88.196401.
-

- [35] Z. MAMIYEV, T. LICHTENSTEIN, C. TEGENKAMP, C. BRAUN, W. G. SCHMIDT, S. SANNA, H. PFNÜR, *Plasmon spectroscopy: Robust metallicity of Au wires on Si(557) upon oxidation*, Phys. Rev. Materials **2**:066002, 2018, doi:10.1103/PhysRevMaterials.2.066002.
- [36] U. KRIEG, Y. ZHANG, C. TEGENKAMP, H. PFNÜR, *Tuning of one-dimensional plasmons by Ag-Doping in Ag-ordered atomic wires*, New Journal of Physics **16**, 4:043007, 2014, doi:10.1088/1367-2630/16/4/043007.
- [37] Y. WADA, T. UDA, M. LUTWYCHE, S. KONDO, S. HEIKE, *A proposal of nanoscale devices based on atom/molecule switching*, Journal of applied physics **74**, 12:7321, 1993, doi:10.1063/1.354999.
- [38] J. PARK, S. W. JUNG, M.-C. JUNG, H. YAMANE, N. KOSUGI, H. W. YEOM, *Self-assembled nanowires with giant rashba split bands*, Physical review letters **110**, 3:036801, 2013, doi:10.1103/PhysRevLett.110.036801.
- [39] H. PFNÜR, C. TEGENKAMP, L. VATTUONE, *Plasmons in one and two dimensions*, Springer Handb. Surf. Sci. 2017, arXiv:1701.05049.
- [40] T. NAGAO, G. HAN, C. HOANG, J.-S. WI, A. PUCCI, D. WEBER, F. NEUBRECH, V. M. SILKIN, D. ENDERS, O. SAITO, M. RANA, *Plasmons in nanoscale and atomic-scale systems*, Sci. Technol. Adv. Mater. **11**, 5:054506, 2010, doi:10.1088/1468-6996/11/5/054506.
- [41] E. CHULKOV, A. BORISOV, J. GAUYACQ, D. SÁNCHEZ-PORTAL, V. SILKIN, V. ZHUKOV, P. ECHENIQUE, *Electronic excitations in metals and at metal surfaces*, Chemical Reviews **106**, 10:4160, 2006, doi:10.1021/cr050166o.
- [42] M. ROCCA, *Low-energy EELS investigation of surface electronic excitations on metals*, Surf. Sci. Rep. **22**:1, 1995, doi:10.1016/0167-5729(95)00004-6.
- [43] R. H. RITCHIE, *Plasma Losses by Fast Electrons in Thin Films*, Phys. Rev. **106**:874, 1957, doi:10.1103/PhysRev.106.874.
- [44] J. R. MANSON, R. H. RITCHIE, *Self-energy of a charge near a surface*, Phys. Rev. B **24**:4867, 1981, doi:10.1103/PhysRevB.24.4867.
- [45] S. DAS SARMA, A. MADHUKAR, *Collective modes of spatially separated, two-component, two-dimensional plasma in solids*, Phys. Rev. B **23**:805, 1981, doi:10.1103/PhysRevB.23.805.
- [46] F. MORESCO, M. ROCCA, V. ZIELASEK, T. HILDEBRANDT, M. HENZLER, *ELS-LEED study of the surface plasmon dispersion on Ag surfaces*, Surface science **388**, 1-3:1, 1997, doi:10.1016/S0039-6028(97)00426-3.

- [47] B. DIACONESCU, K. POHL, L. VATTUONE, L. SAVIO, P. HOFMANN, V. M. SILKIN, J. M. PITARKE, E. V. CHULKOV, P. M. ECHENIQUE, D. FARIAS ET AL., *Low-energy acoustic plasmons at metal surfaces*, Nature **448**, 7149:57, 2007, doi:10.1038/nature05975.
- [48] T. NAGAO, S. YAGINUMA, T. INAOKA, T. SAKURAI, D. JEON, *Sound-Wave-Like Collective Electronic Excitations in Au Atom Chains*, J. Phys. Soc. Japan **76**, 11:114714, 2007, doi:10.1143/JPSJ.76.114714.
- [49] U. KRIEG, C. BRAND, C. TEGENKAMP, H. PFNÜR, *One-dimensional collective excitations in Ag atomic wires grown on Si(557)*, J. Phys. Condens. Matter **25**, 1:014013, 2013, doi:10.1088/0953-8984/25/1/014013.
- [50] T. BLOCK, C. TEGENKAMP, J. BARINGHAUS, H. PFNÜR, T. INAOKA, *Plasmons in Pb nanowire arrays on Si(557): Between one and two dimensions*, Phys. Rev. B **84**, 20:205402, 2011, doi:10.1103/PhysRevB.84.205402.
- [51] E. P. RUGERAMIGABO, C. TEGENKAMP, H. PFNÜR, T. INAOKA, T. NAGAO, *One-dimensional plasmons in ultrathin metallic silicide wires of finite width*, Phys. Rev. B **81**, 16:165407, 2010, doi:10.1103/PhysRevB.81.165407.
- [52] H. YAN, T. LOW, W. ZHU, Y. WU, M. FREITAG, X. LI, F. GUINEA, P. AVOURIS, F. XIA, *Damping pathways of mid-infrared plasmons in graphene nanostructures*, Nature Photonics **7**, 5:394, 2013, doi:10.1038/nphoton.2013.57.
- [53] S. DAS SARMA, W.-Y. LAI, *Screening and elementary excitations in narrow-channel semiconductor microstructures*, Phys. Rev. B **32**:1401, 1985, doi:10.1103/PhysRevB.32.1401.
- [54] L. VATTUONE, M. SMERIERI, T. LANGER, C. TEGENKAMP, H. PFNÜR, V. M. SILKIN, E. V. CHULKOV, P. M. ECHENIQUE, M. ROCCA, *Correlated Motion of Electrons on the Au(111) Surface: Anomalous Acoustic Surface-Plasmon Dispersion and Single-Particle Excitations*, Phys. Rev. Lett. **110**, 12:127405, 2013, doi:10.1103/PhysRevLett.110.127405.
- [55] M. SMERIERI, L. VATTUONE, L. SAVIO, T. LANGER, C. TEGENKAMP, H. PFNÜR, V. M. SILKIN, M. ROCCA, *Anisotropic Dispersion and Partial Localization of Acoustic Surface Plasmons on an Atomically Stepped Surface: Au(788)*, Phys. Rev. Lett. **113**, 18:186804, 2014, doi:10.1103/PhysRevLett.113.186804.
- [56] J. KRÖGER, *Electron–phonon coupling at metal surfaces*, Reports on Progress in Physics **69**, 4:899, 2006, doi:10.1088/0034-4885/69/4/R02.
- [57] A. LIEBSCH, *Electronic Excitations at Metal Surfaces*, Springer, Boston, 1997, doi:10.1007/978-1-4757-5107-9.

- [58] T. INAOKA, T. NAGAO, S. HASEGAWA, T. HILDEBRANDT, M. HENZLER, *Two-dimensional plasmon in a metallic monolayer on a semiconductor surface: Exchange-correlation effects*, Phys. Rev. B **66**, 24:245320, 2002, doi:10.1103/PhysRevB.66.245320.
- [59] W. KOHN, *Image of the Fermi Surface in the Vibration Spectrum of a Metal*, Phys. Rev. Lett. **2**:393, 1959, doi:10.1103/PhysRevLett.2.393.
- [60] W.-K. TSE, B. Y.-K. HU, S. DAS SARMA, *Chirality-Induced Dynamic Kohn Anomalies in Graphene*, Phys. Rev. Lett. **101**:066401, 2008, doi:10.1103/PhysRevLett.101.066401.
- [61] J. J. RITSKO, D. J. SANDMAN, A. J. EPSTEIN, P. C. GIBBONS, S. E. SCHNATTERLY, J. FIELDS, *Direct Measurement of One-Dimensional Plasmon Dispersion and Damping*, Phys. Rev. Lett. **34**:1330, 1975, doi:10.1103/PhysRevLett.34.1330.
- [62] D. K. GRAMOTNEV, S. I. BOZHEVOLNYI, *Plasmonics beyond the diffraction limit*, Nature photonics **4**, 2:83, 2010, doi:10.1038/nphoton.2009.282.
- [63] J.-C. WEEBER, J. R. KRENN, A. DEREUX, B. LAMPRECHT, Y. LACROUTE, J. P. GOUDONNET, *Near-field observation of surface plasmon polariton propagation on thin metal stripes*, Phys. Rev. B **64**:045411, 2001, doi:10.1103/PhysRevB.64.045411.
- [64] C. TEGENKAMP, *Vicinal surfaces for functional nanostructures*, Journal of Physics: Condensed Matter **21**, 1:013002, 2008, doi:10.1088/0953-8984/21/1/013002.
- [65] J. N. CRAIN, J. MCCHESENEY, F. ZHENG, M. C. GALLAGHER, P. SNIJDERS, M. BISSEN, C. GUNDELACH, S. C. ERWIN, F. J. HIMPSEL, *Chains of gold atoms with tailored electronic states*, Phys. Rev. B **69**, 12:125401, 2004, doi:10.1103/PhysRevB.69.125401.
- [66] G. GRUNER, *Density waves in solids*, CRC Press, 1994.
- [67] J. LINDHARD, *On the properties of a gas of charged particles*, Mat.-Fys. Medd. **28**:8, 1954.
- [68] T. ARUGA, *Charge-density waves on metal surfaces*, Journal of Physics: Condensed Matter **14**, 35:8393, 2002, doi:10.1088/0953-8984/14/35/310.
- [69] K. ROSSNAGEL, *On the origin of charge-density waves in select layered transition-metal dichalcogenides*, Journal of Physics: Condensed Matter **23**, 21:213001, 2011, doi:10.1088/0953-8984/23/21/213001.
- [70] R. E. PEIERLS, *Quantum theory of solids*, Clarendon Press, 1996.
- [71] H. KÖPPEL, D. R. YARKONY, H. BARENTZEN, *The Jahn-Teller Effect: Fundamentals and Implications for Physics and Chemistry*, volume 97, Springer Science & Business Media, 2009.

-
- [72] A. J. BERLINSKY, *One-dimensional metals and charge density wave effects in these materials*, Reports on Progress in Physics **42**, 7:1243, 1979, doi:10.1088/0034-4885/42/7/004.
- [73] G. GRÜNER, *The dynamics of spin-density waves*, Rev. Mod. Phys. **66**, 1:1, 1994, doi:10.1103/RevModPhys.66.1.
- [74] J. A. BITTENCOURT, *Fundamentals of Plasma Physics*, Springer, New York, NY, 3rd edition, 2004, doi:10.1007/978-1-4757-4030-1.
- [75] U. KRIEG, T. LICHTENSTEIN, C. BRAND, C. TEGENKAMP, H. PFNÜR, *Origin of metallicity in atomic Ag wires on Si(557)*, New J. Phys. **17**, 4:043062, 2015, doi:10.1088/1367-2630/17/4/043062.
- [76] S. DAS SARMA, E. HWANG, *Dynamical response of a one-dimensional quantum-wire electron system*, Phys. Rev. B **54**, 3:1936, 1996, doi:10.1103/PhysRevB.54.1936.
- [77] D. BOHM, D. PINES, *A Collective Description of Electron Interactions. I. Magnetic Interactions*, Phys. Rev. **82**:625, 1951, doi:10.1103/PhysRev.82.625.
- [78] Q. LI, S. DAS SARMA, *Plasmon excitations in one-dimensional lateral-quantum-wire superlattices*, Phys. Rev. B **41**, 14:10268, 1990, doi:10.1103/PhysRevB.41.10268.
- [79] S. DAS SARMA, E. H. HWANG, L. ZHENG, *Plasmon-pole approximation for semiconductor quantum-wire electrons*, Phys. Rev. B **54**:8057, 1996, doi:10.1103/PhysRevB.54.8057.
- [80] J. SÓLYOM, *Fundamentals of the Physics of Solids: Volume 3-Normal, Broken-Symmetry, and Correlated Systems*, volume 3, Springer Science & Business Media, 2010.
- [81] R. K. MOUDGIL, V. GARG, K. N. PATHAK, *Confinement and correlation effects on plasmons in an atom-scale metallic wire*, J. Phys. Condens. Matter **22**, 13:135003, 2010, doi:10.1088/0953-8984/22/13/135003.
- [82] T. ANDO, A. B. FOWLER, F. STERN, *Electronic properties of two-dimensional systems*, Rev. Mod. Phys. **54**:437, 1982, doi:10.1103/RevModPhys.54.437.
- [83] G. Y. HU, R. F. O'CONNELL, *Electron-electron interactions in quasi-one-dimensional electron systems*, Phys. Rev. B **42**:1290, 1990, doi:10.1103/PhysRevB.42.1290.
- [84] K. S. SINGWI, M. P. TOSI, R. H. LAND, A. SJÖLANDER, *Electron Correlations at Metallic Densities*, Phys. Rev. **176**, 2:589, 1968, doi:10.1103/PhysRev.176.589.
- [85] M. JONSON, *Electron correlations in inversion layers*, Journal of Physics C: Solid State Physics **9**, 16:3055, 1976, doi:10.1088/0022-3719/9/16/012.
- [86] K. SINGWI, M. TOSI, *Correlations in electron liquids*, in *Solid State Physics*, volume 36, 177–266, Elsevier, 1982, doi:10.1016/S0081-1947(08)60116-2.
-

- [87] W. I. FRIESEN, B. BERGERSEN, *Dielectric response of a one-dimensional electron gas*, J. Phys. C Solid State Phys. **13**, 36:6627, 1980, doi:10.1088/0022-3719/13/36/016.
- [88] V. ASHOKAN, N. D. DRUMMOND, K. N. PATHAK, *One-dimensional electron fluid at high density*, Phys. Rev. B **98**:125139, 2018, doi:10.1103/PhysRevB.98.125139.
- [89] K. N. ALTMANN, J. N. CRAIN, A. KIRAKOSIAN, J.-L. LIN, D. Y. PETROVYKH, F. J. HIMPSEL, R. LOSIO, *Electronic structure of atomic chains on vicinal Si(111)-Au*, Phys. Rev. B **64**, 3:035406, 2001, doi:10.1103/PhysRevB.64.035406.
- [90] T. INAOKA, T. NAGAO, *Exchange-Correlation Effects on Low-Dimensional Plasmons in an Array of Metallic Quantum Wires*, Mater. Trans. **48**, 4:718, 2007, doi:10.2320/matertrans.48.718.
- [91] L. D. LANDAU, *On the vibrations of the electronic plasma*, Zh. Eksp. Teor. Fiz. **10**:25, 1946.
- [92] M. PUSTILNIK, M. KHODAS, A. KAMENEV, L. I. GLAZMAN, *Dynamic Response of One-Dimensional Interacting Fermions*, Phys. Rev. Lett. **96**:196405, 2006, doi:10.1103/PhysRevLett.96.196405.
- [93] F. HÖTZEL, N. GALDEN, S. BAUR, A. PUCCI, *One-Dimensional Plasmonic Excitations in Gold-Induced Superstructures on Si(553): Impact of Gold Coverage and Silicon Step Edge Polarization*, J. Phys. Chem. C **121**, 553:8120, 2017, doi:10.1021/acs.jpcc.6b11753.
- [94] M. TZSCHOPPE, C. HUCK, F. HÖTZEL, A. BUTKEVICH, Z. MAMIYEV, C. ULRICH, B. GÜNTHER, L. GADE, A. PUCCI, *How adsorbates alter the metallic behavior of quasi-one-dimensional electron systems of the Si(553)-Au surface*, J. Phys. Condens. Matter **31**, 19:195001, 2018, doi:10.1088/1361-648X/ab0710.
- [95] C. DAVISSON, L. H. GERMER, *Diffraction of electrons by a crystal of nickel*, Physical review **30**, 6:705, 1927, doi:10.1103/PhysRev.30.705.
- [96] M. P. SEAH, W. A. DENCH, *Quantitative electron spectroscopy of surfaces: A standard data base for electron inelastic mean free paths in solids*, Surf. Interface Anal. **1**, 1:2, 1979, doi:10.1002/sia.740010103.
- [97] M. HENZLER, *Measurement of surface defects by low-energy electron diffraction*, Appl. Phys. A Solids Surfaces **34**, 4:205, 1984, doi:10.1007/BF00616574.
- [98] M. HORN-VON HOEGEN, *Growth of semiconductor layers studied by spot profile analysing low energy electron diffraction*, Zeitschrift für Krist. **214**, 10:591, 1999, doi:/10.1524/zkri.1999.214.10.591.
- [99] M. RITTER, W. RANKE, W. WEISS, *Growth and structure of ultrathin FeO films on Pt(111) studied by STM and LEED*, Phys. Rev. B **57**:7240, 1998, doi:10.1103/PhysRevB.57.7240.

- [100] M. HENZLER, *Quantitative evaluation of random distributed steps at interfaces and surfaces*, Surf. Sci. **73**, C:240, 1978, doi:10.1016/0039-6028(78)90499-5.
- [101] J. WOLLSCHLÄGER, J. FALTA, M. HENZLER, *Electron diffraction at stepped homogeneous and inhomogeneous surfaces*, Appl. Phys. A Solids Surfaces **50**, 1:57, 1990, doi:10.1007/BF00323955.
- [102] J. WOLLSCHLÄGER, E. Z. LUO, M. HENZLER, *Diffraction characterization of rough films formed under stable and unstable growth conditions*, Phys. Rev. B **57**, 24:15541, 1998, doi:10.1103/PhysRevB.57.15541.
- [103] C. S. LENT, P. I. COHEN, *Diffraction from stepped surfaces - I. Reversible surfaces*, Surf. Sci. **139**, 1:121, 1984, doi:10.1016/0039-6028(84)90013-X.
- [104] M. A. VAN HOVE, W. H. WEINBERG, C.-M. CHAN, *Dynamical LEED Theory*, 145–204, Springer Berlin Heidelberg, 1986, doi:10.1007/978-3-642-82721-1_5.
- [105] H. IBACH, D. L. MILLS, *Electron energy loss spectroscopy and surface vibrations*, Academic Press, 1982.
- [106] D. MILLS, *The scattering of low energy electrons by electric field fluctuations near crystal surfaces*, Surf. Sci. **48**, 1:59, 1975, doi:10.1016/0039-6028(75)90310-6.
- [107] P. THIRY, M. LIEHR, J.-J. PIREAUX, R. CAUDANO, *Electron interaction mechanisms in high resolution electron energy loss spectroscopy*, Physica Scripta **35**, 3:368, 1987.
- [108] F. HÖTZEL, *Infrarotspektroskopie an quasiaendimensionalen Goldatomketten auf vizinalen Siliziumoberfläche*, Doctoral Dissertation, Ruprecht-Karls-Universität Heidelberg, 2017.
- [109] E. P. RUGERAMIGABO, *ELS-LEED study of low-dimensional plasmons in DySi₂ layers and nanowires*, Doctoral Dissertation, Leibniz University of Hannover, 2007.
- [110] K. D. GRONWALD, M. HENZLER, *Epitaxy of Si(111) as studied with a new high resolving LEED system*, Surf. Sci. **117**, 1-3:180, 1982, doi:10.1016/0039-6028(82)90498-8.
- [111] M. HENZLER, *Defects at semiconductor surfaces*, Surf. Sci. **152-153**, 2:963, 1985, doi:10.1016/0039-6028(85)90511-4.
- [112] U. SCHEITHAUER, G. MEYER, M. HENZLER, *A new LEED instrument for quantitative spot profile analysis*, Surf. Sci. **178**, 1-3:441, 1986, doi:10.1016/0039-6028(86)90321-3.
- [113] D. LÜKERMANN, *Spin-Bahn-Kopplung in niedrigdimensionalen Strukturen auf Oberflächen - Wachstum und elektronischer Transport*, Doctoral Dissertation, Leibniz Universität Hannover, 2013.
- [114] *Winspa SPA-LEED control software*, <http://www.winspa.de>, accessed: June 11 2020.

- [115] T. NAGAO, S. HASEGAWA, *Construction of an ELS-LEED: An electron energy-loss spectrometer with electrostatic two-dimensional angular scanning*, Surf. Interface Anal. **30**, 1:488, 2000, doi:10.1002/1096-9918(200008)30:1<488::AID-SIA755>3.0.CO;2-R.
- [116] T. LANGER, *Niedrigdimensionale Plasmonen in epitaktischen Graphenlagen*, Doctoral Dissertation, Leibniz Universität Hannover, 2012.
- [117] A. BAGCHI, C. DUKE, P. FEIBELMAN, J. PORTEUS, *Measurement of surface-plasmon dispersion in aluminum by inelastic low-energy electron diffraction*, Physical Review Letters **27**, 15:998, 1971, doi:10.1103/PhysRevLett.27.998.
- [118] H. CLAUS, A. BÜSSENSCHÜTT, M. HENZLER, *Low-energy electron diffraction with energy resolution*, Rev. Sci. Instrum. **63**, 4:2195, 1992, doi:10.1063/1.1143138.
- [119] M. ROCCA, F. BIGGIO, U. VALBUSA, *Surface-plasmon spectrum of Ag(001) measured by high-resolution angle-resolved electron-energy-loss spectroscopy*, Phys. Rev. B **42**:2835, 1990, doi:10.1103/PhysRevB.42.2835.
- [120] G. SAUERBREY, *Verwendung von Schwingquarzen zur Wägung dünner Schichten und zur Mikrowägung*, Z. Phys. **155**, 2:206, 1959, doi:10.1007/BF01337937.
- [121] R. A. HEISING, *Quartz crystals for electrical circuits: their design and manufacture*, D. Van Nostrand company, inc., New York, 1946.
- [122] U. BISCHLER, *Simple source of atomic hydrogen for ultrahigh vacuum applications*, J. Vac. Sci. Technol. A Vacuum, Surfaces, Film. **11**, 2:458, 1993, doi:10.1116/1.578754.
- [123] A. SUTOH, Y. OKADA, S. OHTA, M. KAWABE, *Cracking Efficiency of Hydrogen with Tungsten Filament in Molecular Beam Epitaxy*, Jpn. J. Appl. Phys. **34**, Part 2, No. 10B:L1379, 1995, doi:10.1143/JJAP34.L1379.
- [124] F. NAKAO, *Determination of the ionization gauge sensitivity using the relative ionization cross-section*, Vacuum **25**, 9-10:431, 1975, doi:10.1016/0042-207X(75)90491-1.
- [125] S. KAR, R. SINGH, D. MISRA, H. IWAI, M. HOUSSA, J. MORAIS, D. LANDHEER, *Physics and technology of high-k gate dielectrics I*, Electrochemical Society, 2006.
- [126] K. TAKAYANAGI, Y. TANISHIRO, S. TAKAHASHI, M. TAKAHASHI, *Structure analysis of Si(111)-7×7 reconstructed surface by transmission electron diffraction*, Surf. Sci. **164**, 2-3:367, 1985, doi:10.1016/0039-6028(85)90753-8.
- [127] A. MUGARZA, J. ORTEGA, *Electronic states at vicinal surfaces*, Journal of Physics: Condensed Matter **15**, 47:S3281, 2003, doi:10.1088/0953-8984/15/47/006.

-
- [128] T. NAGAO, T. HILDEBRANDT, M. HENZLER, S. HASEGAWA, *Dispersion and damping of a two-dimensional plasmon in a metallic surface-state band*, Phys. Rev. Lett. **86**, 25:5747, 2001, doi:10.1103/PhysRevLett.86.5747.
- [129] T. NAGAO, T. HILDEBRANDT, M. HENZLER, S. HASEGAWA, *Two-dimensional plasmon in a surface-state band*, Surf. Sci. **493**, 1-3:680, 2001, doi:10.1016/S0039-6028(01)01282-1.
- [130] H.-C. JEONG, E. D. WILLIAMS, *Steps on surfaces: experiment and theory*, Surface Science Reports **34**, 6-8:171, 1999, doi:10.1016/S0167-5729(98)00010-7.
- [131] J.-L. LIN, D. Y. PETROVYKH, J. VIERNOW, F. K. MEN, D. J. SEO, F. J. HIMPSEL, *Formation of regular step arrays on Si(111)7 × 7*, J. Appl. Phys. **84**, 1:255, 1998, doi:10.1063/1.368077.
- [132] R. J. PHANEUF, E. D. WILLIAMS, *Step-height-tripling transition on vicinal Si(111)*, Phys. Rev. B **41**:2991, 1990, doi:10.1103/PhysRevB.41.2991.
- [133] S. YOSHIDA, T. SEKIGUCHI, K. M. ITOH, *Atomically straight steps on vicinal Si (111) surfaces prepared by step-parallel current in the kink-up direction*, Applied Physics Letters **87**, 3:031903, 2005, doi:10.1063/1.1995946.
- [134] J. VIERNOW, J. L. LIN, D. Y. PETROVYKH, F. M. LEIBSLE, F. K. MEN, F. J. HIMPSEL, *Regular step arrays on silicon*, Appl. Phys. Lett. **72**, 1998:948, 1998, doi:10.1063/1.120882.
- [135] Y. HOMMA, N. AIZAWA, *Electric-current-induced step bunching on Si(111)*, Phys. Rev. B **62**:8323, 2000, doi:10.1103/PhysRevB.62.8323.
- [136] D. BRUNS, S. GEVERS, J. WOLLSCHLÄGER, *Formation and morphology of step bunches during B-segregation on vicinal Si(111)*, Surf. Sci. **605**, 9-10:861, 2011, doi:10.1016/j.susc.2011.01.013.
- [137] M. KOPCIUSZYŃSKI, P. DYNIEC, R. ZDYB, M. JAŁOCHOWSKI, *Regular step distribution of the bare Si(553) surface*, Phys. Rev. B **91**, 23:1, 2015, doi:10.1103/PhysRevB.91.235420.
- [138] F. K. MEN, F. LIU, P. J. WANG, C. H. CHEN, D. L. CHENG, J. L. LIN, F. J. HIMPSEL, *Self-Organized Nanoscale Pattern Formation on Vicinal Si(111) Surfaces via a Two-Stage Faceting Transition*, Phys. Rev. Lett. **88**:096105, 2002, doi:10.1103/PhysRevLett.88.096105.
- [139] A. KIRAKOSIAN, R. BENNEWITZ, J. N. CRAIN, T. FAUSTER, J. L. LIN, D. Y. PETROVYKH, F. J. HIMPSEL, *Atomically accurate Si grating with 5.73 nm period*, Appl. Phys. Lett. **79**, 11:1608, 2001, doi:10.1063/1.1401788.
- [140] A. KIRAKOSIAN, R. BENNEWITZ, J. N. CRAIN, T. FAUSTER, J. L. LIN, D. Y. PETROVYKH, F. J. HIMPSEL, *Atomically accurate Si grating with 5.73 nm period*, Appl. Phys. Lett. **79**, 11:1608, 2001, doi:10.1063/1.1401788.
-

- [141] S. A. TEYS, K. N. ROMANYUK, R. A. ZHACHUK, B. Z. OLSHANETSKY, *Orientation and structure of triple step staircase on vicinal Si(1 1 1) surfaces*, Surf. Sci. **600**, 21:4878, 2006, doi:10.1016/j.susc.2006.08.009.
- [142] D.-H. OH, M. K. KIM, J. H. NAM, I. SONG, C.-Y. PARK, S. H. WOO, H.-N. HWANG, C. C. HWANG, J. R. AHN, *Atomic structure model of the reconstructed Si(557) surface with a triple step structure: Adatom-parallel dimer model*, Phys. Rev. B **77**, 15:155430, 2008, doi:10.1103/PhysRevB.77.155430.
- [143] G. PRÉVOT, F. LEROY, B. CROSET, Y. GARREAU, A. COATI, P. MÜLLER, *Step-induced elastic relaxation and surface structure of the Si (7710) surface*, Surface science **606**, 3-4:209, 2012, doi:10.1016/j.susc.2011.09.019.
- [144] R. ZHACHUK, S. TEYS, J. COUTINHO, M. RAYSON, P. BRIDDON, *Static and dynamic buckling of reconstructions at triple steps on Si (111) surfaces*, Applied Physics Letters **105**, 17:171602, 2014, doi:10.1063/1.4900783.
- [145] C. PEREZ LEON, H. DREES, S. M. WIPPERMANN, M. MARZ, R. HOFFMANN-VOGEL, *Atomically resolved scanning force studies of vicinal Si(111)*, Phys. Rev. B **95**:245412, 2017, doi:10.1103/PhysRevB.95.245412.
- [146] M. KIM, D.-H. OH, J. BAIK, C. JEON, I. SONG, J. NAM, S. WOO, C.-Y. PARK, J. AHN, *Control of a quasi-one-dimensional phase of a Si nanostructure: Vicinal Si (557) surfaces*, Physical Review B **81**, 8:085312, 2010, doi:10.1103/PhysRevB.81.085312.
- [147] S. C. ERWIN, A. A. BASKI, L. J. WHITMAN, *Structure and Stability of Si(114) – (2 × 1)*, Phys. Rev. Lett. **77**:687, 1996, doi:10.1103/PhysRevLett.77.687.
- [148] M. JAŁOCHOWSKI, M. STROŻAK, R. ZDYB, *Gold-induced ordering on vicinal Si(111)*, Surf. Sci. **375**, 2-3:203, 1997, doi:10.1016/S0039-6028(97)80009-X.
- [149] C. KUMPE, O. BUNK, J. H. ZEYSING, Y. SU, M. NIELSEN, R. L. JOHNSON, R. FEIDENHANS'L, K. BECHGAARD, *Low-Temperature Structure of Indium Quantum Chains on Silicon*, Phys. Rev. Lett. **85**:4916, 2000, doi:10.1103/PhysRevLett.85.4916.
- [150] A. KIRAKOSIAN, J. L. MCCHESENEY, R. BENNEWITZ, J. N. CRAIN, J.-L. LIN, F. J. HIMPSEL, *One-dimensional Gd-induced chain structures on Si(111) surfaces*, Surf. Sci. Lett. **498**:L109, 2002.
- [151] O. GURLU, O. A. O. ADAM, H. J. W. ZANDVLIET, B. POELSEMA, *Self-organized, one-dimensional Pt nanowires on Ge(001)*, Appl. Phys. Lett. **83**, 22:4610, 2003, doi:10.1063/1.1630383.
- [152] M. CZUBANOWSKI, H. PFNÜR, C. TEGENKAMP, *Atomic chain ordering with ultra-long periods: Pb/Si (5 5 7)*, Surface science **603**, 19:L121, 2009, doi:10.1016/j.susc.2009.08.013.

-
- [153] G. PROFETA, E. TOSATTI, *Triangular Mott-Hubbard Insulator Phases of Sn/Si(111) and Sn/Ge(111) Surfaces*, Phys. Rev. Lett. **98**:086401, 2007, doi:10.1103/PhysRevLett.98.086401.
- [154] C. GONZÁLEZ, P. C. SNIJDERS, J. ORTEGA, R. PÉREZ, F. FLORES, S. ROGGE, H. H. WEITERING, *Formation of Atom Wires on Vicinal Silicon*, Phys. Rev. Lett. **93**, 12:126106, 2004, doi:10.1103/PhysRevLett.93.126106, arXiv:arXiv:cond-mat/0404285v1.
- [155] S. GHOSE, I. ROBINSON, P. A. BENNETT, F. J. HIMPEL, *Structure of double row quantum wires in Au/Si(553)*, Surf. Sci. **581**, 2-3:199, 2005, doi:10.1016/j.susc.2005.02.053.
- [156] S. HARA, M. YOSHIMURA, K. UEDA, *Atomic Structure of Si(553) Surface Revealed by Scanning Tunneling Microscopy*, Jpn. J. Appl. Phys. **47**, 7:6102, 2008, doi:10.1143/JJAP47.6102.
- [157] P. C. SNIJDERS, S. ROGGE, H. H. WEITERING, *Competing periodicities in fractionally filled one-dimensional bands*, Phys. Rev. Lett. **96**, 7:48, 2006, doi:10.1103/PhysRevLett.96.076801, arXiv:cond-mat/0510574.
- [158] J. N. CRAIN, *Low-dimensional electronic states at silicon surfaces*, Appl. Phys. A **82**:431, 2006, doi:10.1007/s00339-005-3365-3.
- [159] K.-D. RYANG, P. G. KANG, H. W. YEOM, S. JEONG, *Structures and defects of atomic wires on Si(553)-Au: An STM and theoretical study*, Phys. Rev. B **76**, 20:205325, 2007, doi:10.1103/PhysRevB.76.205325.
- [160] S. HASEGAWA, X. TONG, S. TAKEDA, N. SATO, T. NAGAO, *Structures and electronic transport on silicon surfaces*, Prog. Surf. Sci. **60**, 5:89, 1999, doi:10.1016/S0079-6816(99)00008-8.
- [161] H. OKINO, I. MATSUDA, S. YAMAZAKI, R. HOBARA, S. HASEGAWA, *Transport in defective quasi-one-dimensional arrays of chains of gold atoms on a vicinal silicon surface*, Phys. Rev. B **76**, 3:035424, 2007, doi:10.1103/PhysRevB.76.035424.
- [162] S. C. ERWIN, *Self-Doping of Gold Chains on Silicon: A New Structural Model for Si(111)-(5×2)-Au*, Phys. Rev. Lett. **91**:206101, 2003, doi:10.1103/PhysRevLett.91.206101.
- [163] S. C. ERWIN, I. BARKE, F. J. HIMPEL, *Structure and energetics of Si(111)-(5×2)-Au*, Phys. Rev. B **80**:155409, 2009, doi:10.1103/PhysRevB.80.155409.
- [164] S. G. KWON, M. H. KANG, *Identification of the Au Coverage and Structure of the Au/Si(111)-(5×2) Surface*, Phys. Rev. Lett. **113**:086101, 2014, doi:10.1103/PhysRevLett.113.086101.
- [165] T. ABUKAWA, Y. NISHIGAYA, *Structure of the Si(111)-(5×2)-Au Surface*, Phys. Rev. Lett. **110**:036102, 2013, doi:10.1103/PhysRevLett.110.036102.
-

- [166] T. SHIRASAWA, W. VOEGELI, T. NOJIMA, Y. IWASAWA, Y. YAMAGUCHI, T. TAKAHASHI, *Identification of the Structure Model of the Si(111)-(5×2)-Au Surface*, Phys. Rev. Lett. **113**:165501, 2014, doi:10.1103/PhysRevLett.113.165501.
- [167] H. BISHOP, J. RIVIERE, *Segregation of gold to the silicon (111) surface observed by Auger emission spectroscopy and by LEED*, Journal of Physics D: Applied Physics **2**, 12:1635, 1969, doi:10.1088/0022-3727/2/12/302.
- [168] H. LIPSON, K. SINGER, *Disorder in a film of gold deposited on silicon: Investigation by low-energy electron diffraction*, Journal of Physics C: Solid State Physics **7**, 1:12, 1974, doi:10.1088/0022-3719/7/1/010.
- [169] L. D. MARKS, R. PLASS, *Atomic Structure of Si(111)-(5×2)-Au from High Resolution Electron Microscopy and Heavy-Atom Holography*, Phys. Rev. Lett. **75**:2172, 1995, doi:10.1103/PhysRevLett.75.2172.
- [170] T. HASEGAWA, K. TAKATA, S. HOSAKA, S. HOSOKI, *Au-induced reconstructions of the Si (111) surface*, Journal of Vacuum Science & Technology A: Vacuum, Surfaces, and Films **8**, 1:241, 1990, doi:10.1116/1.577075.
- [171] A. A. BASKI, J. NOGAMI, C. F. QUATE, *Si(111)-(5×1)-Au reconstruction as studied by scanning tunneling microscopy*, Phys. Rev. B **41**:10247, 1990, doi:10.1103/PhysRevB.41.10247.
- [172] C. HOGAN, E. FERRARO, N. MCALINDEN, J. F. MCGILP, *Optical Fingerprints of Si Honeycomb Chains and Atomic Gold Wires on the Si(111)-(5×2)-Au Surface*, Phys. Rev. Lett. **111**:087401, 2013, doi:10.1103/PhysRevLett.111.087401.
- [173] I. BARKE, F. ZHENG, S. BOCKENHAUER, K. SELL, V. V. OEYNHAUSEN, K. H. MEIWES-BROER, S. C. ERWIN, F. J. HIMPSEL, *Coverage-dependent faceting of Au chains on Si(557)*, Phys. Rev. B **79**, 15:155301, 2009, doi:10.1103/PhysRevB.79.155301.
- [174] I. BARKE, S. POLEI, V. V. OEYNHAUSEN, K.-H. MEIWES-BROER, *Confined Doping on a Metallic Atomic Chain Structure*, Phys. Rev. Lett. **109**:066801, 2012, doi:10.1103/PhysRevLett.109.066801.
- [175] S. POLEI, I. BARKE, S. C. ERWIN, K.-H. MEIWES-BROER, *Periodic variations in the local surface potential of Si(111)-(5×2)-Au*, Phys. Rev. B **85**:165414, 2012, doi:10.1103/PhysRevB.85.165414.
- [176] F. HÖTZEL, K. SEINO, C. HUCK, O. SKIBBE, F. BECHSTEDT, A. PUCCI, *Metallic Properties of the Si(111) - 5 × 2 - Au Surface from Infrared Plasmon Polaritons and Ab Initio Theory*, Nano Lett. **15**, 6:4155, 2015, doi:10.1021/acs.nanolett.5b01279.
- [177] E. H. DO, S. G. KWON, M. H. KANG, H. W. YEOM, *Structural and electronic effects of adatoms on metallic atomic chains in Si (111) 5×2-Au*, Scientific reports **8**, 1:1, 2018, doi:10.1038/s41598-018-33703-5.

-
- [178] N. MCALINDEN, J. F. MCGILP, *New evidence for the influence of step morphology on the formation of Au atomic chains on vicinal Si(111) surfaces*, EPL (Europhysics Lett. **92**, 6:67008, 2010, doi:10.1209/0295-5075/92/67008.
- [179] J. KAUTZ, M. W. COPEL, M. S. GORDON, R. M. TROMP, S. J. VAN DER MOLEN, *Titration of submonolayer Au growth on Si(111)*, Phys. Rev. B **89**:035416, 2014, doi:10.1103/PhysRevB.89.035416.
- [180] E. H. DO, H. W. YEOM, *Electron Quantization in Broken Atomic Wires*, Phys. Rev. Lett. **115**:266803, 2015, doi:10.1103/PhysRevLett.115.266803.
- [181] D. GROZEA, E. BENGU, L. MARKS, *Surface phase diagrams for the Ag-Ge(111) and Au-Si(111) systems*, Surf. Sci. **461**, 1:23, 2000, doi:https://doi.org/10.1016/S0039-6028(00)00491-X.
- [182] W. SWIECH, E. BAUER, M. MUNDSCHAU, *A low-energy electron microscopy study of the system Si(111)-Au*, Surface science **253**, 1-3:283, 1991, doi:10.1016/0039-6028(91)90599-N.
- [183] T. NAGAO, S. HASEGAWA, K. TSUCHIE, S. INO, C. VOGES, G. KLOS, H. PFNÜR, M. HENZLER, *Structural phase transitions of Si(111)-($\sqrt{3}\times\sqrt{3}$)R30°-Au: Phase transitions in domain-wall configuration*, Phys. Rev. B **57**, 16:10100, 1998, doi:10.1103/PhysRevB.57.10100.
- [184] I. COLLINS, J. MORAN, P. ANDREWS, R. COSSO, J. O'MAHONY, J. MCGILP, G. MARGARITONDO, *Angle-resolved photoemission from an unusual quasi-one-dimensional metallic system: a single domain Au-induced 5×2 reconstruction of Si(111)*, Surface science **325**, 1-2:45, 1995, doi:10.1016/0039-6028(94)00735-7.
- [185] J. MCCHESENEY, J. CRAIN, V. PÉREZ-DIESTE, F. ZHENG, M. GALLAGHER, M. BISSEN, C. GUNDELACH, F. HIMPSEL, *Electronic stabilization of a 5×4 dopant superlattice on Si(111) 5×2-Au*, Physical Review B **70**, 19:195430, 2004, doi:10.1103/PhysRevB.70.195430.
- [186] R. LOSIO, K. N. ALTMANN, F. J. HIMPSEL, *Fermi surface of Si(111)7×7*, Phys. Rev. B **61**:10845, 2000, doi:10.1103/PhysRevB.61.10845.
- [187] T. MILLER, A. SAMSAVAR, G. E. FRANKLIN, T. C. CHIANG, *Quantum-Well States in a Metallic System: Ag on Au(111)*, Phys. Rev. Lett. **61**:1404, 1988, doi:10.1103/PhysRevLett.61.1404.
- [188] K. TAGUCHI, K. SUMIDA, Y. OKUDA, K. MIYAMOTO, A. KIMURA, T. OGUCHI, T. OKUDA, *Spectroscopic evidence of quasi-one-dimensional metallic Rashba spin-split states on the Si(111)5×2-Au surface*, Phys. Rev. B **101**:045430, 2020, doi:10.1103/PhysRevB.101.045430.
- [189] Z. MAMIYEV, H. PFNÜR, *View on Si(111)-(5×2)-Au with plasmon spectroscopy*, Phys. Rev. B **102**, 07:075438, 2020, doi:10.1103/PhysRevB.102.075438.
-

- [190] A. STEPNIAK, M. KRAWIEC, G. ZAWADZKI, M. JAOCHOWSKI, *Electronic stabilization of the Si(111)5x2-Au surface: Pb and Si adatoms*, J. Phys. Condens. Matter **24**:095002, 2012, doi:10.1088/0953-8984/24/9/095002.
- [191] C. H. PATTERSON, S. BANERJEE, J. F. MCGILP, *Reflectance anisotropy spectroscopy of the Si(111)-(5 × 2)Au surface*, Phys. Rev. B **94**:165417, 2016, doi:10.1103/PhysRevB.94.165417.
- [192] A. KIRAKOSIAN, R. BENNEWITZ, F. J. HIMPSEL, L. BRUCH, *Correlations in a one-dimensional lattice fluid on Si(111)5×2-Au*, Phys. Rev. B **67**, 20:205412, 2003, doi:10.1103/PhysRevB.67.205412.
- [193] R. LOSIO, K. N. ALTMANN, F. J. HIMPSEL, *Continuous Transition from Two- to One-Dimensional States in Si(111)-(5×2)-Au*, Phys. Rev. Lett. **85**, 4:808, 2000, doi:10.1103/PhysRevLett.85.808.
- [194] C. LIU, T. INAOKA, S. YAGINUMA, T. NAKAYAMA, M. AONO, T. NAGAO, *The excitation of one-dimensional plasmons in Si and Au-Si complex atom wires*, Nanotechnology **19**, 35:355204, 2008, doi:10.1088/0957-4484/19/35/355204.
- [195] T. LICHTENSTEIN, J. AULBACH, J. SCHÄFER, R. CLAESSEN, C. TEGENKAMP, H. PFNÜR, *Two-dimensional crossover and strong coupling of plasmon excitations in arrays of one-dimensional atomic wires*, Phys. Rev. B **93**, 16:161408, 2016, doi:10.1103/PhysRevB.93.161408.
- [196] F. HÖTZEL, K. SEINO, S. CHANDOLA, E. SPEISER, N. ESSER, F. BECHSTEDT, A. PUCCI, *Metal-to-Insulator Transition in Au Chains on Si(111)-5x2-Au by Band Filling: Infrared Plasmonic Signal and Ab Initio Band Structure Calculation*, J. Phys. Chem. Lett. **6**, 18:3615, 2015, doi:10.1021/acs.jpcllett.5b01530.
- [197] J. M. LAYET, J. Y. HOARAU, H. LÜTH, J. DERRIEN, *Dispersion of the dangling-bond surface states of Si(111)-(7×7)*, Phys. Rev. B **30**:7355, 1984, doi:10.1103/PhysRevB.30.7355.
- [198] Z. MAMIYEV, S. SANNA, F. ZIESE, C. DUES, C. TEGENKAMP, H. PFNÜR, *Plasmon Localization by H Induced Band Switching*, The Journal of Physical Chemistry C **124**, 1:958, 2019, doi:10.1021/acs.jpcc.9b10688.
- [199] W. H. CHOI, P. G. KANG, K. D. RYANG, H. W. YEOM, *Band-Structure Engineering of Gold Atomic Wires on Silicon by Controlled Doping*, Phys. Rev. Lett. **100**, 12:126801, 2008, doi:10.1103/PhysRevLett.100.126801.
- [200] S. C. ERWIN, P. C. SNIJDERS, *Silicon spin chains at finite temperature: Dynamics of Si(553)-Au*, Phys. Rev. B **87**, 23:235316, 2013, doi:10.1103/PhysRevB.87.235316.
- [201] B. HAFKE, T. FRIGGE, T. WITTE, B. KRENZER, J. AULBACH, J. SCHÄFER, R. CLAESSEN, S. C. ERWIN, M. HORN-VON HOEGEN, *Two-dimensional interaction of spin chains in the Si(553)-Au nanowire system*, Phys. Rev. B **94**, 16:161403, 2016, doi:10.1103/PhysRevB.94.161403.

-
- [202] I. BARKE, F. ZHENG, T. K. RÜGHEIMER, F. J. HIMPSEL, *Experimental Evidence for Spin-Split Bands in a One-Dimensional Chain Structure*, Phys. Rev. Lett. **97**, 22:226405, 2006, doi:10.1103/PhysRevLett.97.226405.
- [203] T. OKUDA, K. MIYAMOTO, Y. TAKEICHI, H. MIYAHARA, M. OGAWA, A. HARASAWA, A. KIMURA, I. MATSUDA, A. KAKIZAKI, T. SHISHIDOU, T. OGUCHI, *Large out-of-plane spin polarization in a spin-splitting one-dimensional metallic surface state on Si(557)-Au*, Phys. Rev. B **82**:161410, 2010, doi:10.1103/PhysRevB.82.161410.
- [204] H. W. YEOM, S. W. JUNG, J. S. SHIN, J. KIM, K. S. KIM, K. MIYAMOTO, T. OKUDA, H. NAMATAME, A. KIMURA, M. TANIGUCHI, *Direct observation of the spin polarization in Au atomic wires on Si(553)*, New J. Phys. **16**, 9:093030, 2014, doi:10.1088/1367-2630/16/9/093030.
- [205] M. KRAWIEC, M. KOPCIUSZYŃSKI, R. ZDYB, *Different spin textures in one-dimensional electronic bands on Si(5 5 3)-Au surface*, Appl. Surf. Sci. **373**:26, 2016, doi:10.1016/j.apsusc.2015.09.219.
- [206] I. SONG, D.-H. OH, H.-C. SHIN, S.-J. AHN, Y. MOON, S.-H. WOO, H. J. CHOI, C.-Y. PARK, J. R. AHN, *Direct Momentum-Resolved Observation of One-Dimensional Confinement of Externally Doped Electrons within a Single Subnanometer-Scale Wire*, Nano Lett. **15**, 1:281, 2015, doi:10.1021/nl503558g.
- [207] J. AULBACH, S. C. ERWIN, J. KEMMER, M. BODE, J. SCHÄFER, R. CLAESSEN, *Parity breaking in a double atomic chain system*, Phys. Rev. B **96**, 8:081406(R), 2017, doi:10.1103/PhysRevB.96.081406.
- [208] J. AULBACH, J. SCHÄFER, S. C. ERWIN, S. MEYER, C. LOHO, J. SETTELEIN, R. CLAESSEN, *Evidence for Long-Range Spin Order Instead of a Peierls Transition in Si(553)-Au Chains*, Phys. Rev. Lett. **111**, 13:137203, 2013, doi:10.1103/PhysRevLett.111.137203.
- [209] S. C. E. P. C. SNIJDERS, P. S. JOHNSON, P. GUISSINGER, F. J. HIMPSEL, *Spectroscopic evidence for spin-polarized edge states in graphitic Si nanowires*, New J. Phys. **14**, 14:103004, 2012, doi:10.1088/1367-2630/14/10/103004.
- [210] S. POLEI, P. C. SNIJDERS, K.-H. MEIWES-BROER, I. BARKE, *Current-dependent periodicities of Si(553)-Au*, Phys. Rev. B **89**, 20:205420, 2014, doi:10.1103/PhysRevB.89.205420.
- [211] T. TAKAYAMA, W. VOEGELI, T. SHIRASAWA, K. KUBO, M. ABE, T. TAKAHASHI, K. AKIMOTO, H. SUGIYAMA, *Structural Study of the Si(553)-Au Surface*, e-Journal of Surface Science and Nanotechnology **7**:533, 2009, doi:10.1380/ejsnt.2009.533.
- [212] W. VOEGELI, T. TAKAYAMA, T. SHIRASAWA, M. ABE, K. KUBO, T. TAKAHASHI, K. AKIMOTO, H. SUGIYAMA, *Structure of the quasi-one-dimensional Si(553)-Au surface: Gold dimer row and silicon honeycomb chain*, Phys. Rev. B **82**, 7:075426, 2010, doi:10.1103/PhysRevB.82.075426.
-

- [213] P. C. SNIJDERS, S. ROGGE, H. H. WEITERING, *Competing Periodicities in Fractionally Filled One-Dimensional Bands*, Phys. Rev. Lett. **96**:076801, 2006, doi:10.1103/PhysRevLett.96.076801.
- [214] C. BRAUN, U. GERSTMANN, W. G. SCHMIDT, *Spin pairing versus spin chains at Si(553)-Au surfaces*, Phys. Rev. B **98**:121402, 2018, doi:10.1103/PhysRevB.98.121402.
- [215] Z. MAMIYEV, M. TZSCHOPPE, C. HUCK, A. PUCCI, H. PFNÜR, *Plasmon Standing Waves by Oxidation of Si (553)-Au*, The Journal of Physical Chemistry C **123**, 14:9400, 2019, doi:10.1021/acs.jpcc.9b01372.
- [216] I. SONG, J. S. GOH, S.-H. LEE, S. W. JUNG, J. S. SHIN, H. YAMANE, N. KOSUGI, H. W. YEOM, *Realization of a Strained Atomic Wire Superlattice*, ACS Nano **9**, 11:10621, 2015, doi:10.1021/acsnano.5b04377.
- [217] P. HECQUET, *Stability of vicinal surfaces and role of the surface stress*, Surface Science **604**, 9-10:834, 2010, doi:10.1016/j.susc.2010.02.009.
- [218] L. PEDRI, L. TOPPOZINI, M. C. GALLAGHER, *Au-induced nanofaceting and the stoichiometry of the Si(775)-Au surface*, Surf. Sci. **601**, 4:924, 2007, doi:10.1016/j.susc.2006.11.031.
- [219] L. J. PEDRI, W. WU, M. C. GALLAGHER, *Au-Induced Nanostructuring of Vicinal Si Surfaces*, J. Phys. Conf. Ser. **61**:322, 2007, doi:10.1088/1742-6596/61/1/065.
- [220] C. BRAUN, C. HOGAN, S. CHANDOLA, N. ESSER, S. SANNA, W. G. SCHMIDT, *Si(775)-Au atomic chains: Geometry, optical properties, and spin order*, Phys. Rev. Materials **1**:055002, 2017, doi:10.1103/PhysRevMaterials.1.055002.
- [221] H. TEIKEN, *SPA-LEED und EELS-LEED Untersuchungen an atomaren Au-Ketten auf Ge(100) und Si(553)*, Master's Thesis, Leibniz Universität Hannover, 2014.
- [222] M. JAŁOCHOWSKI, R. ZDYB ET AL., *Gold-induced ordering on vicinal Si (111)*, Surface science **375**, 2-3:203, 1997, doi:10.1016/S0039-6028(97)80009-X.
- [223] H. OKINO, I. MATSUDA, T. TANIKAWA, S. HASEGAWA, *Formation of facet structures by Au adsorption on vicinal Si (111) surfaces*, e-Journal of Surface Science and Nanotechnology **1**:84, 2003, doi:10.1380/ejssnt.2003.84.
- [224] R. HILD, C. SEIFERT, M. KAMMLER, F.-J. MEYER ZU HERINGDORF, M. HORN-VON HOEGEN, R. ZHACHUK, B. OLSHANETSKY, *Kinetics of Au induced faceting of vicinal Si(111)*, Surf. Sci. **512**, 1-2:117, 2002, doi:10.1016/S0039-6028(02)01666-7.
- [225] M. CZUBANOWSKI, A. SCHUSTER, S. AKBARI, H. PFNÜR, C. TEGENKAMP, *Adsorbate induced refaceting: Pb chains on Si(557)*, New J. Phys. **9**, 111, 2007, doi:10.1088/1367-2630/9/9/338.

- [226] L. SEEHOFER, S. HUHS, G. FALKENBERG, R. JOHNSON, *Gold-induced faceting of Si(111)*, Surf. Sci. **329**, 3:157, 1995, doi:10.1016/0039-6028(95)00058-5.
- [227] Z. MAMIYEV, F. CHRISTA, K. HOLTGREWE, H. PFNÜR, S. SANNA, *Enhancing structural order in atomic wires by atomic adsorption*, submitted 2020.
- [228] I. K. ROBINSON, P. A. BENNETT, F. J. HIMPSEL, *Structure of Quantum Wires in Au/Si(557)*, Phys. Rev. Lett. **88**, 9:096104, 2002, doi:10.1103/PhysRevLett.88.096104.
- [229] S. RIIKONEN, D. SÁNCHEZ-PORTAL, *Interplay between electronic and atomic structures in the Si(557)-Au reconstruction from first principles*, Phys. Rev. B **76**:035410, 2007, doi:10.1103/PhysRevB.76.035410.
- [230] D. SÁNCHEZ-PORTAL, R. M. MARTIN, *First principles study of the Si(557)-Au surface*, Surf. Sci. **532-535**:655, 2003, doi:10.1016/S0039-6028(03)00224-3.
- [231] F. EDLER, I. MICCOLI, J. P. STÖCKMANN, H. PFNÜR, C. BRAUN, S. NEUFELD, S. SANNA, W. G. SCHMIDT, C. TEGENKAMP, *Tuning the conductivity along atomic chains by selective chemisorption*, Phys. Rev. B **95**, 12:125409, 2017, doi:10.1103/PhysRevB.95.125409.
- [232] J. R. AHN, H. W. YEOM, H. S. YOON, I.-W. LYO, *Metal-Insulator Transition in Au Atomic Chains on Si with Two Proximal Bands*, Phys. Rev. Lett. **91**, 19:196403, 2003, doi:10.1103/PhysRevLett.91.196403.
- [233] J. R. AHN, H. W. YEOM, E. S. CHO, C. Y. PARK, *Electronic transition of Au-induced atomic chains on Si(5512): A strong similarity with the Au/Si(557) system*, Phys. Rev. B **69**:233311, 2004, doi:10.1103/PhysRevB.69.233311.
- [234] H. W. YEOM, J. R. AHN, H. S. YOON, I. W. LYO, H. JEONG, S. JEONG, *Real-space investigation of the metal-insulator transition of Si(557)-Au*, Phys. Rev. B **72**, 3:1, 2005, doi:10.1103/PhysRevB.72.035323.
- [235] H. S. KIM, S. Y. SHIN, S. H. UHM, C. C. HWANG, D. Y. NOH, J. W. CHUNG, *Evidence of metallic nature of the surface bands of Au/Si(557)*, Phys. Rev. B **80**:033412, 2009, doi:10.1103/PhysRevB.80.033412.
- [236] M. SAUTER, R. HOFFMANN, C. SÜRGER, H. V. LÖHNEISEN, *Temperature-dependent scanning tunneling spectroscopy on the Si(557)-Au surface*, Phys. Rev. B **89**, 7:075406, 2014, doi:10.1103/PhysRevB.89.075406.
- [237] B. PERSSON, J. DEMUTH, *Inelastic scattering of slow electrons from Si(111) surfaces*, Phys. Rev. B **30**, 10:5968, 1984, doi:10.1103/PhysRevB.30.5968.

- [238] T. NAGAO, *Characterization of atomic-level plasmonic structures by low-energy EELS*, Surf. Interface Anal. **40**, 13:1764, 2008, doi:10.1002/sia.3002.
- [239] E. P. RUGERAMIGABO, T. NAGAO, H. PFNÜR, *Experimental investigation of two-dimensional plasmons in a DySi 2 monolayer on Si(111)*, Phys. Rev. B **78**, 15:1, 2008, doi:10.1103/PhysRevB.78.155402.
- [240] T. LICHTENSTEIN, Z. MAMIYEV, E. JECKELMANN, C. TEGENKAMP, H. PFNÜR, *Anisotropic 2D metallicity: Plasmons in Ge(100)-Au*, J. Phys. Condens. Matter **17**, 31:175001, 2018, doi:10.1088/1361-648X/ab02c5.
- [241] J. M. PITARKE, V. M. SILKIN, E. V. CHULKOV, P. M. ECHENIQUE, *Theory of surface plasmons and surface-plasmon polaritons*, Reports Prog. Phys. **70**, 1:1, 2007, doi:10.1088/0034-4885/70/1/R01.
- [242] A. POLITANO, G. CHIARELLO, *The influence of electron confinement, quantum size effects, and film morphology on the dispersion and the damping of plasmonic modes in Ag and Au thin films*, Prog. Surf. Sci. **90**:144, 2015, doi:10.1016/j.progsurf.2014.12.002.
- [243] F. GIUSTINO, *Electron-phonon interactions from first principles*, Rev. Mod. Phys. **89**:015003, 2017, doi:10.1103/RevModPhys.89.015003.
- [244] F. CARUSO, D. NOVKO, C. DRAXL, *Phonon-assisted damping of plasmons in three- and two-dimensional metals*, Physical Review B **97**, 20:205118, 2018, doi:10.1103/PhysRevB.97.205118.
- [245] B. HALBIG, M. LIEBHABER, U. BASS, J. GEURTS, E. SPEISER, J. RÄTHEL, S. CHANDOLA, N. ESSER, M. KRENZ, S. NEUFELD, W. G. SCHMIDT, S. SANNA, *Vibrational properties of the Au-($\sqrt{3} \times \sqrt{3}$)/Si(111) surface reconstruction*, Phys. Rev. B **97**:035412, 2018, doi:10.1103/PhysRevB.97.035412.
- [246] E. SPEISER, J. PLAICKNER, S. CHANDOLA, N. ESSER, B. HALBIG, J. GEURTS, *Raman Spectroscopy on Surface Phonons of Si (hkk) Surfaces Modified by Au Submonolayers*, physica status solidi (b) **256**, 2:1800341, 2019, doi:10.1002/pssb.201800341.
- [247] I. BARKE, F. ZHENG, A. R. KONICEK, R. C. HATCH, F. J. HIMPSEL, *Electron-Phonon Interaction at the Si(111)7×7 Surface*, Phys. Rev. Lett. **96**:216801, 2006, doi:10.1103/PhysRevLett.96.216801.
- [248] H. IBACH, J. ROWE, *Hydrogen adsorption and surface structures of silicon*, Surface Science **43**, 2:481, 1974, doi:10.1016/0039-6028(74)90271-4.
- [249] H. KOBAYASHI, K. EDAMOTO, M. ONCHI, M. NISHIJIMA, *Reactions of atomic hydrogen with the Si(111) (7x7) surface by high resolution electron energy loss spectroscopy*, J. Chem. Phys. **78**, 12:656, 1983, doi:10.1063/1.444733.

-
- [250] M. B. NARDELLI, F. FINOCCHI, M. PALUMMO, R. DI FELICE, C. M. BERTONI, F. BERNARDINI, S. OSSICINI, *Hydrogen covered Si (111) surfaces*, *Surface science* **269**:879, 1992, doi:10.1016/0039-6028(92)91364-H.
- [251] M. DÜRR, U. HÖFER, *Hydrogen diffusion on silicon surfaces*, *Progress in Surface Science* **88**, 1:61, 2013, doi:10.1016/j.progsurf.2013.01.001.
- [252] J. A. SCHAEFER, J. ANDERSON, G. J. LAPEYRE, *Water adsorption on cleaved silicon surfaces*, *J. Vac. Sci. Technol. A Vacuum, Surfaces, Film.* **3**, 3:1443, 1985, doi:10.1116/1.572756.
- [253] H. IBACH, H. D. BRUCHMANN, H. WAGNER, *Vibrational study of the initial stages of the oxidation of Si(111) and Si(100) surfaces*, *Applied Physics A* **29**, 3:113, 1982, doi:10.1007/BF00617767.
- [254] Z. MAMIYEV, T. LICHTENSTEIN, C. TEGENKAMP, H. PFNUER, *Tuning of 1D Plasmon properties in Au-induced quantum wires on Si(hhk) surfaces*, in *APS March Meeting Abstracts*, volume 2018 of *APS Meeting Abstracts*, V17.002, 2018.
- [255] H. V. CHUNG, C. J. KUBBER, G. HAN, S. RIGAMONTI, D. SANCHEZ-PORTAL, D. ENDERS, A. PUCCI, T. NAGAO, *Optical detection of plasmonic and interband excitations in 1-nm-wide indium atomic wires*, *Appl. Phys. Lett.* **96**, 101, 2010, doi:10.1063/1.3451461.
- [256] M. KLEVENZ, S. WETZEL, M. TRIELOFF, H.-P. GAIL, A. PUCCI, *Vibrational spectroscopy of SiO on Si (111)*, *phys. stat. sol. b* **247**, 9:2179, 2010, doi:10.1002/pssb.200945550.
- [257] F. NEUBRECH, T. KOLB, R. LOVRINCIC, G. FAHSOLD, A. PUCCI, J. AIZPURUA, T. W. CORNELIUS, M. E. TOIMIL-MOLARES, R. NEUMANN, S. KARIM, *Resonances of individual metal nanowires in the infrared*, *Appl. Phys. Lett.* **89**, 25:253104, 2006, doi:10.1063/1.2405873.
- [258] M. TZSCHOPPE, C. HUCK, F. HÖTZEL, A. PUCCI, *C70 increases the plasmonic signal of gold-atom chains on Si (553)*, *Surface Science* 2018.
- [259] T. LANGER, J. BARINGHAUS, H. PFNÜR, H. W. SCHUMACHER, C. TEGENKAMP, *Plasmon damping below the Landau regime: the role of defects in epitaxial graphene*, *New J. Phys.* **12**, 3:033017, 2010, doi:10.1088/1367-2630/12/3/033017.
- [260] T. LICHTENSTEIN, C. TEGENKAMP, H. PFNÜR, *Lateral electronic screening in quasi-one-dimensional plasmons*, *J. Phys. Condens. Matter* **28**, 35:354001, 2016, doi:10.1088/0953-8984/28/35/354001.
- [261] P.-G. KANG, J. S. SHIN, H. W. YEOM, *Point defects along metallic atomic wires on vicinal Si surfaces: Si(557)-Au and Si(553)-Au*, *Surf. Sci.* **603**, 16:2588, 2009, doi:10.1016/j.susc.2009.06.012.
-

- [262] Z. MAMIYEV, C. TEGENKAMP, H. PFNÜR, ATMOS TEAM, *Non-classical effects of extrinsic doping on Au quantum wires*, in *APS March Meeting Abstracts*, volume 2019 of *APS Meeting Abstracts*, B45.007, 2019.
- [263] J. SCHMIDT, C. STUHLMANN, H. IBACH, *Adsorption and decomposition of diethylsilane and diethylchlorosilane on Si(100)(2 × 1) and Si(111)(1 × 1)*, *Surf. Sci.* **302**, 1:10, 1994, doi: [https://doi.org/10.1016/0039-6028\(94\)91092-8](https://doi.org/10.1016/0039-6028(94)91092-8).
- [264] H. WAGNER, H. IBACH, *Hydrogen and oxygen bonding on silicon surfaces*, in *Festkörperprobleme 23*, 165–177, Springer, 1983, doi:10.1007/BFb0107974.
- [265] S. SUCHKOVA, C. HOGAN, F. BECHSTEDT, E. SPEISER, N. ESSER, *Selective adsorption of toluene-3,4-dithiol on Si(553)-Au surfaces*, *Phys. Rev. B* **97**:045417, 2018, doi:10.1103/PhysRevB.97.045417.
- [266] Z. MAMIYEV, F. PFEIFFER, H. PFNÜR, S. SANNA, *Electronic and structural properties of Si(775)-Au*, in preparation 2020.
- [267] F.-C. CHUANG, C.-H. HSU, H.-L. CHOU, C. P. CRISOSTOMO, Z.-Q. HUANG, S.-Y. WU, C.-C. KUO, W.-C. V. YEH, H. LIN, A. BANSIL, *Prediction of two-dimensional topological insulator by forming a surface alloy on Au/Si(111) substrate*, *Phys. Rev. B* **93**:035429, 2016, doi:10.1103/PhysRevB.93.035429.
- [268] J. AIZPURUA, G. W. BRYANT, L. J. RICHTER, F. J. GARCÍA DE ABAJO, B. K. KELLEY, T. MALLOUK, *Optical properties of coupled metallic nanorods for field-enhanced spectroscopy*, *Phys. Rev. B* **71**:235420, 2005, doi:10.1103/PhysRevB.71.235420.
- [269] S. BERNADOTTE, F. EVERS, C. R. JACOB, *Plasmons in molecules*, *The Journal of Physical Chemistry C* **117**, 4:1863, 2013, doi:10.1021/jp3113073.
- [270] H. J. SCHULZ, *Wigner crystal in one dimension*, *Phys. Rev. Lett.* **71**:1864, 1993, doi:10.1103/PhysRevLett.71.1864.
- [271] T. NEUMAN, C. HUCK, J. VOGT, F. NEUBRECH, R. HILLENBRAND, J. AIZPURUA, A. PUCCI, *Importance of plasmonic scattering for an optimal enhancement of vibrational absorption in SEIRA with linear metallic antennas*, *The Journal of Physical Chemistry C* **119**, 47:26652, 2015, doi:10.1021/acs.jpcc.5b08344.
- [272] J. VOGT, C. V. HOANG, C. HUCK, F. NEUBRECH, A. PUCCI, *How Intrinsic Phonons Manifest in Infrared Plasmonic Resonances of Crystalline Lead Nanowires*, *The Journal of Physical Chemistry C* **120**, 34:19302, 2016, doi:10.1021/acs.jpcc.6b05674.
- [273] U. TESCHNER, K. HÜBNER, *IR-Spectroscopic Data of Thin Insulating Films on Semiconductors. New Methods of Interpretation and Analysis*, *physica status solidi (b)* **159**, 2:917, 1990, doi:10.1002/pssb.2221590239.

- [274] M. TZSCHOPPE, C. HUCK, F. HÖT, A. PUCCI, *C70 increases the plasmonic signal of gold-atom chains on Si (553)*, *Surface Science* **678**:32, 2018, doi:10.1016/j.susc.2018.02.007.
- [275] R. TOBIN, *Mechanisms of adsorbate-induced surface resistivity-experimental and theoretical developments*, *Surface science* **502**:374, 2002, doi:10.1016/S0039-6028(01)01978-1.
- [276] J. PISCHEL, O. SKIBBE, A. PUCCI, *Anisotropic Resistance of the Clean and Oxygen-Covered Cu (110) Surface in the Infrared*, *The Journal of Physical Chemistry C* **116**, 26:14014, 2012, doi:10.1021/jp303134r.
- [277] M. HEIN, P. DUMAS, A. OTTO, G. WILLIAMS, *Friction of conduction electrons with adsorbates: Simultaneous changes of DC resistance and broadband IR reflectance of thin Cu (111) films exposed to CO*, *Surface science* **419**, 2-3:308, 1999, doi:10.1016/S0039-6028(98)00815-2.
- [278] B. PERSSON, *Adsorbate-induced surface resistivity and nonlocal optics*, *Chemical physics letters* **197**, 1-2:7, 1992, doi:10.1016/0009-2614(92)86012-7.
- [279] G. FAHSOLD, M. SINTHER, A. PRIEBE, S. DIEZ, A. PUCCI, *Adsorbate-induced changes in the broadband infrared transmission of ultrathin metal films*, *Phys. Rev. B* **65**:235408, 2002, doi:10.1103/PhysRevB.65.235408.
- [280] K. BIEDERMANN, S. REGENSBURGER, T. FAUSTER, F. J. HIMPEL, S. C. ERWIN, *Spin-split silicon states at step edges of Si(553)-Au*, *Phys. Rev. B* **85**, 24:245413, 2012, doi:10.1103/PhysRevB.85.245413.

Curriculum Vitae

Personal Information

Name Zamin Mamiyev
Date of Birth July 21, 1988
Place of Birth Masalli, Azerbaijan

Education

2015 – 2020 Doctoral studies, Gottfried Wilhelm Leibniz Universität Hannover
 Thesis: *Plasmonic excitations and coupling in atomic wires*
2011 – 2013 Master of Science, Baku State University
 Thesis: *Preparation and characterization of CdS nanoparticles on the basis of Maleic Anhydride/Octene-1 co-polymer matrix*
2006 – 2010 Bachelor of Science, Baku State University
 Thesis: *Designing new polymer adsorbates for radioactive ions*
1995 – 2005 Middle School, Masalli, Azerbaijan

Working experiences

2018 – 2020 Scientific Researcher, Institute of Solid State Physics, Gottfried Wilhelm Leibniz Universität Hannover, *Atomar and Molecular Structures (ATMOS) department*
2013 – 2015 Scientific Researcher, Institute of Physics, Azerbaijan National Academy of Sciences (ANAS), *X-ray crystallography and thin film structures laboratories*
2012 – 2013 Scientific Researcher, Faculty of Chemistry, Baku State University
 High Molecular Compounds Chemistry department

List of Publications

- [1] Z. MAMIYEV, S. SANNA, T. LICHTENSTEIN, C. TEGENKAMP, H. PFNÜR, *Extrinsic doping on the atomic scale: tuning metallicity in atomic Au chains*, Phys. Rev. B **98**, 24:245414, 2018, doi:10.1103/PhysRevB.98.245414
- [2] Z. MAMIYEV, T. LICHTENSTEIN, C. TEGENKAMP, C. BRAUN, W. G. SCHMIDT, S. SANNA, H. PFNÜR, *Plasmon spectroscopy: Robust metallicity of Au wires on Si(557) upon oxidation*, Phys. Rev. Mater **2**, 06:066002, 2018, doi:10.1103/PhysRevMaterials.2.066002
- [3] T. LICHTENSTEIN, Z. MAMIYEV, C. BRAUN, S. SANNA, W. G. SCHMIDT, C. TEGENKAMP, H. PFNÜR, *Probing quasi-one-dimensional band structures by plasmon spectroscopy*, Phys. Rev. B **97**, 16:165421, 2018, doi:10.1103/PhysRevB.97.165421
- [4] MICHAEL TZSCHOPPE, CHRISTIAN HUCK, FABIAN HÖTZEL, BENJAMIN GÜNTHER, ZAMIN MAMIYEV, ANDREY BUTKEVIC, CONSTANTIN ULRICH, LUTZ H GADE, ANNAMARIA PUCCI, *How adsorbates alter the metallic behavior of quasi-1D electron systems of the Si(553)-Au surface*, J. Phys.: Condens. Matter **31**, 195001, 2019, doi:10.1088/1361-648X/ab0710
- [5] T. LICHTENSTEIN, Z. MAMIYEV, C. TEGENKAMP, E. JECKELMANN, H. PFNÜR, *Anisotropic 2D metallicity: plasmons in Ge(100)-Au*, J. Phys.: Condens. Matter **31**, 175001, 2019, doi:10.1088/1361-648X/ab02c5
- [6] S. SANNA, T. LICHTENSTEIN, Z. MAMIYEV, C. TEGENKAMP, H. PFNÜR, *How one-dimensional are atomic Au chains on a substrate?*, J. Phys. Chem. C **44**, 122, doi:10.1021/acs.jpcc.8b08600 .
- [7] Z. MAMIYEV, M. TZSCHOPPE, C. HUCK, A. PUCCI, H. PFNÜR, *Plasmon standing waves by oxidation of Si(553)-Au*, J. Phys. Chem. C **14**, 123, doi:10.1021/acs.jpcc.9b01372
- [8] Z. MAMIYEV, S. SANNA, F. ZIESE, C. DUES, C. TEGENKAMP, H. PFNÜR, *Plasmon localization by H-induced band switching*, J. Phys. Chem. C **1**, 124, doi:10.1021/acs.jpcc.9b10688

- [9] Z. MAMIYEV AND H. PFNÜR, *A view on Si(111)-(5×2)-Au with plasmon spectroscopy*, Phys. Rev. B **102**, 07:075421, 2020, doi:10.1103/PhysRevB.102.075438
- [10] NARMINA O. BALAYEVA, ZAMIN MAMIYEV, RALF DILLERT, NAN ZHENG, DETLEF W. BAHNEMANN, *Rh/TiO₂-photocatalyzed acceptorless dehydrogenation of N-heterocycles upon visible-light illumination*, ACS Catal. 2020, **10**, 10, 5542–5553, doi:10.1021/acscatal.0c00556
- [11] D. ABDELBAREY, J. KOCH, Z. MAMIYEV, C. TEGENKAMP, H. PFNÜR, *Thickness-dependent electronic transport through epitaxial nontrivial Bi quantum films*, Phys. Rev. B **102**, 11:115409, doi:10.1103/PhysRevB.102.115409
- [12] Z. MAMIYEV, C. FINK, K. HOLTGREWE, H. PFNÜR, S. SANNA, *Enforced long-range order in 1D wires by coupling with higher dimensions*, submitted (2020)
- [13] Z. MAMIYEV, C. TEGENKAMP, H. PFNÜR, *Plasmon localization by adatoms in gold atomic wires on Si(775)*, submitted (2020)
- [14] Z. MAMIYEV, F. PFEIFFER, H. PFNÜR, S. SANNA, *Electronic and structural properties of Si(775)-Au*, in preparation (2020)
- [15] Z. MAMIYEV, C. TEGENKAMP, H. PFNÜR, *Metal-insulator transitions and instabilities on Si(111)-(5×2)-Au*, in preparation (2020)
- [16] Z. MAMIYEV, C. TEGENKAMP, H. PFNÜR, *Gold atomic chains on Si surfaces: role of substrate and gold coverage*, in preparation (2020)

Acknowledgements

This thesis was carried out between October 2017 and July 2020. Although my Ph.D. fellowship began in May 2015, due to lack of access to the experimental setup, the measurements presented in this thesis started in October 2017. Indeed, the completion of the present dissertation, together with several publications, within a short period of time was the result of extremely hard work, self-motivation, a well-defined scientific plan, and of course, very fruitful collaborative work.

Hereby, I wish to sincerely thank many people who have been involved in the work leading to this thesis. First of all, I would like to thank Prof. Dr. Herbert Pfnür for giving me the opportunity to work on this exciting project and supervising this thesis. I am very grateful for the independence he granted me in his group, which ultimately helped me develop my ability to generate new ideas and thrive as an independent scientist. I also thank Prof. Dr. Simone Sanna and Prof. Dr. Mario Rocca for being co-referees of this thesis.

During my Ph.D. project, I collaborated with many colleagues for whom I have great regard, and I would like to extend my warmest thanks to all those individuals.

I am highly indebted to Prof. Dr. Simone Sanna and his group at the University of Giessen for the fruitful collaborations throughout this project. Without his consistent calculations, this work could not have been realized in its present form. Indeed, discussions with him often led to the development of new perspectives or a deeper analysis of the experimental observations.

I also thank Prof. Dr. Annamaria Pucci and her students Dr. Christian Huck and M.Sc. Michael Tszchoppe at the University of Heidelberg, for their fruitful collaboration to realize the IR experiments on atomic wires.

I am immensely thankful to the NTH-School committee for accepting my application for this Ph.D. position within the School for Contacts in Nanosystems. In particular, I am thankful to Prof. Dr. Rolf Haug for leading such an outstanding school, which really provided me the opportunity to develop my scientific career. I also thank all members of the “School for Contacts in Nanosystems” for many valuable conversations and great time during the workshops.

I would like to thank Prof. Dr. Christoph Tegenkamp for a number of helpful and productive discussions on this topic.

ACKNOWLEDGEMENTS

I would like to thank Dr. Tammo Block and Dr. Eddy Rugeramigabo for all their help during my Ph.D. I very much appreciate their willingness to share their knowledge of the experimental setup and other related subjects.

I am very grateful to Mrs Heike Kahrs, who, during my stay in the group, made all the administrative works simple and a lot of other help. I am also very grateful for all the support I have received from the workshop at the Institut für Festkörperphysik.

I devote my deepest gratitude to my family; it would not have been possible without your support. My mother, who started my passion for science and made a great sacrifice to be far from her son in the last few years. My brother, who supported and encouraged me in every step I have made towards my goals. Special thanks go to my wonderful wife, Dr. Narmina Balayeva, for her unconditional love, support, and patience throughout the past years.